Development of silicon based bottom cell for tandem photoelectrochemical water splitting device structures

Bae, Dowon

Publication date:
2015

Document Version
Publisher's PDF, also known as Version of record

Technical University of Denmark

Development of silicon based bottom cell for tandem photoelectrochemical water splitting device structures

Ph.D. dissertation

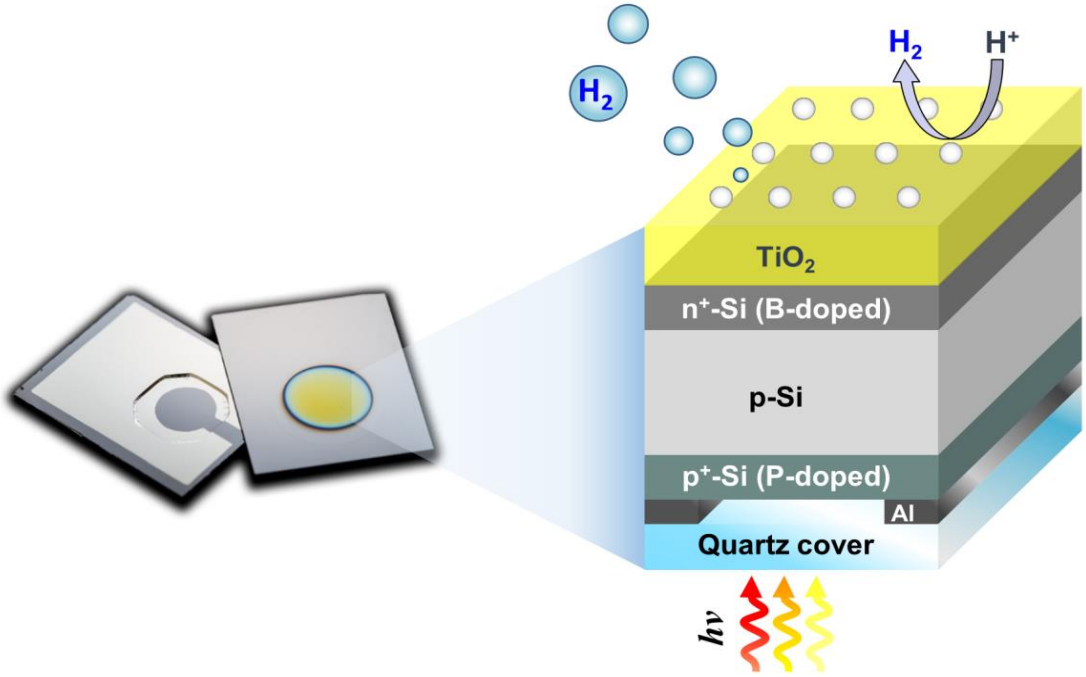

Dowon Bae
Center for Individual Nanoparticle Functionality
Department of Physics
Technical University of Denmark
September, 2015

DTU Physics
Department of Physics

Development of silicon based bottom cell for tandem photoelectrochemical water splitting device structures

Ph.D dissertation

by

Dowon Bae

Center for Individual Nanoparticle Functionality

Department of Physics

Technical University of Denmark

September 2015

Supervisor: Prof. Ib Chorkendorff

Co-supervisors: Prof. Ole Hanse, Prof. Peter C. K. Vesborg

Danmarks Tekniske Universitet

DTU

Preface

The present work has been performed between the 1st of September 2012 and 14th of September 2015 in the Center for Individual Nanoparticle Functionality (CINF) at the Department of Physics of the Technical University of Denmark. I gratefully acknowledge the Danish National Research Foundation for funding the CINF (DNRF54). This PhD project has been carried out under the supervision of Prof. Ib Chorkendorff, Prof. Ole Hansen and Prof. Peter C. K. Vesborg. I would like to thank both Prof. Ib Chorkendorff and Peter Vesborg for giving me great opportunity to work in Denmark with experts at this world class leading group. Particularly, I would like to acknowledge Prof. Peter Vesborg for an in-depth discussion on the research direction and useful suggestions throughout this 3-years-preiod project. In addition, I would like also to thank Prof. Ole Hansen for his guidance for theoretical studies.

A special thanks to Thomas Pedersen (Nanotech, DTU) for the productive collaboration in device fabrication and process design. Most of clean room process has been done in this collaboration. I would like also to thank Prof. Brian Seger for the great assistance in laboratory given during the first few months, and for the time dedicated to proofread my publications included in this thesis. I am very thankful to Bastian Mei and Rasmus Frydendal for their contribution on making of metal oxide catalysts and X-ray analysis. Rasmus is also acknowledged for the translation of the abstract to Danish version.

I would like to thank also Prof. Stacey Bent and Katie Roelofs (currently at DuPont) for making my external research stay in Stanford University very pleasant and productive. I am grateful to Prof. Ib Chorkendorff, Peter Vesborg and Danish Agency for Science, Technology and Innovation for providing me this exciting experience.

Last but not least, I would like to thank my family for staying with me during my PhD study in Denmark which is one of the furthermost countries from their home. Especially, I am grateful to my wife, Yoonjung Kim, for supporting me with the invaluable faith, compassion and love.

Kongens Lyngby,
September 12th, 2015 *Dowon Bae*

Abstract

Photoelectrochemical solar fuel conversion by water splitting is a promising approach to provide clean and storable fuel (hydrogen) directly from sunlight. Tandem water splitting device consisting of two different band gap materials can provide sufficient photovoltage for water splitting. However, state-of-the-art III-V based tandem water splitting devices are too expensive to scale-up due to prohibitive manufacturing cost.

The present dissertation reports the development of cost-effective silicon-based photoanode and photocathode as a narrow band gap bottom cell which is suited to work efficiently in a tandem water splitting configuration. A ring-shaped Al/n^+-Si (or Al/p^+-Si) back contact enables illumination from the side opposing the solid/liquid interface while mimizing series resistance, and allows mimic the actual working condition of bottom cell in a tandem water splitting device. Owing to this light permeable back contact design, Si photoelectrodes were able to perform oxygen and hydrogen evolution successfully. A back-illuminated Al/n^+pp^+-Si photoanode coupled to Co/$NiCoO_x$ protective oxygen evolution catalyst layer showed excellent photocatalytic activity as well as long-term stability in highly concentrated alkaline media, which makes it a prospective candidate for the practical oxygen evolution photoanode. A Si with the same configuration coupled to Ir/IrO_x was evaluated in acid media under the back illumination for the comparative study. For the hydrogen production, an inverted photoelectrode design with Al/p^+pn^+-Si configuration was investigated. From a modelling work, it was found that the balance between charge collection probability and light absorber thickness is an important design parameter, since pn-junction is formed at the solid/liquid interface side. A 50 µm thick thinned Al/p^+pn^+-Si/Ti/TiO_2/Pt photocathode sample showed a maximum photocurrent (17.0 mA cm^{-2}), whereas a 350 µm thick sample showed only 6.1 mA cm^{-2}. In contrast, a 30 µm thick sample showed slightly lower photocurrent due to its limited light absorption. Further modelling shows that surface recombination on the back side of the silicon is the dominant current loss mechanism for the thinned photocathode, and this was proven through the Al_2O_3 passivated thinned sample (Al/Al_2O_3/p^+pn^+-Si/Ti/TiO_2/Pt) which showed 19.0 mA cm^{-2} under the back side illumination.

In addition to these efforts for the realization of practical bottom cell, various approaches has been attempted to improve the electrical quality and chemical stability of Si based photoelectrode. By using carrier-selective contact (Si/SiO_2/pc-Si) design, around 70 mV was

provided additionally compared to the conventional pn-junction design. A high power impulse magnetron sputtering (HiPIMS) grown TiO_2 successfully protected Si photocathode from an alkaline electrolyte (pH = 14) without any loss in photovoltage and photocurrent by providing high film density of the protection layer which is 12% higher than that of TiO_2 grown by conventional DC-sputtering.

Consequently, putting these results together, the demonstrated Si photoelectrode can be stated as a ‘ready-made bottom cell’ for tandem water splitting devices, which can be applied regardless of type of the electrolyte (acid or alkaline) and the required reaction (oxygen or hydrogen evolution).

Resumé

Photoelektrokemisk vandsplitning er en lovende metode til at producere et rent brændsel (hydrogen) direkte fra sollys. Tandem vandsplitningsenheder består af to forskellige båndgabsmaterialer, der kan levere tilstrækkelige fotospændinger til at splitte vand. Desværre er state-of-the-art III-V baserede enheder for dyre til at blive opskaleret, hvilket er på grund uoverkommelige produktionsomkostninger.

I denne afhandling rapporteres udvikling af omkostningseffektive siliciumbaserede fotoanoder og fotokatoder, der kan bruges som bundceller med lavt båndgab. Disse er specielt egnede til tandem vandsplitningskonfigurationer. En ringformet Al/n^+-Si (or Al/p^+-Si) bagkontakt faciliterer belysning fra den modsatte side af væske – fast fase overfladen, samtidig med at seriemodstanden minimeres. Derved efterlignes realistiske betingelser for sådanne celler i tandem vandsplitningsenheder. På grund af det gennemsigtige bagkontaktdesign er det derfor muligt for disse Si fotoelektroder at udvikle ilt og brint. En bagbelyst Al/n^+pp^+-Si fotoanode kombineret med et katalytisk aktivt Co/$NiCoO_x$ beskyttelseslag viste fremragende fotokatalytisk aktivitet og langtidsstabilitet i koncentreret alkalisk medium. Den samme type fotoabsorber blev også testet med Ir/IrO_x som beskyttelseslag og katalysator, hvilket gjorde det muligt at demonstrere bagbelyst fotokatalyse i syre. Disse resultater gør elektrodekonfigurationen til en lovende kandidat som iltudviklende fotoanode.

For brintudvikling blev et inverteret fotoelektrodedesign undersøgt, bestående af Al/p^+pn^+-Si. Ved hjælp af et modelleringsstudie viste det sig at balancen mellem ladningsopsamlingssandsynlighed og lysabsorbertykkelse er en vigtig designparameter, idet en pn-overgang dannes ved væske – fast fase overfladen. En 50 µm tyk Al/p^+pn^+-Si/Ti/TiO_2/Pt fotokatode prøve viste den højeste fotostrøm (17.0 mA/cm^2), mens en 350µm tyk prøve kun viste 6.1 mA/cm^2. I kontrast til disse resultater viste en 30 µm tyk prøve en smule lavere fotostrøm på grund af mindre lysabsorbering. Yderligere modellering viste at overfladerekombination på bagsiden af Si er den dominerende tabsmekanisme for de tyndede fotokatoder og dette blev bevist via Al_2O_3-passiverede, tyndede prøver (tyk Al/Al_2O_3/p^+pn^+-Si/Ti/TiO_2/Pt, som viste 19.0 mA/cm^2 under bagsidebelysning.

Udover disse forsøg på at realisere en bundcelle, blev flere forsøg gjort på at forbedre den elektriske kvalitet og kemiske stabilitet af siliciumbaserede fotoelektroder. Ved at benytte et ”carrier-selective” kontakt design (Si/SiO_2/pc-Si), blev en ekstra spænding på 70 mV leveret, sammenlignet med det

konventionelle pn-overgangsdesign. ”High power impulse magnetron sputtering” (HiPIMS) TiO_2 på Si fotokatoder, blev med succes brugt som beskyttelseslag til test i alkalisk elektrolyt (pH = 14). Beskyttelseslaget, der har 12 % højere tæthed end ved konventionel sputtering, medvirkede til konstant ydelse uden tab i fotostrøm og fotospænding.

Når disse resultater kombineres, er de undersøgte Si fotoelektroder at betragte som færdiglavede bundceller til brug i tandem vandsplitningsenheder, der kan benyttes uanset elektrolyt eller reaktion (ilt eller brintudvikling).

Thesis outline

Chapter 1. Introduction and background

World energy consumption trend and resource breakdown together with related global warming and energy shortage issues are described. As an extension of this discussion, utilization of solar energy and photocatalytic water splitting is suggested as a solution to provide clean and storable chemical energy.

Chapter 2. Experimental setups and analysis techniques

Experimental setup and various analysis techniques employed in this work are described in this chapter. (Photo) electrochemical setup, x-ray analysis (e.g. XPS, XRD, XRR), composition analysis (e.g. EDX), gas chromatography, microscopic analysis techniques are introduced.

Chapter 3. Using Si as a photoanode bottom cell

Silicon based photoanodes with IrO_x, CoO_x and $NiCoO_x$ oxygen evolution catalyst are investigated under back-illumination. The present photoanodes configuration successfully showed water oxidation reaction in alkaline (CoO_x, $NiCoO_x$) and acid (IrO_x) media. Time-dependent photoelectrochemical behaviour of the photoanode and structural change of the $NiCoO_x$ catalyst are shown in this chapter.

Chapter 4. Using Si as a photocathode bottom cell

Silicon based photocathodes with Pt hydrogen evolution catalyst are investigated under the same condition used in previous chapter. A pn-junction is formed at the side opposing the light illumination, and thus analytical modelling is provided to obtain optimized thickness and required surface recombination rate for minimizing carrier loss. The modelling work is verified using photochathode with various thickness and surface passivation treatment.

Chapter 5. Strategies for improving Si photocathode performance

Carrier-selective contact design and high power impulse magnetron sputtering (HiPIMS) technique are introduced as alternative method for improving the electrical performance and photoelectrochemical stability of the silicon-based photocathode, respectively.

Chapter 6. Summary and outlook

Significances and impact of the present silicon bottom cell are listed and prospective tandem water splitting device designs with the silicon bottom cell are demonstrated.

List of publications

List of appended publications

1. **D. Bae**, T. Pedersen, B. Seger, M. Malizia, A. Kuznetsov, O. Hansen, I. Chorkendorff, P. C. K. Vesborg, *Back-illuminated Si photocathode: a combined experimental and theoretical study for photocatalytic hydrogen evolution*, Energy & Environmental Science, 8 (2015) 650-660. DOI: 10.1039/C4EE03723E

2. B. Mei, A. A. Permyakova, R. Frydendal, **D. Bae**, T. Pedersen, P. Malacrida, O. Hansen, I. E. L. Stephens, P. C. K. Vesborg, B. Seger, I. Chorkendorff, *Iron-treated NiO as a highly transparent p-type protection layer for efficient Si-based photoanodes,* Journal of Physical Chemistry Letters, 5 (2014) 3456-3461. DOI: 10.1021/jz501872k

3. **D. Bae**, B. T. Mei, R. Frydendal, T. Pedersen, B. Seger, O. Hansen, P. C. K. Vesborg, I. Chorkendorff, *Back-illuminated Si based photoanode with nickel cobalt oxide catalytic protection layer*, Journal of Material Chemistry A (submitted).

4. **D. Bae**, S. Shayestehaminzadeh, E. B. Thorsteinsson, T. Pedersen, O. Hansen, B. Seger, Peter C.K. Vesborg, S. Olafsson, I. Chorkendorff, *Protection of Si photocathode using TiO_2 deposited by high power impulse magnetron sputtering for H_2 evolution in alkaline media*, Solar Energy Materials and Solar Cells (submitted).

List of other publications

1. B. Mei, T. Pedersen, P. Malacrida, **D. Bae**, R. Frydendal, O. Hansen, P. C. K. Vesborg, B. Seger, I. Chorkendorff, Crystalline TiO_2: *A generic and effective electron-conducting protection layer for photoanodes and -cathodes*, Journal of Physical Chemistry C, 119 (2015) 15019-15027. DOI: 10.1021/acs.jpcc.5b04407

2. E. Kemppainen, A. Bodin, B. Sebok, T. Pedersen, B. Seger, B. Mei, **D. Bae**, P. C. K. Vesborg, J. Halme, O. Hansen, P. D. Lund, I. Chorkendorff, *Scalability and feasibility of photoelectrochemical H_2 evolution: the ultimate limit of Pt nanoparticle as an HER catalyst*, Energy & Environmental Science (accepted).

Table of contents

Chapter 1

1. Introduction and background

1.1 World energy resources

The drastic increase in world population in the last centuries raises the enormous energy consumption, and consequently the tremendous effort toward the securing economical energy sources. According to recent study, world energy consumption (Figure 1.1) mostly based on fossil fuels, such as oil, gas and coal, and furthermore, is increasing. During the last 10 years the global energy consumption has been increased steadily by 22.4% (from 2004 to 2014). The continuing trend is due to several factors including the rapid growth in the non-industrialized word and the developing countries [1]. Energy consumption increases in those countries are closely related to an increase in living standard, and this means that as the non-industrialized and developing countries increase their consumption to obtain a standard of living closer to that of the industrialized world, the global energy consumption is bound to steadily increase. As the population in those countries continue to grow, this trend will be maintained for several decades. In addition to this, an increase in the explosive growth of the heavy and chemical industries in the Asian countries including China and India is also correlated to an increase in global energy consumption, despite the reduced consumption rates in Europe and North America [2]. Fortunately, according to the United Nations' World Population Prospects report [3], the average birth rate tends to drop below the level needed to sustain the current population around 2050, reaching 9 billion in world population. However this still requires enormous energy supply equivalent to 60 TW (~ 525,600 TWh year) to sustain the population.

Among the various energy sources, fossil fuel including oil, gas and coal takes up around 94% of the overall energy consumption (Figure 1.1). However, the amount of these fossil fuels is practically limited due to its geological slow process [4], and it is expected to reach a maximum, so called 'peak oil', after which the rate of production is expected to enter terminal decline in the future [5]. Some studies [6,7] predict that the oil will last for a number of decades taking the new

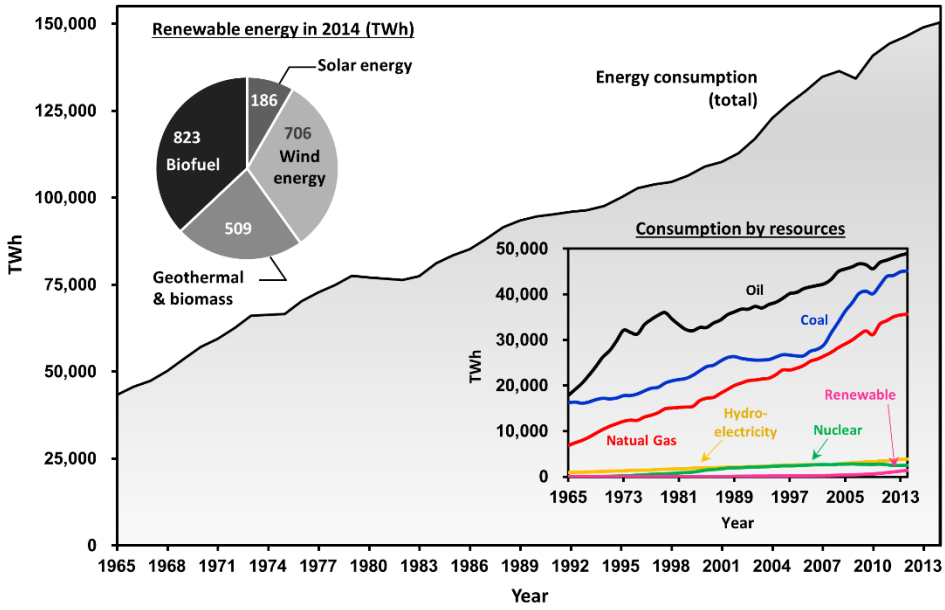

Figure 1.1 World energy consumption between 1965 and 2014, expressed in TWh (terawatt hour) [2]. One TWh equals approximately 0.086 MTOE (million tonnes of oil equivalent). Energy consumption by resource type is also shown as an inset (right bottom). Category 'renewable' contains biofuel, solar energy, wind energy and geothermal & biomass. Breakdown of this renewable energy by its source also shown as an inset (left top).

oil sources, such as shale oil [8], in which oil companies are actively investing in recent years, into account. According to the British Petroleum review [2], the reserve-to-production ratio (ratio between the proved reserve and the annual production of oil) equals 53.83 years. Natural gas represents a somewhat clean alternative, and currently it is widely used as a transportation fuel, mostly in public transit. World total proven natural gas reserves at the end of 2014 stood at 187.1 trillion cubic meters (tcm), sufficient to meet 54.1 years of global production [2]. Coal is the unique type of fossil fuel that shows estimated reserves-to-production ratio (R/P ratio) that exceed 100 years by far the largest R/P ratio for any fossil fuel (110 years at the end of 2014 [2]). According to newly released data [9], China's coal use accounts for 49% of global coal consumption – almost as much as the rest of the world combined. Electric generation is responsible for around 80% of entire annual electricity generation in China, and it is expected to retain as a major source of energy at least through the next several decades [9].

The use of fossil fuels is relevant to a number of issues. Carbon dioxide (CO_2) emission into the atmosphere is the representative environmental issue owing to the consumption of the fossil fuels. As is well known, CO_2 is the primary greenhouse gas emitted through the combustion of fossil fuels. Emissions and removal of CO_2 by natural processes tend to balance. However, adding CO_2

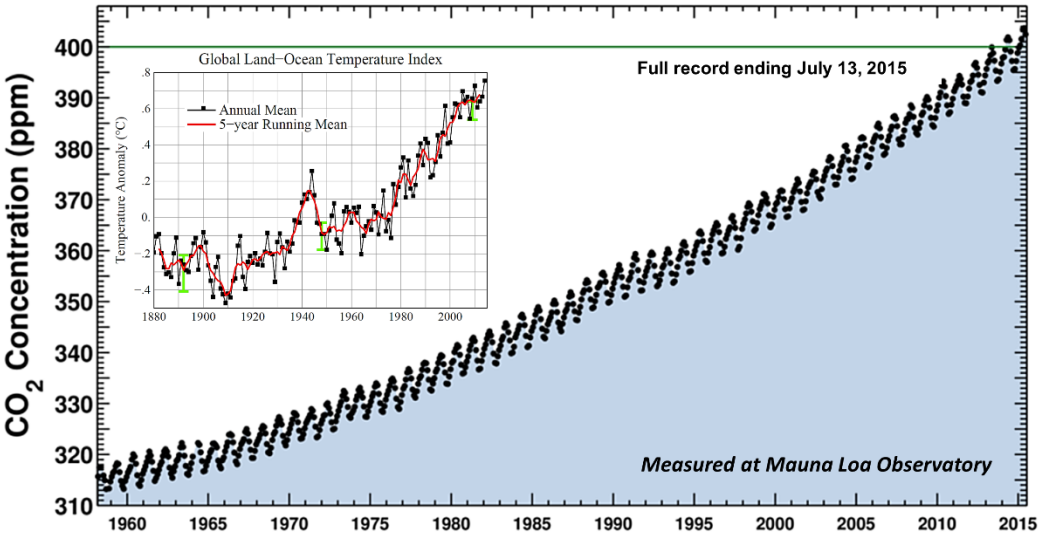

Figure 1.2 Atmospheric CO_2 concentration in ppm measured at Mauna Loa Observatory under Scripps CO_2 program. Global land-ocean temperature index is also shown as an inset (top left). Reproduced from the references [11] and [12].

by human activities has contributed substantially to the climate change since the industrial revolution began around 1750 [10]. The emitted CO_2 into the atmosphere is not fixed by nature at a fast rate and therefore it stays in the atmosphere. The continuous measurements taken at the Mauna Loa Observatory in Hawaii by Scripps CO_2 program (Figure 1.2) [11] show concentrations that CO_2 underwent a regular seasonal cycle, reflecting the seasonal growth and decay of land plants in the northern hemisphere, as well as a regular long-term rise driven by the burning of fossil-fuels. During ice ages, the CO_2 levels were around 200 ppm, and during the warmer interglacial periods the levels were around 280 ppm according to the previous study [12], while the current level in 2015 is around 400 ppm. Part of the emitted CO_2 has been taken up by ocean, causing a slight acidification of the sea water.

Above all, global mean temperature increase with high probability stems from the increased release of CO_2 in the atmosphere [13]. This global warming of the earth leads to the loss of the sea ice and rise of sea level consequently. The data shown in the inset of Figure 1.2 taken from the online report by NASA [14] demonstrates that increase of CO_2 emission in atmosphere well correlates with the global land-ocean temperature increasing tendency (~ 0.2˚C/decade since 1980). Unfortunately, a severe reduction in use of fossil fuels will not be succeed in a near-term period despite the international effort towards the using non-fossil energy sources, considering

the steady increase in needs of abovementioned developing countries that require to use more energy for increasing living standard and keeping their energy-intensive industries.

Among the non-fossil fuels, hydroelectricity energy represents a reliable and clean alternative energy source. As shown in an inset of Figure 1.1, the total hydroelectric energy consumption has increased steadily from 922.5 to 3884.6 TWh in the period 1965 – 2014. However, construction of dams for the hydroelectric power plant requires environmental disruption of the land and surrounding ecosystem. Moreover, the energy production is affected by seasonal variations and unpredictable disaster, such as heavy drought. Nuclear fission energy has often been considered as an efficient and sustainable energy. However, there also has been a lot of controversy over the further operation of this energy source due to its potential risks, such as radiation exposure during operation and disposal of nuclear waste. Actually, the well-known disaster in Fukushima in Japan (2011), in which 3 nuclear reactors has been melt down subsequently due to the tsunami [15], tip the balance towards negative opinions. And this case is starting to make the many countries reconsider their energy policy. In addition, the fact that there are no permanent facilities has influenced governmental policies, even though approximately 270,000 metric tons of high level radioactive waste has accumulated in 30 countries and an additional 9,000 metric tons are being added annually [16]. Japan has closed existing nuclear power plants to meet the public demands, and Germany aims to close all nuclear power plants by 2022 [17]. Such international actions has been reflected in reduction of nuclear energy consumption trend in the period of 2011 – current (see Figure 1.1). Global nuclear energy consumption has decreased from 2767.28 (2010) to 2536.84 TWh (2014), which corresponds to a decrease of 8.3%.

Above mentioned problems of the traditional non-fossil fuels emphasizes the need of introducing of other types of technologies which can provide us clean and sustainable energy with TW scale within a foreseeable future. Renewable sources, such as solar, wind, geothermal and bio fuel, can be considered as candidates which meet abovementioned requirements. However, only 1% of total energy consumed in 2014 has produced from the renewable energy sources due to the undeveloped infrastructure and the lack of economies of scale [18] that most people or groups don't have the resources to front without government subside policies that makes the renewable energy sources uncompetitive. Despite of such current situation, luckily, renewable energy is in

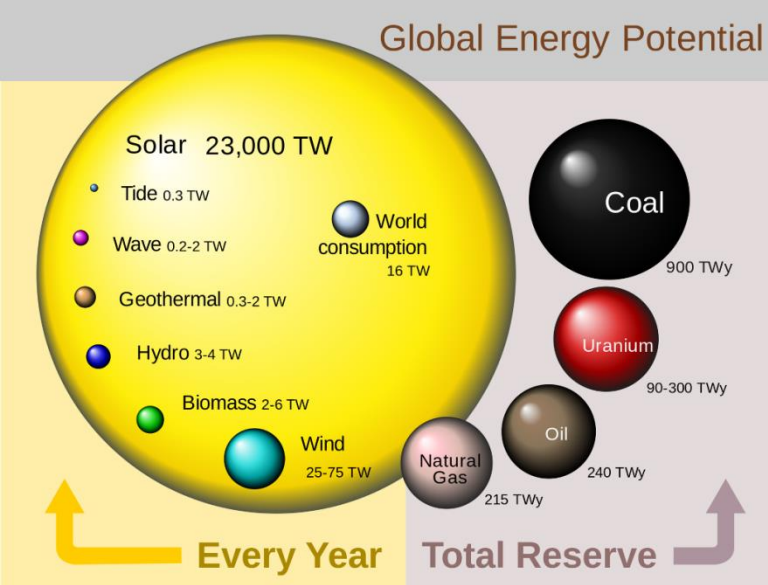

Figure 1.3 Global energy potential breakdown by resource. Renewable energy sources are arranged on the left side of the figure, and traditional fossil fuel and nuclear source (uranium) are arranged on the right side of the figure. Values of the renewable energy sources is in TW per year, not total reserve. Reproduced from the reference [19].

the growing stages, showing approximately 4.2% growth during the last 10 years while the fossil fuels showed only 1.2% during the same period. Among the renewable energy sources, solar energy is responsible for this rapid growth rate of the energy consumption, having growth rate by 71.3% in 2014 compared to that in 2004. Solar energy, which is provided externally, in form of solar irradiation and/or wind energy seems a viable solution, since we cannot revert to an energy consumption level that is sustainably supplied from earth.

1.2 Solar energy and photocatalysis

1.2.1 Solar energy

The amount of irradiated energy from the Sun is sufficiently huge that an effective utilization of this energy source can be enough to cover most of global energy demands. As shown in Figure 1.3 [19], annual solar energy potential is around 23,000 TW, whereas global energy consumption level merely reaches 16 TW, demonstrating the Earth receives the energy from the Sun in just few hours, which surpasses the annual world energy consumption. This number is even10 times higher than the sum of the reserve of all traditional fossil fuels and uranium (nuclear energy). This tremendous energy is generated in the core of the Sun due to the conversion of the hydrogen into helium by nuclear fusion process, and diffuses into the Earth in form of kinetic energy of

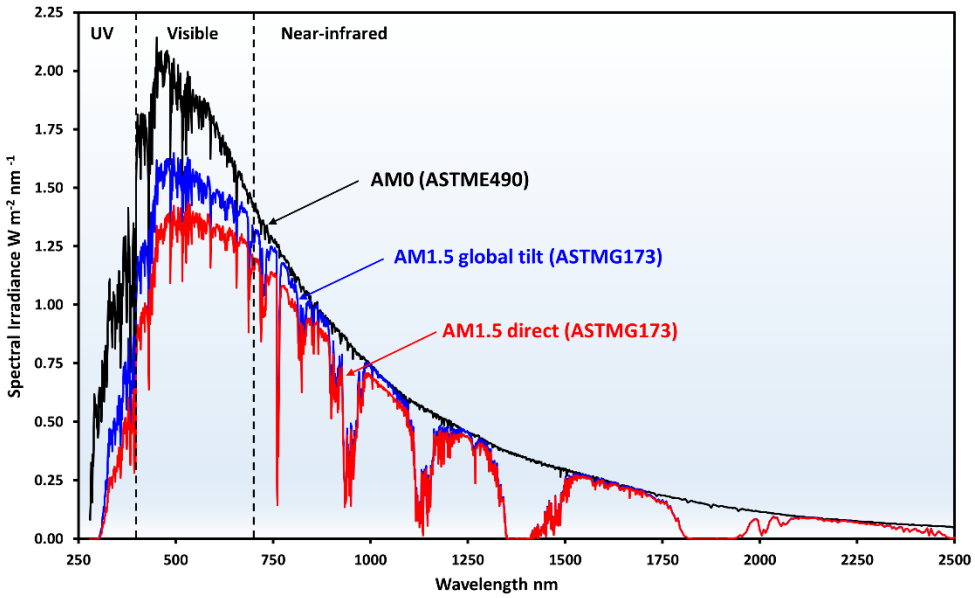

Figure 1.4 Solar spectrum irradiances: Extraterrestrial (black, AM0), AM 1.5 global on 37° tilted surface (blue, AM1.5 global tilt), and AM 1.5 direct normal (red). Reproduced from the reference [20].

photons (light irradiation). The solar light, as already well known, is responsible for the all climate changes as well as energy for the all living organism directly and/or indirectly.

The solar light irradiated to the Earth has a typical spectral behavior due to the temperature of the Sun (black body radiation). Furthermore, the atmosphere of the Earth including air mass and its compound, such as H_2O and O_2, affect the light spectrum by the scattering and absorption, and this leads to a specific solar spectrum which can be obtained at the sea level of the Earth for standard condition (AM 1.5, see Figure 1.4 [20]). There are two types of standard spectra: a standard direct normal spectral irradiance and a standard global for a 38˚ tilted surface from horizontal (hereinafter AM 1.5G). The direct normal spectrum is the direct component contributing to the total global (hemispherical) spectrum without diffused radiation. The total power density of AM 1.5G is 1000 W m^{-2}, of which 850.1 W m^{-2} is concentrated in wavelength range of 280 – 1100 nm, corresponding to the energy between 4.1 and 0.9 eV.

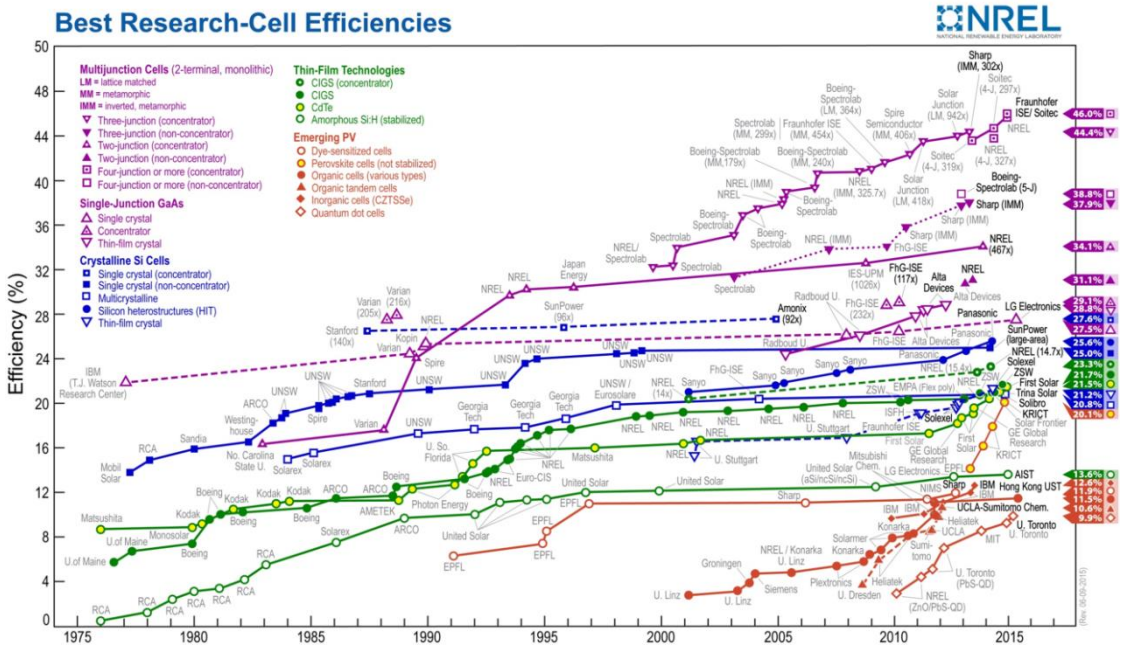

Figure 1.5 The increase in efficiency of lab-scale PV cells based on different types of materials and device structures, i.e. junction numbers between 1975 and 2015.

This solar energy can be readily converted into the ready-to-use energy, such as electricity, using photovoltaic (PV) effect of semiconductor materials. When we bring p-type and n-type semiconductors together in form of p-n junction, diffusion occurs on the surface between them. Electrons start to diffuse from n-type to p-type. Similarly, holes diffuse from p-type region to n-type region. This diffusion creates an electron-hole free region in a very short distance at the interface region, so called depletion region, and the junction creates a slope in the resulting energy bands, through which electrons at a higher energy level subsequently "roll down" into a lower energy band, generating the photo current. More detail description with schematic drawings will be discussed later in this chapter. There has been a huge increase in energy conversion efficiency of this photovoltaic-based solar cell over the past few decades as shown in Figure 1.5 [21]. Among the various types of solar cells, crystalline silicon PV cells, with over 60 years of development, have the longest production history and now account for the largest share of production, comprising up to 92% of all the solar cells produced in 2014 [22]. Silicon (Si) is one of the most abundant resources on Earth, representing 26% of the crust. This abundance as well as safety of Si as a resource grants the Si a dominant position among all the various kinds PV materials. As shown in the lab-scale solar cell efficiency chart in Figure 1.5, single junction based crystalline Si PV cell (non-concentrated) has a record efficiency of 25.0%, whereas the

other type of commercially available thin film based solar cells, such as CdTe and CIGS ($Cu(In,Ga)Se_2$) just passed over the efficiency of 21% (21.5% and 21.7%, respectively). Among the emerging PV solar cells, the development speed of perovskite solar cell (organometallic halide perovskite) is noteworthy. The lead halide based perovskite ($CH_3NH_3PbI_3$) solar cells are rapidly catching up with the conventional solar cells, reaching 20.1% just few years after the first certified record has been reported in 2013.

Despite of these recent achievements in solar cells, a disadvantage of PV based technology, which is given by the difficulty of storing and transferring the converted electric energy, hinder the wide use of this technology as a major renewable energy source. The state-of-the-art commercial Li-ion battery shows about 60 times less gravimetric density (Wh/kg) than that of gasoline [23], so that the electric energy converted by solar cells can be stored only for the limited period. This disadvantage of conventional PV technology has aroused the need of the direct conversion of the incoming solar energy into a chemical fuel, such as hydrogen, methane and so on, which can be stored and has higher energy density. Solar water splitting is one of the representative technology, by which direct production of hydrogen from the water can be realized utilizing the solar radiation. Along with the recent dissemination of the fuel cell as an alternative power source for the vehicles, the solar water splitting comes into the spotlight in recent years.

1.2.2 Solar fuel and photocatalysis

The previous section described that we need to rely on solar energy in somewhat storable form in order to solve emerging energy consumption issue in the future. Since the focus of the present thesis is the development of photoelectrochemical (PEC) water splitting device, the fundamental of photocatalysis and water splitting reaction will be described in this section.

Photocatalytic water splitting is oxidation of water into oxygen and protons, similarly to the photosynthesis in nature, but unlike in plants, the protons are reduced to hydrogen. PEC water splitting device is defined by performing a water splitting reaction under the light illumination. The light, in this case, is the energy source to promote the reaction by the charge generation in the semiconductor much like the applied bias potential does in electrochemical water splitting reaction. The chemical equations for the water splitting reaction are shown in Figure 1.6.

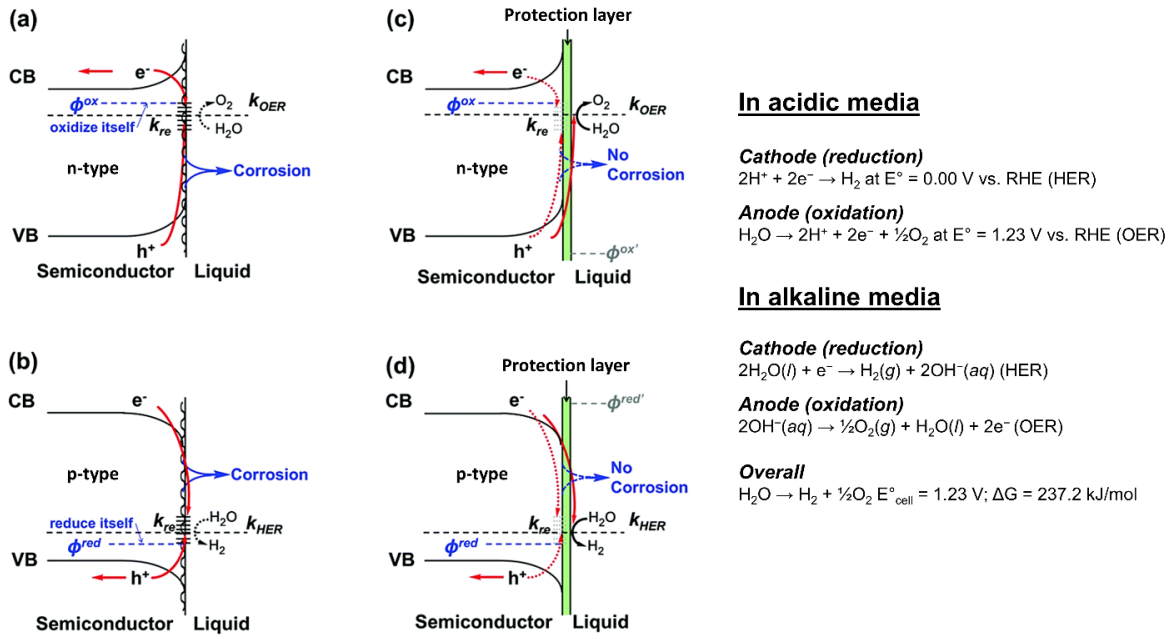

Figure 1.6 Schematic band diagram for n-type (a, c) and p-type (b, d) semiconductors interacting with an electrolyte which has redox couple ($H_2O \leftrightarrow O_2$). Schemes c and d well demonstrate how to prevent the corrosion of absorber layer by having a protection layer having oxidation potential (Φ_{ox}) positive of the VB of the absorber material (negative of CB in case of n-type material). Chemical reactions on cathode and anode in both acidic and alkaline media are also described in right side. Reproduced from the literature [24].

As described in Figure 1.6, the anode performs the oxygen evolution reaction and cathode performs the hydrogen evolution reaction in both the acidic and alkaline media. It is obviously seen from the Gibbs free energy that the overall water splitting is an uphill reaction, which means this reaction will not be driven spontaneously in nature, and a minimum of 1.23 V (at 25˚C and 1 atm standard condition) is required to drive the reaction on the assumption that ideal catalysts are applied at the semiconductor/liquid junction. For the hydrogen evolution (HER), platinum (Pt) is the most widely used catalyst having 0V overpotential (potential difference between a thermodynamically defined reduction potential and the experimentally observed redox potential). In case of the oxygen evolution reaction (OER), state-of-the-art catalysts are dominated by oxide catalysts based on the scarce element, such as RuO_2 and IrO_2, which have overpotential of 0.2 – 0.3V to drive the reaction [25]. In this respect, it's obvious that photovoltage at least ≥ 1.43V is required to drive water splitting reaction. Furthermore, this number increases to operate water splitting system due to the extra potential required for the feasible current level.

Unlike the PV cell's solid/solid configuration, PEC device has semiconductor/electrolyte (solid/liquid) interface that leads to the formation of a built-in potential, upon which photovoltage can be generated at the junction. As shown in Figure 1.6a and b, semiconductor's Fermi level (E_F) equilibrates with the redox potential in the electrolyte when they are brought into contact. This interaction at the solid/liquid junction leads to the depletion region due to the deficiency of the majority carrier at the semiconductor's surface. Consequently, the conduction band (CB) and valence band (VB) downwards and upwards for the n-type and p-type semiconductors, respectively. This band bending causes a formation of built-in potential (V_{bi}) at the solid/liquid interface. When the illumination is externally applied on the semiconductor, the E_F is divided into electron quasi-Fermi level ($E_{F,n}$) and hole quasi-Fermi level ($E_{F,p}$), and the difference between these levels equals to the photovoltage (V_{ph}) that can be produced by the given solid/liquid junction. Actually, most common semiconductor materials are thermodynamically unstable and photocorrosion occurs when the potential for the material oxidation (Φ_{ox}) is more negative than the oxygen evolution potential, E_{OER}, as shown in (Figure 1.6a). Similar arguments can be made for a p-type semiconductor which will be act as a photocathode in PEC condition (Figure 1.6b). Alternatively, when Φ_{ox} is positive of the VBM, the material is thermodynamically stable. Thus, a protection layer, which has its Φ_{ox} of the surface layer is positive than the VB of the photoabsorber (photoanode), is commonly used. TiO_2 is the most representative protection layer which has been used for photocathode as well as photoanode [26]. When used as a photoanode protection layer, Φ_{ox} of TiO_2 will be more positive than the VB of the underlying photoabsorber material, hence it protects photoanode during the PEC condition.

A single wide band gap (E_g) semiconductor would be sufficient to realize the overall water splitting. Since there always is a loss of 0.5 ~ 0.7 eV for the recombination of charge carriers and thermodynamic limitations known as Shockley-Queisser limit [27] in the semiconductor and since an overpotential of about 0.2 ~ 0.3 eV, as mentioned above, is required for the oxygen evolution, a band gap greater than 2.0 eV is needed for the overall water splitting reaction. However, semiconductor absorbs the energy of a photon which is equal to or greater than its band gap, hence, as expected, efficiencies are low for the wide E_g materials since few electron-hole pairs are generated. In theory [27], semiconductor with E_g of 2.0 eV can provide only around 15 mA cm^{-2}, and this corresponds to solar-to-hydrogen efficiency (STH%) of 18.5 % in

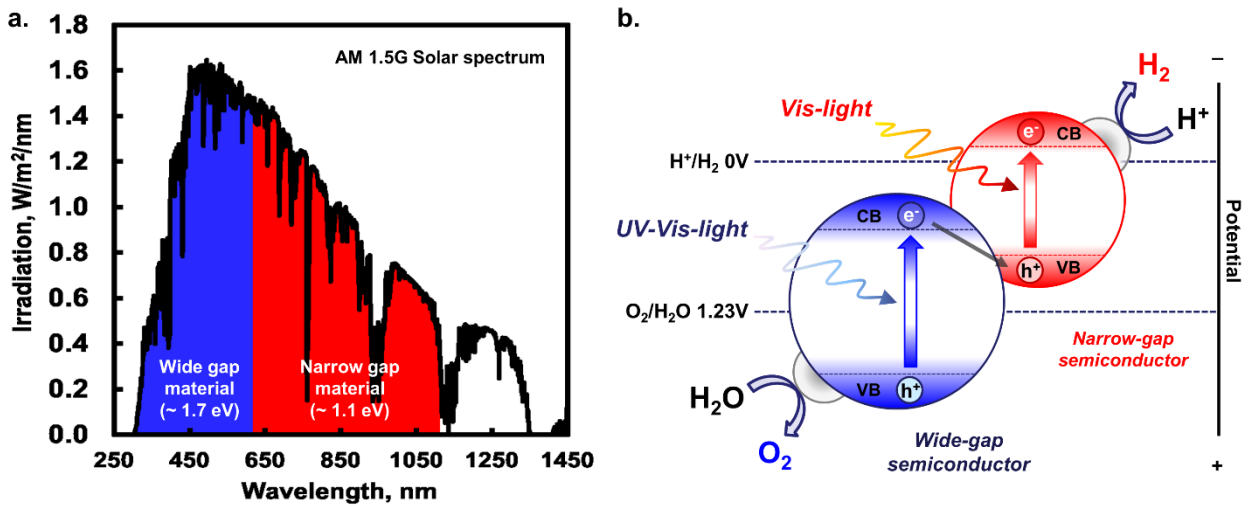

Figure 1.7 Solar spectrum (AM 1.5G) coverage by dual absorbers (a) based on a Z-scheme (b). The scheme b illustrates the carrier transfer along the band alignment under incident light. The short wavelength part of the light spectrum is absorbed by wide gap material to oxidize water, while the longer wavelengths are absorbed by the narrow gap material to produce H_2 gas. The reserved case (wide gap – for hydrogen evolution; narrow gap – for water oxidation) is also possible.

ideal case. Considering that potential competitors, such as PV cells, currently demonstrate higher energy conversion efficiency, using single semiconductor would not be a viable approach for commercialization of this technology. This obstacle arouses a need of more wise approach, such as dual band gap (in tandem) structure to improve the situation.

1.2.3 Tandem configuration for water splitting device

This section is partly based on our recent publication [28].

As mentioned in previous section, increasing E_g of semiconductor to provide sufficiently V_{ph} leads to the low photocurrent (J_{ph}) due to the optical loss. Dual photo-absorber approach (sometimes called Z-scheme), having two semiconductors of different E_g, can be considered as an alternative way to achieve wide spectral coverage as shown in Figure1.7. Effectively, the dual-absorber system works by series-connecting the wide bandgap- and narrow bandgap-cells enabling a higher total voltage at the expense of current density. Theoretically, this tandem configuration with 1.7 + 1.0 eV band gap combination can lead STH% up to 28 % [29], whereas single device barely can perform ~ 11.5 % [30] at E_g = 2.2 eV.

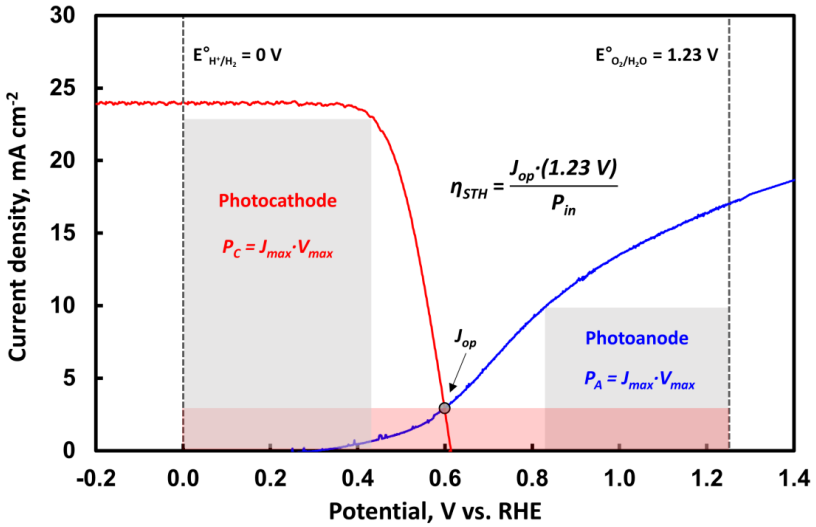

Figure 1.8 Overlaid current density-potential (I-V) behavior for photocathode (red) and an photoanode (blue), with overall efficiency projected by the power generated $P_{STH} = J_{op} \cdot (1.23\ V)$ (red box) by the overall water splitting device.

The overall water splitting reaction of the tandem structure would take place only if sum of photovoltage from both photocathode and photoanode is over 1.23 V. Once V_{ph} of the integrated tandem structure is higher than this value, then the overall STH% is determined by operating current density (J_{op}) that can be estimated by the intersection of I-V curves (see Figure 1.8). The highest efficiency for the tandem device will be obtained when this intersect closest to their individual maximum power points ($P_{max} = J_{mp} \cdot V_{mp}$), i.e. high fill factor (FF). Increasing the FF

for one or both of the photoelectrodes (photocathode and photoanode) has a significant effect on the STH%, due to the steep increase in J_{op} that are produced by small changes in the FF. For the PEC device, the FF mainly depends on the kinetics of catalyst, the series resistance of the device. An efficient catalyst having low overpotential for the chosen reaction (HER or OER) performs steep increase in J_{ph}. Series resistance has three causes: firstly, the bulk resistance of photoabsorber; secondly, the contact resistance between the ohmic contact at the back side and the photoabsorber; and finally the resistance of the contact resistance between the top layer (for instance, protection layer) and the catalyst.

To build-up a practical PEC device, consideration of the ohmic drop, which is originated from the resistance of the electrolyte, also should be important. To minimize this ohmic loss, acidic (low pH) or alkaline electrolytes (high pH) are widely used. However, there is a trade-off between the benefits of the using these concentrated electrolytes and the risk of degradation of

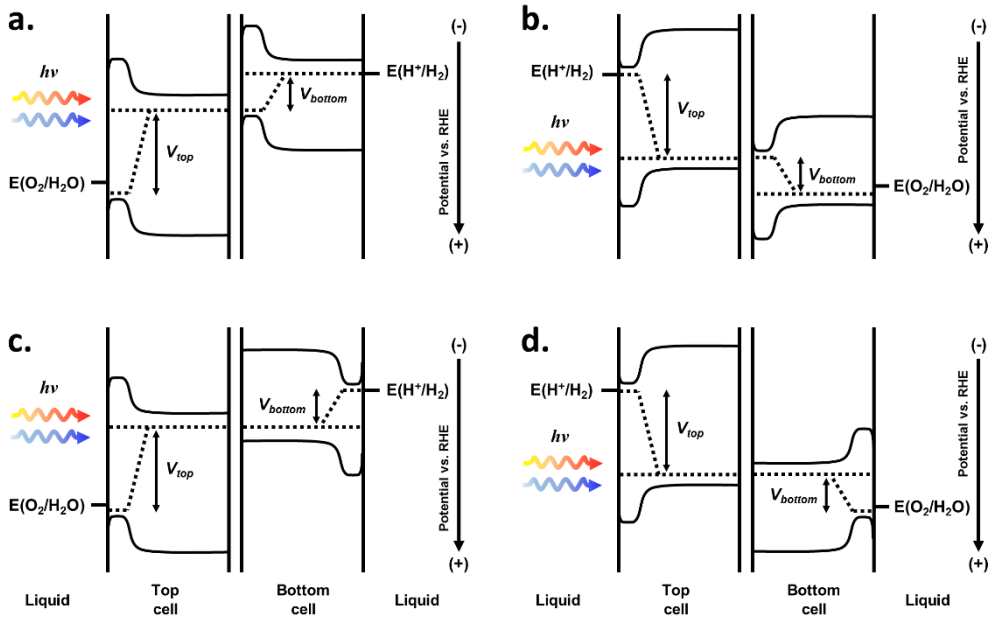

Figure 1.9 Schematic energy band diagrams of tandem PV assisted PEC system for the configuration (a) with photoanode at the light incoming side (Type I – a and c) and photocathode at the light incoming side (b and d). These configurations also can be categorized as: buried junction (bottom cell in a and b) and semiconductor/liquid junction (bottom cell in c and d).

the device due to the corrosion or oxidation of the semiconductor. A reasonable way to avoid this issue is given by a conducting protection layer. As mentioned earlier, previous research [26], has shown that TiO_2 can be used as an intermediate layer between the photocathode and the catalyst with good chemical stability at pH 0 as well as pH 14 [31]. For the photoanode side, Ni based p-type metal oxides, such as NiO [32] and $Ni_xFe_{(1-x)}O$ [33,34], are most widely used in recent year.

Figure 1.9 illustrates the configurations, in which a photocathode and a photoanode are connected back-to-back with an Ohmic contact (or recombination junction). These configurations demonstrate how the Z-scheme water splitting can be realized in practical tandem device. The photogenerated minority-carrier electrons drift and diffuse to the photocathode/electrolyte interface and reduce H^+ to H_2 (HER), whereas the photogenerated minority-carrier holes drift and diffuse to the photoanode/electrolyte interface and oxidize water to O_2 (OER). The majority carriers (holes in the photocathode and electrons in the photoanode) recombine at the recombination junction that connects both photoelectrodes back to back. In general, recombination junction is composed of two different conductivity type (n^+/p^+) to recombine holes from the top cell and electrons from the bottom cell. The key feature is to make valence band edge of p^+ layer well align with conduction band edge of n^+ layer. Simply forming

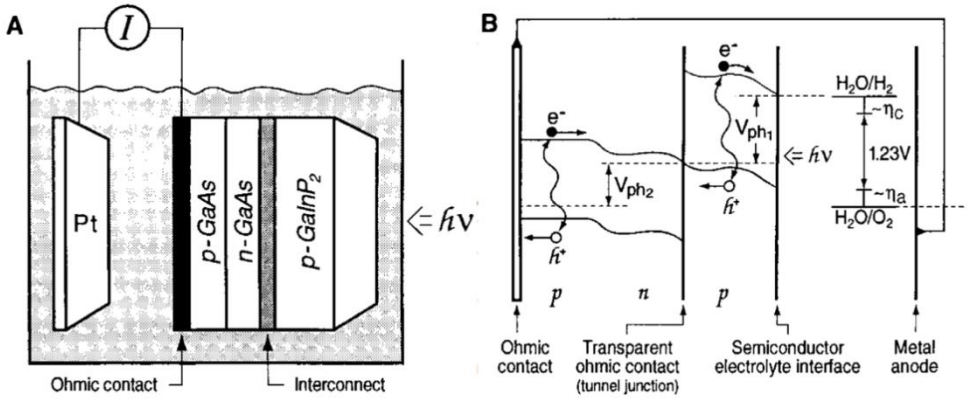

Figure 1.10 Schematic of the PEC device consisting of p-Ga0.52In0.48P on a GaAs PV cell (a), and band diagram of this device illustrating how charged carriers are transferred. Reproduced from the reference [35].

an Ohmic contact also can be a solution. Depending on the reaction type at the light-illumination side, tandem water splitting devices can be categorized by 2 types: Type I (a,c) has a photoanode for OER at the light incoming side and a photocathode for HER at the side opposing the light irradiation, and type II (b,d) is the other way around. In case of photoelectrodes with pn-junction, these devices also can be categorized by the pn-junction position: Buried junction device (bottom cells in a,b) whose pn-junction at the semiconductor/liquid interface pn-junction is formed on the light incoming side, and unburied junction device (bottom cells in c,d) pn-junction at the semiconductor/liquid interface. The selection of device configuration should be determined considering electrical, optical properties, and chemical stability of materials which will constitute the tandem device.

1.2.4 Selected state of the art water splitting devices

This section is partly based on our recent publication [28].

In the following section, three of the state of the art tandem water splitting devices are described. They have been selected because they are representative of tandem device strategies for PEC water splitting, and inspired experimental plans of the present thesis.

In 1988, Turner's group in NREL (National Renewable Energy Laboratory) demonstrated a dual band gap water splitting device using III-V semiconductors in tandem configuration [35]. The device consists of p-$GaInP_2$ grown on the GaAs PV cell and Pt plate connected with wire (see Figure 1.9), showing an impressive STH% of 12.4%. However, this device showed a poor

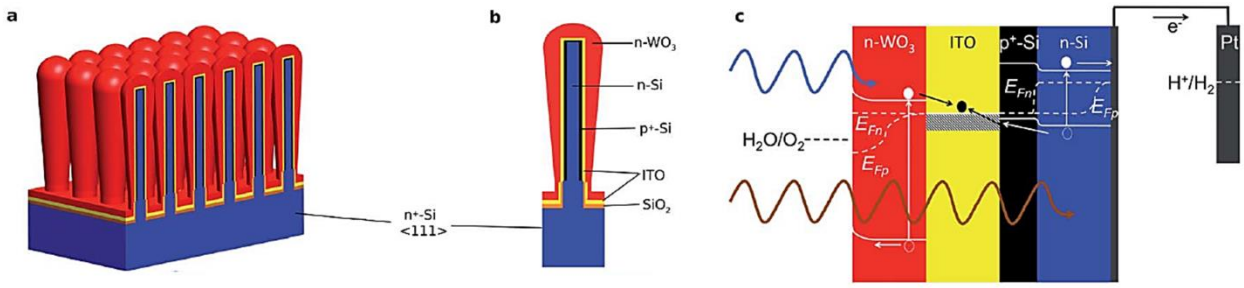

Figure 1.12 Schematic of the PEC device consisting of microwire Si with pn-junction upon which n-type WO_3 is deposited (a) and its cross-sectional scheme (b). Band diagram of this device is also illustrated (c). Reproduced from the reference [37].

stability in acidic electrolyte (< 24h in 3M H_2SO_4). This result well demonstrates the need of suitable protection layer in operating of the PEC device. Unfortunately, even if the stability issue could be avoided, III-V materials, especially Ga and In, are currently too expensive for large-scale applications. It seems that these materials also have severe scalability issues because these elements which are by-products (of aluminum and zinc, respectively) and ultimately price-inelastic [36].

To solve this potential cost issue, Lewis' group of JCAP (Joint Center for Artificial Photosynthesis) produced in 2014 two photo device using crystalline Si (c-Si) microiwire structure upon which n-type WO_3 was deposited (see Figure 1.10) [37]. This approach can provide significantly low cost advantage compared with previously introduced III-V structure, since both Si and W are earth abundant elements. However, the modest photo current density level of such structures ($J_{ph,\,max} \approx 0.4$ mA cm^{-2}) [37] result in a low efficiency for water splitting. Nevertheless, progress is being made using oxides of lower band gap. A respectable state-of-the-

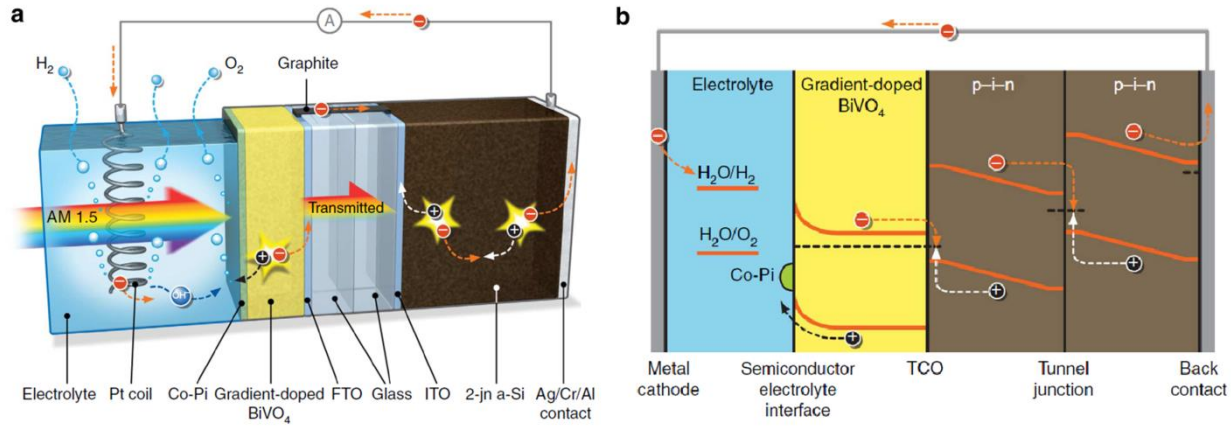

Figure 1.11 Schematic of the PEC device consisting of dual-junction a-Si PV cell and n-$BiVO_4$ photoanode as a top cell (a) and its cross-sectional scheme with band diagram of this structure (b). Reproduced from the reference [38].

art 3.6% and 4.9% of STH% tandem water splitting devices based on a doped $BiVO_4$ photoanode in combination with single and multi-junction a-Si solar cell, respectively, were demonstrated by van de Krol's group in 2014 [38]. Despite these recent progress, developing a relatively simple dual absorber tandem structure is still an engineering challenge.

Chapter 2

2. Experimental setups and analysis techniques

2.1 Photoelectrochemical setup

Since the photocatalytic water splitting technology is a combination of the harvesting of solar energy and the electrolysis of water into a single device, the photon energy is converted to electrical energy, which is directly used to split water into hydrogen, when a semiconductor with the right set of properties is immersed in an aqueous electrolyte and irradiated with sunlight. A general schematic of a laboratory photoelectrochemical (PEC) cell is shown in Figure 2.1. As shown on this figure, a double compartment 3-electrode cell was used for most work of this thesis. A saturated Hg/Hg_2SO_4 electrode (VWR International) filled with saturated K_2SO_4 solution was used as a reference electrode (RE), and Pt mesh as a counter electrode (CE). The RE compartment is connected to the working electrode (WE) compartment by a Luggin capillary, equipped with a small glass valve. Together with this electrochemical cell, potentiostat (Bio-Logic VSP) was used as a bias voltage source, and EC Lab software for the electrochemical measurements. In this work hydrogen gas bubbling using glass gas bubbler was used for electrolyte circulation and hydrogen gas saturation inside of vessel during HER experiments. In case of OER experiments, the solution was purged with N_2 gas for 30 minutes prior to the any experiments. Most cyclic voltammetry (CV) and chronoamperometry (CA) experiments were done in acidic medium using 1M $HClO_4$ (Aldrich 99.99%) electrolyte.

For the PEC experiments in alkaline media, reference was a Teflon incased Hg/HgO electrode (Koslow Scientific Company). Glass corrodes in an alkaline solution and the arising contaminants and/or poisoning of the electrodes (mainly due to lead and silica) [39] can significantly influence the HOR/HER activity, and therefore 3 electrode one chamber quartz glass cell was used to minimize corrosion rate of the glass. 1M KOH from highly purified chemical (Aldrich, 99.995%) was used as an electrolyte. All glass ware constituting PEC cell was cleaned using freshly prepared aqua regia solution ($HCl:HNO_3$ = 3:1 volume ratio).

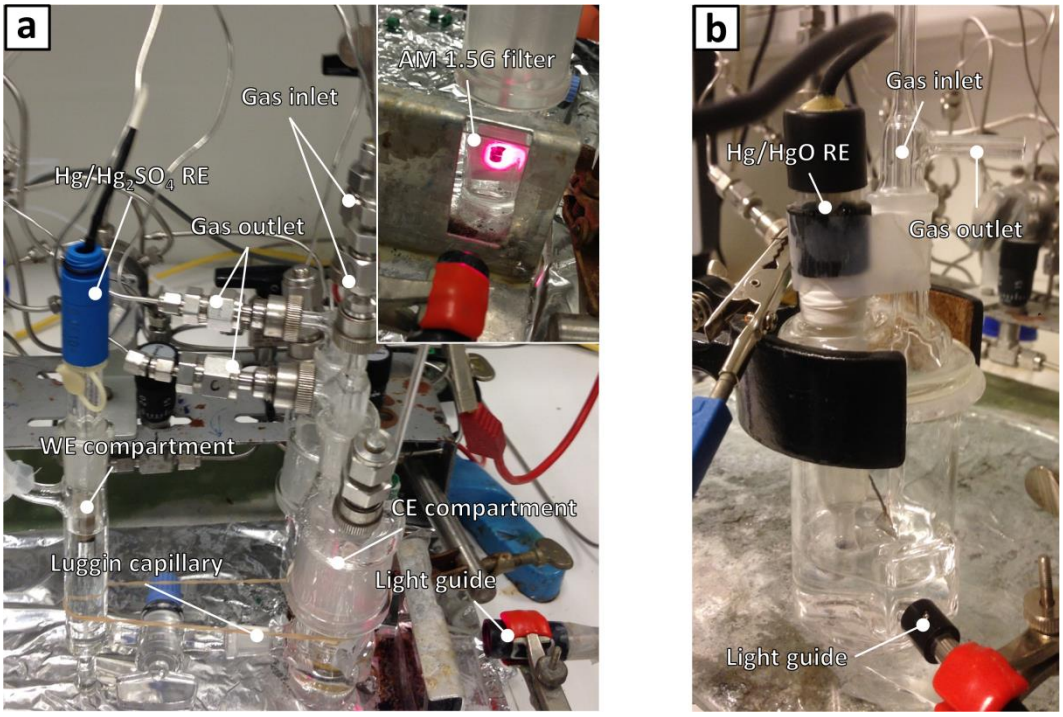

Figure 2.1 Picture representing the PEC cell which was used in most of this work (a), and PEC cell made from quartz to minimize glass corrosion during the experiment in alkaline media (b). The WE is illuminated using the light guide and AM 1.5 filter as shown in inset of (a).

For Hg/Hg_2SO_4 and Hg/HgO RE, the potential with respect to the standard hydrogen electrode (SHE) equals 0.68 and 0.098V, respectively. And thus the potential of the WE vs. RE can be converted to potential vs. reversible hydrogen electrode (RHE) as:

$$E_{WE,RHE} = E_{WE,Hg/Hg_2SO_4} + 0.68V + 0.059 \cdot pH = E_{WE,Hg/Hg_2SO_4} + 0.68\text{V} \quad \text{for 1M } HClO_4 \quad (2.1)$$

$$E_{WE,RHE} = E_{WE,Hg/HgO} + 0.098V + 0.059 \cdot pH = E_{WE,Hg/HgO} + 0.924\text{V} \quad \text{for 1M KOH} \quad (2.2)$$

As a light source, a 1000 W Xenon lamp (Oriel) was used with (or without) a 635 nm cut-off filter and an AM1.5 filter to simulate the red part or standard full spectrum of the solar spectrum. The light intensity reaching the sample was measured via a spectrophotometer (International Light Technologies Inc, RPS 900-R), and the light intensity was adjusted to match that of the total light intensity of red light ($\lambda > 635$ nm, 41.8 mW cm^{-2}) and white light of AM 1.5G solar spectrum (100 mW cm^{-2}). Red light filter was used in this work because Si was used as a photocathode and it will be used as a mid-long range photo-absorber in dual bandgap structure. In general, Xe lamp is used for realize solar spectrum in laboratory, because its spectrum is similar to the solar spectrum. But as shown in Figure 2.2, there is still subtle difference between the real solar spectrum and spectrum

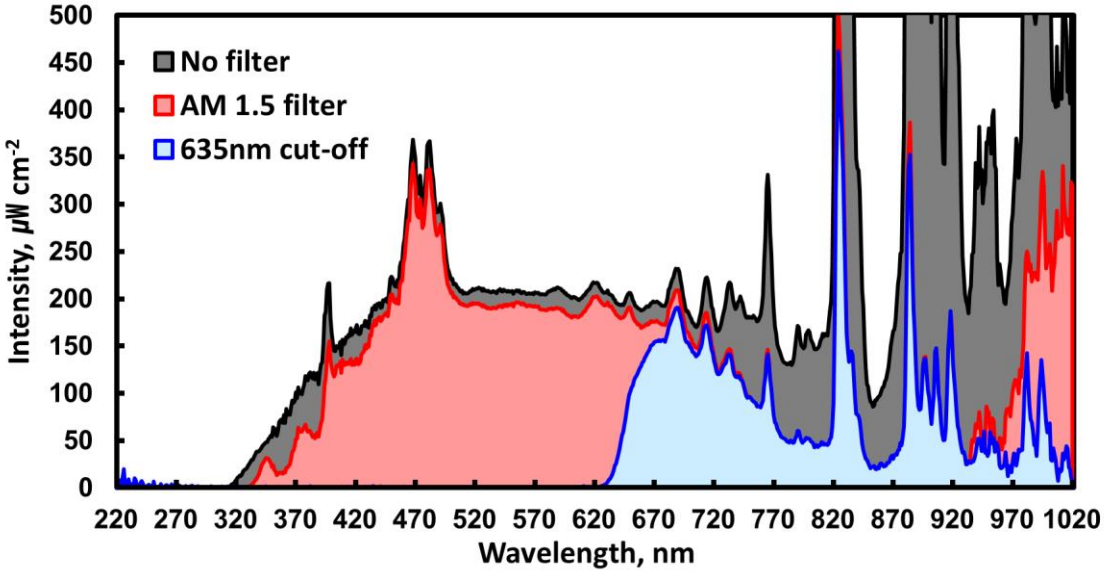

Figure 2.2 Spectral irradiance distribution for the Xe lamp used in this work without any filter (gray), with AM 1.5G filter (red) and AM 1.5G together with 635 nm cut-off filters (blue). The AM 1.5 filtered light spectrum was used for wide-gap top cell and AM 1.5 with 635 cut-off filtered light was used for narrow-gap bottom cell.

realized by Xe lamp. Especially, we found specific character peak at the 800 nm wavelength region from the Xe lamp. There is no artificial solar simulator which perfectly matches with natural solar spectrum. However, we adjust the sum of intensity to match with the light intensity under the AM 1.5 condition by using abovementioned AM 1.5 filter and adjustment of focal length.

To determine efficiency as a function of wavelength, incident photon to current efficiency (IPCE) measurements were employed. An Oriel 74100 monochromator was combined with the Xenon lamp mentioned above to give monochromatic light. IPCE measurements were carried out from 500 to 900 nm. In order to determine the photocurrent at specific wavelength, the electrodes were tested at a potential where the saturated photocurrent of CV can be observed using the same set-up and conditions as the CV measurements.

2.2 Electrochemical setup

The results in present work cover the electrochemical (EC) stability and catalytic activity of the photoelectrodes, and therefore, emphasis also has been put on electrochemical measurement procedures under the dark condition. For this purpose a similar three electrodes setup to the Figure 2.1 has been employed. The three electrode setup for this EC has RE, CE and WE as same as

previous PEC setup. Current flows between the WE and the CE under bias potential, which corresponds to the potential difference between the RE and WE. In the case of OER, the CE performs a cathodic reaction, for instance HER.

In order to distinguish properties of experimental objects from the effect of setup system, ohmic loss correction is important. As mentioned in previous section, the ohmic loss comes from mainly the resistance of the electrolyte (i.e. ionic conductivity), but also resistance of wire and connections. The ohmic loss was corrected in practice using a simple ohmic law:

$$\Delta E_{\Omega} = j \cdot R \tag{2.3}$$

where ΔE_{Ω} is the potential shift due to the ohmic loss, j is the measure current, and R is the resistance. 85% of the ohmic loss is corrected using a feature in the potentiostat.

2.3 Electrochemical quartz crystal microbalance

In addition to the electrochemical stability measurement, electrochemical quartz crystal microbalance (EQCM) was also applied in this work. The EQCM provides a way to monitor the mass change that occurs during the electrochemical reaction [40]. The key feature is measuring the resonant frequency of the quartz crystal which changes with the amount of materials adsorbed on top of the surface. A sample image of EQCM can be found in Figure 2.3 [41,42]. The resonance of the quartz crystal arises from the piezoelectric effect, where the mechanical force (or stress) on crystal generates an electric potential due to a net change in dipole moment of the structure [43]. The frequency change can be described as:

$$\Delta \mathrm{f} = -\frac{2f_0^2}{A\sqrt{\rho_q \mu_q}}\Delta m = -C_f \cdot \Delta m \tag{2.4}$$

where f_0 is the nominal frequency of the crystal, A is the active area, ρ_q is the density of the quartz and μ_q the shear modulus of an quartz crystal. C_f is a constant that can be calibrated (56.6 Hz/μg·cm^2 in this work) using electrodeposited silver, and Δm is a mass change of the material sit on QCM substrate. A clean EQCM substrate was immersed in a 0.5M HNO_3 solution with 50 mM

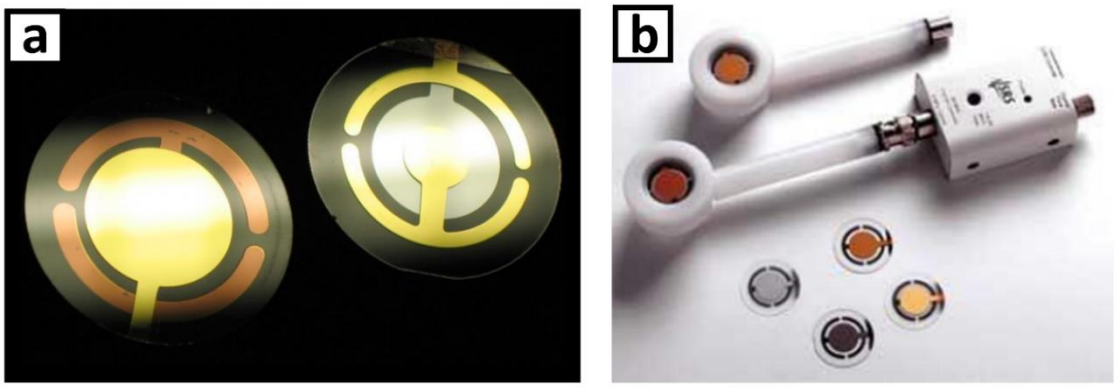

Figure 2.3 Sample image of both sides of EQCM crystals (a), and crystals equipped with holder and controller (b). A Teflon holder prevents electrical shunt and makes fixed active area for every measurement.

$AgNO_3$ and negative 50 μA current was applied until a frequency change of 60 Hz is reached for Ag deposition. This Ag deposition was repeated 6 times. In practice, the EQCM measurement was carried out using a QCM200 (Stanford Research Systems). The crystals were AT-cut and had a nominal resonant frequency of 5 MHz. The active area to frequency measurement was 0.38 cm^2.

2.4 Mott-Schottky analysis

To determine conduction band of semiconductors, we provided Mott-Shottky analysis using n^+ Si as a conducting substrate. The n^+ Si was chosen to prevent unexpected photovoltage effect. The sample was tested electrochemically in 1 M $HClO_4$ or 1M KOH electrolyte. For this experiment a modulation frequency of 10 kHz, perturbation amplitude of 35 mV has been used. The flat band potential of deposited semiconductor can be estimated by using Mott-Shottky equation shown below:

$$\frac{1}{C^2} = \frac{2}{q\varepsilon_r\varepsilon_0 A N_D}\left(E - E_{FB} - \frac{kT}{q}\right) \tag{2.5}$$

where *C* is the measured differential capacitance per area, A is the area, N_D is the number of donors, E is the applied voltage, k is the Boltzmann's constant, T is the absolute temperature, q is the electronic charge, ε_0 is the permittivity in vacuum, and ε_r is the relative permittivity of the object. Using this equation results in a flat band potential and dopant (or acceptor) density can be obtained. Then the conduction band can be found using the equation shown below:

$$E_C = E_{FB} - \frac{kT}{q} Ln\left(\frac{N_D}{N_C}\right) \tag{2.6}$$

here N_c is the density of states in conduction band.

2.5 Gas chromatography

This section is partly based on our recent publication [28].

The GC system is connected to a PEC cell, and the produced H_2 quantification was carried out using a gas chromatograph (Hewlett Packard 5890 Series II) equipped with a Molsieve-5A PLOT column (carrier gas: Ar), a thermal conductivity detector and automated gas sampling. A diaphragm pump (KNF, NF5RPDCB-4) was used to keep the gas in the working electrode compartment flowing through the gas chromatograph (GC) closed sample loop and bubbling through the electrolyte. Before the reactions, both the counter and the working electrode compartments were flushed with Ar gas and the cell was closed off. The headspace gas composition of the working electrode was sampled every 10 minutes throughout the entire length of the experiments (as the red dots in the plot below). A pure Pt wire was used as a standard to calibrate the H_2 signal before the experiment using the same GC. The number of moles of H_2, n_{H_2}, was then extracted using the ideal gas law. Finally, the corresponding charge, Q_{H_2}, was obtained via the equation $Q_{H_2} = 2F\, n_{H_2}$, where F is the Faraday constant.

The GC is equipped with an inlet for gas injection, an automated sampler, and a piece of glass or metal tubing called a column (see Figure 2.4a [44]). The gaseous compounds being analyzed interact with the walls of the column, which is coated with a stationary phase. This causes each compound to elute at a different time, known as the retention time of the compound. The comparison of retention times is what gives GC its analytical usefulness. The most commonly used detectors are the flame ionization detector (FID) and the thermal conductivity detector (TCD).

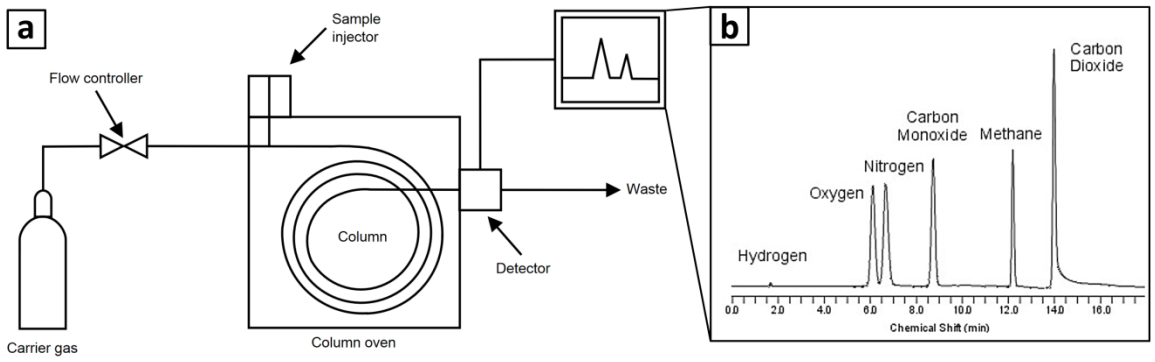

Figure 2.4 Schematic diagram of the GC system (a) and example of data as a function of retention time (b). The gas is injected into the column by the carrier gas, reaching the outlet of the column. The TCD and the FID are connected in series and are locate at the end of the column (shown as detector in figure a).

Both are sensitive to a wide range of components, and both work over a wide range of concentrations. While TCDs are essentially universal and can be used to detect any component other than the carrier gas (as long as their thermal conductivities are different from that of the carrier gas, at detector temperature), FIDs are sensitive primarily to hydrocarbons, and are more sensitive to them than TCD. Each detector is unable to distinguish between different gases and is only used to measure how much gas is passing through, and thus the chemical information comes from the difference in retention time as shown in Figure 2.4b [45], which must be measured on a standard beforehand. The area under a peak is proportional to the amount of gas present in the chromatogram. By calculating the area of the peak using the mathematical function of integration, the concentration of a gas in the original sample can be determined.

2.6 X-ray diffraction

X-ray diffraction (XRD) technique is a method used for determining the atomic and molecular structure of a crystal, in which the crystalline atoms cause a beam of X-rays to diffract into may specific directions. In present work, XRD data collection was done using PANalytical X'pert Pro diffractometer, which is equipped with a monochromatic X-ray radiation source (Cu Kα, λ = 1.5418 Å). When X-rays are incident on an atom, they make the electronic cloud move as does any electromagnetic wave. In crystals, X-rays irradiated at certain specific wavelengths and angles produce intense peaks of reflected radiation, and reflections from the various planes interfere constructively when the phase shift is a multiple of 2π (Bragg condition: see Figure 2.5a), and this can be described by using Bragg's law:

$$n\lambda = 2d \cdot sin\theta \tag{2.7}$$

where n is an integer, λ is the wavelength of incident wave, d is the spacing between the planes in the atomic lattice, and θ is the angle between the incident ray and the scattering planes. 2dsinθ term is the path difference between two waves undergoing constructive interference. A diffraction pattern is obtained by measuring the intensity of scattered waves as a function of scattering angle. Strong intensities known as Bragg–peaks are obtained in the diffraction pattern when scattered waves satisfy the Bragg condition aforementioned.

In addition, width of XRD peaks also provides useful information, such as crystal size (e.g. single crystal and amorphous), strain effect. Thus, it is possible to gain information about the dominant crystal size from the XRD patterns using Scherrer equation:

$$B(2\theta) = \frac{K\lambda}{Lcos\theta} \tag{2.8}$$

In other words, peak width (B) is inversely proportional to crystallite size (L). Full width at half-maximum (FWHM, Figure 2.5b) can be used instead of B in this equation. The constant of proportionality, K (the Scherrer constant) depends on the how the width is determined, the shape of the crystal, and the size distribution (it varies from 0.62 to 2.08).

2.7 X-ray photoelectron spectroscopy

The X-ray photoelectron spectroscopy (XPS) analysis was carried out in an UHV (ultra-high vacuum) system provided by Thermo Scientific. The XPS is a widely used tool for investigation of the surface composition. The fundamental principle is based on the ejection of electrons from a surface by radiation due to the photoelectric effect. The sample is hit by X-ray photons resulting the photoemission of electrons from the core levels of the atoms. In this work, Al Kα X-ray source emitting photons with an energy 1486.7 eV has been used. The kinetic energy of the emitted

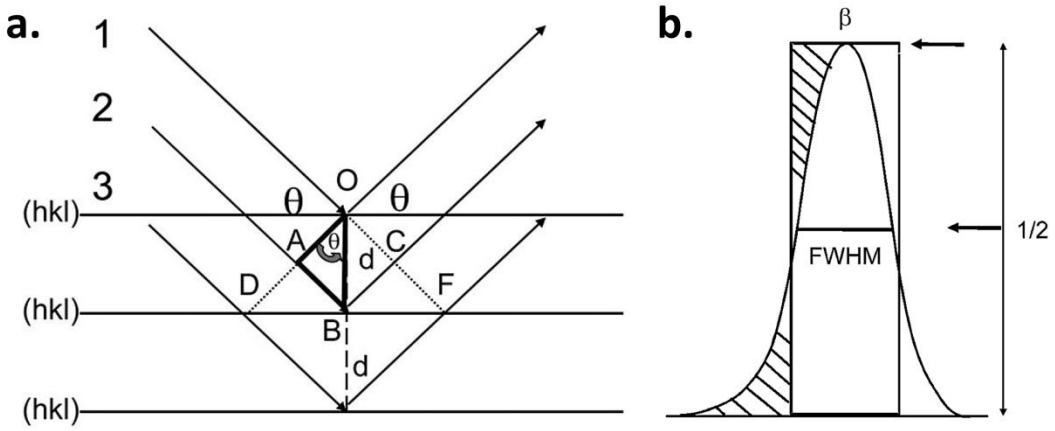

Figure 2.5 Illustration of the interaction between the X-ray radiation and a crystal lattice resulting the constructive interference (a) and a simple guide how to define full width at half maximum (FWHM) from the XRD peaks (b). For specific angles and interplanar distances the Bragg conditions are fulfilled and this cna be detected by XRD measurement.

electrons from the surface is related to the initial binding energy that characterize type of element and its chemical state. The kinetic energy of the photoemitted electrons (E_k) is given as:

$$E_k = hv - E_b - \Phi_a \tag{2.9}$$

here E_b is the binding energy of the photoemitted electron, and Φ_a is the workfunction of the analyzer. Since the XPS is a surface sensitive characterization method, compositional depth profile was obtained using XPS/sputtering sequential steps. The sputtering was performed by and ion-gun source with noble gas.

2.8 X-ray reflectometry

In order to determine the structural properties and stoichiometry of TiO_2 films X-ray reflectometry (XRR) measurement was performed using a same equipment used for XRD measurement. A line focus was used with a beam width of approximately 1 mm. The Parratt formalism [46] for reflectivity was used to fit the XRR data and gave an accuracy of 0.1 nm for thickness analysis. Using low–angle XRR measurements, the film thickness, film density and surface roughness can be obtained with an angular resolution of 0.001°. If the interface is not perfectly sharp and smooth then the reflected intensity will deviate from that predicted, and the deviations can then be analyzed to obtain the density profile of the interface normal to the surface.

The basic idea behind the technique is to reflect a beam of X-rays from a flat surface and to then measure the intensity of X-rays reflected in the specular direction (reflected angle equal to incident angle). The basic mathematical relationship which describes specular reflectivity is fairly straightforward. When an interface is not perfectly sharp, but has an average electron density profile given by $\rho_e(z)$, then the x-ray reflectivity can be approximated by:

$$R(Q)\Big/R_F(Q) = \left|\frac{1}{\rho_\infty}\int_{-\infty}^{\infty} e^{iQz}\left(\frac{d\rho_e}{dz}\right)dz\right|^2 \tag{2.10}$$

Here R(Q) is the reflectivity, $Q = 4\pi\cdot\sin(\theta)/\lambda$, λ is the X-ray wavelength, ρ_∞ is the density deep within the material and θ is the angle of incidence. Typically one can then use this formula to compare parameterized models of the average density profile in the z-direction with the measured

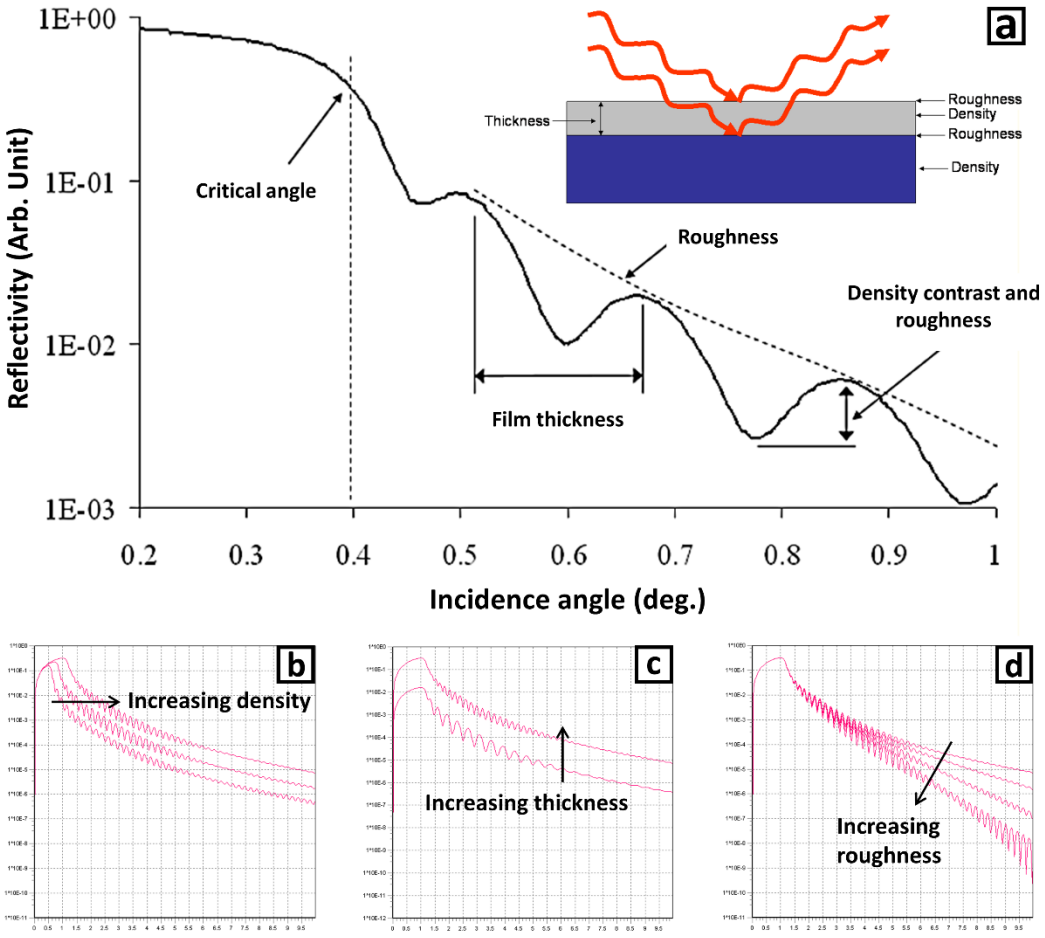

Figure 2.6 Example of XRR data interpretation (a) and behaviors of XRR curve depending on the film density (b), thickness (c), and roughness (d).

x-ray reflectivity and then vary the parameters until the theoretical profile matches the measurement. An example of XRR data interpretation are shown in Figure 2.6. The critical angle for a layer is a function of its electron density (Figure 2.6b), and the distance between the fringes is inversely proportional to the thickness of the layer (Figure 2.6c). Roughness of the film causes X-rays to be scattered rather than reflected, and thus this produces a decay in the reflected beam intensity as shown in Figure 2.6d. A rougher surface produces more diffuse scatter, causing the reflected beam intensity to decay more with the incidence angle.

2.9 Scanning microscopy measurement and energy dispersive spectroscopy

The scanning electron microscope (SEM) is a type of electron microscope that images the sample surface by scanning it with a high-energy beam of electrons in a raster scan pattern. The electrons

interact with the atoms that make up the sample producing signals that contain information about the sample's surface topography, composition and other properties such as electrical conductivity. The beam from the gun is rastered and pattern from the specimen and this pattern used to produce the gray image on the monitor. Since the size of the monitor raster pattern is constant, magnification of the SEM image can be defined as follows: magnification = area scanned on the monitor / area scanned on the specimen. In present work, SEM technique was mainly applied for morphology analysis for the corroded surface.

From the operating point of view, knowing the physical meaning of the contrast on the monitor is very important. The difference between white and black colored surface defines the height of the object from the surface. In general, SEM imaging is based on the brightness (contrast relative with the background level) converted from the intensities of secondary electron (SE) signal. Thus, bright area can be considered as a point close to the detector, and dark area is the opposite. But SEM imaging by using the back scattered electron (BSE) detector gives different physical information. BS efficiency increases with the increasing in atomic number. And this results in bright color from the elements with high atomic number and dark color from the elements with low atomic number in the image (i.e. compositional information). In present work, only SE mode was used, and thus contrast of the scanned image corresponds to the physical morphology (distance from the detector) of the surface. The SEM in practice has been preceded using Quanta FEG SEM equipment in CEN at DTU, and provided electron beam power has a range of 5 to 20 kV with working distance of around 10 cm.

Energy-dispersive X-ray spectroscopy (EDS or EDX), is an analytical technique used for the elemental analysis or chemical characterization of a sample. Its characterization capabilities are due in large part to that each element has a unique atomic structure allowing unique set of X-ray emission spectrum and peaks [47]. To stimulate the emission of characteristic X-rays, a high-energy X-ray beam, is focused into the sample being studied. The incident beam may excite an electron from the inner shell of atom, ejecting it from the shell while creating a hole where the electron was. An electron from an outer, higher-energy shell then fills the hole, and the difference in energy between the higher-energy and the lower-energy shell is released in the form of an X-ray. At last, the number and energy of the X-rays emitted from a sample is measured by detector. As the energies of the X-rays are characteristic of the difference in energy between the two shells

and of the atomic structure of the emitting element, EDS allows the elemental composition of the sample. Since this technique is suitable for the bulk composition analysis, it was used as a qualitative analysis tool for the detection of the particular element in the sample.

2.10 Ultraviolet-visible spectroscopy

The transmittance spectra and band-gap estimation were carried our using ultraviolet-visible spectroscopy (UV-Vis) technique. For this measurement Varian Cary 1E UV-Vis spectrometer equipped with two light sources: deuterium lamp (UV range) and tungsten lamp (Vis-NIR range). The wavelength of the light is controlled by a monochromator, and the light transmitted to the sample is analyzed by the detector. The transmittance (T%) of the sample can be described by the Beer-Lambert law:

$$T\% = 100 \cdot T = 100 \cdot \frac{I}{I_0} = 100 \cdot e^{-\sigma/N} \tag{2.10}$$

where I_0 is the intensity of the incident light, I is the intensity of the transmitted light, σ is the attenuation cross section, and N is the concentration of attenuating volume. The absorbance (A) can be expressed as:

$$\mathrm{A} = 2 - log_{10} T\% = log_{10} \frac{1}{T} = \varepsilon l c \tag{2.11}$$

where ε is the absorption coefficient, l is the thickness of the object, and c is the density of attenuator (or concentration of the compound or solution).

The recorded spectrum was analyzed to estimate the E_g of the film by using the Tauc plot that displays the optical absorption spectrum of a material. Typically, a Tauc plot shows the quantity hν (the energy of the light) on the abscissa and the quantity $(\alpha h\nu)^{1/r}$ on the ordinate, where α is the absorption coefficient of the material. The value of the exponent r denotes the nature of the transition: 1/2 for direct allowed transitions, 3/2 for direct forbidden transitions, 2 for indirect allowed transitions, and 3 for indirect forbidden transitions [48]. By extrapolating the linear region of the converted curve to the abscissa yields the energy of the E_g of the material.

Chapter 3

3. Using Si as a photoanode bottom cell

For efficient hydrogen (H_2) production via water splitting reaction, both hydrogen evolution reaction (HER) and oxygen evolution reaction (OER) have to proceed with high-rate. However, the kinetically slow OER process has been a major bottleneck [49], which is accompanied by several intermediate steps with high activation energy barriers requiring high overpotential (η) to transfer 4 electrons: $2H_2O \rightarrow 4H+ + O_2 + 4e^-$ (in acid) or $4OH^- \rightarrow 2H_2O + O_2 + 4e^-$ (in alkaline). To overcome this problem, efficient OER catalysts are required, such as IrO_2 and RuO_2 [50,51]. However, due to the high cost for these rare materials, earth-abundant transition metal oxides, such as NiO and CoO, have been intensively investigated to develop cost-effective alternative OER materials with high activity [52,53].

In this chapter time-dependant behaviour of the OER kinetics of CoO_x and NiCoOx thin films in 1M KOH (pH = 14) electrolyte is demonstrated, i.e. the OER kinetic variation of the sample according to the operating time is evaluated. According to the Pourbaix diagram, both nickel and cobalt oxide can be converted to hydroxides during potential cycling in alkaline electrolyte [54,55], and thus these binary oxide have been used as a protection layer of Si photoabsorbers with frontal illumination[32,56,57]. However, this approach requires a balance between the thickness of the protection layer and maximum photocurrent output, because there is always a loss due to the light absorption by the protection layer. Furthermore in actual tandem device operation conditions the low band gap absorber, such as Si, should be used as bottom cell of the tandem water splitting device, where the light is incident from the “dry” side of the photoanode. Thus, the light was illuminated from the side opposing the solid/liquid interface in this work. Since the photons are irradiated from the back contact side, transparency of the protection layer is not a required property anymore, indicating that thick non-transparent protection layers can be employed.

This chapter is mainly based on previous publication [58].

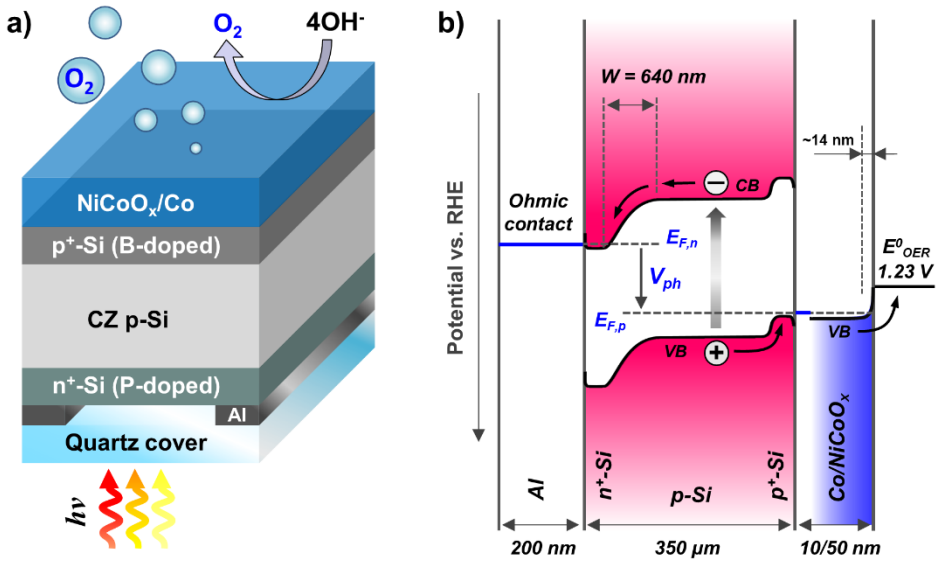

Figure 3.1 (a) Schematic drawing of the back illuminated photoanode with Al/n^+pp^+-Si/Co/$NiCoO_x$ ($NiCoO_x$ on top) and (b) band alignment under illumination. Detail energy diagram calculation process will be discussed in following section.

3.1 Sample fabrication methods

The shallow n^+p-junction was produced in p-type (100) czochralski (CZ) Si wafers (Topsil, 1-20 ohm-cm, boron-doped, acceptor density $N_A \approx 5 \cdot 10^{19}$ cm^{-3}) by a shallow phosphorous ion implantation at 36 keV with a dose of 3×10^{15} cm^{-2} to form n^+ layer (donor density N_D of approximately $1 \cdot 10^{20}$ cm^{-3}), which is expected to form a depletion width of 640 nm. After annealing a mesa-isolated n^+p-Si structure with height of 3 µm is formed at the back side (light illumination side) by photolithography and dry etching (Here, we used Ar, O_2 and CHF_3 gases in an Oxford Instruments RIE80). The front side of the same samples was also doped with boron doping using ion implantation at 100 keV with a dose of 5×10^{16} cm^{-2} to form a thin p^+ layer. An Al charge collecting layer with a circular hole for light irradiation was deposited by e-beam evaporation with a metallic shadow mask to make circular rings for light irradiation.

The Al layer was masked to create a circular hole over the active area in order to allow light transmission to the silicon. The p^+ doped layer near the electrode-electrolyte interface was formed an ultrathin space-charge region which allows electron tunnelling through the interface from the bulk silicon to the electrocatalyst. Without such a layer the charge separation becomes very inefficient [59]. Consequentially, the sample can be stated as a ‘ready-made photoanode bottom cell’ for tandem water splitting devices.

As mentioned above, two different metal oxides (CoO_x, and $NiCoO_x$) were evaluated in this chapter. An IrO_x deposited sample was also tested for the comparative study with noble metal. Note that the IrOx coated sample was evaluated in 0.5M H_2SO_4. Prior to the deposition of these OER catalysts, the Si was sputtered in Ar to clean the surface and remove the native oxide. Subsequently, a 10 nm Ni or Co metallic film was reactively sputtered in 3 mTorr of pure Ar followed by the deposition of 50 nm of metal oxides in 3 mTorr at an O_2/Ar ratio of 40% by sputtering of Co or Ni with Co (in case of $NiCoO_x$, Ni:Co deposition rate was ≈ 1:1). In case of electrochemical quartz crystal microbalance (EQCM) and glass substrates, metal/metal oxide thin films were deposited using same process conditions mentioned above. Samples prepared only with cobalt oxide (Co/CoO_x) are used to verify qualitatively the role of the Ni component in the binary oxide layer during the reaction. The Co interlayer was introduced to prevent oxidation of the Si surface during the metal oxide deposition at high temperature, and to provide an efficient pathway for the carrier injection by forming an Ohmic contact.

The back side of the samples was covered with a 300 μm thick quartz glass to protect back side from direct contact with the electrolyte. The quartz cover glass was mounted directly onto the Al layer, and finally the sample was covered with epoxy. The resulting active area was measured by image analysis using ImageJ 1.46r after the experiments. Schematic cross-sectional configuration and its energy diagram are shown in Figure 3.1. Thickness and material information also can be found in Table 3.1. As shown in this scheme, the electron-hole pairs are separated by a built-in electric field which the n^+p junction provides. The holes are then transferred to the solid/liquid interface though the valence band of CoO or $NiCoO_x$ using Mott-Shottky analysis (detail calculations procedure will be discussed in following sections).

Table 3.1 Information of layers classified by its function.

Function	Material	Thickness	Method
Cover window	Quartz glass	300 μm	Epoxy bonding
Charge collector	Cu wire	N/A	Ag-paste
Back contact	Al	500 nm	E-beam evaporator
Emitter layer (n^+ layer)	Phosphorous-doped Si	~ 100 nm	Ion-implantation
Light absorber (p)	p-type Si	350 μm	(100) CZ wafer
Back surface field (p^+) layer	Boron-doped Si	~ 200 nm	Ion-implantation
Protective catalyst	Co/CoO_x or $Co/NiCoO_x$	10/50 nm	DC sputtering with O_2 flow

3.2 Calculation for band diagram

3.2.1 Calculation at n^+p-junction

Most of this band diagram has already been demonstrated in our previous works [28,60]. The p-Si wafer has a band gap (E_g) of 1.124 eV, an acceptor density (N_A) of $3 \cdot 10^{15}$ cm^{-3}. The bulk p-Si valence band (VB) can be determined as a function of working potential (E):

$$E_{V,p-Si} = E - \frac{kT}{e} ln\left(\frac{N_{A,p-Si}}{N_{V,Si}}\right) \tag{3.1}$$

The working potential corresponds to the hole quasi-Fermi level. k is Boltzmann's constant, T is temperature (298 K), e is the elementary charge, and $N_{V,Si}$ is the density of states in the valence band, which is $1.8 \cdot 10^{19}$ cm^{-3} for Si [61]. Assuming the pinning of the band edges of the semiconductor at the interface (0 V vs. RHE) the $E_{V,p-Si}$ is 0.22 V.

The Surface of the p-Si was doped with phosphorous by ion implantation process and n^+ emitter layer was formed at the surface. The process simulation program (Athena, SILVACO) was used to determine the donor density (N_D), which is approximately $5 \cdot 10^{19}$ cm^{-3}. The bulk valence band of the n^+ Si can be determined via equation:

$$E_{C,n-Si} = E + \frac{kT}{e} ln\left(\frac{N_{D,n-Si}}{N_{C,Si}}\right) \tag{3.2}$$

where N_C stands for the density of states in the conduction band, which is $2.8 \cdot 10^{19}$ cm^{-3} for Si [61]. Under the same assumption as above the $E_{C,n-Si}$ is 0.015 V.

At the pn^+-junction a built-in potential will be formed which can be determined in the dark via equation:

$$V_{bi} = \frac{kT}{e} Ln\left(\frac{N_{D,n-Si} \cdot N_{A,p-Si}}{n_i^2}\right) \tag{3.3}$$

where n_i is intrinsic carrier density of Si, which is approximately $1.5 \cdot 10^{10}$ cm^{-3} at room temperature, and V_{bi} was found to be 0.9 V. Under illumination V_{bi} at open circuit voltage conditions will simply be the V_{bi} in the dark minus the photo voltage (V_{ph}):

$$V_{bi,OCV} = V_{bi} - V_{ph} \tag{3.4}$$

If it is assumed that there are no interfacial losses at the pn$^+$-junction, the V_{bias} is distributed between the p-Si and n$^+$-Si as followed:

$$V_{bi,p-Si} = V_{bi,OCV}\frac{N_{D,n-Si}}{N_{A,p-Si} + N_{D,n-Si}} \tag{3.5}$$

$$V_{bi,n-Si} = V_{bi,OCV}\frac{N_{A,p-Si}}{N_{A,p-Si} + N_{D,n-Si}} \tag{3.6}$$

Using above equations, the $V_{bi,p\text{-}Si}$ is 0.43 V and $V_{bi,n\text{-}Si}$ is $1.3\cdot10^{-5}$ V. The depletion width can be determined via equation:

$$\mathrm{W} = \sqrt{\frac{2\varepsilon_0\varepsilon_{Si}(N_{D,n-Si} + N_{A,p-Si})V_{bi}}{eN_{D,n-Si}N_{A,p-Si}}} \tag{3.7}$$

where ε_0 ($8.8\cdot10^{-12}$ F/m) [62] is the permittivity in vacuum, and ε_{Si} is the relative permittivity of Si (11.7) [63]. From the equation mentioned above the sample was determined to have a depletion width of 640 nm. The depletion width is distributed between the p-Si and n$^+$-Si as followed:

$$x_p = \frac{N_{D,n-Si}}{N_{A,p-Si} + N_{D,n-Si}}W \tag{3.8}$$

$$x_n = \frac{N_{A,p-Si}}{N_{A,p-Si} + N_{D,n-Si}}W \tag{3.9}$$

From the equation above mentioned, most of depletion width will be in p-Si side and only 0.2 nm will be in n$^+$-Si layer.

3.2.2 Calculation at pp$^+$-Si junction

The shallow doped p$^+$-Si VB can be determined through the flat band:

$$E_{V,p^+-Si} = E - \frac{kT}{e}ln\left(\frac{N_{A,p^+-Si}}{N_{V,Si}}\right) \tag{3.10}$$

Using acceptor density values of p$^+$ Si $N_{A,p+\text{-}Si}$ ($1\cdot10^{20}$ cm^{-3}), the valence band of p$^+$ layer is 0.04 V. There are no simple expressions predicting the depletion width, but the width is on the order of a Debye length:

$$L_D = \sqrt{\frac{\varepsilon_0 \varepsilon_{Si} kT}{e^2 N_{A,p-Si}}} \tag{3.11}$$

Considering all values used above, the depletion width is approximately 75 nm.

3.2.3 Calculation at p^+-Si/Co interface

Assuming that the p^+-Si/Co interface forms a Schottky barrier with no metal induced gap states or Fermi level pinning, the built-in potential $\Phi_{i,Si}$ at the p^+-Si/Co interface is the difference between the Co work function (Φ_{Co} = 5.0 V) [64] and the p-Si ionization energy ($\Phi_{p\text{-}Si}$) plus the deviation between the flat band potential and the valence band. Assuming that $\Phi_{p\text{-}Si}$ is close to the sum of electron affinity of Si (χ_{Si} = 4.15 V) [65] and band gap of Si, this is shown in equation below:

$$\Phi_{i,Si} = \chi_{Si} + \frac{E_g}{e} - \Phi_{Co} - \frac{kT}{e} ln\left(\frac{N_{V,Si}}{N_{A,p-Si}}\right) \tag{3.12}$$

$\Phi_{i,Si}$ was found to be 0.38 V. Since Co is a metallic layer, and has a high carrier density compared to the Si, thus the bias will be distributed entirely over the p^+ Si region. The band bending distance in the n^+-Si can be determined by equation:

$$W_{n^+Si/Ti} = \sqrt{\frac{2\varepsilon_{Si}\varepsilon_0 \Phi_i}{eN_{D,n-Si}}} \tag{3.13}$$

The barrier width was found to be approximately 1.5 nm, and electron transfer from the Si to the Ti would most probably have to occur through tunneling.

3.2.4 Calculation at $NiCoO_x$/liquid interface

From the Mott-Schottky analysis the flat band potential ($E_{FB,NiCoOx}$) of $NiCoO_x$ was determined to be around 0.85 V vs. RHE, the accepter density was $3.1 \cdot 10^{18}$ cm^{-3}, and the valence band was 0.90 V vs. RHE. Since the valence band position is lower than water oxidation redox potential, the $NiCoO_x$/liquid interface has downward barrier height after Fermi pinning.

The depletion region width of TiO_2 at the interface is given by:

$$W_{NiCoO_x/liquid} = \sqrt{\frac{2\varepsilon_o \varepsilon_{NiCoO_x} \Phi_{i,NiCoO_x}}{eN_{A,NiCoO_x}}} \quad (3.14)$$

ε_{NiCoOx} is the relative permittivity of $NiCoO_x$ (12.3) [66], $N_{A,NiCoOx}$ is the doping density of $NiCoO_x$ obtained from Mott-Shottky analysis (from the chapter 3.2.2). $\Phi_{i,NiCoOx}$ is the built-in potential at $NiCoO_x$/liquid interface, and it can be simply calculated by:

$$\Phi_{i,NiCoO_x} = E_{FB,NiCoO_x} - E_{O_2/H_2O} - \frac{kT}{e} ln\left(\frac{N_{V,NiCoO_x}}{N_{A,NiCoO_x}}\right) \quad (3.15)$$

where $N_{V,NiCoOx}$ is the density of states in the valence band. However, it was impossible to find valid value for ternary $NiCoO_x$, thus valence band states for NiO ($N_{V,NiO}$ = $1.63 \cdot 10^{19}$ cm^{-3}) has been used. The $N_{v,NiO}$ was derived from the following equation:

$$N_V = 2\left(\frac{2\pi m_h kT}{h^2}\right)^{3/2} \quad (3.16)$$

where m_h is effective hole mass of NiO (0.75) [67].

Since we assume that interface forms Fermi level pinning, above-mentioned equation results in upward $\Phi_{i,NiCoOx}$ of 0.25 V. Applying this values results in $W_{NiCoOx/liquid}$ of 1.2 nm.

3.3 Characterization of $NiCoO_x$ film

SEM images of the $NiCoO_x$ with Co interlayer deposited on Si substrate are shown in Figure 2. Figure 3.2 a and b correspond to cross-sectional and top-view image of the film, respectively. The cross-sectional SEM image indicates that the $NiCoO_x$ film is continuous above the Si substrate and has a thickness of about 50 nm, and thus the surface is covered completely. This also can be found from the top-view SEM image (Figure 3.2b) exposing a dense $NiCoO_x$ surface without any obvious cracks or pin-holes. Note that the investigated films were deposited on the Si photoelectrodes using the same conditions as those used for the PEC samples, and the presence of nickel and cobalt in the binary oxide layer was confirmed by EDX analysis (Figure 3.2 c and d).

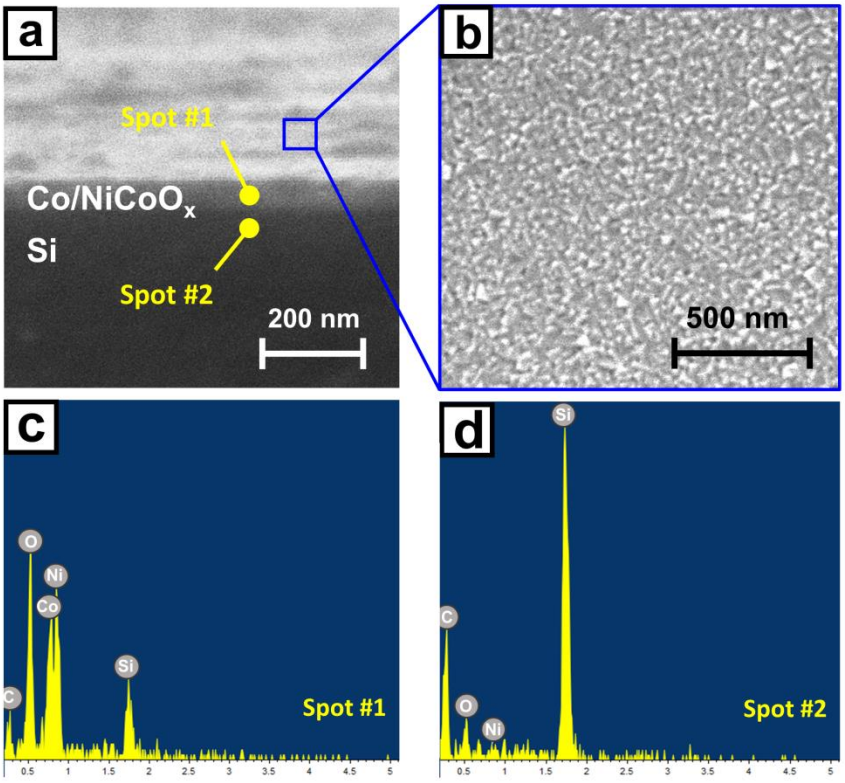

Figure 3.2 (a) Cross-sectional SEM image of $n^+pp^+Si/Co/NiCoO_x$ and (b) top-view SEM. The $NiCoO_x$ film was deposited at 300℃. These SEM images well demonstrate excellent surface coverage without any obvious crack or pinholes. EDX spectra in (c) and (d) also prove the presence of NiCoOx film deposited above the Si substrate.

The optical behaviour of the deposited films was investigated by UV-Vis transmittance spectra as shown in Figure 3.3. Transmittance of deposited $NiCoO_x$ shows approximately 53% at 600 nm in wavelength in spite of its wide band-gap of 3.4 eV extracted from the Tauc plot (inset). As shown in our previous work [32] NiO thin film with 50 nm thickness shows over 80% transmittance at 600 nm wavelength due to its high band gap (3.5 ~ 3.6 eV), and thus it is suggested that the optical loss of $NiCoO_x$ can be attributed to the mixed cobalt oxide phase which shows a drastic increase of absorption coefficient with increased growth temperature [68]. A CoO_x layer with same thickness shows transmittance of 43% at the same wavelength having a band-gap of around 2.8 eV. This illustrates how back illumination approach is beneficial for photoanode based on such overlayers.

$NiCoO_x$ is a well-known p-type, mixed-valence oxide with Ni occupying octahedral sites and Co distributed over both octahedral and tetrahedral sites [69]. To confirm the conductivity type of the present $NiCoO_x$ thin film, electrochemical impedance measurements were performed (i.e. Mott-Schottky analysis). The resulting Mott−Schottky plot (Figure 3.4) shows a negative slope,

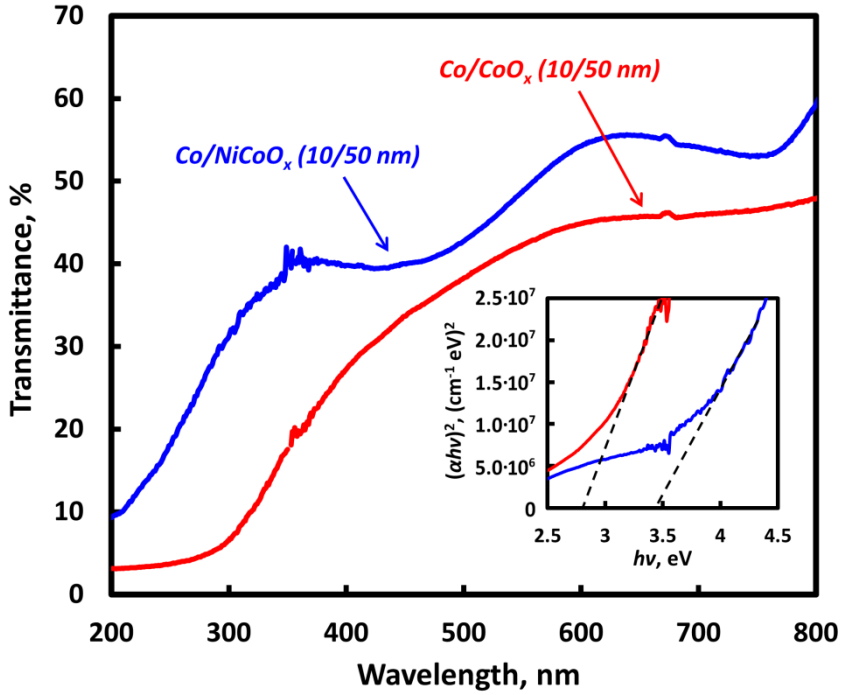

Figure 3.3 Band gap of $NiCoO_x$ and CoO_x deposited on quartz substrate with 10 nm thick Co interlayer were determined from the Tauc plot obtained from the (c) UV-Vis transmittance spectra. The noise from the quartz substrate was substracted as a background spectrum.

confirming the p-type behaviour of the deposited $NiCoO_x$ films. The flat band potential (E_{FB}) and the acceptor density (N_A) were estimated to be $E_{FB} \approx 0.85$ V versus RHE and $N_A \approx 3.1 \cdot 10^{18}$ cm^{-3}, respectively, and this high dopant density should provide a sufficient conductivity to transport holes through the valence band. To determine the $NiCoO_x$ valence band and flat band potential which have been used in previous section, Mott-Shottky analysis using 10/100 nm Co/$NiCoO_x$ deposited on p^+-Si is provided. Then this sample was tested electrochemically in 1M KOH electrolyte. For this experiment a modulation frequency of 16 kHz was used. Figure 3.2 shows the result of this experiment. The flat band potential of $NiCoO_x$ can be estimated by using Mott-Shottky equation shown below:

$$\frac{1}{C^2} = \frac{2}{q\varepsilon_{TiO_2}\varepsilon_0 A N_{D,TiO_2}}\left(E - E_{FB} - \frac{kT}{e}\right) \tag{3.17}$$

where C is the measured differential capacitance per area. Using this equation results in a flat band potential of 0.85 V vs. RHE and dopant density of $3.1 \cdot 10^{18}$ cm^{-3}.

The valence band can be found using the equation shown below:

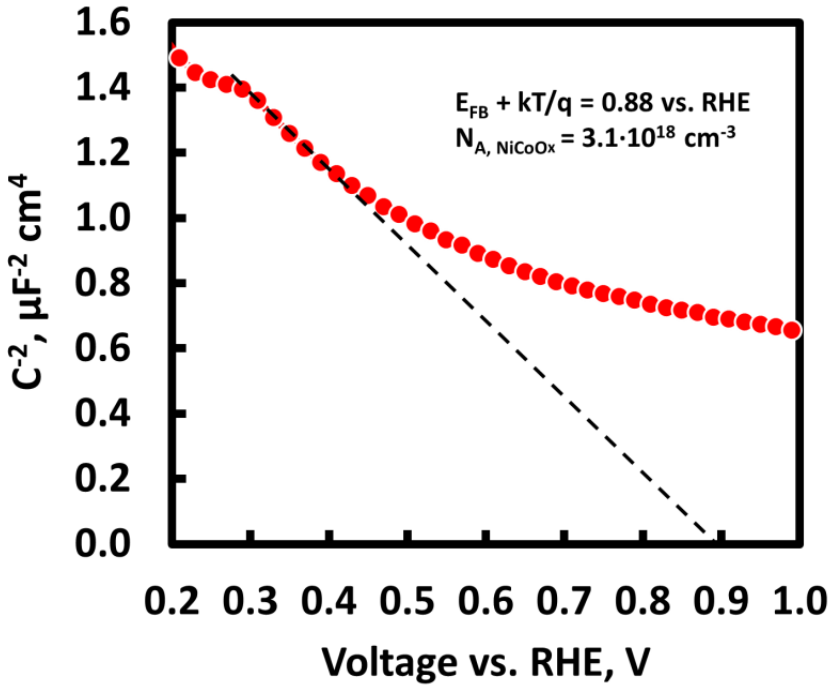

Figure 3.4 Mott-Schottky plot measured in 1M KOH using a sputtered 10/50 nm Co/$NiCoO_x$ on p^+-Si surface. This result well demonstrates that $NiCoO_x$ has p-type conductivity.

$$E_V = E_{FB} - \frac{kT}{e} Ln\left(\frac{N_{A,NiCoO_x}}{N_{V,NiCoO_x}}\right) \tag{3.18}$$

The equation results in a conduction band at 0.90 V vs. RHE.

3.4 Photoelectrochemical study

To verify the photoelectrochemical properties of $NiCoO_x$, this film was coupled with the n^+pp^+-Si photoanode with Co interlayer between the p^+-Si and $NiCoO_x$ regions, and the sample was examined by CV and IPCE measurements. The difference between the overpotentials (η) required to obtain a 10 mA cm^{-2} with the p^+-Si/Co/$NiCoO_x$ (under dark) and n^+pp^+-Si/Co/$NiCoO_x$ (λ > 635 nm, 41.8 mW cm^{-2} under the back illumination) reveals a photovoltage (V_{ph}) of ~ 510 mV (Figure 3.5). However, its onset potential (~ 1.13 V at 10 mA cm^{-2}) still lag behind that of the sample with noble catalyst (IrO_x, red; ~ 1.07 V at 10 mA cm^{-2}).

Figure 3.6 shows spectrally resolved IPCE measurement results of the n^+pp^+-Si/Co/$NiCoO_x$ photoanode under back side and front side illumination. Each data point was measured at an applied bias of 1.4 V vs. RHE, at which the sample shows a saturated photocurrent for both front and back side illumination. As shown in Figure 3.6, the IPCE under the back side illumination

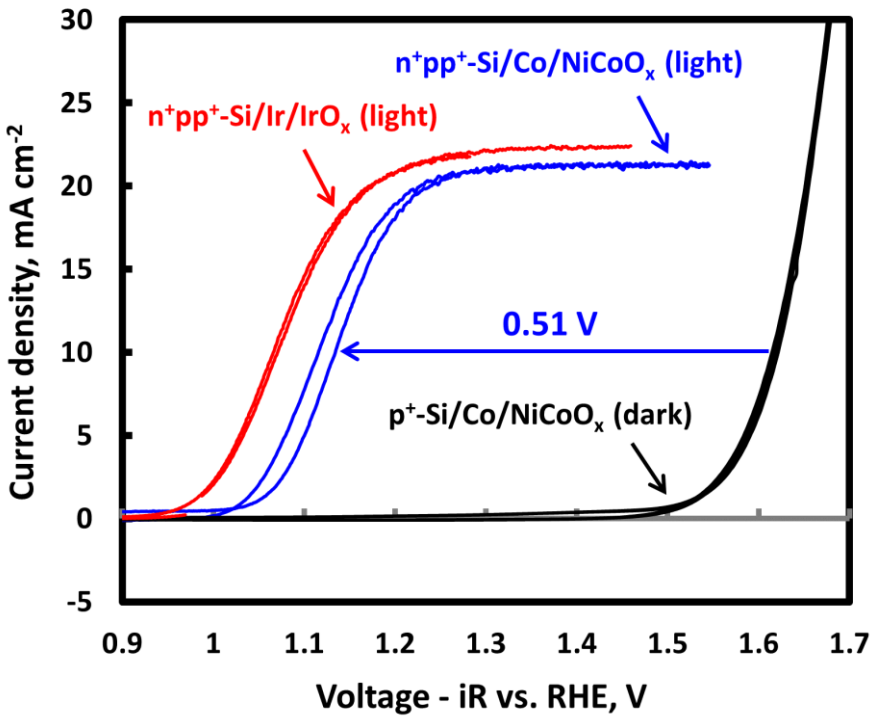

Figure 3.5 Photoelectrochemical behavior of n^+pp^+-Si/Co/$NiCoO_x$ photoanode in aqueous 1.0 M KOH under back-side illumination (blue) and p^+-Si/Co/$NiCoO_x$ in the dark condition (black). The difference of onset voltage at 10 mA cm^{-2} between this two curves shows that n^+pp^+-Si photoanode exhibits photovoltage of 0.51 mV. CV of n^+pp^+-Si/Ir/IrO_x also shown (red) for the comparative study with noble metal based catalyst.

increases gradually and shows over 90% at 550 nm for photons, which are absorbed near the back side of the sample. Considering the light absorption depth of Si as a function of the wavelength [28], this high IPCE response is natural since the charge collecting pn-junction is placed at the back side of the sample, and this shows that this n^+pp^+-Si/Co/$NiCoO_x$ structure is an efficient configuration to be used as a bottom cell of the tandem device. The low IPCE response at low wavelength range (~ 500 nm) is mainly attributed to the high recombination rate at the n^+-Si surface. Note that we didn't apply any surface passivation treatment, and there is no significant optical loss due to the quartz cover glass in this wavelength range [28].

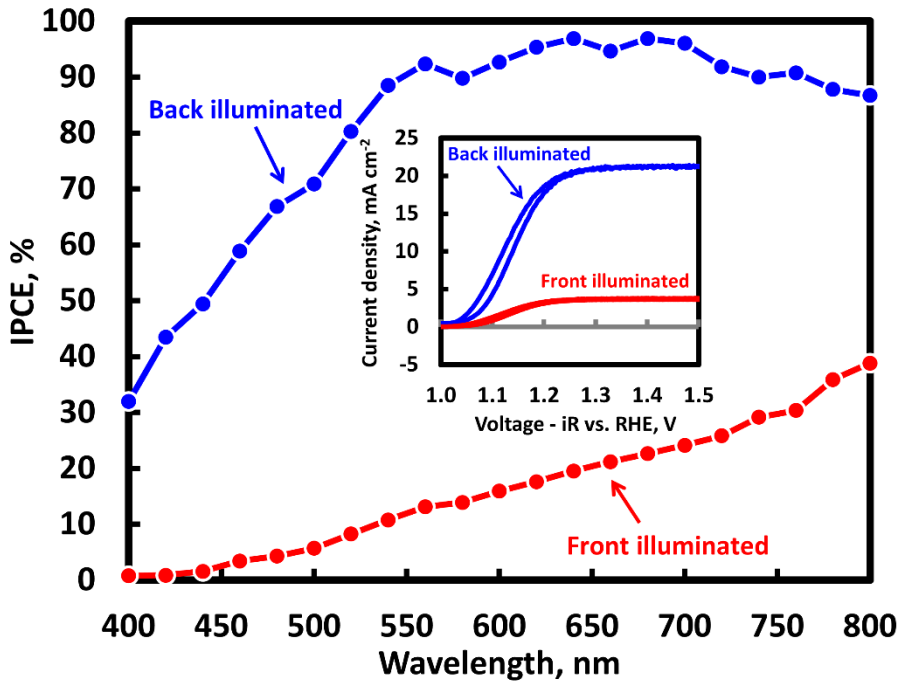

Figure 3.6 IPCE measurement results under front and back-illumination using n^+pp^+Si/Co/$NiCoO_x$ photoanode sample, and the inset is CV scans under front and back side illumination (AM 1.5G and 635 nm cut-off filters were used in the CV scans).

Conversely, the same sample showed the IPCE under front side illumination increases slowly from the short wavelength region and reaches merely 35% at a wavelength of 800 nm because most of the electron-hole pairs are generated far from the pn-junction under the front illumination. This difference in IPCE behaviour between the front and back side illumination is reflected in the CV measurement results (inset in Figure 3.6). The saturated photocurrent of the n^+pp^+-Si/Co/$NiCoO_x$ photoanode sample is around 21 mA cm^{-2} under the back side illumination with approximate AM 1.5G + 635 nm long pass filters, whereas significantly lower photocurrent, less than 5 mA cm^{-2} was measured under front illumination.

In order to investigate time-dependant behaviour of the sample, repeated CV's with long-term CA measurements were carried out. As shown in Figure 4a, the potential required to achieve a photocurrent density (J_{ph}) of 10 mA cm^{-2} was found to depend on the operating time. An applied potential of 1.13 V was required for the initial CV curve, This performance can be compared with as-deposited NiO in our previous study which showed relatively gradual slope, having onset potentials of ~ 1.24 V (at 10 mA cm^{-2}) [32]. This enhanced performance of $NiCoO_x$ is in good agreement with that from the previous electrochemical study on as-deposited Ni-Co-O OER catalyst [70], and this can be attributed to the favourable electric properties towards the OER.

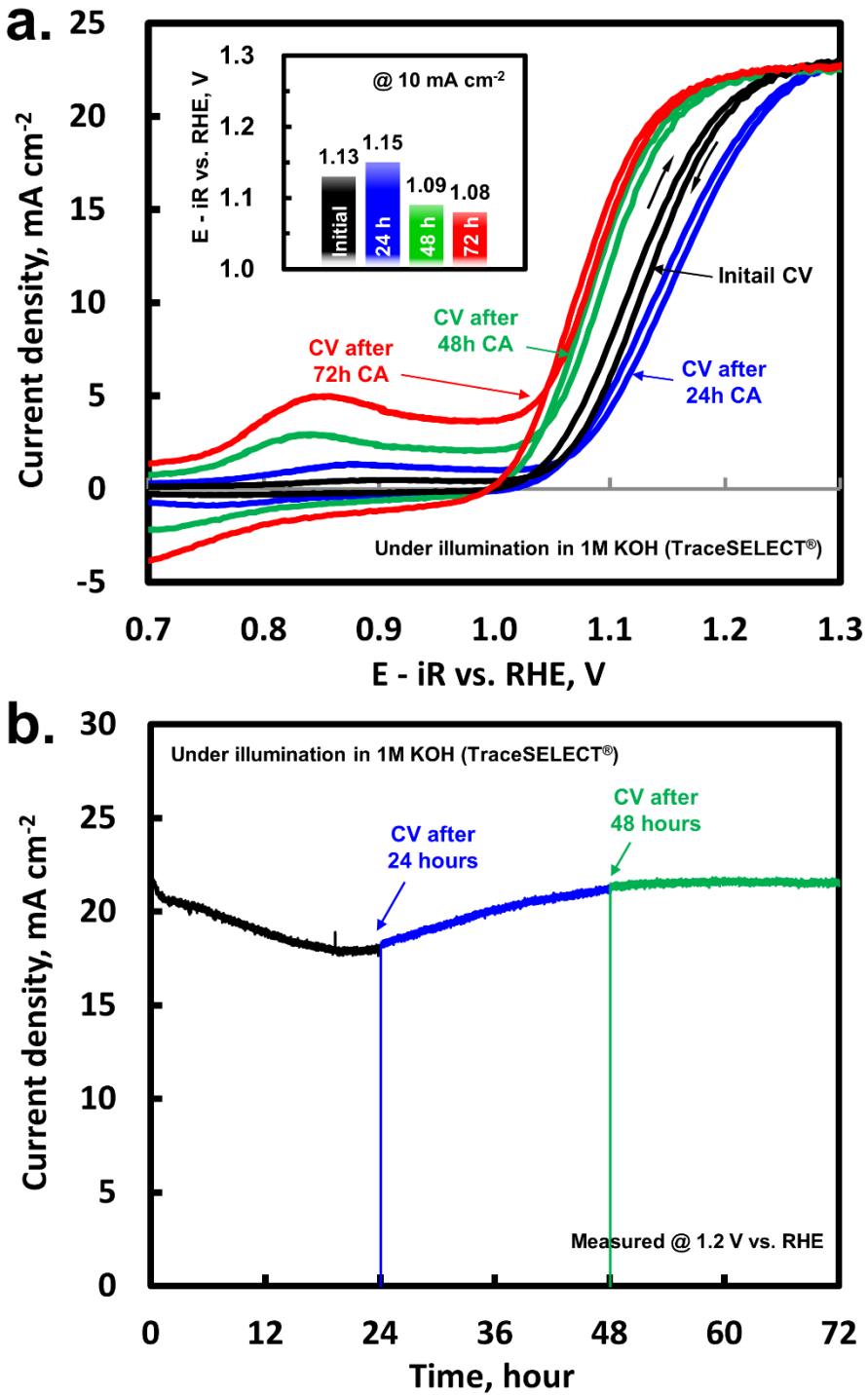

Figure 3.7 CVs of $n^+pp^+Si/Co/NiCoO_x$ photoanode measured before CA measurement (black), after the 24 hours long CA (blue), after the 48 hours (green), and after the 72 hours long CA (red). (b) CA measurements carried out at 1.2 V vs. RHE. The potentials required to achieve a photocurrent density of 10 mA cm^{-2} measured every 24 hours can be found in inset of 4a.

Addition of Co, which abounds in the spinel structure of nickel oxide, is known to provide more

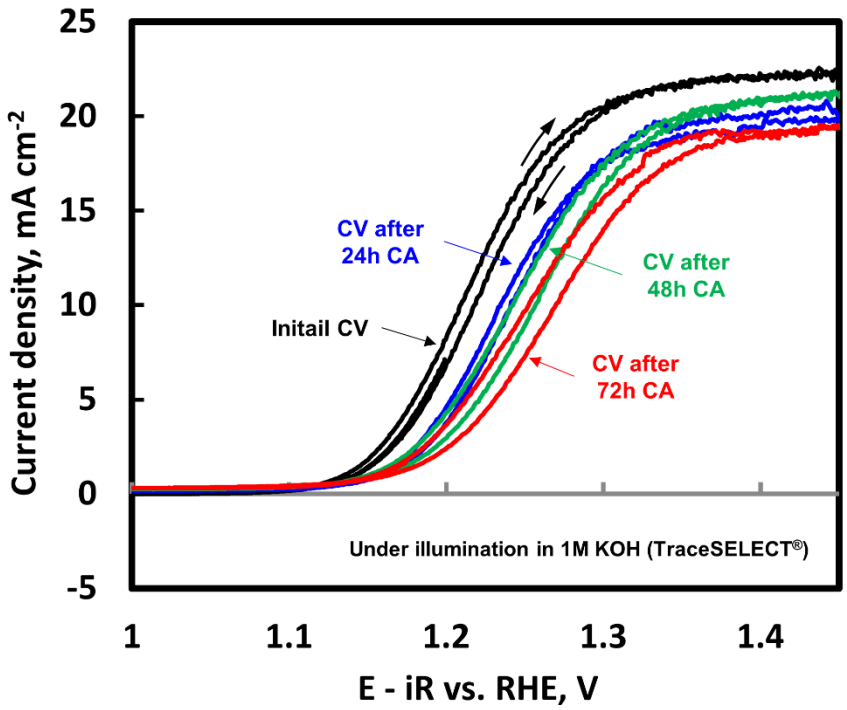

Figure 3.8 CVs of $n^+pp^+Si/Co/CoO_x$ photoanode measured before CA measurement (black), after the 24 hours long CA (blue), after the 48 hours (green), and after the 72 hours long CA (red). Unlike $NiCoO_x$ case, photoanode coupled to pure CoO_x degrades slowly without OER activity recover, indicating that increased activity and stability of $NiCoO_x$ are attributed to Ni component.

active sites, and reduce intrinsic electrical resistivity [71,72]. Tseung and Jasem [73] suggested that the mixed valences of the nickel and cobalt cations are helpful in the reversible adsorption of oxygen by providing donor-acceptor sites for chemiabsorption, lowering overpotential. Such synergetic effects are not limited to Ni-Co oxides, for instance recent studies on Ni-Fe-O oxides [34,74] can be understood in the same context.

Nevertheless, 1.18 V (at 10 mA cm^{-2}) was required for the CV measured after 24 hours CA test at 1.2 V, reflecting the changes in OER kinetics. These CV curves (initial and 24h after) showed somewhat similar saturation J_{ph} (~ 22 mA cm^{-2}), but behaved differently. Compared with the initial CV curve, the CV taken after 24 hours had an anodic shift of 20 mV at 10 mA cm^{-2} and decreased slope resulting a significant loss in maximum power point (i.e. lower fill factor), which can result in significant loss of operating current density in tandem devices [75] and can be attributed to the $NiCoO_x$ catalyst layer. The anodic shift accompanying with the decreased slop might be explained by the reaction of Co-O compounds with the alkaline electrolyte. Boettcher's group reported in their recent work that iron impurities in KOH electrolyte substitute

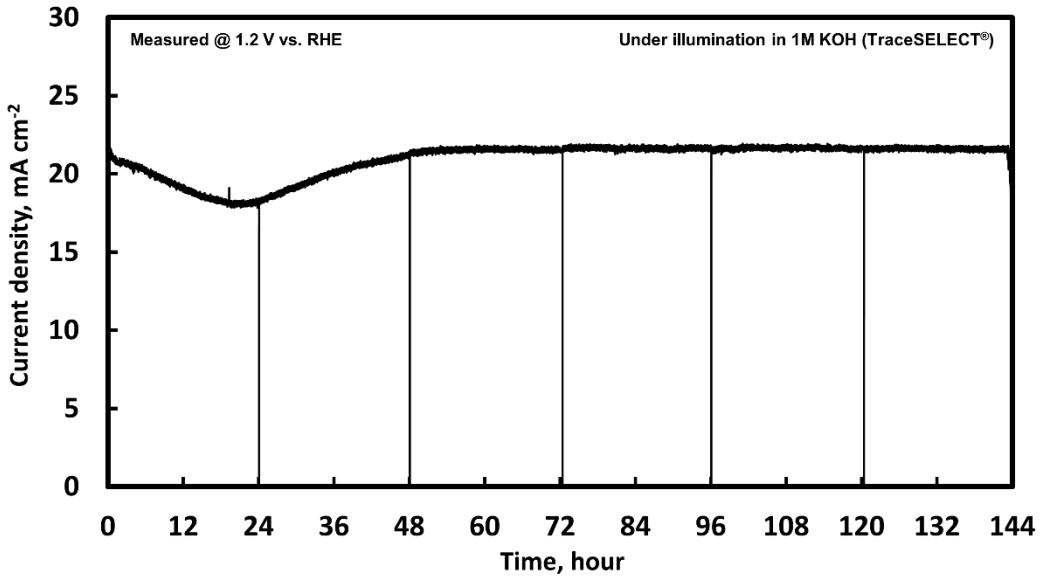

Figure 3.9 CA measurements carried out at 1.2 V vs. RHE using $n^+pp^+Si/Co/NiCoO_x$ photoanode for 6 days in 1M KOH. The sample showed an initial decrease and then starts to increase after the 20th hours. Once the photocurrent reaches its maximum, the sample showed stable photocurrent output until the 6th day of CA experiment.

for Co^{3+} under the applied potential, and this substitution incorporation decreases the electrical conductivity of the CoOOH phase [76]. In this report, the reduced conductivity appears to the lowered fill factor (i.e. decreased slope), since our photoanode sample with sputtered CoO_x showed continuous anodic shift of onset potential with decreased fill factor, resulting in a decrease in overpotential of approximately 40 mV after 3 days operation (Figure 3.8). This is in agreement with the recent report by the Lewis' group that the CoO_x coupled with Si photoanode shows a gradual loss in catalytic activity associated with the conversion of CoO_x to $Co(OH)_2$ and then to ion-permeable cobalt oxyhydroxide (CoOOH) [57].

Interestingly, the required bias potential to reach 10 mA cm^{-2} rebounded in the cathodic direction after the first 24 hours and reached 1.08 V vs. RHE after the 3 days of CA measurement. This value is almost same as initial onset voltage at 10 mA cm^{-2} obtained from the sample with IrO_x (note that n^+pp^+-Si/Ir/IrO_x was tested in 0.5M H_2SO_4, pH = 0) Furthermore, the slope of CV curves increased sharply compared to that of CV measured right after the first 24 hours. Since the photoanode with Co/CoO_x showed continuous anodic shift of onset voltage as well as degradation in photocurrent, it appears reasonable to assume that the increased activity is mainly attributed to the incorporation of Fe^{3+} with Ni^{2+}. A number of recent studies [32,34,74] have revealed that the apparent OER activity of NiO is dramatically affected by small amounts of Fe impurities in alkaline electrolyte, causing a cathodic shift in the OER onset potential. The

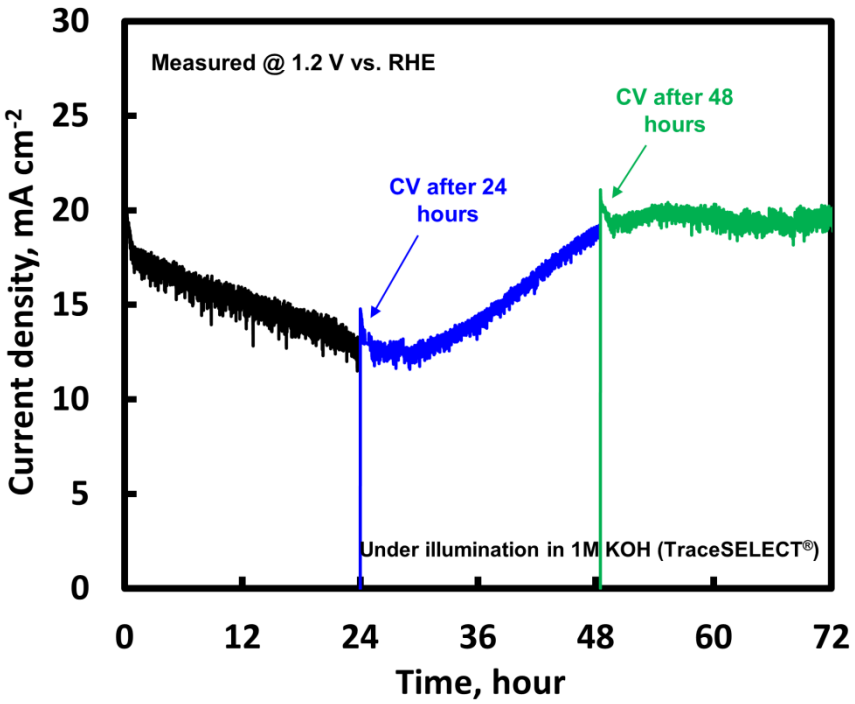

Figure 3.10 Repeated CA measurements were carried out at 1.2 V vs. RHE using a new $n^+pp^+Si/Co/NiCoO_x$ photoanode for 3 days in 1M KOH. This behaviour is quite similar to the CA behaviour of Figure 3.7, indicating that V-shape behaviour during the first 2 days was not a coincidence.

increased redox peak in Figure 3.7a also implies a strong interaction of Fe with metal sites, such as Co and/or Ni. The integrated area under the redox feature yields the total charge exchanged between the incorporated ions and the active sites of the electrode [77], and thus the increased redox features shown in Figure 3.7a may indicate that a significant number of metallic sites have become electrochemically accessible. The redox wave peak of the oxidative current slightly shifted cathodically for the CVs taken after 24h and 48h relative to that of the initial CV curve, then anodically shifted toward the OER current peak. The later anodic shift of the redox wave is well known for the binary metal oxides, i.e. CoO_x and NiO. This anodic redox wave shift observed in Figure 3.7a is consistent with the previous reports [34,76] where the redox wave for $Co^{2+/3+}$ and $Ni^{2+/3+}$ shifts anodically as the Fe content in the oxide films increases.

However, only few studies reported the presence of the negative shift of redox peak. J. M. Marioli et al. [78] observed that this negative shift takes place for the Ni-Cr binary oxide films, whereas single component nickel oxide showed only anodic redox peak shift. S. Kim et al. also reported [79] that the shifts in the $Ni^{2+/3+}$ redox features in the negative direction (ca. 50 mV) is induced by the presence of Co in the Ni hydrous oxide lattice. In agreement with the previous

observations by other groups [70,78,79] , no discernible voltammetry features associated with the $Co^{2+/3+}$ redox couple can be identified for the composite Ni-Co oxide film. Despite of a harmony with previous observations, the precise effect on the catalysis mechanism remains unknown.

The CA study performed at 1.2 V versus RHE for 3 days (Figure 3.7b) reflects the above mentioned behaviour of CVs. At a fixed potential of 1.2 V vs. RHE, the J_{ph} of the n^+pp^+-

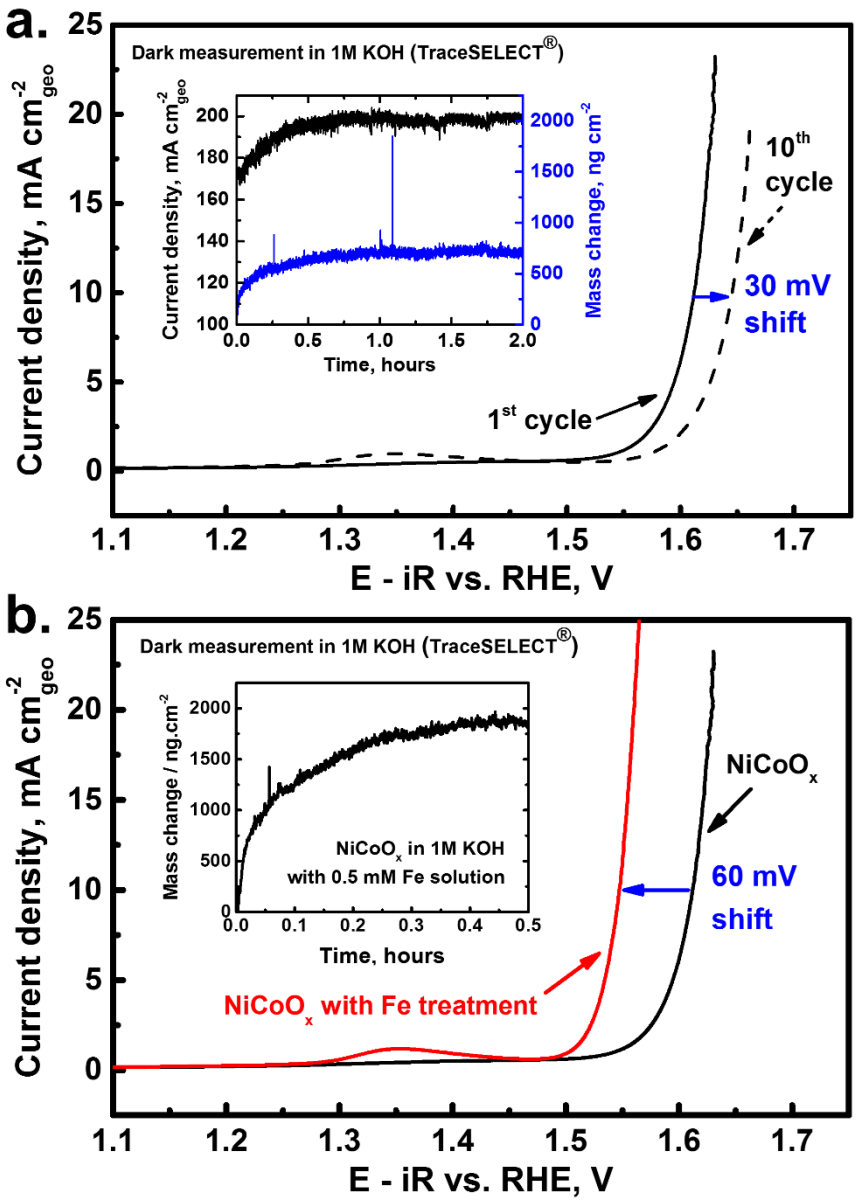

Figure 3.11 (a) Electrochemical CV measurement result for the $NiCoO_x$ deposited on EQCM sample with Co interlayer with subsequent 2 hours long CA and mass change measurement data (inset), and (b) electrochemical current-potential of $NiCoO_x$ before (black) and after Fe-treatment (red). Both CA and mass change measurements were carried out with fixed applied potential of 1.8 V vs. RHE using EQCM's.

Si/Co/$NiCoO_x$ dropped quite quickly from around 22 to 20.5 mA cm^{-2} over about half an hour, after which photocurrent output appears to degrade slowly with constant rate. This degradation continued during the first 20 hours of CA measurement, followed by a slow increase in J_{ph} occurred after around 22 hours followed by stabilized J_{ph} from the 3rd day of the CA experiment. Once the J_{ph} saturated, the sample showed stable J_{ph} output until 144th hours (6 days) without any further changes or degradation (Figure 3.9). Assuming that incorporation rate or diffusion rate of Fe thought the ion-permeable oxyhydroxide structures is independent of time, these CV and CA behaviours are interesting. They suggest that Fe incorporation in the beginning is insufficient to lead to increased activity, but sufficient to lead to decreased activity due to the iron incorporated cobalt oxyhydroxide components. Subsequently the Fe incorporation becomes sufficient to cause an improved OER activity after a certain point. It was found that this V-shape behaviour of the Si photoanode with Co/$NiCoO_x$ is not a coincidence, but reproducible, as an additional CA experiment using a new, but similar, sample showed the same time-dependent behaviour (see Figure 3.10).

3.5 Electrochemical study

The electrochemical properties of $NiCoO_x$ thin film deposited on EQCM sample were investigated by means of CV and CA in 1 M KOH (TraceSelect) under dark condition (Figure 3.11). The as-deposited $NiCoO_x$ films (Figure 3.11, black trace) show quite good performance for the OER. An overpotential of ~ 380 mV is required to achieve a current density of 10 mA cm^{-2} which is in good agreement with the overpotentials obtained in the photoelectrochemical tests (Figure 4a). Nevertheless, after 10 cycles the potential at 10 mA cm^{-2} is shifted anodically by 30 mV. The anodic shift closely resembles the drop in current density in the long-term stability PEC tests and the corresponding anodic shift of the CVs (Figure 3.7a). Subsequent 2 hours long

CA measurement (Figure 3.11a inset) showed increase in current density along with mass change during the first 0.5 hours. Afterwards, the $NiCoO_x$ thin film deposited on EQCM were intentional doped with Fe (Figure $NiCoO_x$ in 0.5 mM Fe/KOH) according to a procedure previously used for NiO thin films [26]. The EQCM result (Figure 3.11b inset) shows a significant increase in mass during treatment of NiO in a Fe-containing solution, which was found to be saturated after ~ 0.5 h of treatment. Irrespective of obtained mass amount, this

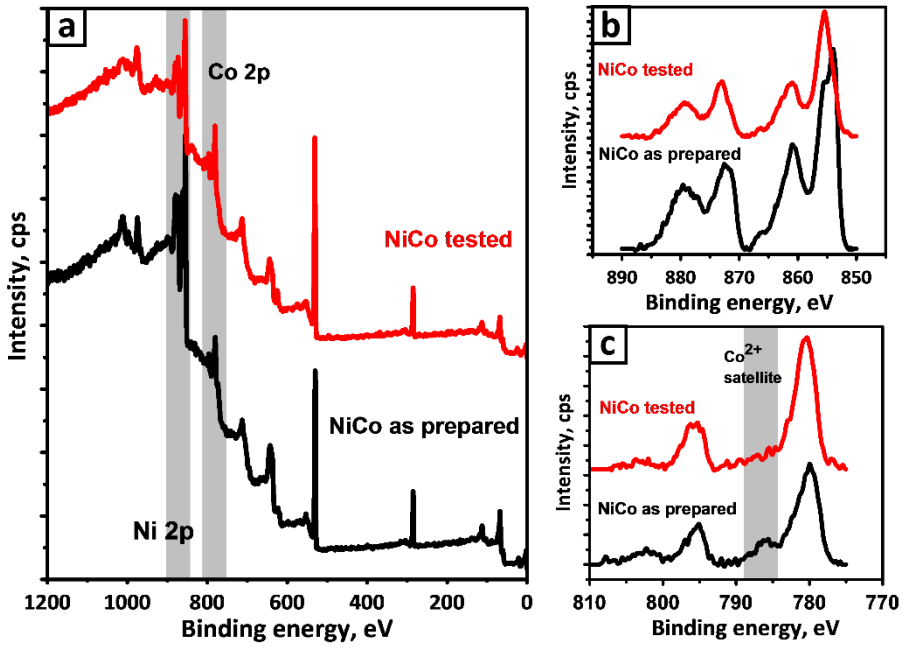

Figure 3.12 (a) XPS survey spectra of the $NiCoO_x$ thin film deposited on EQCM substrate with Co interlayer, and zoomed in (b) Ni 2p XPS spectra, (c) Co 2p region. Black and red color correspond to the curve for the as prepared and after the electrochemical test, respectively.

behaviour is similar to the behaviour of mass change for as-deposited $NiCoO_x$ in Figure 3.11a. We attribute this increase in mass at least partially to Fe incorporation occurring in parallel to oxygen evolution. Interestingly, in the subsequently performed CV (Figure 3.11b) a cathodic shift of 60 mV compared to the as-received $NiCoO_x$ thin film was observed. Thus, an overpotential of ~ 320 mV was required to obtain a current density of 10 mA cm^{-2}. This enhanced performance of the Fe-doped $NiCoO_x$ thin film is in good agreement with the enhancement during prolonged CA of the $NiCoO_x$ thin film used for the back-illuminated PEC studies and can therefore be attributed to a self-driven enhancement of nickel cobalt oxide by metallic Fe-contamination during photoelectrochemical oxygen evolution reaction.

3.6 Post-experimental characterization

XPS measurements were performed on as-prepared $NiCoO_x$ thin films (prepared on EQCM substrates) and on $NiCoO_x$ thin films after 24h of continuous operation at a potential of 1.8 V vs. RHE. Detailed scans of the Ni 2p and Co 2p regions derived from the survey spectra in Figure 3.12a are included in Figure 3.12b and 3.12c. The as prepared $NiCoO_x$ thin film consists of a mixture of Ni^{2+}/Ni^{3+} (at binding energies of 854/856 eV) and Co^{2+}/Co^{3+} (suggested by the satellite feature at 785 eV). After continuous testing for 24 h XPS measurements reveal that Ni

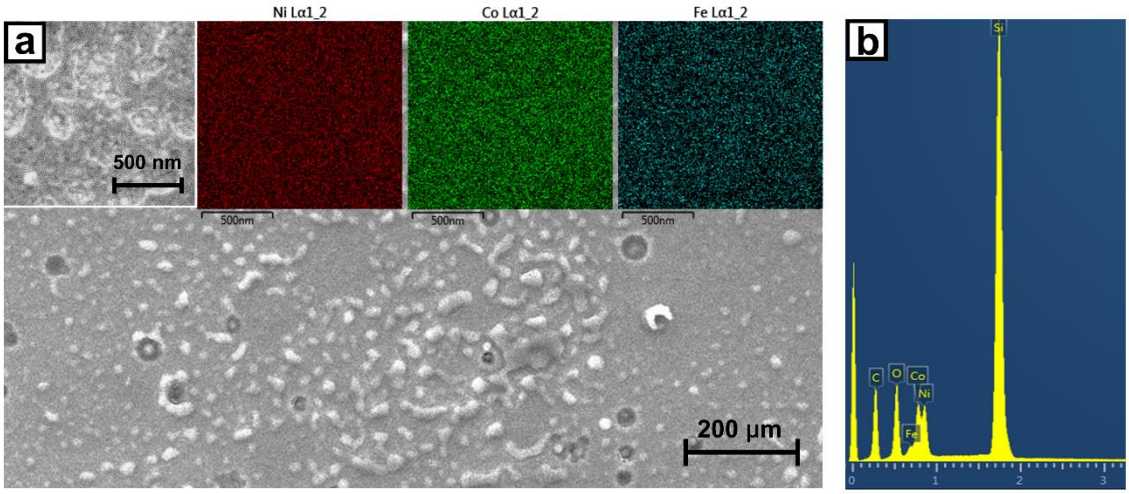

Figure 3.13 (a) SEM picture with the Ni and Fe distribution mapped by EDX of the $NiCoO_x$ thin film deposited on Si photoanode after 6 days of CA testing at 1.2 V versus RHE. Zoomed-in SEM (inset) shows the $NiCoO_x$ has become a porous structure. EDX mapping result (blue color map) and map-sum-spectrum (b) show the presence of Fe on the $NiCoO_x$ film.

and Co are mainly present in their 3+ oxidation state (binding energy of 856 eV for Ni^{3+} shown in Figure 3.12b. For Co^{3+} a characteristic binding energy of 780.5 eV was measured. Furthermore, the characteristic Co^{2+} satellite signal at 785 eV was significantly reduced as shown in Figure 3.12c). The presence of different oxidation states in the as-prepared $NiCoO_x$ thin film as well as its further oxidation during prolonged testing is in good agreement with previously reported NiO thin films prepared and tested under similar conditions [26] and can be ascribed to the transformation into its more porous NiOOH and CoOOH oxidation states which act as host for Fe-impurities [56,76]. The direct detection of Fe by means of XPS is not possible in this case due to the Al source due to the strong overlap with Ni LMM Auger signal and the unfavorable Fe cross section. However, the transformations into more open NiOOH and CoOOH in the $NiCoO_x$ thin film accompanied with the presented data of $NiCoO_x$ studied on EQCM substrate strongly suggest the self-driven enhancement of nickel cobalt oxide by metallic Fe-contamination during prolonged photoelectrochemical oxygen evolution reaction. In addition, Ni and Fe distribution mapped by EDX (Figure 3.13) of the porous $NiCoO_x$ deposited on the Si photoanode after 6 days of CA testing at 1.2 V versus RHE also supports the presence of Fe, along with above mentioned EQCM results.

3.7 Concluding remarks

A back-illuminated n^+pp^+-Si has been coupled to earth-abundant Ni-Co based catalysts and investigated as photoanode for the oxygen evolution reaction in alkaline media (1M KOH, pH = 14). Specifically we have demonstrated the performance of a n^+pp^+-Si/Co/$NiCoO_x$ structure, whose pn-junction is formed at the side opposing the solid/liquid interface, may efficiently drive the OER under back side (dry side) illumination which is the actual operational condition in a tandem water splitting device. Importantly, taking advantage of the synergetic effects between nickel and cobalt, the $NiCoO_x$ OER catalyst coating exhibit excellent catalytic activity as well as long-term stability in highly concentrated alkaline media, which makes it a prospective candidate for the practical OER catalysts. Its onset voltage reached almost 1.08 V at 10 mA cm^{-2} which is very close to that of the sample with IrO_x, which was tested in acid media (0.5M H_2SO_4, pH = 0). Interestingly, the photoanode samples coupled to $NiCoO_x$ showed a non-trivial time-dependent current-voltage behaviour in OER activity. The sample studied exhibits an anodic shift of onset potential, then rebounded cathodically 1M KOH – likely due to Fe incorporation with NiOOH and CoOOH which act as a host for Fe incorporation. This work highlights an approach to using a low band gap photoanode in actual tandem device operation condition, and enhancing its photocatalytic activity simply by aging process.

Chapter 4

4. Using Si as a photocathode bottom cell

In this work we evaluate the experimental and theoretical maximum photocurrent density ($J_{L,\,max}$) limit from the Si based photoelectrochemistry (PEC) system for hydrogen production (HER) under the back side illumination using same Si electrode in chapter 3, but inverted configuration (p^+pn^+). However, using p^+pn^+ Si as the bottom cell (i.e. under back-illumination – where light is incident from the "dry" side of the photoelectrode), a series of experiments [80,81] showed that the photocurrent of a Si bottom cell was limited. The reason is that under back-illumination the electrode-electrolyte interface, which is the electron drain, is on the opposite side with respect to the incident light and since the wafer thickness is larger than the carrier diffusion length (L_e) most electrons are lost to recombination near the back surface. This problem of opposed light absorption and electrochemistry under back-illumination thus dictates a different approach to maximize the charge carrier utilization.

Despite of this unfavorable configuration for the charge carrier utilization, this inverted configuration comes into the spotlight due to the several key benefits: i) its ability to reduce the recombination loss of charge carriers by moving the pn-junction to opposite side with respect to the incident light since the presence of dopants increase local bulk recombination [82,83] and ii) fixed band bending in the silicon at electrode-electrolyte interface can be provided by adding along a shallow a pn^+-junction, whereas the conventional buried junction design requires a very highly doped layer (p^+) near the electrode-electrolyte interface to form a space-charge region which allows electron tunnelling through the interface from the n-type bulk Si to the electrocatalyst. On the other hand - moving the pn-junction to the shadow-side of the device requires excellent surface passivation of the light incident side, as we shall see in this chapter.

This chapter is mainly based on previous publication [28].

4.1Theoretical study of inverted Si-based photocathode design

4.1.1 Ideal current density vs. effective thickness

Crystalline silicon has an indirect band gap (1.12 eV) and must therefore be thicker than most direct band gap light absorbers in order to have substantial optical absorption and electron-hole pair generation [84]. Figure 4.1 shows, as an inset, the available photons versus wavelength in the reference solar spectrum (AM 1.5G) [20]. The figure also shows the (red filtered) simulated solar spectrum used in this work where a Xe-lamp illumination is filtered using AM 1.5 and 635-nm-cut-off filters (*i.e.* $\lambda > 635$ nm to approximate the wavelengths and intensity would be received in a real tandem device).

The irradiance of solar light can be converted into a photo-generated electron-hole density (mA cm^{-2}) per unit wavelength for a Si-slab device of finite thickness. The resulting (integrated) current density is shown in Figure 4.1 for both the AM 1.5G reference and for our simulated solar spectrum. If Si were to exhibit ideal behaviour of 100% internal quantum efficiency, *i.e.* zero recombination and infinite diffusion length, this electron-hole density ($J_{theo,\ max}$) would correspond to the measured photocurrent density. In the calculation of $J_{theo,max}$ the surface

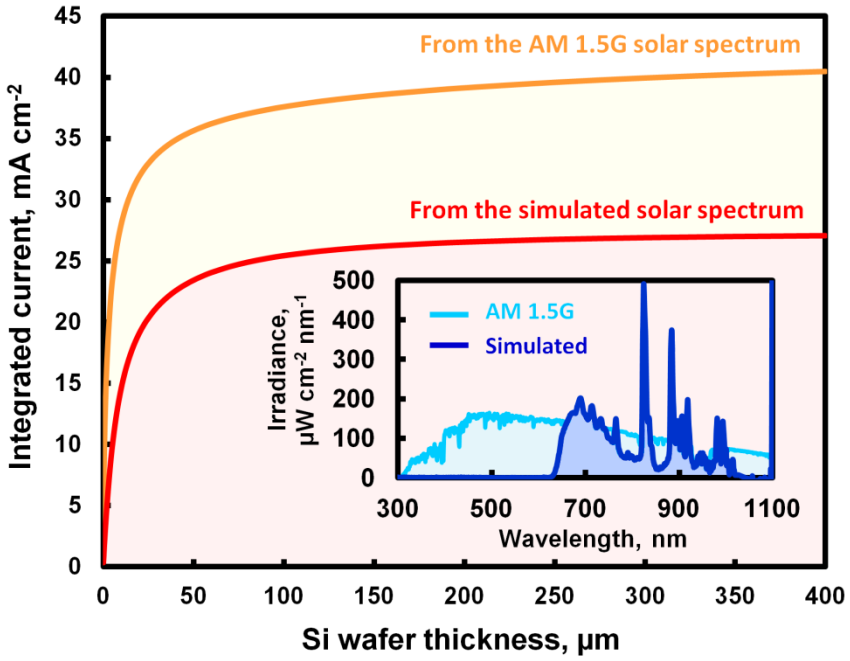

Figure 4.1 Theoretical light-induced maximum current density in term of Si wafer thickness and the light spectrum of AM 1.5G and solar simulator with AM 1.5 and 635-nm-cut-off filters as an inset. The total irradiance of the simulated solar spectrum is 41.8mW cm^{-2}, and for the standard AM 1.5G spectrum – 85.1 mW cm^{-2} with range from 250 to 1100 nm in wavelength.

reflectance has been set to zero. The effect of surface reflectance will be addressed in detail later in this section. The current density due to photons which are absorbed during a single pass through the Si wafer with a certain thickness *x* can be theoretically calculated as follows:

$$J_{L,x} = \int_{\lambda_{\min}}^{\lambda_g} q \frac{\lambda P(\lambda)}{hc} a(\lambda) d\lambda \tag{4.1}$$

The integration limits are λ_g (the absorption edge of material), and λ_{min} (the shortest wavelength of the light) taken as 1100 nm and 250 nm in this work. The total irradiance of the (red filtered) simulated solar spectrum measured in this range was 41.8 mW cm^{-2}, which corresponds to the total light intensity of the standard AM 1.5G spectrum with range from 635 nm to 1100 nm. $a(\lambda)$ is the absorbance of the Si slab with a certain thickness, and can be approximated by Beer-Lambert law [85] (assuming that light only passes once through the cell and all light generated carriers are collected):

$$a(\lambda) = \frac{\alpha(\lambda)}{ln10} L \tag{4.2}$$

where *L* is Si thickness, and *n* is the index of refraction of the Si slab. The absorption coefficient $\alpha(\lambda)$ as a function of wavelength used in this work can be found in Figure 4.2.

The absorbed light flux depends on the absorption length of the light in the silicon. As shown in Figure 4.1, approximately 40 and 27 mA cm^{-2} of current density can be harvested in an ideal Si photo absorber (if the Si is sufficiently thick), from AM 1.5G and (red filtered) simulated solar

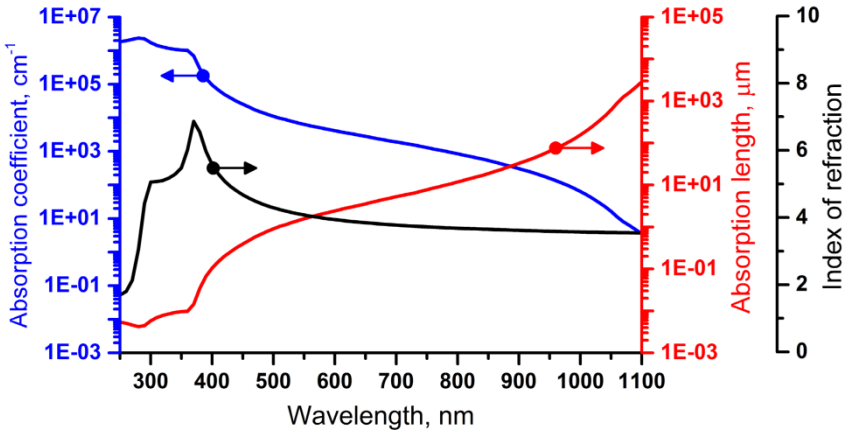

Figure 4.2 Absorption coefficient of silicon in cm-1 as a function of the wavelength (blue) and absorption length in silicon (red). Silicon is an indirect band gap semiconductor so there is a long tail in absorption out to long wavelengths. The data is graphed on a log scale, and the drop in absorption at the band gap (around 1100 nm) is sharper than might first appear. The n value, i.e. index of refraction, of silicon is also plotted (black).

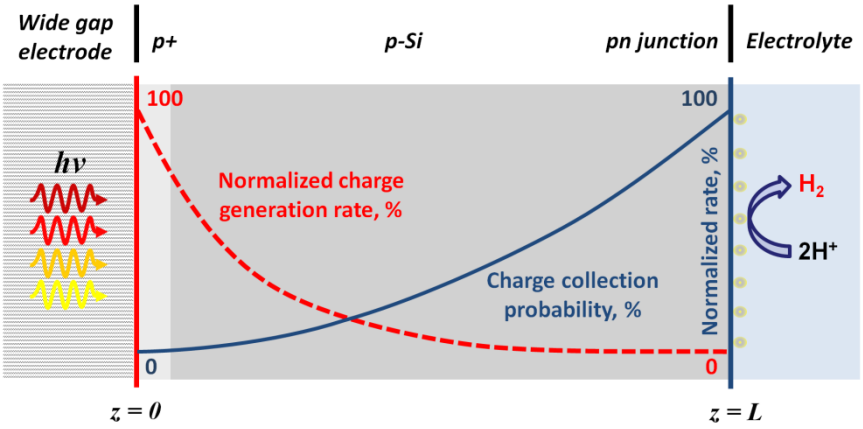

Figure 4.3 Schematic of the simplified back-illuminated model device which is used in theoretical modelling. The normalized charge generation and charge collection probabilities in the device are also illustrated (not to scale) as a function of depth (z) inside the absorber with thickness L. It was assumed that optical properties of Si are homogeneous regardless of doping type.

spectrum respectively. This figure also indicates that the integrated current density begins to saturate at thicknesses around 50 µm Si with a current density level of approximately 35.7 mA cm^{-2} and 23.5 mA cm^{-2}, under AM 1.5G and (red filtered) simulated solar spectrum respectively. This reveals that there is no need for using a thick wafer. In fact, a silicon back-electrode of just 15 - 25 µm thickness would be able to current match a 10 mA cm^{-2} - or even 15 mA cm^{-2} top electrode in a tandem device. However, as we shall see below, introduction of realistic losses recommends a somewhat thicker silicon absorber.

4.1.2 Charge collection model in a real Si device

In real Si devices finite charge recombination and charge diffusion lengths are major limiting factors reducing $J_{L,\,max}$. It is important to note that neither front nor back surface treatment for light trapping are used in experiments. Therefore we introduce the non-light trapping charge generation rate ($G(z)$), and the charge collection probability ($C_P(z)$) to quantify $J_{L,max}$ in real devices. Thus a simplified device model based on Si with a shallow pn^+-junction at the electrode-electrolyte interface was introduced as shown in Figure 4.3. $C_P(z)$ depends on the distance that a light-generated carrier must travel compared to the diffusion length, L_e, and also on the surface properties of the device. If the carrier is generated further away from the junction than a diffusion length, ($z > L_e$), then the collection probability of this carrier is quite low. Similarly, if the carrier is generated closer to a region with high recombination (*e.g.* a non-passivated surface) than the junction, the carrier will recombine. Under, broad-band illumination most of the

absorption (and electron-hole generation) takes place very close to the incident light surface Further absorption of low energy photons takes place throughout the bulk of the silicon, but the excitation density is small. However, the charge collection probability is highest near the pn^+-junction – *i.e.* the back side with respect to illumination. The dilemma is illustrated in Figure 4.3.

The generation rate is the number of electron-hole pairs generated at each point in the device due to the absorption of photons [86]. Neglecting reflection, the amount of incident light which is absorbed by a material depends on the absorption coefficient α(λ) (unit cm^{-1}) and the thickness of the absorber. Assuming that the absorption of photons directly causes the generation of an electron-hole pair, the $G(z)$, in a thin slice of absorber is determined by finding the change in light intensity across this thin slice, and consequently the electron-hole generation rate at any point in the device can be defined as follows:

$$G(z) = \alpha H_0 e^{-\alpha z} \tag{4.3}$$

where H_0 is spectral photon flux density at the surface (photons/sec/unit-area/wavelength increment), and z is distance into the absorber. The rate of light-generated carriers, G, as a function of depth z in Si can be theoretically calculated:

$$G(z) = \int_{\lambda_{min}}^{\lambda_g} \alpha(\lambda) H_0(\lambda) e^{(-\alpha(\lambda)z)} d\lambda \tag{4.4}$$

The spectral photon flux density H_0 can be calculated from measured irradiance $P(\lambda)$ of the solar simulator as the ratio of irradiance to photon energy using the equation shown below:

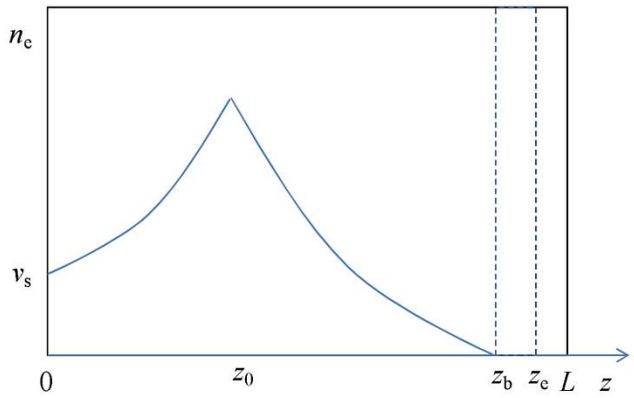

Figure 4.4 Simple photoabsorber model with pn-junction. The blue curve illustrates how electron density changes with depth in photoabsorber when the electron-hole pair generation occurs at point z_0.

$$H_0 = \frac{\lambda P(\lambda)}{hc} \tag{4.5}$$

where λ is wavelength, c is the speed of light in vacuum, and *h* is Plank's constant. In the case where the surface is not perfectly non-reflecting, the irradiance is corrected by measured reflectivity at each wavelength (Figure 4.2). The charge collection probability as a function of depth, $C_P(z)$, was calculated under the assumption that there is no excess electron density at the junction boundary (i.e. $n_e = 0$) while at z = 0 the surface recombination velocity requires $dn_e/dz = Sn_e$, where $S = v_s/D$ is the normalized surface recombination velocity, and v_s is the surface recombination velocity and *D* is diffusivity of Si. The excess electron density in steady state is governed by the steady state continuity equation:

$$\frac{d^2 n_e}{dz^2} = \frac{n_e}{L_e^2} \tag{4.6}$$

where $L_e = (D\tau_e)^{1/2}$ is the minority carrier diffusion length, and τ_e is carrier lifetime. The collection probability $C_P(z)$ is the probability that an electron-hole pair generated at a certain depth, z, will be collected (separated) by the pn-junction and consequently contribute to the photocurrent. The solution of the equation 4.5 is:

$$n_e = n_{e0} \frac{\cosh\frac{L-z}{L_e} + SL_e \sinh\frac{L-z}{L_e}}{\cosh\frac{L}{L_e} + SL_e \sinh\frac{L}{L_e}} \tag{4.7}$$

The electron flux density is then:

$$F = -D\nabla n_e = \frac{D}{L_e} n_{e0} \frac{\sinh\frac{L-z}{L_e} + SL_e \cosh\frac{L-z}{L_e}}{\cosh\frac{L}{L_e} + SL_e \sinh\frac{L}{L_e}} \tag{4.8}$$

Assume now electron hole pair generation at $z = z_0$ in a simple pn-junction model, where the total absorber thickness is *L* and the depletion layer has the boundaries at $z = z_b$ and $z = z_e$ while the back side at $z = 0$ has normalized recombination rate *S*. At the junction boundaries $n_{e0} = 0$ is assumed. The minority carrier electrons generated at z_0 will diffuse to the left and right and create the steady state excess carrier profile shown in Figure 4.4; only the electron flux density at z_b contributes to the collected electrons. Thus the collection probability $C_P(z)$ is the flux density

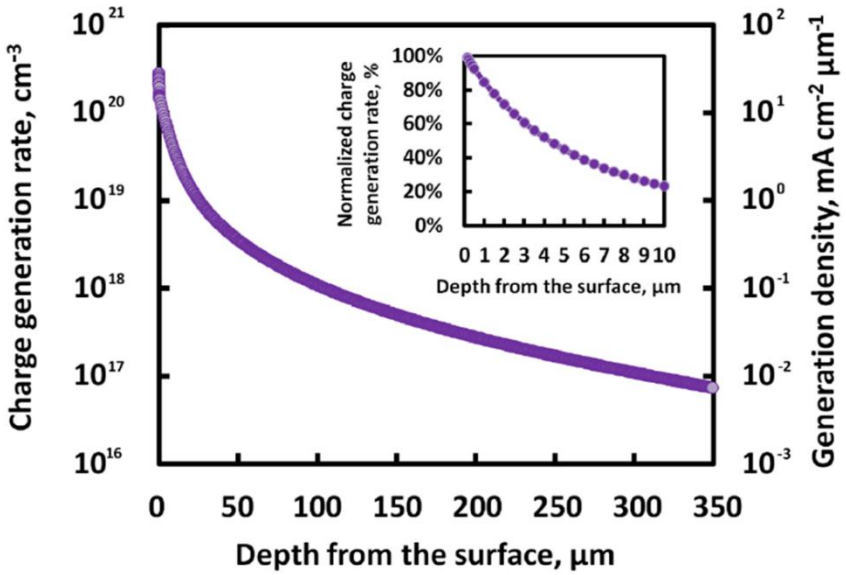

Figure 4.5 Calculated charge generation induced by the light from the (red) simulated solar spectrum shown in Figure 4.1. The normalized charge generation rate is ratio of charge generation rate to that at the surface (z = 0), where the value shows its maximum.

at z_b divided by the sum of flux density magnitudes at z_0. The flux densities magnitudes can be written as follows:

$$F(z_b) = \frac{D}{L_e} n_{e,z_0} \frac{1}{\sinh\frac{z_b - z_0}{L_e}}, \text{ Note } S \to \infty \text{ at } z = z_b; \tag{4.9}$$

$$F(z_0)_{right} = \frac{D}{L_e} n_{e,z_0} \frac{\cosh\frac{z_b - z_0}{L_e}}{\sinh\frac{z_b - z_0}{L_e}}; \tag{4.10}$$

$$F(z_0)_{left} = \frac{D}{L_e} n_{e,z_0} \frac{\sinh\frac{z_0}{L_e} + SL_e\cosh\frac{z_0}{L_e}}{\cosh\frac{z_0}{L_e} + SL_e\sinh\frac{z_0}{L_e}} \tag{4.11}$$

and thus the collection probability becomes:

$$C_P(z) = \frac{F(z_b)}{F(z_0)_{right} + F(z_0)_{left}} = \frac{1}{\cosh\frac{z_b - z_0}{L_e} + \sinh\frac{z_0}{L_e} \cdot \frac{\sinh\frac{z_0}{L_e} + SL_e\cosh\frac{z_0}{L_e}}{\cosh\frac{z_0}{L_e} + SL_e\sinh\frac{z_0}{L_e}}} \tag{4.12}$$

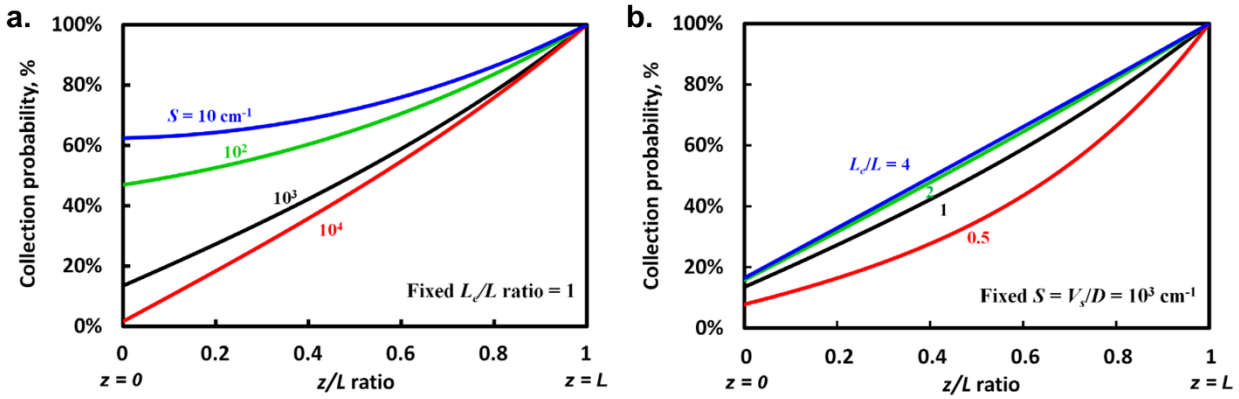

Figure 4.6 Calculated collection efficiency with various $S = v_s/D$ (b) and L_e/L (c) ratio using the equation 4.12.

In the depletion layer the $C_P(z)$ is 1. As already shown in the previous chapter 3, the depletion layer of our pn^+ Si is approximately 640 nm, but its contribution under the back-illumination is negligibly small since the normalized charge generation rate $G(z)$ is close to zero at the junction boundary.

Figure 4.5 shows behavior of $G(z)$ in terms of the depth from the light incident surface based on the equation 4.4. An interesting point from Figure 8a is that $G(z)$ drops below 50% of its initial value (*i.e.* at $z = 0$) just 5 μm from the surface. In fact, charge generation is almost zero at the junction boundary. This underscores the importance of charge collection probability ($C_P(z)$) since only collected charge become external photocurrent. The $C_P(z)$ as a function of depth, z, can be calculated from the equation 4.12, and this can be found in Figure 4.6.

As shown in Figure 4.6a and b, as one moves away from the junction at $z = L$, the collection probability drops. $C_P(z)$ becomes quite low at the surface (at $z = 0$) where electron-hole generation is fastest. The impact of surface recombination velocity and diffusion length on collection probability is also illustrated by varying S (and L_e/L) in equation 4.12. As shown in Figure 4.6c, $C_P(z)$ increases with the L_e/L ratio, and begins to saturate from an approximate ratio of $L_e/L = 2$ with $C_P(z)$ below 20% at the surface. Likewise, $C_P(z)$ increases with decreasing S, but unlike the L_e/L ratio, $C_P(z)$ at the surface ($z = 0$) increases significantly as S value decreases. This indicates that increasing the diffusion length (L_e) increases the charge collection efficiency ($C_P(z)$) only up to a certain point. Beyond this point further increase of diffusion length of the Si (i.e. the bulk quality of the Si) has little benefit for charge collection since in that limit the total recombination is dominated by surface recombination. This behavior of $C_P(z)$, and consequently

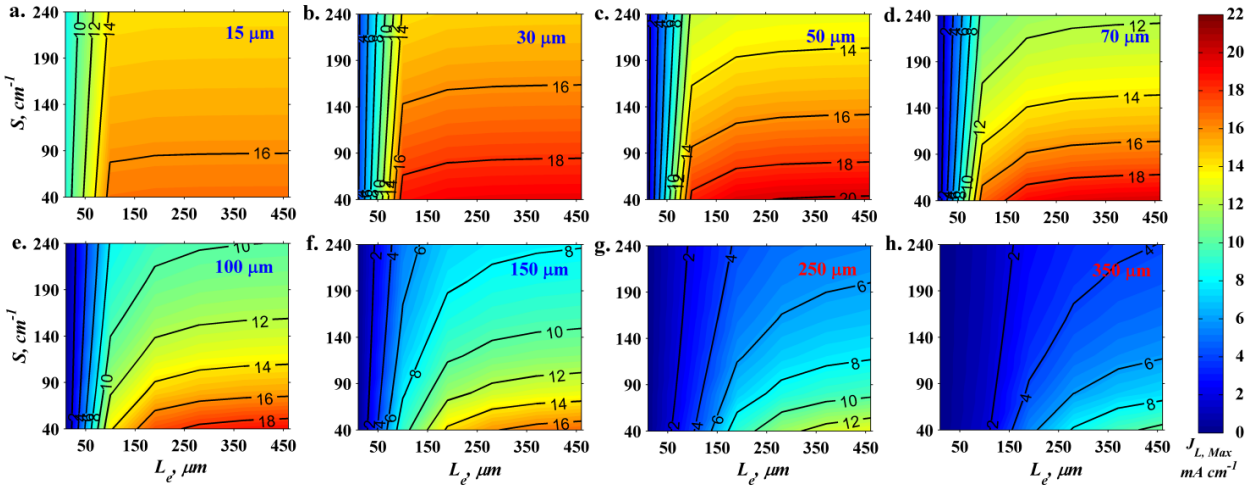

Figure 4.7 Contour plots of theoretical maximum current density versus diffusion length and surface recombination rate for 15 µm thick (a), 30 µm thick (b), 50 µm thick (c), 70 µm thick (d), 100 µm thick (e), 150 µm thick (f), 250 µm thick (g), and 350 µm thick (h) bottom cell under the simulated bottom cell illumination (see Figure 4.1). These plots illustrate impact of S and L_e on theoretical current density, and at the same time how these impacts change with Si thickness.

$J_{L,max}$ for different thicknesses is shown as a function of S and L_e in Figure 4.7. The $J_{L,max}$ can be calculated from the equation shown below by multiplying $G(z)$and $C_P(z)$ of the carriers:

$$J_{L,max} = q\int_0^L G(z)C_p(z)dz \tag{4.13}$$

As shown in each plot of Figure 4.7, once L_e reaches a certain value comparable to the absorber thickness, surface recombination (S) starts to become more significant. As shown in Figure 4.7a (L = 15 µm), the slopes of contour lines are relatively moderate in the short diffusion length region and the gap between the lines have been broadened. This indicates J_L in a real device will be less sensitive to device parameters, but the maximum current for 15 µm thick Si is limited below 17 mA cm^{-2} while a 30 µm thick Si (Figure 4.7b) can reach almost 20 mA cm^{-2}. The thinnest samples are limited by photons with long wavelength passing through the Si with little absorption. On the other hand, a 350 µm thick device (Figure 4.7f) shows a J_L limited at approximately 10 mA cm^{-2} and even this value requires good surface passivation and a very high L_e level which only canbe achieved by using quality material such as float zone (FZ) Si.

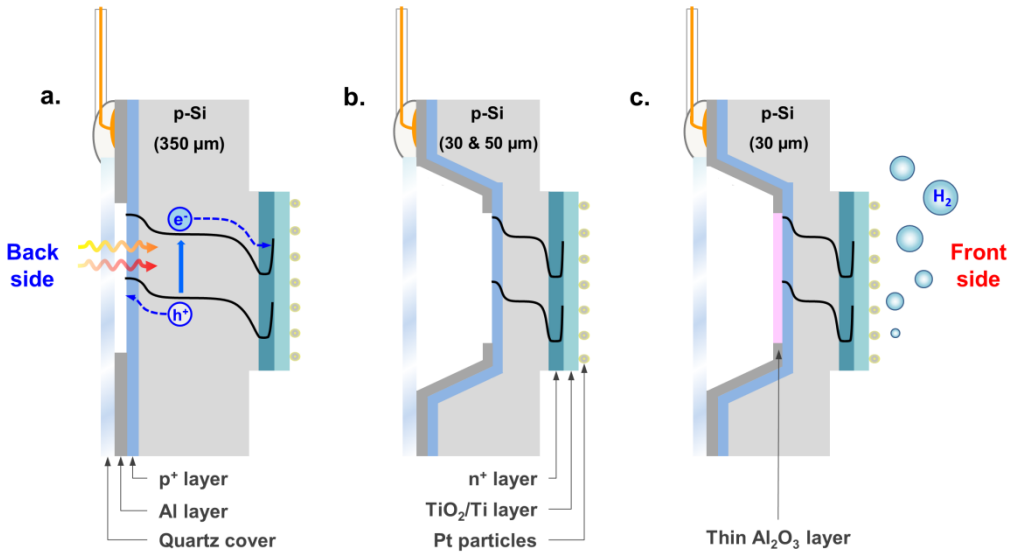

Figure 4.8 Schematic cross section of the unthinned (a), thinned device (b), and thinned device with surface passivation layer (Al_2O_3) used for photocatalytic activity (HER) experiments. The light is incident from the back side and HER occurs on the front side. In real device testing the back side of sample was protected by Quartz glass cover with epoxy to prevent corrosion in acidic electrolyte of the Cu-wire for electrical connection (covered with glue).

The reason is that charge collection probability with identical S and L_e decreases with increased Si thickness due to the decreased L_e/L ratio and the impact of this ratio increases significantly as thickness of Si increases as already shown in Figure 4.6b. Clearly, the choice of thickness is strongly dependent on L_e and S and must be optimized with respect to cost. Considering that conventional solar cell grade CZ Si wafer shows L_e of 100 ~ 300 µm [85] using Si with thickness around 50 µm seems an appropriate compromise. As shown in Figure 8c, 50 µm thick Si shows peak values up to 20.2 mA cm^{-2} under the $\lambda > 635$ nm simulated spectrum. This is a high J_L value compared to the other thicknesses with identical S and L_e.

4.2 Experimental study

4.2.1 Sample fabrication methods

CZ-Si based photocathodes are fabricated with different wafer thickness in order to vary the L_e/L ratio (L= 30 ~ 350 µm) on otherwise similar electrodes. The thickness of the Si was varied by sample thinning (using photolithography and wet etching) of p-type Si substrates. Schematic drawings of samples used in this work are shown in Figure 4.8. The shallow pn^+-junction was produced in p-type (100) Si wafers (Topsil, 1-20 ohm-cm, boron-doped, acceptor density $N_A \approx 5 \cdot 10^{19}$ cm^{-3}) by previously mentioned ion implantation in chapter 3. As shown in our previous

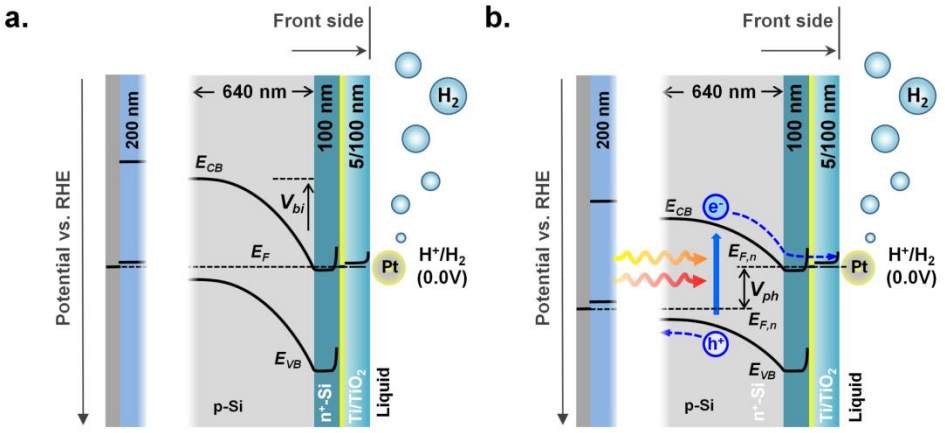

Figure 4.9 Schematic energy diagram of the pn^+ Si with Ti-TiO_2 surface in the dark in equilibrium with the H^+/H_2 reaction (a), and illuminated condition with photovoltage (b).

work [60], this n^+ doping at the solid/liquid interface screens the band-bending in the silicon from the electrolyte, which allows for increased photovoltage [87]. As shown in Figure 4.9, the electron-hole pairs are separated by a built-in electric field which the pn^+ junction provides. The electrons are then transferred to the solid/liquid interface though the conduction band of TiO_2 determined by using Mott-Shottky analysis (detail calculations are shown in following section). A mesa-isolated pn^+-Si structure was formed in the same manner as described in chapter 3. The back side of the same samples were also doped with a thin p^+ doping (see detail in chapter 3). A ring-shaped, light permeable, Al back contact layer was also deposited as described in chapter 3, but it was formed at the p^+-side in this case. The resulting active area was precisely measured by image analysis using ImageJ 1.46r after the experiments.

The p^+ doped layer in this device, likely to that of n^+pp^+-Si photoanode in chapter 3, reduces overall series resistance by providing parallel path ways for holes to reach the Al charge collecting layer. Furthermore in actual tandem device operation condition it can also act as a part of the recombination layer (tunnel junction) for the injected holes from photocathode and the electrons from photoanode. Samples prepared without the p^+ doped layer are used to quantify the importance of the p^+ sheet-conducting layer (see schemes in Figure 4.10). All layers for those samples are fabricated using same process as mentioned earlier. Figure 4.10 shows the CV for photocatalytic H_2 evolution of the pn^+-Si electrodes with direct back contact at the middle of the sample and back contact on Al charge collector under front side illumination. H_2 could be visually observed bubbling off from the semiconductor/liquid interface as the current increased. The pn^+-Si with direct back contact has an onset of 0.49 V vs. RHE with J_L approximately 24

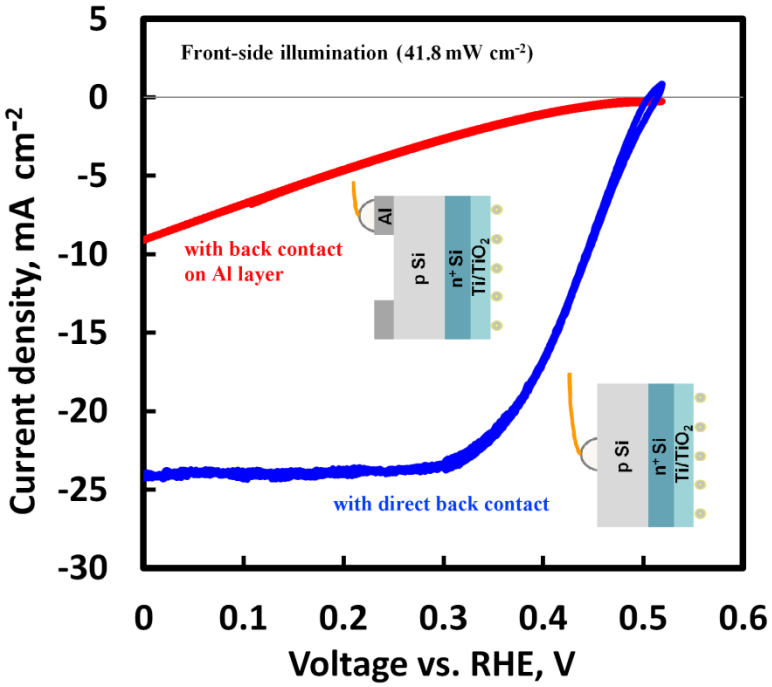

Figure 4.10 CV of a pn$^+$-Si photocathode with direct back contact (blue) and one with back contact on Al charge collection layer (red) under front-illumination. This illustrates the severe series-resistance problem and thus the need for a transparent interlayer to form an efficient pathway for carriers.

mA cm^{-2} under these conditions. On the other hand, the sample with an Al layer (red curve) back contact has a similar V_{oc}, but it has a very low J_L at 0 V vs. RHE due to a high series resistance.

This shows that simply adding a ring-shaped Al charge collector layer is not sufficient to provide an efficient pathway for injected holes from Si. Thus there is a need for an additional transparent layer with low lateral resistance (R_l) in order to transfer the holes to the Al layer without significant ohmic loss. Furthermore, since we wish to illuminate from the back, this transport layer must be transparent. This was achieved via a shallow boron doped p$^+$ layer, which is formed between the Al back contact and the p-Si substrate as shown in Figure 4.8. This structure makes the overall series resistance of the device comparable to a conventional Si device with direct back contact. It was estimated that a doping concentration of 10^{20} cm^{-3} ($5 \cdot 10^{16}$ at/cm^2 at 100 keV) of boron could provide a sufficiently low sheet resistance to the Si surface [88] and consequently an efficient carrier transport pathway.

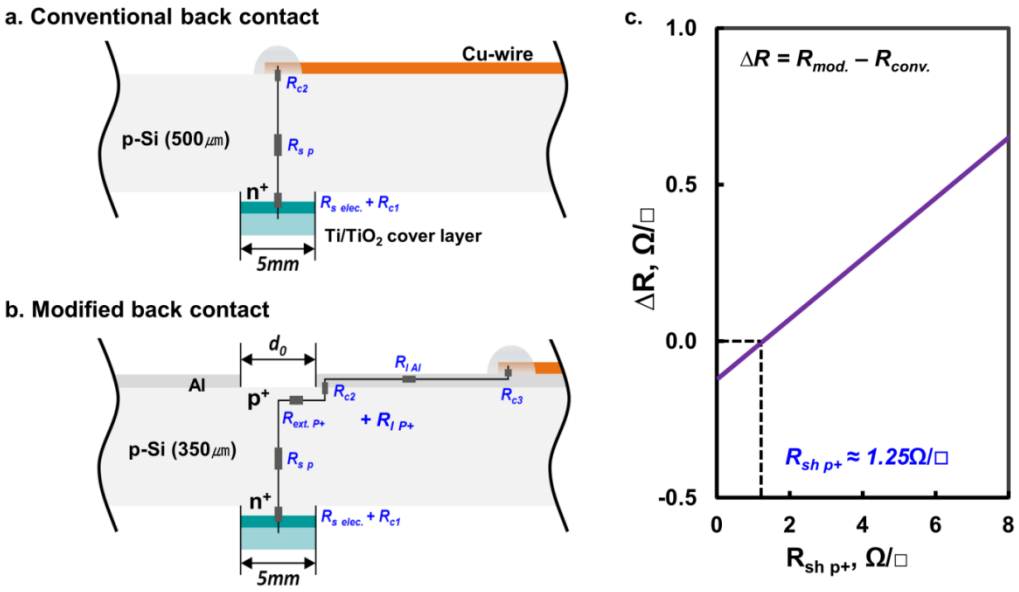

Figure 4.11 Cross-sectional schemes with resistance breakdown for the conventional direct back contact (a) and modified back contact (b). Difference between the sums of resistance elements for each design is plotted in (c), indicating that sheet resistance of the p^+ layer should be close to 1.25 Ω/□ to avoid ohmic resistance issue.

Abovementioned doping concentration for p^+ layer was determined based on the simplified calculation for the total series resistance as shown in Figure 4.11. The required sheet resistance of p^+ layer ($R_{sh\ p+}$) was set to reach the same total series resistance of the device with direct back contact (direct Cu-wire on the back side without any additional doped layer) by using a simple calculation:

$$\Delta R = R_{mod.} - R_{conv.} \tag{4.14}$$

where $R_{mod.}$ And $R_{conv.}$are the sum of resistance components for the modified back contact design and conventional direct back contact design, respectively. If we assume that contact resistance between the semiconductor and metallic layers is close to 0, the equation 4.14 can be described as:

$$\left(R_{S,Thin\ P} + R_{l,p^+} + R_{ext,p^+} + R_{l,Ti}\right) - R_{S,Thick\ P} = 0 \text{ for ideal case} \tag{4.15}$$

$$R_{S,Thin\ P}\ and\ R_{S,Thick\ P} = \rho\frac{l}{A} \tag{4.16}$$

$$R_{l,p^+} \approx \frac{1}{8\pi}R_{sh,p^+} \tag{4.17}$$

$$R_{ext,p^+} = \frac{R_{sh,p^+}}{2\pi}\ln\frac{d_0}{5} \tag{4.18}$$

$$R_{l,Al} \approx \frac{1}{8\pi}R_{sh,Al} \tag{4.19}$$

where $R_{S,P}$ is series resistance of p-type Si, ρ is resistivity, l is thickness of Si, A is area, $R_{l,p+}$ is lateral resistance factor of p^+ layer, $R_{sh,p+}$ is sheet resistance of p^+ layer, $R_{ext,p+}$ is external resistance (or coaxial resistance), d_0 is diameter of hole at back side of Si, $R_{l,Al}$ and $R_{sh,Al}$ are lateral and sheet resistance of Al contact layer, respectively.

According to the plot of ΔR in Figure 4.11c, the total series resistance of the modified back contact sample becomes similar to that of the conventional back contact design when $R_{sh\ p+}$ reaches 1.25 Ω/□ (under assumption that d_0 is fixed as 8 mm as same as that of Si photoanode used in chapter 3). The previous study on the relationship between the sheet resistance of Si and doping concentration [88] reveals that boron doping concentration should be level of 10^{18} cm^{-3} to match with the required $R_{sh\ p+}$ calculated in this work. Since the boron doping concentration used for the p^+ layer exceeds 10^{20} cm^{-3}, it is reasonable to assume that there is no resistance issue originated from the modified back contact design.

In order to prevent the Si surface from photo-corrosion during the photo-electrochemical measurements, a Ti/TiO_2 (5/100 nm) protection layer was sputtered on the n^+ doped side (electrolyte side) of samples using previously published methods [60,82]. In case of TiO_2, Ti was reactively sputtered in an oxygen background. Prior to sputter deposition all wafers were dipped in buffered HF for 30 sec, rinsed in Millipore water, dried and were then immediately placed in the sputter chamber to prevent the Si surface from deactivation by native oxide formation. All samples were cleaned with "piranha" solution (3:1 H_2SO_4 (96%) : H_2O_2 (30%)), washed with ultrapure water (18 MΩ cm) and dried before having 250 ng (Pt basis) of a dinitrosulphatoplatinate solution (Johnson Matthey) drop-cast on them. Pt was used as a co-catalyst in order to achieve high catalytic activity for HER. The thickness of the wafers was controlled using photolithographically thinned p-type Si substrates to keep the L_e value the same for all samples. Finally, they were coated with Teflon tape with a hole punched out yielding an active area of approximately 0.2 cm^2. Unlike previously studied Si-photoanode case, this work was carried out in acid media (1M $HClO_4$, pH = 0), the sample is not required to be sealed with epoxy. The unprotected Si area is just deactivated by the acid electrolyte, thus unexpected electrical shunt can be avoided. However, the back side of the samples was covered with 300 µm thick quartz glass (see chapter 3) using epoxy as same as Si-photoanode in 1M KOH (chapter 3), because Al back contact is prone to corrosion.

4.2.2 Understanding band diagram

4.2.2.1 Calculation at pn$^+$-junction

Most of this band diagram has already been demonstrated in chapter 3 and our previous works [28]. In explaining the band diagram, we will start from the pn-junction of electrode and move towards the electrolyte. Since exactly the same Si configuration fabricated in the same manner as described in chapter 3, band bending and energy positions in bulk Si should be same as those of Si photoanode which was used in chapter 3. The only difference is that Si photocanode in this chapter has an inverted band diagram (mirror-like), since pn-junction, in this case, is placed at the solid/liquid side. Thus, study on n$^+$-Si/Ti/TiO_2/Pt/liquid interfaces will be discussed in this part. For the band diagram calculation of the Si-bulk and back contact side, refer the chapter 3.2.1 and 3.2.2.

4.2.2.2 Calculation at n$^+$-Si/Ti interface

In this work we assume the n$^+$-Si/Ti interface forms a Schottky barrier with no metal induced gap states or Fermi level pinning. If this is the case, the built-in potential $\Phi_{i,Si}$ at the n$^+$-Si/Ti interface is the difference between the Ti work function (Φ_{Ti} = 4.33 V) [89] and the n$^+$-Si ionization energy ($\Phi_{n+\text{-}Si}$) plus the deviation between the flat band potential and the conduction band. Assuming that $\Phi_{n+\text{-}Si}$ is close to the electron affinity of Si (χ_{Si} = 4.15 V) [65] This is shown in equation below:

$$\Phi_{i,Si} = \Phi_{Ti} - \chi_{Si} + \frac{kT}{e} ln\left(\frac{N_{C,Si}}{N_{D,n^+-Si}}\right) \tag{4.20}$$

$\Phi_{i,Si}$ was found to be 0.15 V. Since Ti is a metallic layer, and has a high carrier density compared to the Si, thus the bias will be distributed entirely over the n$^+$ Si region. The band bending distance in the n$^+$-Si can be determined by equation:

$$W_{n^+Si/Ti} = \sqrt{\frac{2\varepsilon_{Si}\varepsilon_0\Phi_i}{eN_{D,n^+-Si}}} \tag{4.21}$$

The barrier width was found to be approximately 1.4 nm, and electron transfer from the Si to the Ti would most probably have to occur through tunneling.

4.2.2.3 Calculation at TiO_2/liquid interface

4. Using Si as a photocathode bottom cell

From the Mott-Schottky analysis the TiO_2 conduction band was determined to be -0.09 V vs. RHE, the donor density was $4.5 \cdot 10^{19}$ cm^{-3}, and the flat band potential was -0.07 V vs. RHE. Since the $E_{FB,\ TiO2}$ is very close to the work function of Ti, thus it can be assumed this junction will show Ohmic behavior. From our previous works we have seen that TiO_2-Pt system forms an ohmic contact, thus there shouldn't be a barrier at the interface [60].

The depletion region width of TiO_2 at the interface is given by:

$$W_{TiO_2/liquid} = \sqrt{\frac{2\varepsilon_o \varepsilon_{TiO2} \Phi_{B,TiO2}}{eN_{D,TiO_2}}} \tag{4.22}$$

ε_{TiO2} is the relative permittivity of TiO_2 (75) [90], $N_{D,TiO2}$is the doping density of TiO_2 obtained from Mott-Shottky analysis ($4.5 \cdot 10^{19}$ cm^{-3}). $\Phi_{B,TiO2}$ is the barrier height at TiO_2/liquid interface, and it can be simply calculated by:

$$\Phi_{B,TiO_2} = E_{H^2/H_2} - E_{FB,TiO_2} + \frac{kT}{e} ln\left(\frac{N_{D,TiO_2}}{N_{C,TiO_2}}\right) \tag{4.23}$$

where $N_{C,TiO2}$ is the density of states in the conduction band, which is $6.8 \cdot 10^{20}$ cm^{-3} for TiO_2 [91]. Since we assume that interface forms Fermi level pinning, above-mentioned equation results in

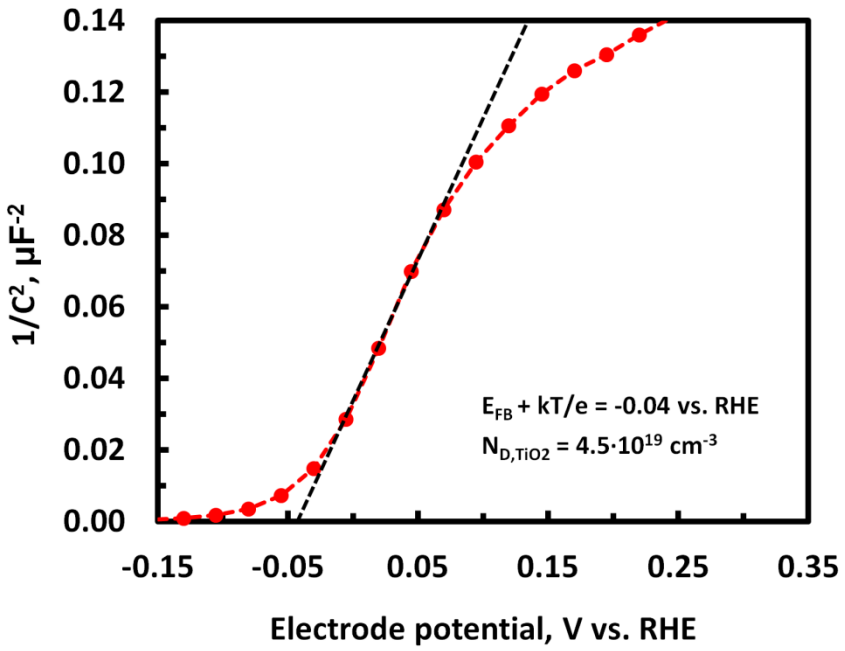

Figure 4.12 Mott-Schottky plot of sputtered 100 nm TiO_2/5 nm Ti on n^+ Si surface. The curve with increasing $1/C^2$ with electrode potential indicates n-type behavior of deposited TiO_2 layer.

$\Phi_{B,TiO2}$ of 0.038 V. Applying this values results in $W_{TiO2/liquid}$ of 1.02 nm.

Material and device parameters which have been used for the calculation can be found in Appendix A.

4.2.2.4 Mott-Schottky analysis

To determine the TiO_2 conduction band, we provided Mott-Shottky analysis using 100 nm TiO_2/5 nm Ti deposited on n^+ Si. The n^+ Si was chosen to prevent unexpected photovoltage effect. This sample was tested electrochemically in 1 M $HClO_4$ electrolyte. For this experiment a modulation frequency of 10 kHz, perturbation amplitude of 35 mV has been used. Figure 4.12 shows the result of this experiment. The flat band potential of TiO_2 can be estimated by using Mott-Shottky equation (see equation 2.5), and then conduction band E_{CB} of TiO_2 can be calculated using equation 2.6. Using these equations a flat band potential of -0.07 V vs. RHE and dopant density of $4.5 \cdot 10^{19}$ cm^{-3}, and consequently E_{CB} at -0.09 V vs. RHE were calculated.

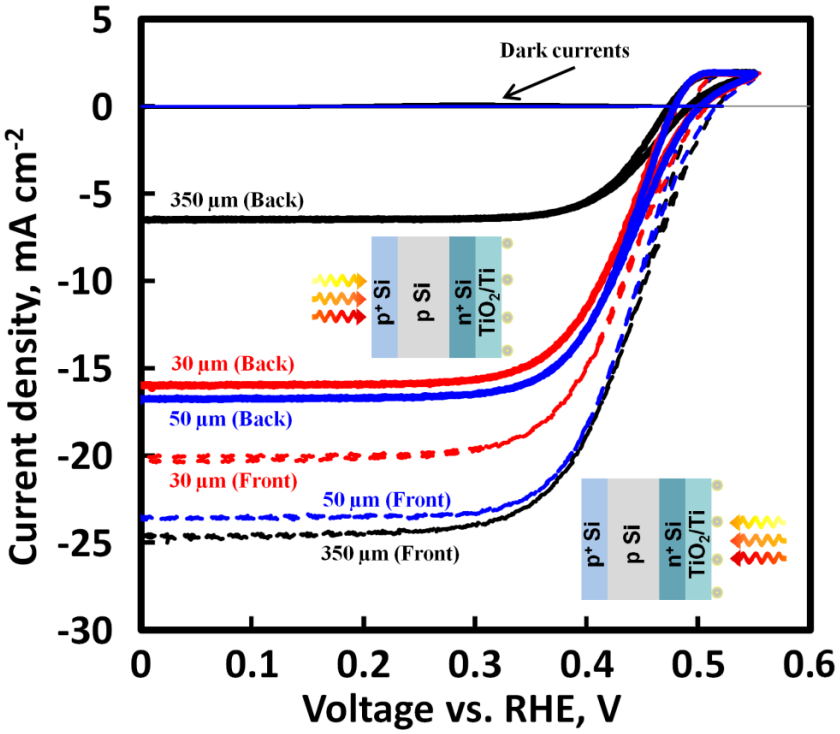

Figure 4.13 CVs of Si photocathodes with unthinned design (black solid), b with 50 µm thick active area (blue solid) and 30 µm thick active area (red solid) under back-illumination, and under front-illumination (dotted lines). The total irradiance is 41.8 mW cm^{-2}. Assuming that L_e of all samples is same, this shows how L_e/L affects J_L of the device. The comparative study between back and front illumination indicates that the thinner the Si absorber is, the larger the ratio of J_L under back and front illumination is. However the J_{Lmax} of 30 µm thick samplewith thinned design (red solid) is outperformed by the 50 µm thick sample indicating that absorption losses start to dominate the charge collection losses at around 50 µm thickness.

4.2.3 Photoelectrochemical study

The photoelectrochemical properties of the p^+pn^+-Si photocathodes with different thicknesses (L = 350, 50 and 30 µm) were compared by measuring CV curves. As shown in Figure 4.13 the fill-factor and photocurrent of 350 µm thick p^+pn^+-Si under front illumination (black dot) was considerably enhanced compared to that of the pn^+-Si in Figure 4.10. This demonstrates that adding the p^+ transport layer between the Al charge collector and p-Si significantly reduces the series resistance of the device. Under back-illumination the 350 µm thick p^+pn^+-Si sample showed a J_L of 6.2 mA cm^{-2}. This is significantly less current than the same sample generates under front-illumination. With the thinned design (Figure 4.8b) a 50 µm Si slab increased the J_L to 17 mA cm^{-2} under back-illumination at the same light intensity. Since the only change between these samples is thickness, L, this can be considered a result of L_e/L ratio on overall charge to current conversion efficiency. As the *b* sample was thinned from its back side from 350 to 50 µm the L_e/L ratio should be seven fold larger. Since the diffusion length is the average distance that the excess carriers can cover before they recombine, increased L_e/L ratio should lead to improved J_L. Furthermore, V_{oc} of the thinned p^+pn^+-Si samples shifted slightly cathodic

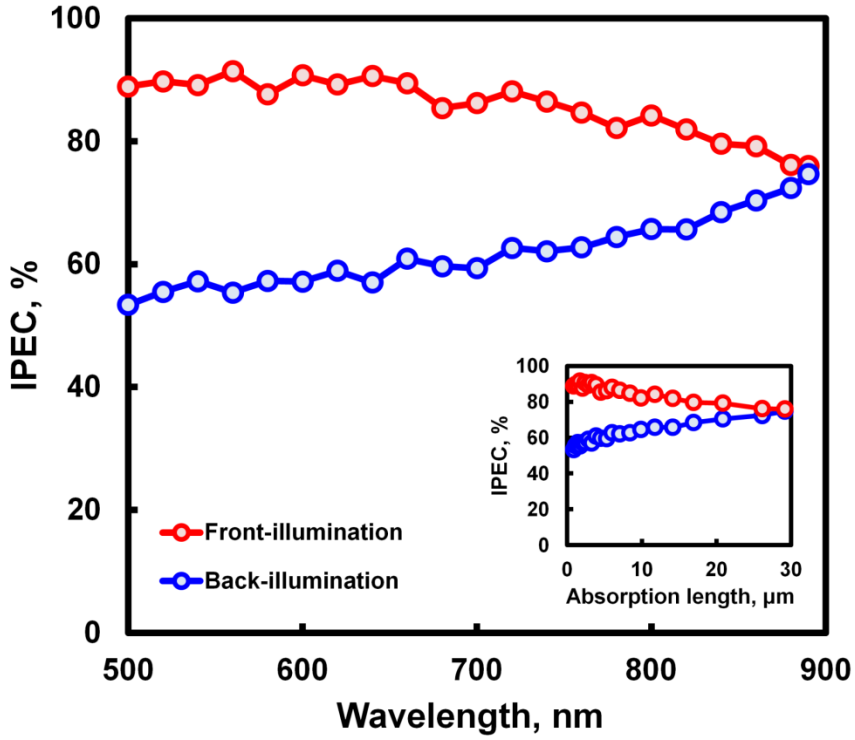

Figure 4.14 IPCE measurement results under front and back-illumination using 50 µm thick thinned Si sample, and the inset is IPCE curve versus light absorption length in Si (from Figure 4.2).

with increased J_L, and their slope improved under the back side illumination. This is likely due to the increased concentration of excited charge carriers. Indeed, the light induced open circuit voltage is given by the equation:

$$V_{oc} = \frac{nkT}{q} ln\left(\frac{J_L}{J_0} + 1\right) \tag{4.24}$$

where n is ideality factor of device, T is operating temperature, k is Boltzmann's constant, q is the electronic charge and J_0 is dark saturation current. Under the assumption that all samples have similar dark current and ideality factor, increased J_L leads to higher V_{oc}. In contrast, comparing unthinned sample with the thinned design (Figure 4.8b) under front-illumination shows that thinning results in a lower J_L. The reason is that charge generation on average occurs closer to the pn-junction under front-illumination. As a result of the lower photocurrent density the V_{oc} is slightly lower under back-illumination than under front-illumination. This is probably due to a higher effective recombination velocity at the highly doped p^+ side than at the pn^+-side of the device. Note also that the 30 µm thick Si sample with thinned design showed slightly

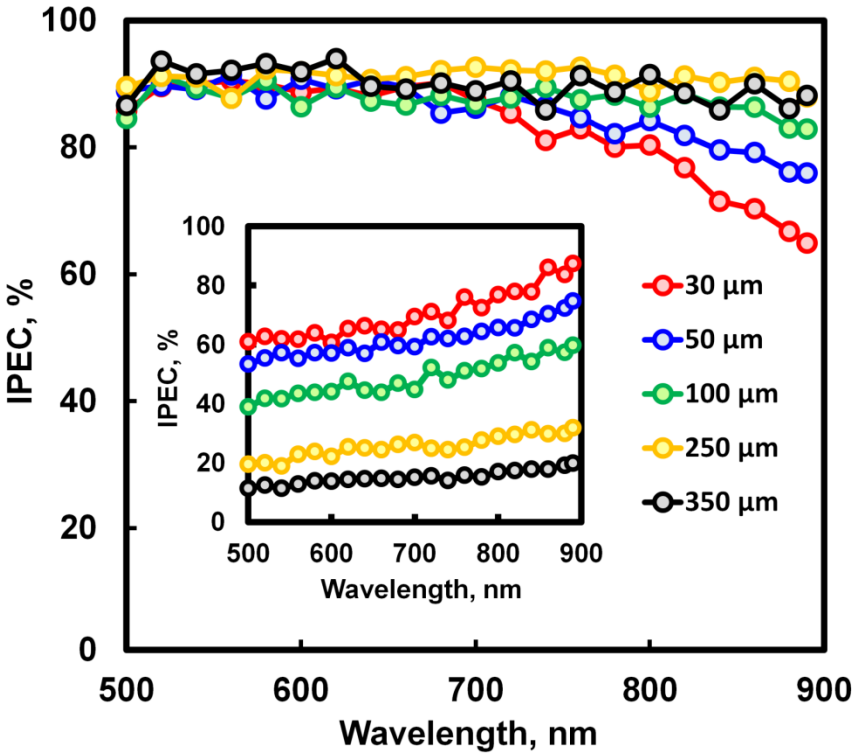

Figure 4.15 IPCEfrom the Si photocathodes with various thicknesses under front and the back-illumination (inset). The slop and intensity of IPCE increase gradually with decrease of Si thickness under the back-illumination, whereas for the front-illuminated case intensity decreases slightly with decrease of the thickness only in the long wavelength range.

lower current density (16.5 mA cm^{-2}) under back-illumination compared to the otherwise similar 50 µm thick sample even though it has a higher L_e/L ratio. This indicates a thickness of 30 µm is already below the critical thickness where the J_L starts to decrease (*i.e.* loss of photon absorption outweighs gain in $C_P(z)$).

Our spectrally resolved IPCE measurement results agree with this explanation. As shown in Figure 4.14, the IPCE of a sample with thinned design increases gradually with wavelength under back-illumination, whereas it decreases gradually under the front-illumination. The absorption length δ_p is the distance into a material at which the light intensity drops by a factor of $1/e$ of its original intensity (*i.e.* the effective light penetration depth). Converting wavelength to δ_p in Si allows experimental estimation of $C_P(z)$ under the assumption of similar charge transfer and diffusion efficiency. As shown in the inset of Figure 4.14, the IPCE was over 90% under front-illumination for photons, which are absorbed near the front side of the sample. Conversely, the same sample showed only approximately 50% IPCE under back-illumination. This shows that the pn^+- junction region separates charges better than the p^+p-region. The IPCE under back-illumination increases slowly from the short wavelength region and reaches a maximum at a wavelength near 900 nm. This behavior can be explained as follows: Photons with longer

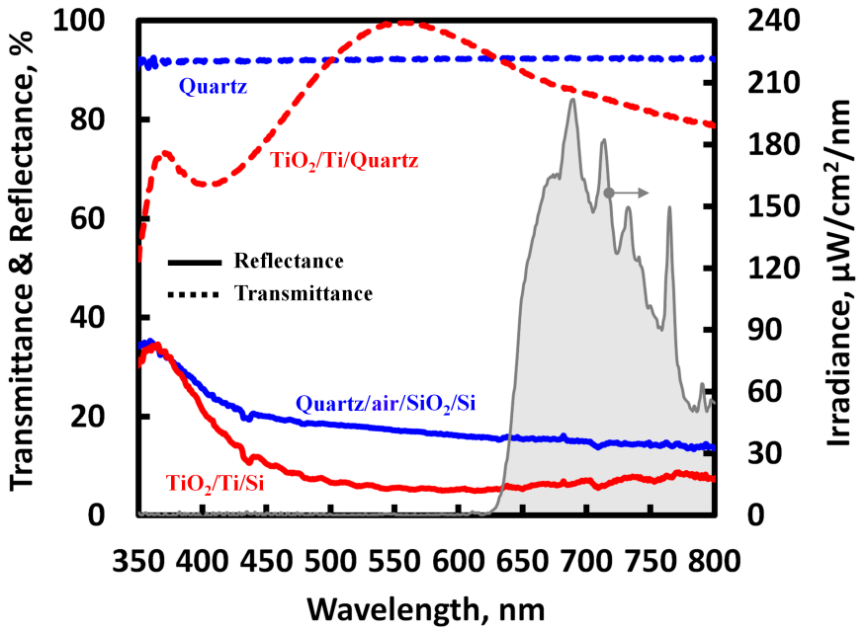

Figure 4.16 Reflectance of Quartz/air/SiO_2/Si and TiO_2/Ti/Si are given (solid) with the transmittance of 300-µm-thick Pyrex and 100-nm-thick TiO_2 which are used as a cover glass for the back-side and a protection layer for the front-side, respectively (dot). Irradiance of the light from the solar simulator used in this work is also given.

wavelengths penetrate deeper into the silicon. So under back-illumination electron-hole pairs generated from longer wavelength photons are therefore generated closer to the pn^+-junction boundary, whereas front illuminated case the photoabsorption depth as a function of wavelength is inverted, thus the IPCE shows the opposite behavior. This also can be supported by decrease of IPCE of thick samples under back illumination while IPCE under illumination from front side was almost invariable (Figure 4.15). Since the sample used for this IPCE measurement has a 50 µm thick Si slab, the IPCE response under both back and front illumination almost converge for wavelengths close to 900 nm.

4.2.4 Comparative experimental and theoretical studies

In order to compare to experimental results it is necessary to include the surface reflectance from the light incident side. Considering measured reflectance from the back side of the device (solid blue curve in Figure 4.16), the theoretical maximum current with surface reflectance $J'_{L,\max}$ can be calculated. The result is reduced charge generation rate $G'(z)$ due to the surface reflectance. As shown in Figure 4.17, it is observed that the overall current level is decreased by more than

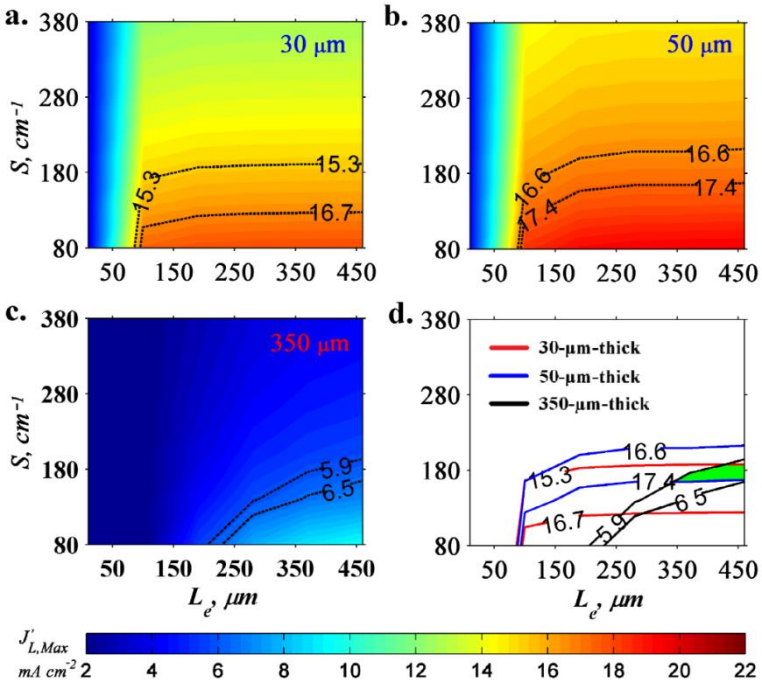

Figure 4.17 Contour plot of theoretical $J_{L,max}$ under simulated illumination (Figure 4.1) considering reflectance from the surface of the back side versus L_D and S for 30 µm thick (a), 50 µm thick (b), 350 µm thick (c). Overlapped contour lines (d) which correspond to the experimental uncertainty are also given to estimate L_D and surface S of the samples used for this work. Uncertainty ranges for each panel were derived from the uncertainty of the saturated current I_L and the active area measurement A, i.e. $I_L/A \pm (\Delta I_L + \Delta A)$.

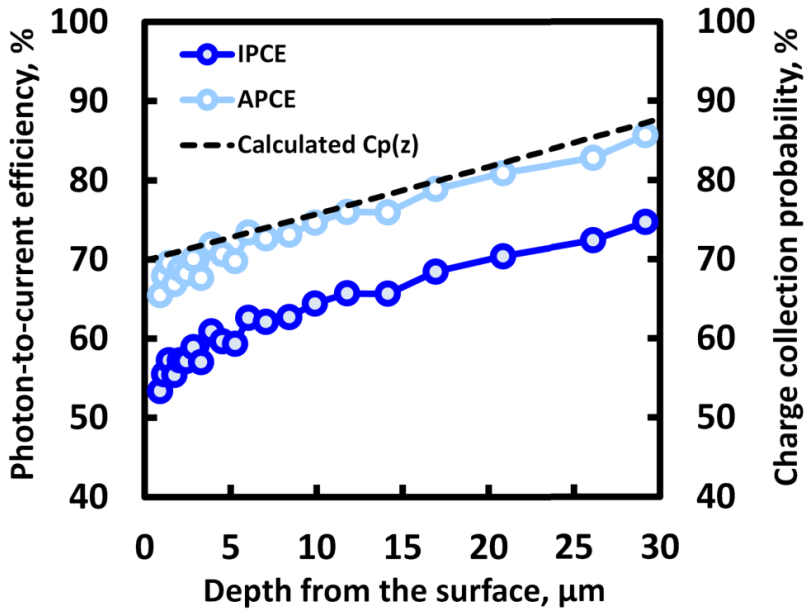

Figure 4.18 Incident photon to current efficiency (IPCE, dark blue) and APCE (light blue), which was converted from IPCE considering the reflectance of back side. Calculated $C_P(z)$ is also shown to compare with APCE.

15% for all three thicknesses due to the surface reflectance. Overlapping contour lines, which correspond to the experimental values with uncertainty, allows estimating approximate L_e and S values of the Si device used in this work (green colored area in Figure 4.17d). It was found that a L_e of approximately 350 µm and S of 80 cm^{-1} best fit the experimental data. Assuming that Si has an electron diffusivity, $D \leq 36$ cm^2 s^{-1} [85], we estimate the surface recombination velocity, V_s, to be approximately $3 \cdot 10^3$ cm/s ($S = V_s/D$). This high value clearly indicates that there is room for improvement. Using these traced values one can determine the theoretical Absorbed Photon-to-Current Efficiency (APCE). For Pt, a material with fast HER kinetics, the yield of electron injection into the electrolyte is ~ 1, and therefore APCE can be obtained by dividing J_L by absorbed photon expressed as a current density (J_{abs}) [92]. It was determined that the APCE, which was calculated from the measured IPCE, was quite similar to $C_P(z)$ with L_e of 350 µm and S of 80 cm^{-1} (Figure 4.18), indicating that the measured experimental behaviour agrees well with the model.

In Figure 4.19, the five experimentally measured CVs from the various thicknesses are shown, and the saturation photocurrent densities of these CVs are plotted with the calculated current density (using an empirical L_e and S extracted from Figure 4.16) in Figure 4.20). Calculated photocurrent density with enhanced L_e and S cases are also shown to point out how additional improvements can be made with further structural design modification. An important point is the impact of surface recombination velocity on $J'_{L,\,max}$. According to the modeled data in Figure 4.18, an improvement of S (dashed line) gives higher impact on $J_{L,\,max}$ than an improvement in L_e. Case in point: $J_{L,\,max}$ increased by 12% when S is reduced by 1/2, whereas a model of a device with approximately 3 times higher L_e (dot-dash line) shows only slight increase in current density with decreased thickness sensitivity. This analysis strongly suggests using (back) surface passivation – *e.g* via application of a thermally grown SiO_2 layer [93] or an overlayer of ZnO or Al_2O_3 [94] – in order to reduce the S. As described in Figure 4.8, the back side surface of the Si samples (the top surface in figure) is exposed to atmosphere, and thus one would expect there to be a native grown SiO_2 layer (~1 nm) of poor quality, which does not provide good surface passivation. Furthermore, since the back side of bottom cell must provide an ohmic contact with

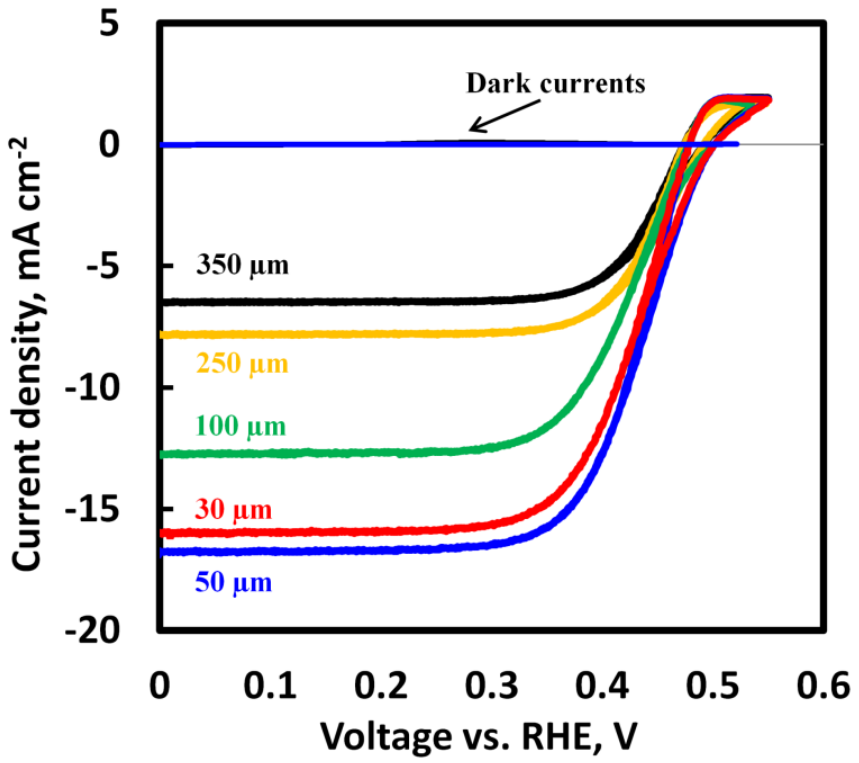

Figure 4.19 CVs of Si photocathodes with various thicknesses. The total irradiance is 41.8 mW cm^{-2}. Assuming that S and L_e of all samples is same, this shows how L_e/L affects J_L of the device.

the top cell in tandem designs the internal passivation layer should be conductive as well as transparent. This suggests that either a transparent conducting oxide (TCO) with locally opened-point contacts [95,96] or a design with a very thin dielectric passivation layer is attractive [93,94]. Amorphous Si (a-Si:H) with a TCO overlayer can be an excellent candidate as demonstrated by Panasonic HIT cell [83], since a-Si:H has excellent passivation capability and enable good carrier transport. It should be noted that the conduction band position of the n-type TCO layer should be close to the valence band of p^+ Si surface [97], since these layers should work as a tunnel junction in practical tandem device.

In this work, a thin Al_2O_3 layer (10 nm) grown by atomic layer deposition (ALD) was used to verify *S* effect on the PEC performance (see Figure 4.21). As mentioned earlier, Al_2O_3, together with other oxide film, such as SiO_2, is a widely used surface passivation layer. In Figure 4.21, Si photocathode sample with 10 nm thick Al_2O_3 on the light incoming side showed enhanced J_L of 19 mA cm^{-2} with V_{oc} of 0.5 V under the back side illumination. Compared with the sample without any surface passivation layer, J_L and V_{oc} were increased by around 12% and 8%,

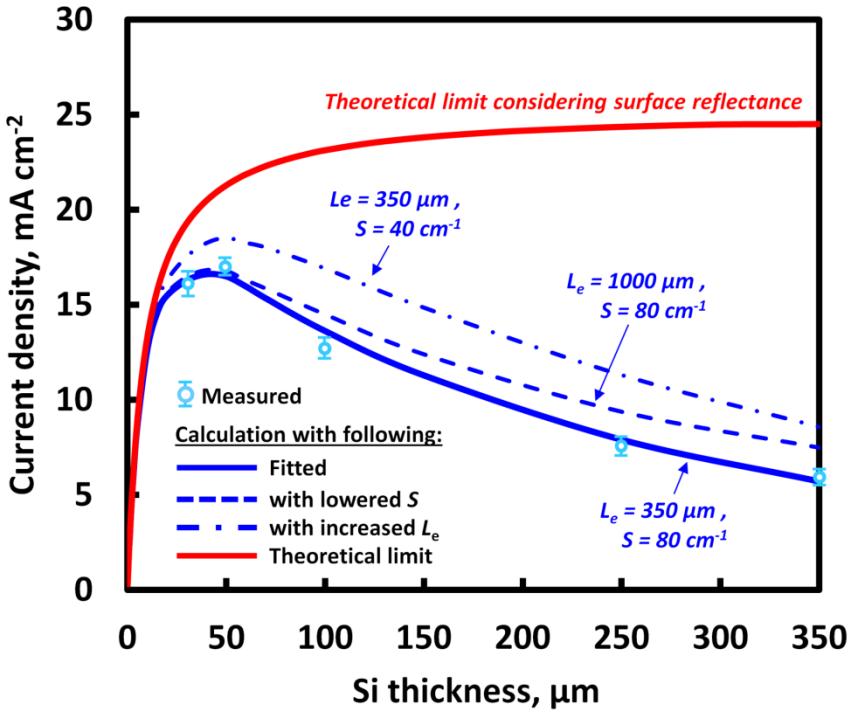

Figure 4.20 Calculated theoretical limits of the current density: curve from the Si device with recombination rate and diffusion length value traced from the IPCE and modelling data (L_e= 175 µm; S = 0.48 cm^{-1}) (blue solid), and estimated behavior from the device with increased L_e and S (blue dots). Theoretical limit of an ideal Si device, i.e. $L_e = \infty$ and S = 0 (red curve) with surface reflectance is also given for comparison.

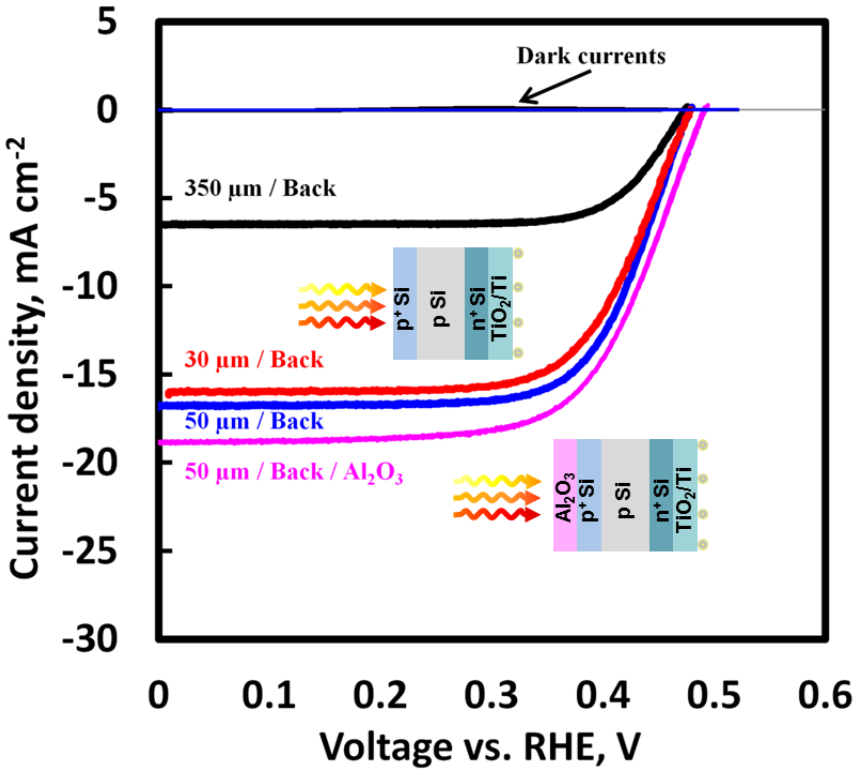

Figure 4.21 CV of Si photocathodes with Al_2O_3 passivation layer on the light incoming side (pink). Compared with the same thickness sample without any passivation layer on the back side, the Al_2O_3 passivated sample showed enhanced J_L and V_{oc}.

respectively. This results strongly support the prediction in Figure 4.20 that reduced surface recombination rate at the light incoming side may increase $J_{L,max}$ significantly. It is well known that the fixed negative charge density within the Al_2O_3 layer induces an accumulation layer at the p-Si surface, and as a consequence, the Al_2O_3 provides a very effective field-effect passivation without the additional contribution of recombination in the space charge region. However, a conducting passivation layer is still required, since Al_2O_3 is well known insulator, and thus carrier transfer through this layer is not available.

4.3 Concluding remarks

A back-illuminated photocathode, which is suited to work efficiently in a tandem PEC stack, was successfully demonstrated. Specifically it has been shown that a photocathode with a p^+pn^+-Si – structure, whose pn-junction is formed at the solid/liquid side, can be used as a HER photoelectrode under back side (dry side) illumination which is similar to actual operational conditions in tandem water splitting devices. From an analytical calculation study, it was found that the balance between charge collection probability and light absorber thickness is an important design parameter to produce efficient back-illuminated devices. The photoelectrochemical investigation of p^+pn^+-Si with Si-thickness as parameter clearly demonstrates the impact of L_e/L ratio estimated from the abovementioned theoretical results. A 50 µm thick thinned p^+pn^+-Si electrode showed a maximum J_L (17.0 mA cm^{-2}) under back-illumination, whereas a 350 µm thick sample, with a 7 times lower L_e/L ratio, showed only 6.1 mA cm^{-2}. In contrast, despite its enhanced L_e/L ratio, a 30 µm thick sample showed only slightly lower J_L due to its limited light absorption (loss of infrared photons). These results demonstrate how the charge collection limitation of a photocathode with its pn-junction at solid/liquid can be overcome. Importantly, the increased fill factor and increased V_{oc} of the thinned back-illuminated samples owe their success mostly to increased J_L, and such designs should lead to increased operational current density when coupled with a photoanode. Building on the experimental input, further modelling shows that surface recombination on the back side of the silicon is the dominant current loss mechanism. A 10 nm thick ALD grown Al_2O_3 layer was applied on the back side of the electrode, and this provided additional J_L and V_{oc} as estimated from the abovementioned modelling work. However, since this Al_2O_3 is an insulator, a conducting passivation layer, which allows transport of the carriers with minimum optical loss, seems one of the critical challenges to reduce the back side recombination rate and consequently enhance photocatalytic performance of practical Si-bottom cell.

Chapter 5

5. Strategies for improving photocatalytic performance of Si

5.1 Carrier-selective contact design

Efficient H_2 production (HER) with open circuit voltage over 0.5 V and photocurrent over 20 mA cm^{-2} has been shown experimentally using pn^+-Si homojunction with Pt co-catalyst in previous chapter. But, as current performance of Si PEC cells is far behind its theoretical limit [98], the need for different approach increases. Up to date, tremendous efforts have been investigated to improve the performance. Above all, carrier-selective contacts design with efficient carrier transport and low recombination comes into the spotlight recently [93,99,100]. One of the outstanding examples of this approach is the ITO/a-Si:H/Si heterojunction photovoltaic (PV) cell which reached open circuit voltage (V_{oc}) of 750 mV due to the lowered recombination by high purity hydrogenated amorphous Si (a-Si:H) at the passivated contacts [101]. However, this approach can significantly reduce the FF due to the lowered attributed to the alloying of a-Si:H with oxygen during transparent conducting oxide (TCO) deposition process [102]. Meanwhile, Feldmann et al. recently demonstrated remarkable FF (81.1%) with V_{oc} of 693.5 mV using metal-oxide-semiconductor (MOS, see Figure 5.1b) based p-Si/SiO_2/pc-Si/ITO structure [92]. The key feature of this structure is chemical surface passivation by SiO_2 tunneling interlayer and selective carrier transport due to an energy barrier for majority carrier by highly doped pc-Si. In spite of above-mentioned advantages, very little work has been done studying photocatalytic HER with MOS structure. Talin's group demonstrated HER using p-Si/SiO_2/Ti/Pt with V_{oc} of 490 mV [103], but it has inevitable limitation in current density due to the light absorption by metallic layers. In this section p-Si/SiO_2/pc-Si structure (see Figure 5.1a) is demonstrated for both front and back contacts which provide interface passivation and selective injection of minority and majority carrier to solid/liquid interface and back contact, respectively. The main focus is on evaluation of the impact of applied passivating carrier-selective back and front contacts on photocathodic performance.

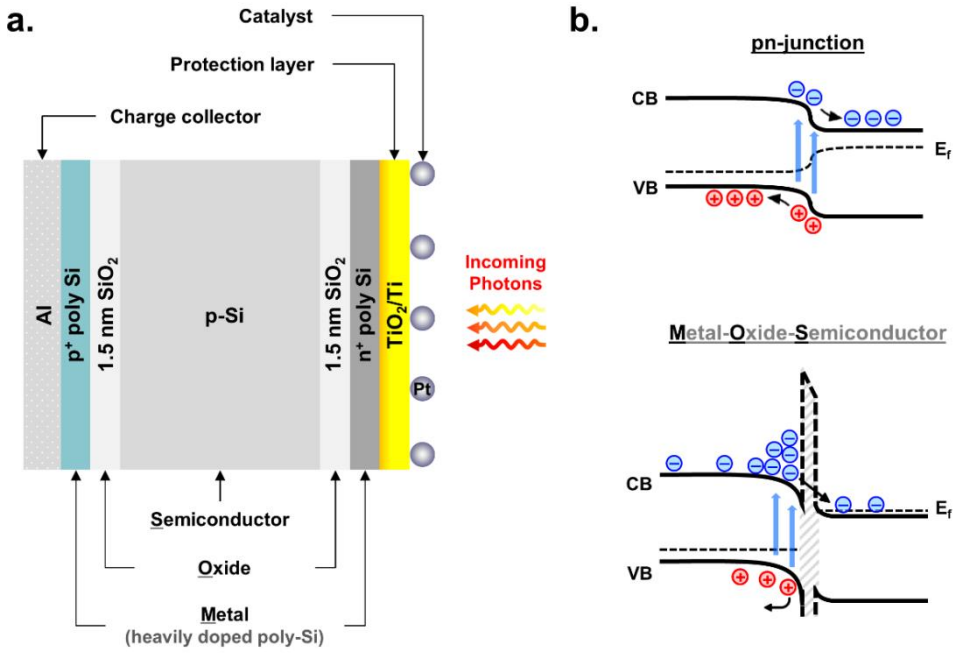

Figure 5.1 Schematic cross section of the Si photocahode with carrier selective contacts at both front and back side (a). Unlike conventional pn-junction (b, upper), carrier selective contact consist of semiconductor (Si), oxide (SiO_2) and metallic layer (highly doped pc-Si in this work) as shown in lower image of (b).

5.1.1 Sample fabrication

Si based MOS photocathodes were fabricated using 350 µm thick CZ c-Si wafers (Topsil, 1-20 ohm-cm, boron-doped, acceptor density $N_A \approx 5 \cdot 10^{19}$ cm^{-3}) as a substrate, on which thin SiO_2 (~ 1.5 nm) layers were chemically grown by oxidation in 68% HNO_3 solution at 95˚C for 10 min. Then, the a-Si films were grown at 580˚C in an low-pressure chemical vapor deposition (LPCVD) furnace at 200 mTorr with a 80 sccm silane flow and a 7 sccm PH_3 or B_2H_6 flow, depending on the conductivity type (n^+ or p^+), resulting in growth of 20 nm and 50 nm of n^+ and p^+ polycrystalline Si layers (pc-Si:P and pc-Si:B, respectively). Subsequently, the samples were annealed at 800˚C for an hour in an atmospheric tube furnace under N_2 flow. A mesa-isolated pc-Si/SiO_2/c-Si structure (hereafter carrier-selective contact) with height of 3 µm is formed at the front side by photolithography and dry etching (Here, we used SF_6, O_2 and C_4F_8 gases in a Pegasus DRIE system from SPTS Technologies). A metallic charge collecting layer was deposited at room temperature by e-beam evaporation of Al, then Cu-wire was attached onto it using Ag-paste for electrical connect as described in chapter 3 and 4. In order to prevent the Si surface from photo-corrosion during the photo-electrochemical measurements, a Ti/TiO_2 (5/100 nm) protection layer was sputtered on the n^+ pc-Si using previously described in the section 4.2.

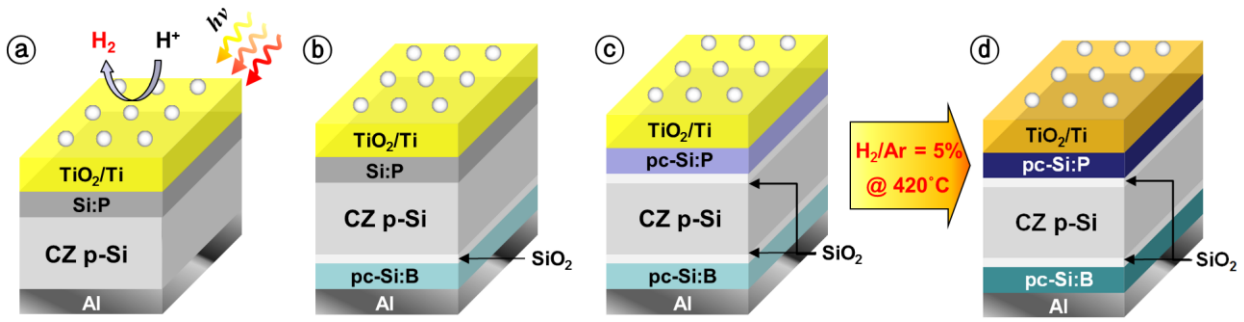

Figure 5.2 Schematic drawings of the photoelectrodes used in this work. Si photocathode with conventional pn-junction was used as a reference (a, named as Ref.), with carrier selective contact only at the back-side (b, named as CS-1), and with carrier selective contacts at both front and back side (c, named as CS-2). CS-3 (d) has same configuration as CS-2, but FG annealing treated.

Prior to sputtering process all wafers were dipped in buffered HF for 30 sec, rinsed in Millipore water, dried and then immediately placed in the sputter chamber to prevent deactivation by native oxide formation. Some samples then received a 30-minute annealing at 420˚C in forming gas (5% H_2, 95% Ar) to improve the passivation quality [104,105]. The sample surface was cleaned using a piranha solution (66% H_2SO_4 + 34% H_2O_2), then washed with Millipore water and dried. Pt was used as a co-catalyst in order to achieve high catalytic activity for HER by having 250 ng of a dinitrosulphatoplatinate solution (Johnson Matthey) drop-cast on TiO_2 surface. In some samples, alternatively, conventional homogeneous pn^+-junction was formed using same manner as in previous section and were used as reference cells for comparison with those having carrier-selective back and/or front contacts. All samples were sealed with epoxy (Loctite 1C Hysol) yielding an exposed surface area of approximately 0.2 cm^2 at the front side. This number was also precisely adjusted by optical image analysis (ImageJ 1.46r) after the experiments. Structures of samples used in this work are also summarized in Table 4.2, and schematic drawing of samples are shown as insets of Figure 4.23.

Table 5.1 Detail structure of the samples

Sample	Structure	Remark
Ref.	Pt/TiO_2/Ti/n^+p-Si/Al	Conventional pn-junction
CS-1	Pt/TiO_2/Ti/n^+p-Si/SiO_2/pc-Si:B/Al	Carrier selective contact (back only)
CS-2	Pt/TiO_2/Ti/pc-Si:P/SiO_2/p-Si/SiO_2/pc-Si:B/Al	Carrier selective contact (back and front)
CS-3	Pt/TiO_2/Ti/pc-Si:P/SiO_2/p-Si/SiO_2/pc-Si:B/Al	Carrier selective with FG annealing

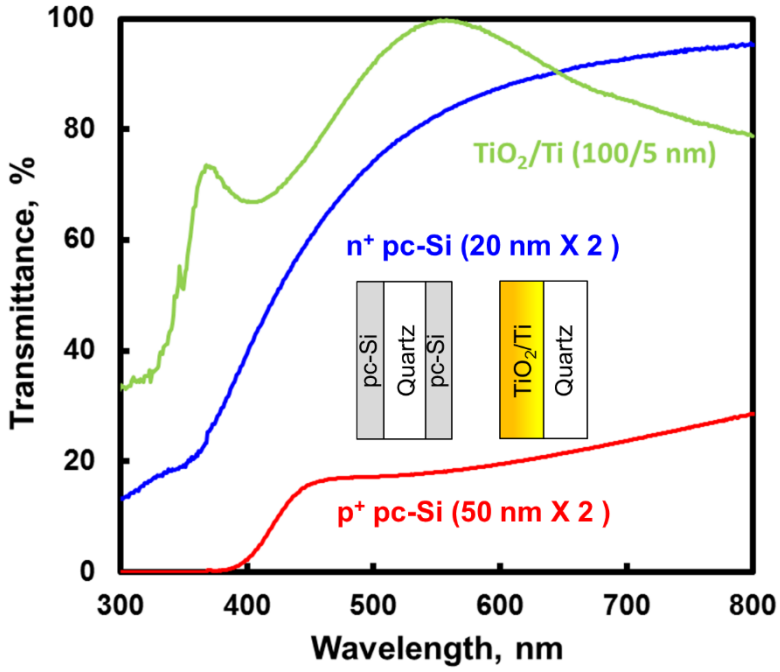

Figure 5.3 UV-Vis transmittance spectra for TiO_2/Ti (solid green), n^+ pc-Si (solid blue) and p^+ pc-Si deposited on quartz glass. In case of pc-Si samples, both side of the quartz glasses were coated with pc-Si films.

5.1.2 Material characterization

The UV-Vis transmittance spectra (see Figure 4.23) show negligible absorption for both pc-Si:B and pc-Si:P and TiO_2 layers. Since transmittance (T%) of the both pc-Si:P (20 x 2 nm thick) and TiO_2 (100 nm thick) on quartz glass shows more than 80% at 600 nm in wavelength, and thus it is considered that the optical loss due to these layers can be negligible. A pc-Si:B (50 x 2 nm thick) layer shows T% of around 20% at the same wavelength under same condition. Note that both n^+ and p^+ pc-Si were deposited on both sides of the substrate. The precise mechanism of this low transmittance for the pc-Si:B remains unknown, however, there should not be any effect on the optical property of the device, since the pc-Si:B is used for the back contact. Note that in case of pc-Si samples, both sides of the quartz glasses were coated with pc-Si films, whereas TiO_2/Ti was deposited only on single side of the quartz substrate.

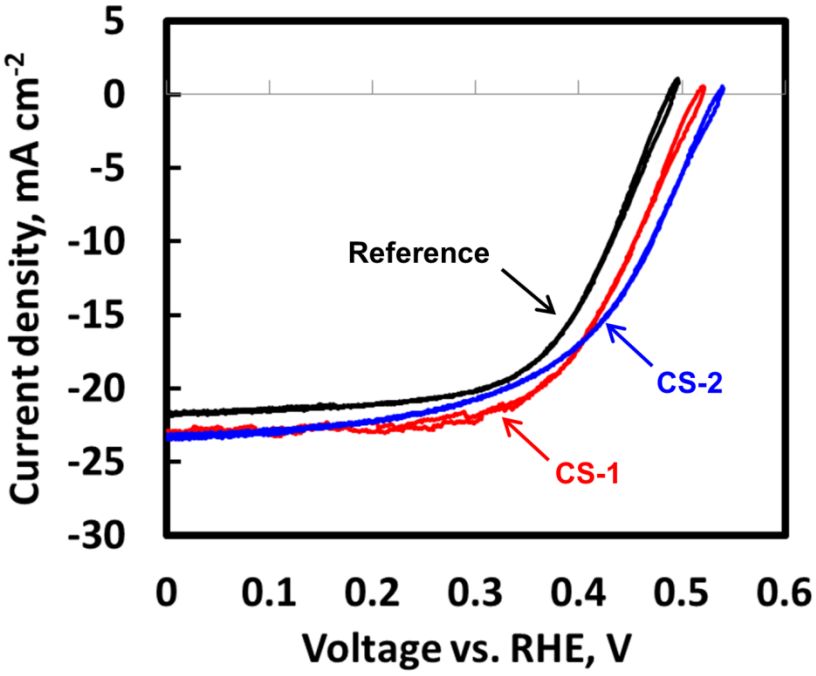

Figure 5.4 CVs of Si photocathodes with conventional pn-junction (black solid), with carrier selective back contact and pn-junction at front side (red solid), and with carrier selective contacts at both front and back side (blue solid) under front-illumination. The total irradiance is same as that of Figure 4.1. While V_{oc} and J_L output of the CS-2 sample surpass those of CS-1 and reference samples, fill factor (*FF*) of the CS-2 sample significantly decreased having 58%, indicating shunt issue takes a place at front contact.

The positioning of flat band potential and doping density of TiO_2 were found in previous chapter (4.2.2.4) by electrochemical impedance spectroscopy (EIS), and these values were reused for this work.

5.1.3 Photoelectrochemical performance

The effect of carrier selective contacts on PEC properties of the photocathodes were evaluated by measuring cyclic voltammetry in 1M $HClO_4$ under illumination filtered using AM 1.5 and 635-nm-cut-off filters (i.e. $\lambda > 635$ nm to approximate the wavelengths and intensity would be received in a tandem device [28]). As shown in Figure 5.4, V_{oc} of photocathodes with carrier selective contacts was considerably enhanced compared to that of reference pn^+-Si sample. The addition of carrier selective contacts at back and front gives an additional V_{oc} of 48 mV, reaching a value of 533 mV vs. RHE. It was estimated that highly doped pc-Si:B and pc-Si:P layers could provide a sufficiently low sheet resistance to the device, since the overall series resistance of the device comparable to a conventional pn^+-Si device with direct back contact. These results demonstrate that adding carrier selective contacts provide good passivation of both contacts and

sufficient doping of the pc-Si layers. It is worth noticing that the very carrier selective back contact with conventional pn^+-junction (CS-1) provides an enhanced V_{oc} of +27 mV. This can be explained with thin tunnel oxide (SiO_2) layer which reduces interface recombination of majority carrier [96] and reflection barriers for minority carriers built by pc-Si yield enhanced V_{oc} [99].

In case of sample with carrier selective contacts both at front and rear side (CS-2), its V_{oc} appears to be increased by +21 mV with respect to the sample CS-1, indicating that conventional homogeneous pn^+-junction was successfully substituted by heterogeneous MOS junction. In addition, its saturation photocurrent density (J_L) reaches ≈ 24 mA cm^{-2} at 0 V vs. RHE, which exceeds the 90% of theoretical upper limit [28] despite absorption of visible light in the pc-Si:P thin film, as previously shown from the UV-Vis data (Figure 5.3). Similarly to the previous back contact case, we attribute this increase in V_{oc} and J_L to the excellent surface passivation by tunneling oxide layer as well as the enhanced minority carrier injection to pc-Si layer, which reflects majority carriers by relatively lower valence band position than that of c-Si absorber. Details of band energy for these carrier selective contacts will be discussed in following section.

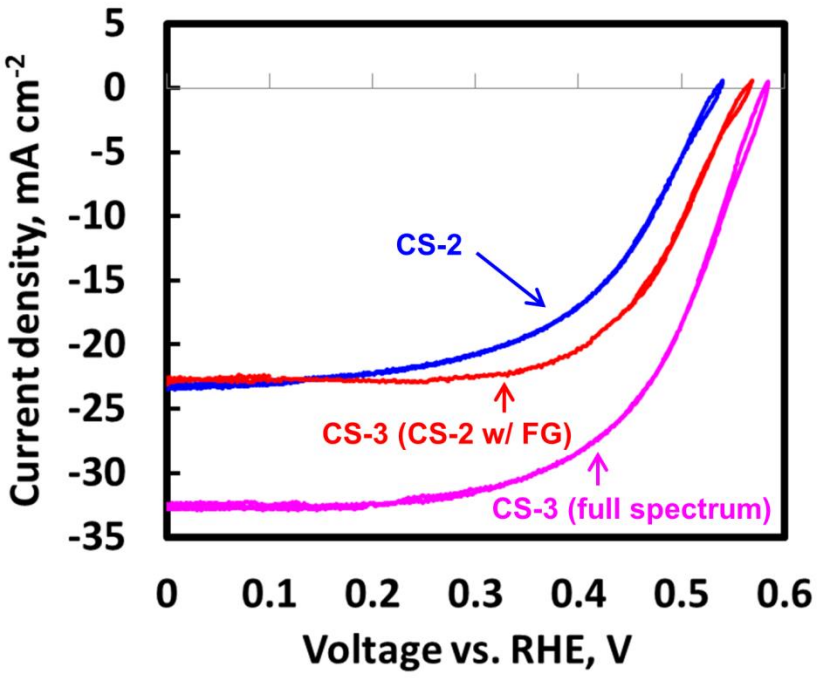

Figure 5.5 CVs of Si photocathodes with carrier selective contacts at both front and back side before FG annealing treatment (blue solid) and after the FG annealing treatment (red solid) under red part of the solar spectrum, and FG annealed sample under the full white light spectrum.

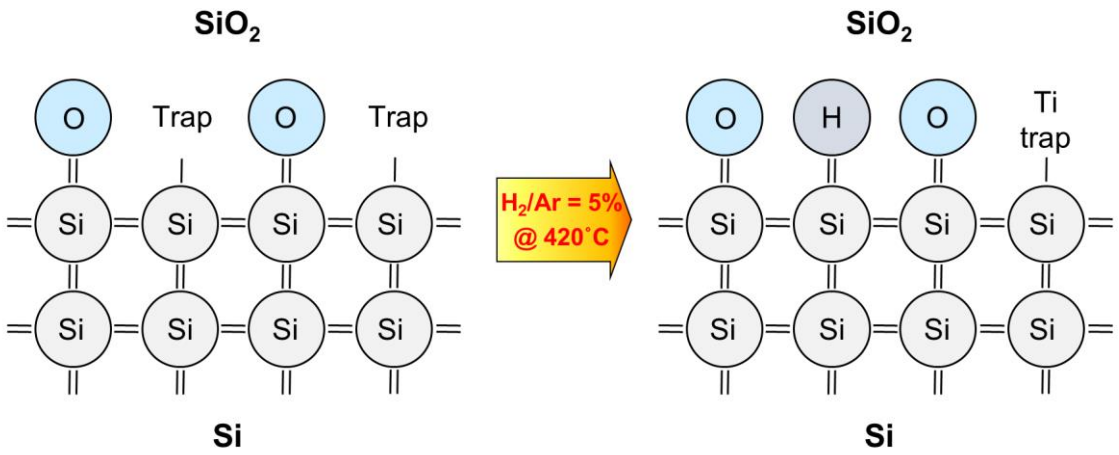

Figure 5.6 Illustration of passivation by the hydrogen ions from the forming gas mixture (H_2/Ar = 5%). Traps formed at interface can be substituted by the thermally diffused hydrogen from the forming gas.

While V_{oc} and J_L output of the CS-2 sample surpass those of CS-1 and reference samples, fill factor (FF) of the CS-2 sample significantly decreased having 58%. Compared with reference and CS-1 samples, CV curve of CS-2 shows increased slop in the saturation photocurrent region, whereas slop at V_{oc} point is quite similar to the other samples. This strongly indicates the formation of the shunt paths reducing shunt resistance (R_{sh}) of the CV curve. Since the photocathode sample CS-2 with carrier selective contact only at the back side showed relatively flat slop in saturation current region, it seems that the decrease of R_{sh} is mainly attributed to the processes for the top layers. Imperfect SiO_2 growth on the Si surface may lead direct contact of c-Si with pc-Si:P layer, forming shunt path at the interface. But it is not relevant, since the CS-2 sample with carrier selective contact at back side has a SiO_2 layer which has been made using same procedure. It is more reasonable to assume that defect or traps were formed during TiO2 sputtering process. Kinetic energy of the sputtered Ti can damage the pc-Si:P and SiO_2 forming shunt paths.

To recover the decreased FF of the sample CS-3, a forming gas (FG) annealing process was applied for the sample CS-3. Forming gas is a mixture of hydrogen and nitrogen or argon (mole fraction varies) [105]. Typical forming gas formulations (5% H_2 in inert gas) are not explosive, and this ratio was also used for this work. It was used in a quartz glass tube chamber, in which 5% ratio H_2 FG gas is heated at 420˚C and continuously flows to drive out moisture and oxygen, and this process leads to the diffusion of hydrogen ions into the sample. It is well known that FG annealing treatment provides surface passivation, and particularly for the Si devices, is known to

increase V_{oc} and FF by substituting trap sites of the damaged film to the hydrogen ions [106]. As shown in Figure 4.25, the FG treated CS-3 sample shows an additional V_{oc} of 37 mV, reaching a value of 567 mV vs. RHE with comparable FF (64%) to that of reference sample. This result demonstrates that additional FG treatment recovers damaged SiO_2/pc-Si by the passivation of the defect and trap sites. A simple scheme of this hypothesis is well illustrated in Figure 5.6. Furthermore, under the AM1.5 full spectrum (white light) the sample with carrier selective contacts at both back and front showed a V_{oc} of 587 mV with J_L of approximately 34 mA cm^{-2}. To the best of our knowledge, this is the highest V_{oc} and J_L reported for a lab scale c-Si based photocathode performing the HER.

5.1.4 Understanding band alignment

In explaining the band diagram, we will start from the MOS (c-Si/SiO_2/highly doped poly-Si) and move towards the electrolyte. The p-Si wafer has a band gap (E_g) of 1.124 eV, an acceptor density (N_A) of $3 \cdot 10^{15}$ cm^{-3}. The intrinsic Fermi level of bulk p-Si can be determined as a function of working potential (*E vs. RHE*):

$$E_{i,p-Si} = E - \frac{kT}{e} ln\left(\frac{N_{A,p-Si}}{n_{i,p-Si}}\right) \tag{5.1}$$

where k is Boltzmann's constant, T is temperature (298 K), e is the elementary charge, and n_i is intrinsic carrier density of Si, which is approximately $1.33 \cdot 10^{10}$ cm^{-3} for Si [107]. Assuming the pinning of the band edges of the semiconductor at the interface (0 V vs. RHE) the $E_{i,\,p\text{-}Si}$ is -0.32 V vs. RHE, and bulk conduction band of the p-Si is approximately -0.88 V vs. RHE (E_i-$E_g/2e$). The potential drop at the p-Si/SiO_2 interface can be determined via equation:

$$\psi_s = \frac{eN_{A,p-Si}\varepsilon_{Si}}{2C_{ox}^2}\left[\sqrt{1 + \frac{2C_{ox}^2(V_g - V_{FB})}{eN_{A,p-Si}\varepsilon_{Si}}} - 1\right]^2 \tag{5.2}$$

where ε_{Si} is the permittivity of Si ($1.04 \cdot 10^{-10}$ F/m) [107], C_{ox} is the capacitance of SiO_2 layer, and V_{FB} is the flat band voltage. V_g is gate voltage and it satisfies $V_g = V_{FB}$ at equilibrium condition and $E = V_g - V_{FB}$. C_{ox} and V_{FB} are can be determined using following equations:

$$C_{ox} = \frac{\varepsilon_{SiO_2}}{\delta} \tag{5.3}$$

$$V_{FB} = \varphi_{m,n^+-Si} - \varphi_{s,p-Si} = \varphi_{m,n^+-Si} - \frac{kT}{e}\ln\left(\frac{N_{A,p-Si}}{n_{i,p-Si}}\right) - \frac{E_g}{2e} - \chi_{Si} \tag{5.4}$$

where ε_{SiO2} is the permittivity of SiO_2 ($3.45 \cdot 10^{-13}$ F/m) [107], δ is the thickness of SiO_2 layer, χ_{Si} is the electron affinity of p-Si (4.05 V) [107], and $\varphi_{m,n+-Si}$ is the work function of n^+ poly Si (4.15 V) [108]. Assuming the thickness of SiO_2 layer is 1.5 nm, C_{ox} is approximately $2.3 \cdot 10^{-6}$ F/cm^2, and V_{FB} is approximately -0.78 V, and Ψ_S of p-Si is around 0.77 V.

The depletion width can be determined via equation [108]:

$$W_d = \sqrt{\frac{2\varepsilon_{Si}\psi_S}{eN_{A,p-Si}}} \tag{5.5}$$

Putting together these values into equation 5.2 and 5.5, we obtain potential drop at the p-Si/SiO_2 interface of 0.54 V and depletion width of around 750 nm at working potential of 0.55 V vs. RHE.

In case of SiO_2/n^+ poly Si interface there will be upward band bending, and depletion width can be determined using following equations [108]:

$$W_{n^+poly} = \sqrt{\frac{2\varepsilon_{Si}V_{n^+poly}}{eN_{D,n^+poly}}} = \frac{\varepsilon_{ox}E_{ox}}{eN_{D,n^+poly}} \tag{5.6}$$

where E_{ox} is electric field in oxide layer, and it can be determined as followed:

$$E_{ox} = \frac{V_{ox}}{\delta} \tag{5.7}$$

where V_{ox} is the voltage drop across the oxide and satisfies $V_g = V_{FB} + \Psi_S + V_{ox}$. Assuming the thickness of SiO_2 layer is 1.5 nm and dopant density of n^+ poly Si is the order of 10^{20} cm^{-3}, the V_{ox} is approximately 15 mV, depletion width $W_{n+\ poly}$ is around $7.2 \cdot 10^{-3}$ nm, and $V_{n+\ poly}$ was found to be approximately $4 \cdot 10^{-6}$ V which means almost zero.

In case of n^+-Si/Ti interface we assume that interface forms a Schottky barrier with no metal induced gap states or Fermi level pinning. If this is the case, the barrier height Φ_B at the n^+-Si/Ti interface is the difference between the Ti work function (φ_{Ti} = 4.33 V) and the n^+-Si work function (φ_{n+} = 4.15 V) plus the deviation between the flat band potential and the conduction band. Using the equation 4.20, φ_B was found to be 0.15 V. Considering the deviation between the flat band potential and the conduction band (0.03 V, the third term of equation 4.20), barrier potential is located at -0.12 V vs. RHE (i.e. upward band bending). Since Ti is a metallic layer, and has a high carrier density compared to the Si, thus the bias will be distributed entirely over the n^+ Si region. The band bending distance in the n^+-Si can be determined by the equation 4.21,

and the barrier width was found to be approximately 0.8 nm, and electron transfer from the Si to the Ti would most probably have to occur through tunneling.

From the previously measured Mott-Schottky plot in chapter 4.2.2.4, the TiO_2 conduction band was determined to be -0.05 V vs. RHE, the donor density was $3 \cdot 10^{20}$ cm^{-3}, and the flat band potential was -0.02 V vs. RHE. Since the flat band potential, $E_{FB,\,TiO2}$, is very close to the work function of Ti, thus it can be assumed this junction will show ohmic behavior. The depletion region width of TiO_2 at the interface is given by the equation 4.22 and 4.23, resulting $W_{TiO2/liquid}$ of 1.02 nm.

In case of a charge free oxide the V_{FB} of the p-Si/SiO_2/p^+-Si structure also can be calculated using the equation 4.39, having a positive value of $V_{FB} \approx 0.34$ V. In equilibrium the magnitude of the potential drop across the junction equals the V_{FB}, and to support this potential drop an accumulation layer forms in the p-type region, while a depletion layer forms in the p+ region. Most of the flatband potential is dropped across the accumulation layer, and this potential drop can be calculated using the equation 5.2, resulting Ψ_S of -0.41 V.

Assuming that SiO_2 layer satisfies the equation - $V_{FB} = \Psi_S + V_{ox}$ (note that this equation is obtained by neglecting the potential drop across the p^+ region), the potential drop across oxide between the p^+ and p type region has value of around 70 mV.

Unfortunately, there are no simple expressions predicting the thickness of accumulation layers, but the width is on the order of a Debye length L_D (≈ 75 nm) which was determined previously in

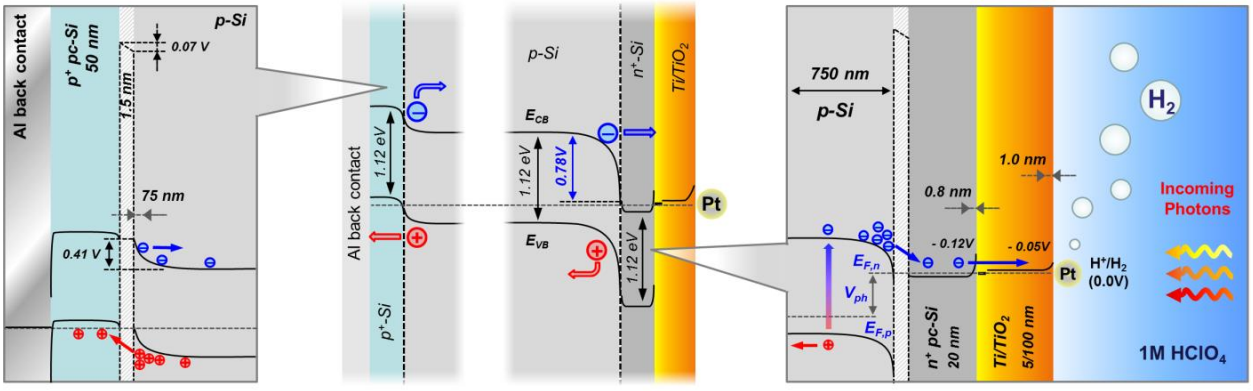

Figure 5.7 Schematic energy diagram of the Si photocathode with back and front carrier selective contacts. The scheme in the middle is in equilibrium with H^+/H_2 reaction, and the zoomed-in schemes for the Al/p^+ pc-Si/SiO_2/p-Si (left) and p-Si/SiO_2/n^+ pc-Si/Ti/TiO_2/liquid (right) are also shown. The values used in this illustration were obtained from the calculation work in this chapter.

chapter 3.2.2.

In case of p^+-Si/Al interface, as same as n^+-Si/Ti case, we assume that interface forms a Schottky barrier with no metal induced gap states or Fermi level pinning. If this is the case, the barrier height Φ_B at the p^+-Si/Al interface is the difference between the Al work function (φ_{Al} = 4.08 V) and the p^+-Si work function (φ_{p+}= 5.27 V) plus the deviation between the flat band potential and the conduction band. Using the equation 4.20, φ_B was found to be -1.19 V, indicating it may hinder the hole injection through this interface. However, depletion width formed in p+ region is less than 0.4 nm, holes injected by the charge separation from the bulk can tunnel through this interface.

Putting all values obtained through the calculation work, we obtained band diagram for this carrier-selective design, and this is illustrated in Figure 5.7.

5.1.5 Concluding remarks

It was demonstrated a Si based photocathode with carrier-selective contacts with improved photovoltage and photocurrent compared to the conventional configuration with pn-junction. Simple dipping process in nitric acid allows to form a SiO_2 thin layer which reduce surface recombination of Si, and to build effective barrier for the unnecessary carriers together with wide band gap pc-Si. Since, both n^+ and p^+ pc-Si are transparent and conductive, this novel charge separation approach can be applied for the back-side illumination condition, indicating that the present configuration can be used in tandem water splitting device as a bottom cell. FG annealing process in this chapter provided significant improvement in photovoltage and fill factor likely due to the passivated trap sites by the incorporation with hydrogen. It is expected that further optimization of this forming gas annealing process would provide additional photovoltage.

5.2 Photocatalytic hydrogen production in alkaline media

As mentioned and demonstrated earlier, Si is one of the most studied materials, which is able to perform effective photocatalytic HER in an acidic electrolyte [26,60,87,109]. While Si easily passivates to SiO_2 in an acidic environment (which covers the surface and hinders current flow), previously shown results in this work along with the previous research [28,60,87], has demonstrated that TiO_2 can be used as an effective intermediate layer between the Si photoabsorber and the catalyst with good chemical stability under the HER condition at pH 0. This approach prevents Si from passivating, thus allowing efficient PEC activity. Even if there are pinholes, which allow the electrolyte to contact the Si, the Si will only be locally passivated (the passivation is self-limiting in acid). Thus there will be no noticeable effect on overall performance.

However, since the eventual role of Si in this chapter is for use as a photocathode in a 2-photon overall water splitting system, Si will need to perform in the same electrolyte as the photoanode side. Also there are no good OER - catalysts without noble metals, which are stable in acid electrolyte, alkaline electrolytes have a key advantage because non-noble OER catalysts with reasonable activity exist which may allow substantial cost savings and better scalability [32,36,110]. Beyond the stability of the catalyst there is also the issue of stability of the light absorber. For instance, most potential absorber materials quite easily dissolve or photocorrode in acidic solution while many show stable photocatalytic performance in neutral and alkaline electrolytes [32,38,56,57,110]. For Si, however, it is the other way around. When Si interacts with alkaline solution it corrodes via dissolution since SiO_2 is not stable under alkaline conditions and therefore the self-limiting passivation mechanism does not work at high pH media. The lack of a self-limiting passivation entails that the underlying Si under any pinholes in a protection layer will corrode continuously. Thus, preventing pinholes in protection layers is mandatory in alkaline environments. In this chapter, evaluation of high power impulse magnetron sputtering (HiPIMS) grown TiO_2 as a conducting protective material for HER in a high pH alkaline solution is demonstrated.

This section is mainly based on the paper [32].

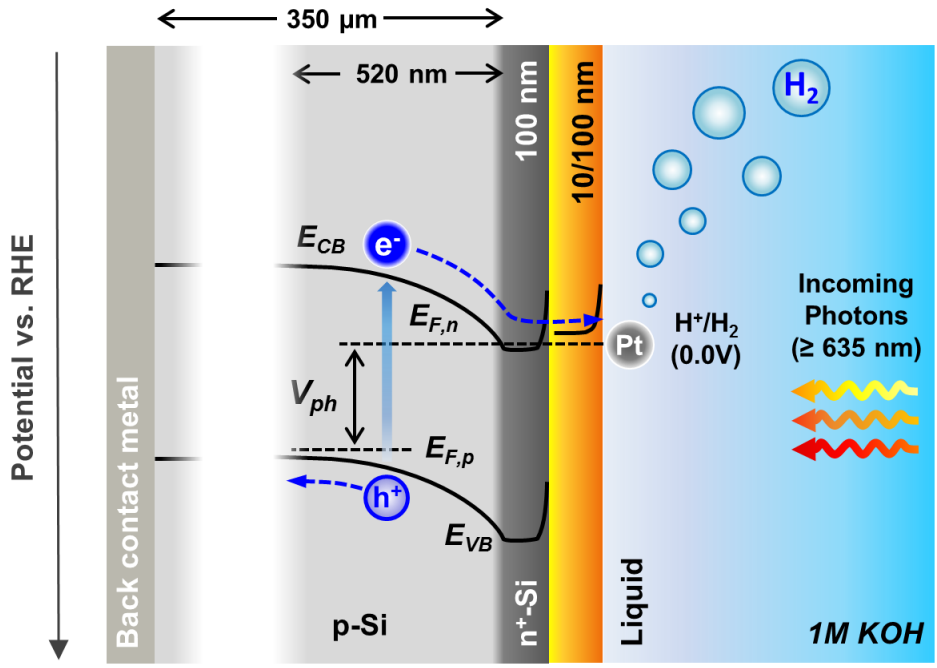

Figure 5.8 Schematic cross section of the sample used for photocatalytic activity (HER) experiments. The light is illuminated at the TiO_2 side. Schematic energy diagram of the illuminated sample in equilibrium with H^+/H_2 reaction is also shown. The detailed procedure for depletion width calculation can be found in chapter 4.2.2.

5.2.1 Sample fabrication process

Czochralski crystalline silicon (CZ c-Si) based photocathodes were fabricated as previously described in chapter 4.2.1. The shallow pn^+-junction was formed on p-type (100) Si wafers (Topsil, 1-20 ohm-cm, boron-doped) with $POCl_3$ as the phosphorus dopant source for n^+ doping using a vapor phase surface doping process in an atmospheric pressure tube furnace. The doping process was carried out at 900℃ for 10 min. Subsequently a shallow pn^+-junction was formed on the surface of the p-type wafer, which was expected to form a depletion width of approximately 500 nm [60]. A 3 µm deep part of the pn^+-Si was patterned by photolithography technique and etched away by reactive ion etching to fabricate a 10 mm diameter isolated circular pn^+-junction area (mesa structure). Detail process was already described in chapter 4.2.1.

Ti and TiO_2 protecting layers were grown by the DC magnetron sputtering (DCMS) and HiPIMS processes. HiPIMS is a novel ionized physical vapor deposition technique in which its major advantages include a denser coating and smoother surface morphology [111,112] due to a high degree of ionization of plasma (up to10^{13} ions cm^{-3} [113]) containing high fractions of target metal and reactive gas ions. Consequently, the grown film has an enhanced corrosion resistance without large-scale defects [114]. In case of DCMS process, the Si samples were sputter-cleaned

by Ar to remove any adventitious carbon-based contaminations and oxide layers at 35 W for 120 s. Then, approximately 8 nm of Ti was deposited followed by 100 nm of TiO_2 under oxygen and argon gas flow using conventional DC power mode. The base pressure of the vacuum chamber (AJA inc.) was below $8x10^{-8}$ mbar. The detailed procedure can be found elsewhere [28,60].

For the case of HiPIMS process, the samples were cleaned ultrasonically using isopropanol, acetone, and methanol each for 5 min. In order to remove the native oxide, the samples were dipped in HF acid (4%) for 5 min then taken out of HF and put into DI water and carried over to the chamber to be loaded. Before loading, the samples were taken out of the DI water and dried by blowing N_2 on them. A custom-built sputtering chamber was employed to perform the following depositions. The base pressure of the chamber was below $5x10^{-9}$ mbar. A 3 inch (75 mm) Ti target with the purity of 99.995% was used in a planar magnetron system for growth of both Ti and TiO_2 layers. The sputtering gas was Ar (99.999%) for the case of Ti growth and Ar mixed with O_2 (99.999%) in the case of TiO_2 growth. Total growth pressures of $4x10^{-3}$ mbar for the growth of Ti and $7x10^{-3}$ mbar for the growth of TiO_2 were achieved using an adjustable throttle valve. To prevent any deposition gradient due to the chamber geometry, the samples were rotated during growth.

In the case of the HiPIMS grown Ti interlayers, the power was supplied by a SPIK1000A pulse unit (Melec GmbH) operating in the unipolar negative mode at constant voltage, which in turn was charged by a dc power supply (ADL GS30). The discharge current and voltage were monitored using a combined current transformer and voltage divider unit (Melec GmbH). LabVIEW software acquired the data and calculated the average power using the measured discharge current and voltage for each applied pulse and then set pulse repetition frequency. The pulse repetition frequency was 50 Hz. The pulse length was 110 μs and the cathode voltage was set to 485 V. The resulting average power was then 120 – 125 W and the achieved target peak power density was ~ 850 – 900 W cm^{-2}. The Ti interlayer growth temperature was room temperature (hereafter RT). Using such parameters resulted in 5 Å/min of growth rate and approximately 10 nm Ti with native oxide.

The TiO_2 films were grown using the same setup for HiPIMS grown Ti layers. The pulse voltage was 423 V with 200 μs long duration at frequency of 270 Hz. The average power and peak power density during growth were 340 W and 240 W cm^{-2}, respectively. The TiO_2 layers were

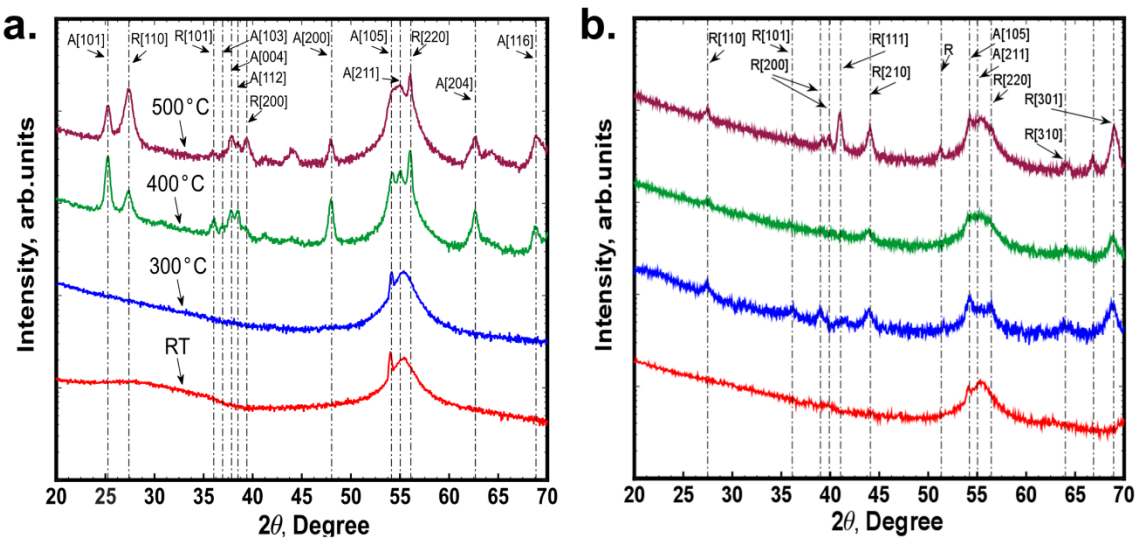

Figure 5.9 GIXRD patterns of DCMS grown (a) and HiPIMS grown (b) TiO_2 deposited on Si substrate at various temperatures (RT, 300˚C, 400˚C and 500˚C). The anatase and rutile phases of TiO_2 are marked with *A* and *R*, respectively.

grown at various growth temperatures of RT, 300, 400, and 500˚C. The mentioned growth parameters resulted in growth rate of 5 nm/min and the growth time of 20 min produced 100 nm TiO_2 layers. The growth temperature was kept steady during the deposition.

Ohmic contacts were made using a eutectic gallium-indium alloy and Cu-wire on the backside of the Si substrates as described in previous chapter (4.2.1). The inactive parts of the electrodes were covered with epoxy, and the Pt was deposited as a co-catalyst by drop-casting on the TiO_2 surface as described also in previous chapter (4.2.1). Schematic drawings of samples used in this work are shown in Figure 5.8.

5.2.2 Characterization of TiO_2 layers

Physical properties of TiO_2 layers were investigated by GIXRD, XRR, and cross sectional SEM measurements. Detail description of these methods can be found in chapter 2. In general, the rutile phase is the most stable structure of TiO_2, while the anatase phase can transform to rutile phase at high temperatures (500 ~ 700˚C [115]). In order to determine the structural properties and stoichiometry of TiO_2 films X-ray reflectometry (XRR) and grazing incidence diffractometry (GIXRD) measurements were performed. In the present work, as expected, TiO_2 shows a strong phase dependency on the substrate growth temperature. The peaks corresponding to the anatase and rutile phases of TiO_2 are marked with *A* and *R* in GIXRD patterns (Figure 5.9a

and b), respectively. The patterns reveal that the crystalline structure of anatase is well preserved even at high temperature with trace of rutile phase, indicating that both DCMS and HiPIMS grown TiO_2 films have a mixture of anatase and rutile phases. However it has to be pointed out that the HiPIMS grown films are mostly in rutile phase for higher growth temperatures. A transition from anatase to rutile is also obvious as the growth temperature is increased and it is more pronounced for the films deposited at 500˚C.

The crystallinity of both anatase and rutile phases obviously increases with increased growth temperature, as shown by the reduced full width at half maximum (FWHM) of the peaks. Based on the relationship between the broadening of XRD peaks and crystallite size by the Scherrer method [116], it was found that the crystallite size of TiO_2 increased with growth temperature. Generally, increasing of the TiO_2 crystallite size is accompanied by a distinct decrease in its

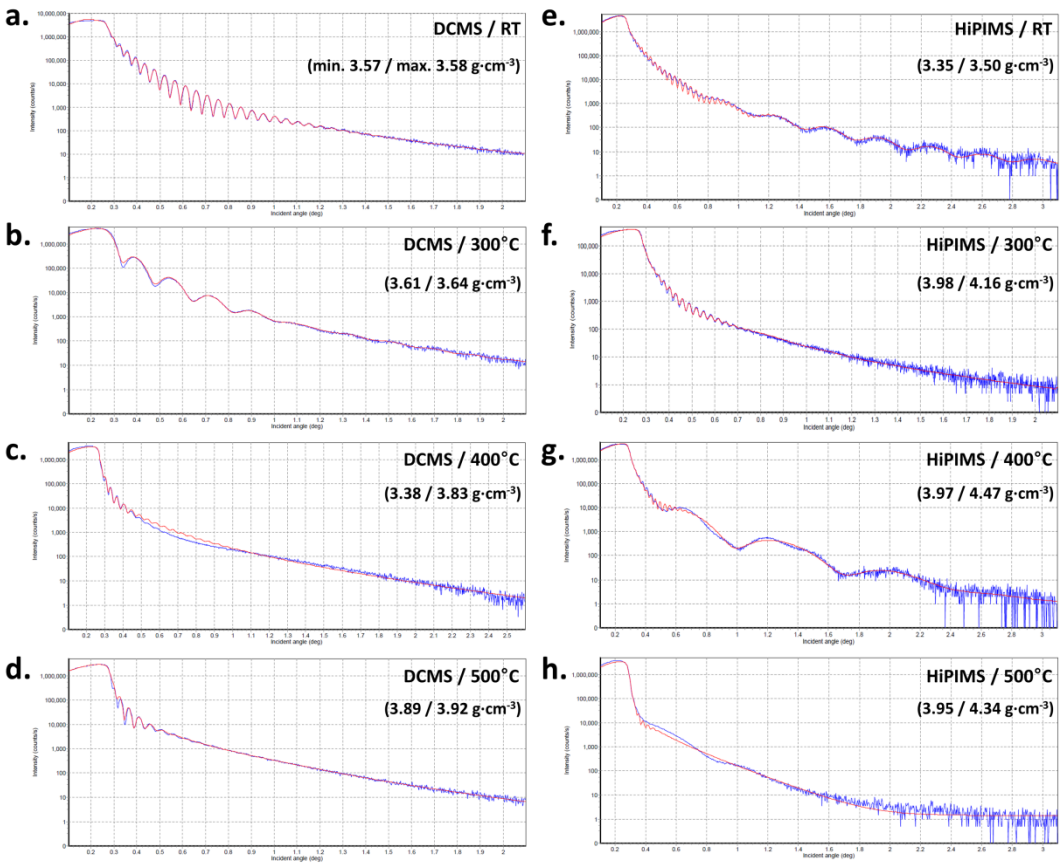

Figure 5.10 X-ray reflectivity (XRR) data from the DCMS (a – d) and HiPIMS (e – h) grown TiO_2 deposited at various temperatures (RT, 300˚C, 400˚C and 500˚C) on Si collected on PANalytical's diffractometer system. The results of a non-linear least squares fit of a model structure to the experimental data (red) are shown with blue color. The automatic fitting process refines the density values of the TiO_2 layer, and its minimum and maximum values are shown in the brackets.

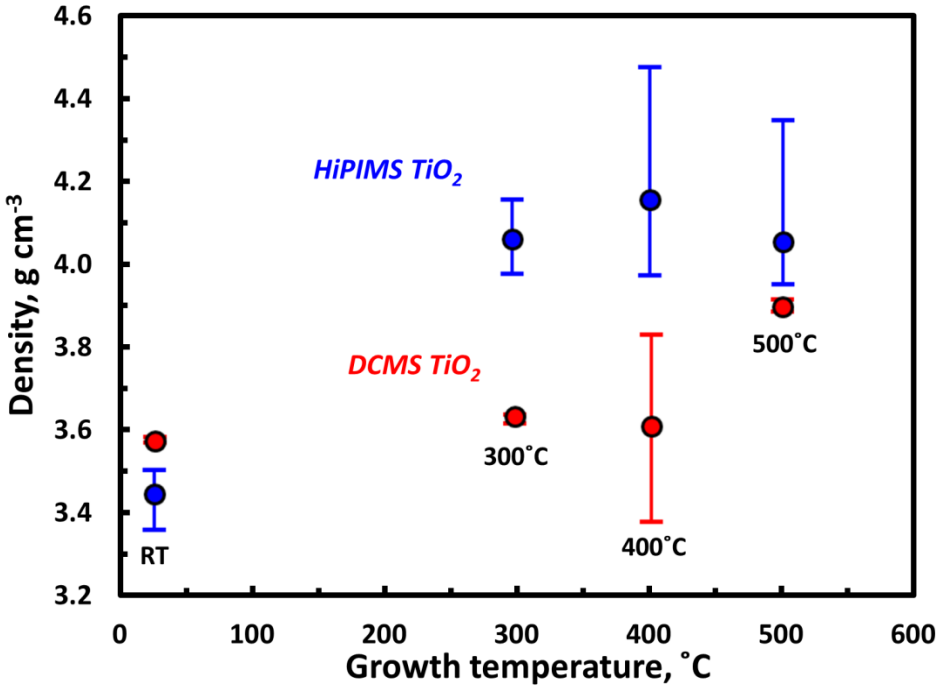

Figure 5.11 The film density of the DCMS grown (red) and HiPIMS grown (blue) TiO_2 deposited on Si substrates at various temperatures (RT, 300˚C, 400˚C and 500˚C) derived from the XRR pattern (Figure 5.10) fitting.

surface area [117,118], and consequently the TiO_2 deposited at high temperature should have relatively less pinholes which can be formed at the grain boundaries. Interestingly, the reference sample protected by the DCMS grown TiO_2 shows peaks from TiO_2 anatase (mainly) and rutile mixed phases in its GIXRD pattern, and this may be due to the relatively low energy distribution of the sputtered ions at DCMS discharge condition which reduce the diffusivity of the incoming species on the substrate surface, and thus forms relatively lower density phase (anantase), restricting densification of the grown film [113,119].

The XRR measurements were conducted to quantify the film density of the TiO_2 layers deposited on the Si substrate. The experimentally measured and numerically fitted XRR pattern data are shown in Figure 5.10, and the density of the films extracted using Parratt formalism [46,120] can be found in Figure 5.11. As expected from the GIXRD measurements, the values plotted in Figure 4.30 demonstrate the film density increases with increasing growth temperature for both DCMS and HiPIMS grown films. In addition, the HiPIMS grown TiO_2 shows a higher film density than the TiO_2 deposited by DCMS. The HiPIMS grown TiO_2 film shows its maximum film density of 4.15 g/cm^3 at 400˚C (see Figure 5.11), which is enhanced by around 20.6 % and 15.0 % compared to that of the sample deposited at room temperature (RT) and the

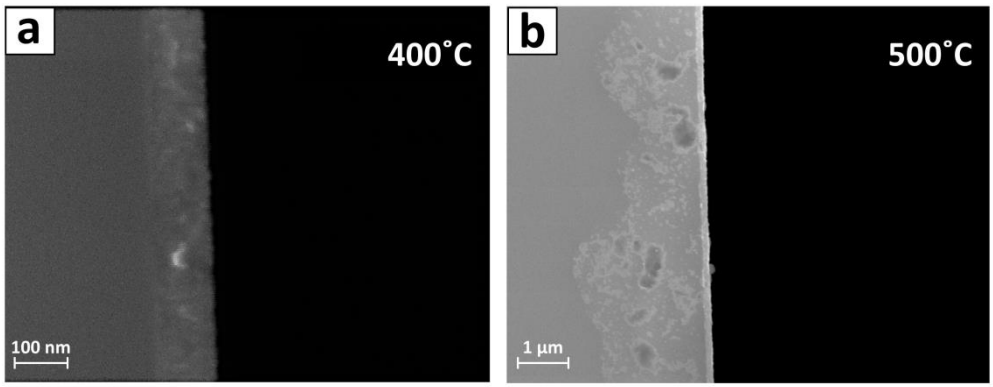

Figure 5.12 Cross-sectional SEM images of TiO_2 deposited on Si substrate at 400˚C (a) and 500˚C (b). A clear planar interface between the Si and the TiO_2 deposited at 400˚C can be found whereas an irregular interface, which is due to the intermixing/interdiffusion of Ti with/into Si (confirmed by EDX), is observed from the TiO_2 sample deposited at 500˚C.

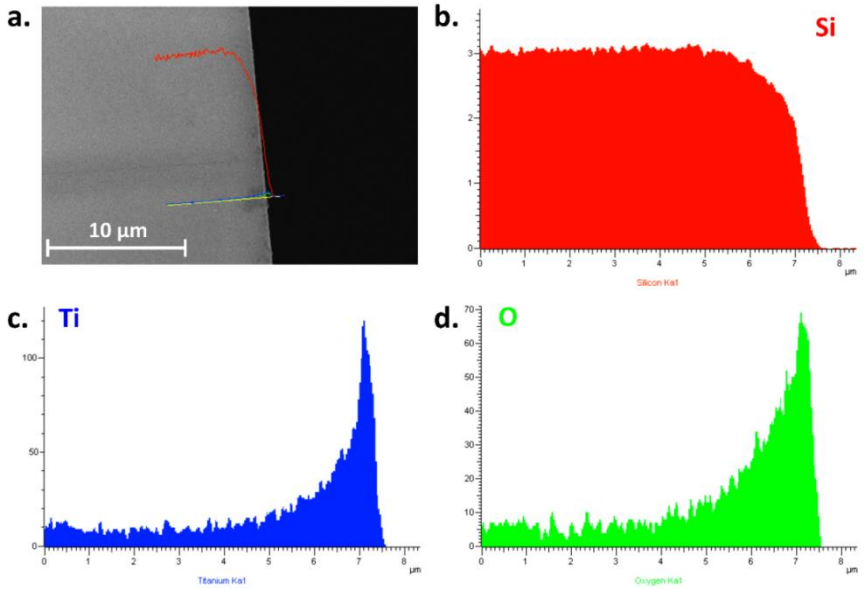

Figure 5.13 Cross sectional SEM image TiO_2 deposited on Si substrate at 500˚C (a), and EDX linear profile for the Si (b), Ti (c) and O (d) across the cross-section of SEM image.

reference sample deposited by DCMS at the same growth temperature, respectively. Another interesting aspect is the decreased film density of TiO_2 grown at 500˚C. On one hand, Alzamani *et al.* reported [121] that a too high growth temperature might lead to non-uniformity and crack formation of TiO_2 films, and increased porosity consequently. However, any obvious microscopic scale crack formation on TiO_2 layer has not been found under SEM investigation (will be discussed later). On the other hand, elevating the growth temperature up to 500˚C can also cause the diffusion of pre-deposited Ti into the Si and formation of an intermixed interface. Cross-sectional SEM investigation (Figure 5.12) well demonstrates the irregular boundary

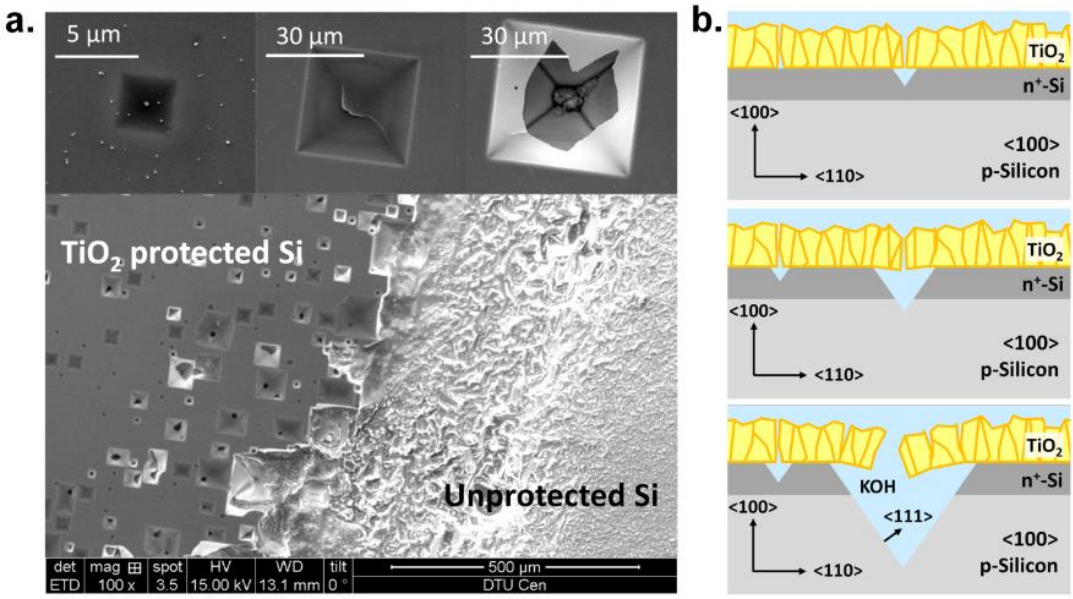

Figure 5.14 SEM images of a <100> oriented Si substrate with and without DCMS deposited TiO_2 at 400˚C after immersion in an 1M KOH electrolyte for 3 days (a), and shape illustrations of the etch profiles of a <100> oriented silicon with TiO_2 protection layer during etching process in KOH solution.

between the Si and TiO_2 layer due to the intermixing of Ti and Si at 500˚C (Figure 5.12b) whereas clear and planar boundary between Si and TiO_2 is observed at 400˚C (Figure 5.12a) indicating that decrease of film density at 500˚C can be ascribed to the thermal diffusion of Ti at too high temperature. The EDX profile across the cross-section of TiO_2 deposited Si sample at 500˚C (see Figure 5.13) proves the diffusion of Ti and O up to several µm under the surface (Figure 5.13b).

5.2.3 Chemical stability test

The main focus is on investigating the effect of TiO_2 packing density and tighter grain boundaries on its protection performance in 1M KOH electrolyte. Hence, the effect of the improved film density on the stability and durability of the films is investigated in high pH electrolyte (1M KOH) under dark conditions. A Teflon beaker with 1M KOH (Sigma-Aldrich 99.995%) was used for this experiment, and as-prepared Si photocathods with TiO_2 protection layers were attached on the cell wall vertically. The high purity 1M KOH has been used for all corrosion test in the dark as well as photoelectrochemical testing. As shown in Figure 5.14a, severe surface damage was observed after a 3 days immersion test from the unprotected Si surface, whereas the Si surface protected by the DCMS grown TiO_2 layer at 400˚C showed a flat surface with distributed typical pyramid-like pits in the Si due to due to the anisotropic corrosion

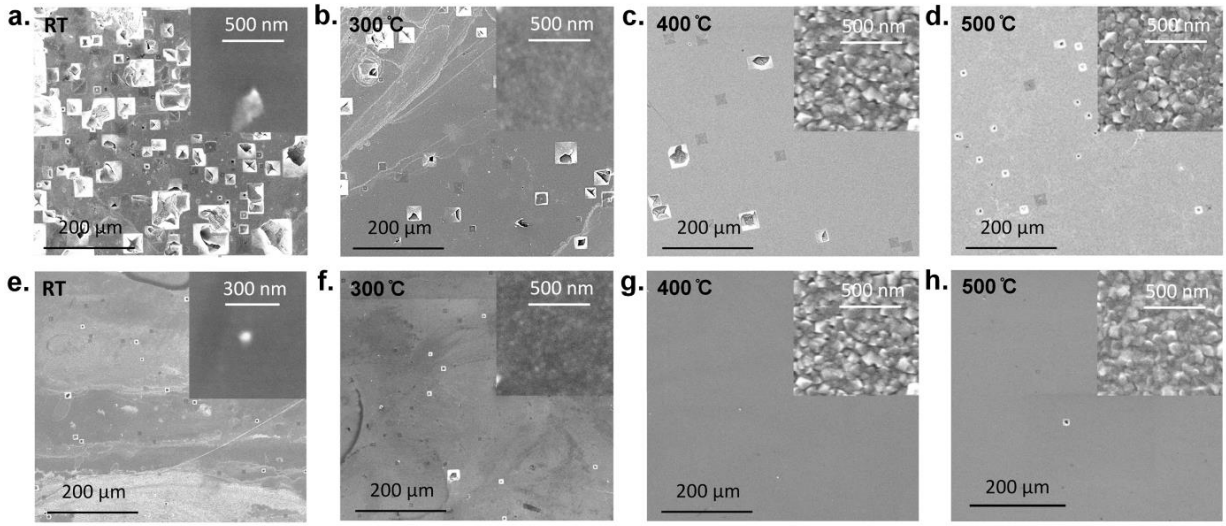

Figure 5.15 Surface SEM images of Si photoelectrodes with TiO_2 film deposited by DCMS (a ~ d) and HiPIMS (e ~ h) at different growth temperatures (a, e – room temperature; b, f - 300˚C; c, g - 400˚C and d, h - 500˚C).

rate between the <100> and <111> planes of Si [122]. The formation of a large number of (inverse) pyramids on TiO_2 protected side is clear evidence that the current sputtered TiO_2 layer cannot properly prevent the corrosion of Si in KOH. The high magnification plane-view SEM micrographs (see insets of Figure 5.14a) further show that the damage (i.e. etching process) begins on the Si underneath the TiO_2 protection layer. The Si etching can be explained by the presence of pin-holes within the TiO_2 layer, through which highly concentrated KOH permeates, and results in the corrosion of the underlying Si as illustrated in Figure 5.14b. As the etching process progresses, the width of pyramid increases, which leaves the top TiO_2 protection layer without a substrate to support it. Thus underetching of TiO_2 eventually occurs and causes delamination of the film. Logically, the higher film density results in minimizing the number of pinholes, and thus enhances the protection of the underlying Si.

While the vast majority of the pinholes led to square-like etch pits, there were a few large cracks in the film that were irregularly shaped. Upon careful examination it was realized that this is most likely due to dust particles that had settled on the Si before Ti or TiO_2 deposition. Dust particles can easily be larger than the TiO_2 thickness. These large dust particles could potentially form cracks in the TiO_2 film and subsequently increased corrosion. In this case the shape of the Si corrosion pit should be as irregular as the dust particle which causes it. Neither the DCMS nor the HiPIMS sputter chamber was located in a clean room, so dust deposition was an issue we could minimize, but not eliminate. Nevertheless, the degradation effect caused by pinholes was

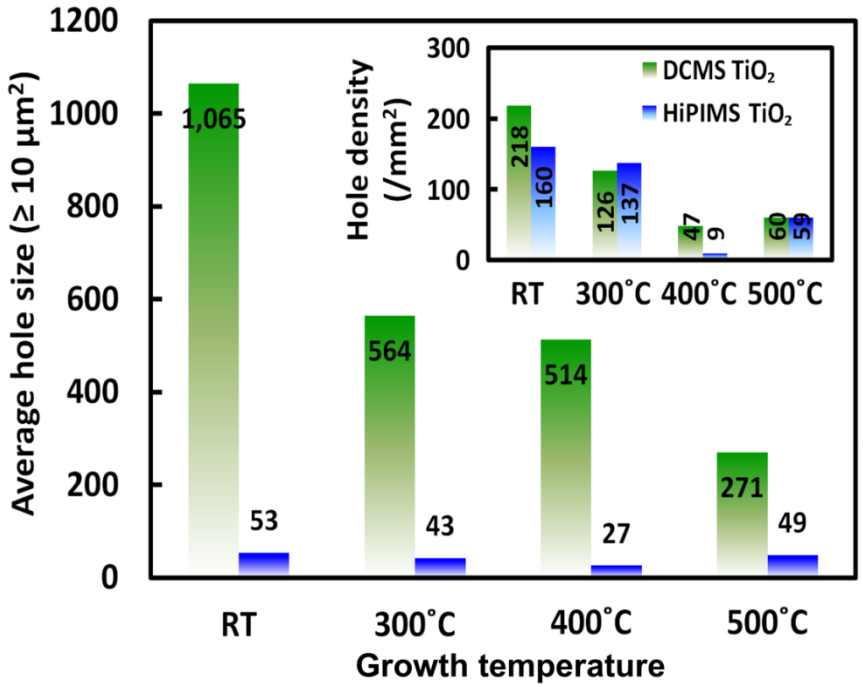

Figure 5.16 Average hole size and the hole density as an inset (counted larger than 10 μm^2 only) measured from the samples in Figure 5.15 after the 3 days dipping test in 1M KOH under the dark.

more pronounced than that of caused by dust (as seen by the SEM images in Figure 5.15 for both DCMS and HiPIMS). Therefore the dust issue has no bearing on the comparison between the two methods.

Both the DCMS and HiPIMS grown TiO_2 layers at various growth temperatures have been evaluated in 1M KOH for 3 days under dark condition. As shown in Figure 5.15 (a ~ h), the Si electrodes with the HiPIMS grown TiO_2 protection layer shows superior stability to those with the DCMS grown TiO_2 layer for all growth temperatures. The number of pyramid etch pits and their average size have been used as indicators to quantify the protection efficiency of the TiO_2 films. To quantify the number and size of the cavities an image analysis program ImageJ (1.46r) was used after the experiments. Figure 5.16 shows that the advantage of using HiPIMS for the growth of TiO_2 as a protection layer is a significantly reduced average etch pit size. The HiPIMS deposited TiO_2 samples showed 5 ~ 20 times smaller size compared to the DCMS deposited TiO_2 samples for the entire growth temperature range. It is worth noticing that the number of holes per specific area (inset) is almost unchanged regardless of deposition type but varies with the growth temperature. This result agrees well with previous reports that the elevated growth temperature enhances the packing density of TiO_2 film [123] due to the improved mobility of

adatoms on the film surface [124], and consequently, this implies that sufficient thermal energy should be provided to secure good surface coverage as well as high density of sputtered ions as mentioned earlier. Also note that both DCMS and HiPIMS deposited TiO_2 samples at 500˚C show slightly increased hole density compared to those that deposited at 400˚C. Naturally, this can be attributed to the decreased film density owing to the Ti and Si intermixing as shown in Figure 5.12 and 5.13.

5.2.4 Photoelectochemical test

The primary purpose of this work is to protect Si photoelectrode during its photocatalytic HER in 1M KOH electrolyte. In the previous section it was observed that the HiPIMS grown TiO_2 layer has significantly enhanced protection properties compared to that deposited by DCMS, but it does not directly show that it can be applied to a photoelectrode as a protection layer. The photoelectrode must remain conductive during photoelectrochemical testing, in order that the injection of photo-generated carriers toward the electrolyte through the Pt catalysts is not limited as shown in schematic drawing of Figure 5.8.

To examine the effectiveness of the HiPIMS grown TiO_2 film as a protection layer, CAs with periodical CVs were conducted in 1M KOH electrolyte for 24 hours under the red-part of AM 1.5G illumination (635 nm cut-off filter and AM 1.5g filters have been used for experiments). The samples were re-platinized every 8 hours since the corroded Si and other trace metals may lead contamination of Pt, and consequently lower the current density [39]. The CV characteristics in Figure 5.17 reflect both the protection property of the HiPIMS grown TiO_2 film and charge transfer occurring across the solid/liquid interface. Throughout all growth temperatures, the initial CVs of samples with the HiPIMS grown TiO_2 films illustrate that the charge transfer through the HiPIMS grown TiO_2 film has good conductivity and the TiO_2/Pt interface seems to have a good ohmic contact since they showed similar onset voltage (~ 0.5 V vs. RHE) and slopes to that of the reference sample with the DCMS grown TiO_2 protection layer. In addition, the sample with the HiPIMS grown TiO_2 film at 400˚C showed considerably enhanced stability compared to the sample grown by DCMS with TiO_2 protection layer at the same growth temperature. As shown in Figure 5.17d, photocurrent saturation of the sample with the HiPIMS grown TiO_2 protection layer at 400˚C decreased by approximately 4% from its initial photocurrent, whereas the reference sample with the DCMS grown TiO_2 protection layer

showed almost 20% decreased photocurrent after 24 hours. On the other hand, it was found that the photocurrent degradation rate of the samples with the HiPIMS deposited TiO_2 at room temperature (Figure 5.17b) and 300˚C (Figure 5.17c) show approximately 30 % and 10 % degradation in photocurrent after 24 hours long-term test. Therefore it indicates that the protection property of TiO_2 increases with the growth temperature up to 400˚C. Interestingly, the stability of the HiPIMS grown TiO_2 sample at RT is less than the reference DCMS grown TiO_2 sample even though it showed smaller etch pit size in Figure 4.36e. It seems that this may be attributed to the TiO_2 layer peeling off from the surface during the hydrogen gas bubbling process due to the residual stress of TiO_2 which could not be relaxed by annealing [124], and consequently lowered the adhesion property of TiO_2 [125].

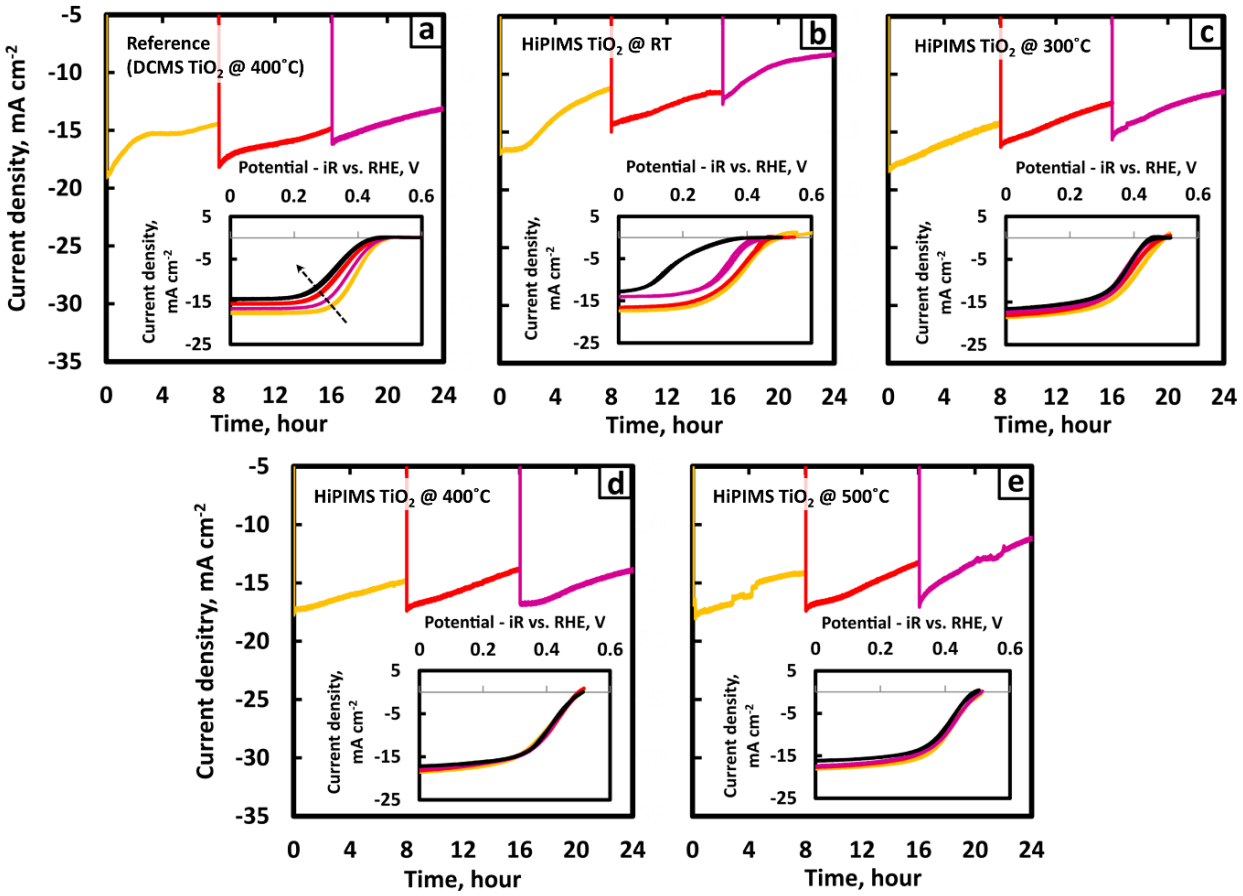

Figure 5.17 CAs of Si photocathodes with the reference DCMS grown TiO_2 (a), HiPIMS deposited TiO_2 at various growth temperatures (b ~ e). CVs (inset) were taken prior to the initial CA measurements (yellow), after 8 hours (red), after 16 hours (purple), and after 24 hours (black). The samples were re-platinized every 8 hours prior to the CV measurements. All measurements were done in 1M KOH electrolyte under illumination (the total irradiance is 38.6 mW/cm^2).

One other remarkable aspect is that the onset voltage is anodically shifted with time concurrent with the decrease of photocurrent. On the assumption that the deposited Pt catalyst reaches the same activity after every re-platinization process, an obvious decrease of onset voltage from Figure 4.38a, b, c is mainly attributed to the damaged pn-junction by KOH. As shown in our previous study, the flat-band potential (V_{FB}) of the p-type Si-water junction places severe restrictions on the voltage in an aqueous electrolyte (≈ 0.2 V vs. RHE), and thus charge separation will only happen at low potential below its V_{FB} [126]. Since the highly doped n^+ region is around 100 nm deep from the liquid/solid interface, long KOH exposure times can significantly etch away this n^+ layer as shown in Figure 5.14b, and thus deteriorate the photovoltage produced by the Si. In the case of the HiPIMS grown TiO_2 at 500˚C, the sample showed a slight increase in photocurrent degradation (≈ 5%) in comparison to that of the sample grown at 400˚C by HiPIMS. This result agrees with the film density measurement results using XRR (Figure 5.11) and hole density measurement as shown in Figure 5.16. However the onset voltage of the HiPIMS grown TiO_2 at 500˚C decreased by approximately 25 mV compared to initial CVs of other samples. As shown in Figure 5.12b, Ti intermixing with Si has been found at 500˚C. The transition metals, such as Ti, Fe, and Cr are well-known metallic defects, which reduce the minority carrier diffusion length of Si significantly [127], and a previous study [128] has demonstrated that Si solar cell defected by metallic impurities have major reductions in their open circuit voltage (V_{oc}) as well as saturation photocurrent (J_{sc}), and this is in good agreement with the present results.

5.2.5 Concluding remarks

It was demonstrated a Si based photocathode protected by the HiPIMS grown TiO_2 layer with good stability as well as high activity in 1M KOH (pH 14) under HER conditions. Deposition of TiO_2 using HiPIMS technique provides enhanced film density which surpassed that of the TiO_2 protection layer deposited by conventional DC sputtering technique. This approach resulted in an apparent enhanced stability owing to the higher degree of ionization for the HiPIMS plasma during sputtering process, and consequently to the minimization of unprotected Si surface. The sample with the HiPIMS grown TiO_2 protection layer at 400˚C shows the minimum degradation rate (4%) in photocurrent after 24 hours long-term stability test, whereas the DCMS deposited TiO_2 at the same temperature shows significantly higher degradation rate (20%) with anodically

shifted onset voltage due to the loss of the pn-junction area of Si. Increased growth temperature improves the stability of the photoelectrodes due to the increased film density of TiO_2 as well as improved adhesion between the TiO_2 and the substrate, but too high growth temperature (500˚C) causes intermixing of protection layer with substrate due to the thermal interdiffusion resulting in lowered photovoltage and photocurrent. Considering these experiments were not carried out in clean-room condition, much less corrosion loss can be obtained by minimizing dust build-up on the surface that potentially can form pin-holes. Furthermore, the Si photocathode protected by HiPIMS grown TiO_2 layer can be coupled with photoanode with co-catalysts, such as NiO, CoO_x, and $NiCoO_x$, which are efficient in alkaline media as shown in the chapter 3 in this thesis.

Chapter 6

6. Summary and outlook

6.1 Significances and impact on science field

The present work addresses the physical and chemical processes taking place in Si-based PEC cells in order to be applied as a bottom cell of the solar water splitting tandem devices. For this purpose, two challenging goals were set: i) to develop bifacial photoelectrochemical (PEC) cell which allows light absorption from its back side and ii) to realize efficient and stable oxygen evolution and hydrogen evolution (OER and HER, respectively). To this end, a light permeable back contact design for both Si photoanode and photocathode was established. A back-illuminated Al/n^+pp^+-Si/Co/$NiCoO_x$ photoanode exhibited excellent OER kinetics which surpass that of the state-of-the-art np^+-Si/NiO_x:Fe photoanode. For the HER, a Al/p^+pn^+-Si/Ti/TiO_2/Pt photocathodes, which has an inverted band diagram to the above mentioned photoanode, were investigated. This approach allows us to use Si photoelectrode either for the OER or HER without changing device structure or conductivity type of Si wafer. However, its current-voltage performance lags behind the Si-based PV cells, thus carrier-selective contacts based on MOS diode (Si/SiO_2/pc-Si) were developed. A Si photocathode with the carrier-selective contacts provided additional 70 mV with enhanced fill factor. In addition, it was shown that film density of protection layer can be increased by using a novel sputtering technique (HiPIMS), and consequently stability of the Si photocathode can be secured. Consequently, putting these results together, the demonstrated Si photoelectrode can be stated as a 'ready-made bottom cell' for tandem water splitting devices, which can be applied regardless of type of the electrolyte (acid or alkaline) and reaction type (oxygen or hydrogen evolution). To recap briefly, significances of this work can be summarized as follows:

1. Efficient and stable back-illuminated n^+pp^+-Si photoanode coupled to Co/$NiCoO_x$ has been successfully demonstrated.
2. Time-dependent PEC behaviour of $NiCoO_x$ and its substitution incorporation with Fe has been demonstrated for the first time.

3. A charge collection model has been studied to estimate effect of thickness, diffusion length, and surface recombination rate on the photocurrent of the inverted Si photocathode (p^+pn^+).
4. Based upon the modelling results, a thinned Si photocathode was fabricated, and HER in acid under the back side illumination for the first time.
5. MOS based carrier selective design for the Si photoelectrode was coupled to Ti/TiO_2 protection layer, providing significant increases in photovoltage and photocurrent.
6. HiPIMS deposition method provided high film density for the TiO_2 protection layer, and this leads to the stable hydrogen evolution under back side illumination in alkaline media.

6.2 Prospective tandem PEC design using Si bottom cell

Putting above mentioned results together, the demonstrated Si photoelectrode can be stated as a 'ready-made bottom cell' for tandem water splitting devices, which can be applied regardless of type of the electrolyte (acid or alkaline) and the required reaction (oxygen or hydrogen

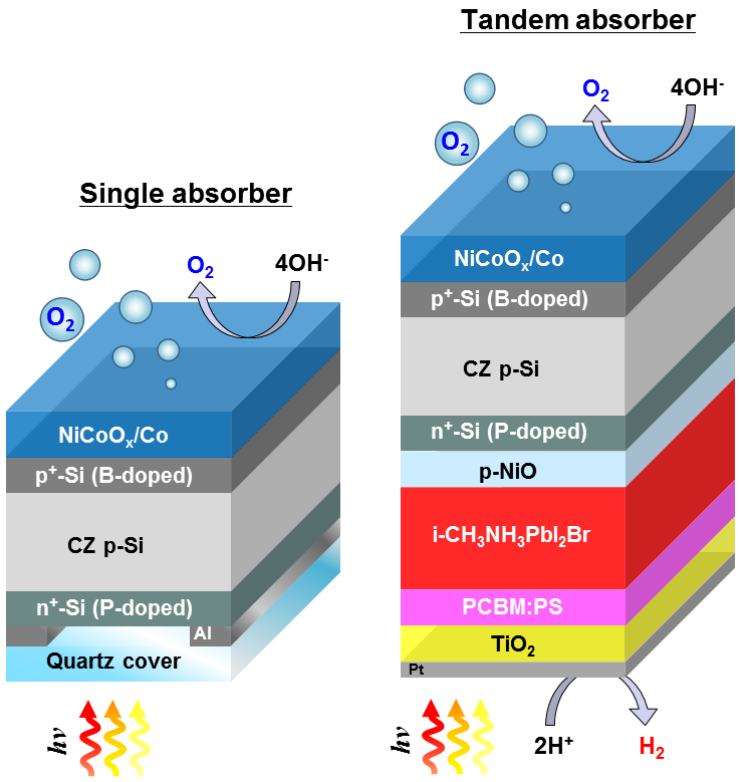

Figure 6.1 Schematic drawing of single absorber photoanode device for OER used in chapter 3 (left), and tandem water splitting device which is made up with the Si based photoanode and wide gap perovskite (right). NiO is suggested as a recombination layer and Pt as a HER catalyst.

evolution). However, cost-effective and chemically stable tandem PEC water splitting device is still far from being realized unless the Si bottom cell is coupled to wide band gap (~ 1.7 eV) top cell for other half reaction. Unlike narrow band gap semiconductors, there are very a few wide band gap semiconductors which can be considered as a candidate for the top cell of the water splitting device. In general, wide band gap semiconductors have higher voltage loss than narrow gap semiconductors. Among the wide band gap semiconductors, organohalide perovskite ($CH_3NH_3PbI_2Br$; ~ 1.8 eV) shows low voltage loss (V_{oc} ~ 1.3 V), indicating that it can be used as wide gap top cell of tandem device. In addition, its simplicity of manufacturing (spin-coating) makes it attractive. Recently wide band gap perovskite solar cell with TiO_2 window layer has been developed in collaboration with Prof. S. Bent's group of Stanford University. This perovskite solar cell has been developed to be used for the top cell of tandem water splitting device in the future, and schematic drawing of this tandem device is demonstrated in Figure 6.1. However, its sensitivity to water necessitates appropriate transparent protection layer. Therefore, the development of dense conducting protection layer, which allows transport of the carriers with minimum optical loss, seems one of the critical challenges to realize the efficient tandem PEC water splitting device.

Bibliography

[1] United Nations, *Industrial Development for the 21st century: Sustainable development perspectives*, Department of economic and social affairs, New York, 2007

[2] British Petroleum, *BP statistical review of world energy 2015*

[3] United Nations, *World Population Prospects: The 2012 revision, highlights and advance tables*, Department of Economic and Social Affairs, Population Division, New York, 2013

[4] S. B. Petukhov, *Geological Paradox*. Anthology "Sotvorenie" volume 2. Palomnik Publishers, Moscow (in Russian), 2004

[5] Peak oil definition from Financial Times Lexicon: http://lexicon.ft.com/Term?term=peak-oil, Financial Times Lexicon. 2009. Retrieved 28 July 2015.

[6] J. Mitchell, V. Marcel, B. Mitchell, *What next for the oil and gas industry*?, The Royal Institute of International Affairs, London, 2012

[7] L. Maugeri, *Oil: The next revolution, geopolitics of energy project*, Belfer Center for Science and International Affairs, John F. Kennedy School of Government, Harvard University, Discussion Paper #2012-10, 2012

[8] *Oil Shale 1982: At and policy primer*, Colorado Energy Research Institute and Colorado School of Mines Research Institute, Golden, Colorado, 1981

[9] *China statistical yearbook 2014*, China Statistics Press, Beijing, 2014

[10] *Causes of climate change*, http://www.epa.gov/climatechange/science/causes.html (Retrieved 28 July 2015).

[11] *The Keeling Curve*, https://scripps.ucsd.edu/programs/keelingcurve/, Scripps Institute of Oceanography (Retrieved 13 July 2015).

[12] NASA/GISS, *Surface temperature analysis*, http://data.giss.nasa.gov/gistemp/graphs_v3/, NASA Global Institue for Space Studies (Retrieved 28 July 2015).

[13] T. F. Stocker, D. Qin (Eds.), *Climate Change 2013: The physical science basis*, Intergovernmental panel on climate change (IPCC), Cambridge University Press, 2013.

[14] J. Hansen, R. Ruedy, M. Sato, K. Lo, *2010: Global surface temperature change*, Rev. Geophys., 48, RG4004

[15] W. Yoko, *New radioactive water leak at Japan's Fukushima Daiichi plant*, http://edition.cnn.com/2014/02/19/world/asia/japan-fukushima-daiichi-water-leak/, CNN news, 20 Feb. 2014 (Retrieved 28 July 2015).

[16] S. E. Hasan, *Chapter 4: International practice in high-level nuclear waste management*, in Concepts and Applications in Environmental Geochemistry, ed. by D. Sarkar, R. Datta and R. Hannigan, Developments in Environmental Science, 5 (2007) 57–77

[17] S. Evans, Germany: *Nuclear power plants to close by 2022*, http://www.bbc.com/news/world-europe-13592208, BBC news, 30 May 2011 (Retrieved 30 May 2015).

[18] G. Ang et al., *Enabling Investment in sustainable energy infrastructure*, OECD→POST-2015, element 4, paper 2, OECD, 2015

[19] R. Perez, M. Perez, *A fundamental look at energy reserves for the planet*, http://asrc.albany.edu/people/faculty/perez/Kit/pdf/a-fundamental-look-at%20the-planetary-energy-reserves.pdf, 2009 (Retrieved 28 July 2015).

[20] ASTM G173-03, *Standard tables for reference solar spectral irradiances: direct normal and hemispherical on 37° tilted surface*, 2012.

[21] NREL`s latest chart of best research-cell efficiencies (up-to-date with the new world record), available on http://www.nrel.gov/ncpv/images/efficiency_chart.jpg (Retrieved 28 July 2015).

[22] NPD solarbuzz, PV equipment quarterly 2014.

[23] F. Cheng, J. Chen, *Metal–air batteries: from oxygen reduction electrochemistry to cathode catalysts*, Chem. Soc. Rev., 41 (2012) 2172-2192

[24] R. Liu, Z. Zheng, J. Spurgeon, X. Yang, *Enhanced photoelectrochemical water-splitting performance of semiconductors by surface passivation layers*, Energy Environ. Sci., 2014, 7, 2504-2517

[25] A. D. Doyle, J. H. Montoya, A. Vojvodic, *Improving oxygen electrochemistry through nanoscopic confinement*, ChemCatChem, 7 (2015) 738–742

[26] B. Mei, T. Pedersen, P. Malacrida, D. Bae, R. Frydendal, O. Hansen, P. C. K. Vesborg, B. Seger, I. Chorkendorff, *Crystalline TiO_2: A generic and effective electron-conducting protection layer for photoanodes and -cathodes*, J. Phys. Chem. C, 119 (2015) 15019-15027.

[27] W. Shockley, H. J. Queisser, *Detailed Balance Limit of Efficiency of p-n Junction Solar Cells*, J. Appl. Phys., 32, (1961) 510–519

[28] D. Bae, T. Pedersen, B. Seger, M. Malizia, A. Kuznetsov, O. Hansen, I. Chorkendorff, P. C. K. Vesborg, *Back-illuminated Si photocathode: a combined experimental and theoretical study for photocatalytic hydrogen evolution*, Energy Environ. Sci., 8 (2015) 650-660.

[29] S. Hu, C. Xiang, S. Haussener, A. D. Berger, N. S. Lewis, *An analysis of the optimal band gaps of light absorbers in integrated tandem photoelectrochemical water-splitting systems*, Energy Environ. Sci., 6 (2013) 2984-2993

[30] M. F. Weber, M. J. Dignam, E*fficiency of splitting water with semiconducting photoelectrode*s, J. Electrochem. Soc., 131 (1984) 1258-1265

[31] D. Bae, S. Shayestehaminzadeh, E. B. Thorsteinsson, T. Pedersen, O. Hansen, B. Seger, Peter C.K. Vesborg, S. Olafsson, I. Chorkendorff, *Protection of Si photocathode using TiO2 deposited by high power impulse magnetron sputtering for H_2 evolution in alkaline media*, submitted.

[32] B. Mei, A. A. Permyakova, R. Frydendal, D. Bae, T. Pedersen, P. Malacrida, O. Hansen, I. E. L. Stephens, P. C. K. Vesborg, B. Seger, I. Chorkendorff, *Iron-treated NiO as a highly transparent p-type protection layer for efficient Si-based photoanodes*, J. Phys. Chem. Lett., 5 (2014) 3456-3461

[33] M. W. Louie, A. T. Bell, *An investigation of thin-film Ni–Fe oxide catalysts for the electrochemical evolution of oxygen*, J. Am. Chem. Soc., 135 (2013) 12329-12337

[34] L. Trotochaud, S. L. Young, J. K. Ranney, S. W. Boettcher, *Nickel–iron oxyhydroxide oxygen-evolution electrocatalysts: The role of intentional and incidental iron incorporation*, J. Am. Chem. Soc., 136 (2014) 6744-6753

[35] O. Khaselev, J. A. Turner, *A monolithic photovoltaic-photoelectrochemical device for hydrogen production via water splitting*, Science, 280 (1998) 425-427.

[36] P. C. K. Vesborg, T. F. Jaramillo, *Addressing the terawatt challenge: scalability in the supply of chemical elements for renewable energy*, RSC Adv., 2 (2012) 7933-7947.

[37] M. R. Shaner, K. T. Fountaine, S. Ardo, R. H. Coridan, H. A. Atwater, N. S. Lewis, *Photoelectrochemistry of core-shell tandem junction n-p+-Si/WO3 microwire array photoelectrodes*, Energ. Environ. Sci., 7 (2014) 779-790.

[38] F. F. Abdi, L. Han, A. H. M. Smets, M. Zeman, B. Dam, R. van de Krol, *Efficient solar water splitting by enhanced charge separation in a bismuth vanadate-silicon tandem photoelectrode*, Nat. Commun., 4 (2013) 2195

[39] K. J. J. Mayrhofer, A. S. Crampton, G. K. H. Wiberg, M. Arenz, *Analysis of the impact of individual glass constituents on electrocatalysis on Pt electrodes in alkaline solution*, J. Electrochem. Soc., 155 (2008) 78-81

[40] J. Eskhult, *Electrochemical deposition of nanostructured metal/metal-oxide coatings*, Dissertation for the degree of Doctor of Philosophy, Uppsala University, 2007

[41] Image taken from Wikipeida web page, https://commons.wikimedia.org/wiki/File:Quartz_resonators_with_front_and_back_electrodes.jpg (Retrieved 3 Aug. 2015).

[42] Image taken from Trade Korea web page, http://www.tradekorea.com/product/detail/P416979/Electrochemical-research-Biosensor-crystal-.html (Retrieved 3 Aug. 2015).

[43] M. Birkholz, *Crystal-field induced dipoles in heteropolar crystals II: physical significance*, EPJ. B, 96 (1995) 333-340

[44] Image obtained from Wikipedia web page, https://en.wikipedia.org/wiki/Gas_chromatography# (Retrieved 29 July 2015).

[45] Image obtained from ChemWiki webpage of University of California at Davis, http://chemwiki.ucdavis.edu/Analytical_Chemistry/Instrumental_Analysis/Chromatography/Gas_Chromatography (Retrieved 29 July 2015)

[46] L. G. Parratt, *Surface studies of solids by total reflection of x-rays*, Phys. Rev., 95 (1954) 359-369

[47] J. Goldstein, D. E. Newbury, D. C. Joy, C. E. Lyman, P. Echlin, E. Lifshin, L. Sawyer, J. R. Michael, *Scanning electron microscopy and X-ray microanalysis (3rd eds.)*, Springer, New York, 2007

[48] E. A. Davis, N. F. Mott, *Conduction in non-crystalline systems V: Conductivity, optical absorption and photoconductivity in amorphous semiconductors*, Philos. Mag., 22 (1970) 903-922

[49] S. Dah, I. Chorkendorff, *Solar-fuel generation: Towards practical implementation*, Nat. Mater., 11 (2012) 100-101

[50] Y. Lee, J. Suntivich, K. J. May, E. E. Perry, Y. Shao-Horn, *Synthesis and activities of rutile IrO_2 and RuO_2 nanoparticles for oxygen evolution in acid and alkaline solutions*, J. Phys. Chem. Lett., 3 (2012) 399-404.

[51] E. A. Paoli, F. Masini, R. Frydendal, D. Deiana, C. Schlaup, M. Malizia, T. W. Hansen, S. Horch, I. E. L. Stephens, I. Chorkendorff, *Oxygen evolution on well-characterized massselected Ru and RuO_2 nanoparticles*, Chem. Sci., 6 (2015) 190-196.

[52] W. Chen, H. Wang, Y. Li, Y. Liu, J. Sun, S. Lee, J.-S. Lee, Y. Cui, *In situ electrochemical oxidation tuning of transition metal disulfides to oxides for enhanced water oxidation*, ACS Cent. Sci. 1 (2015) 244-251.

[53] W. T. Hong, M. Risch, K. A. Stoerzinger, A. Grimaud, J. Suntivich, Y. Shao-Horn, *Toward the rational design of non-precious transition metal oxides for oxygen electrocatalysis*, Energy Environ. Sci., 8 (2015) 1404-1427.

[54] B. Beverskog, I. Puigdomenech, *Revised Pourbaix Diagrams for Nickel at 25−300 °C*. Corros. Sci., 39 (1997) 969-980.

[55] E. M. Garcia, J. S. Santos, E. C. Pereira, M. B. J. G. Freitas, *Electrodeposition of cobalt from spent Li-ion battery cathodes by the electrochemistry quartz crystal microbalance technique*, J. Power Sources, 185 (2008) 549-553.

[56] J. Yang, K. Walczak, E. Anzenberg, F. M. Toma, G. Yuan, J. Beeman, A. Schwartzberg, Y. Lin, M. Hettick, A. Javey, J. W. Ager, J. Yano, H. Frei, I. D. Sharp, *Efficient and sustained photoelectrochemical water oxidation by cobalt Oxide/Silicon photoanodes with nanotextured interfaces*, J. Am. Chem. Soc., 136 (2014) 6191-6194.

[57] X. Zhou, R. Liu, K. Sun, D. Friedrich, M. T. McDowell, F. Yang, S. T. Omelchenko, F. H. Saadi, A. C. Nielander, S. Yalamanchili, K. M. Papadantonakis, B. S. Brunschwig and N. S. Lewis, *Interface engineering of the photoelectrochemical performance of Ni-oxide-coated n-Si photoanodes by atomic-layer deposition of ultrathin films of cobalt oxide*, Energy Environ. Sci., 2015, just accepted, DOI: 10.1039/C5EE01687H.

[58] D. Bae, B. T. Mei, R. Frydendal, T. Pedersen, B. Seger, O. Hansen, P. C. K. Vesborg, I. Chorkendorff, *Back-illuminated Si based photoanode with nickel cobalt oxide catalytic protection layer*, J. Mater. Chem. A (submitted)

[59] J. J. H. Pijpers, M. T. Winkler, Y. Surendranath, T. Buonassisi, D. G. Nocera, *Light-induced water oxidation at silicon electrodes functionalized with a cobalt oxygen-evolving catalyst*, Proc. Natl. Acad. Sci. U. S. A., 25 (2011) 10056-10061.

[60] *B.* Seger, T. Pedersen, A. B. Laursen, P. C. K. Vesborg, O. Hansen, I. Chorkendorff, *Using TiO_2 as a conductive protective layer for photocathodic H_2 evolution*, J. Am. Chem. Soc., 135 (2013) 1057-1064.

[61] L. Vivien, L. Pavesi, *Handbook of silicon photonics*, Taylor & Francis, Boca Raton, 2013, ch. 1.3., p. 26.

[62] *The NIST reference on constants, units, and uncertainty*, http://physics.nist.gov/cgi-bin/cuu/Value?ep0 (accessed Sep. 11, 2015).

[63] M. –K. Lee, H. –C. Lee, C. –M. Hsu, *High dielectric constant titanium oxide grown on amorphous silicon by metal-organic chemical vapour deposition*, Semicond. Sci. Technol., 21 (2006) 604-607.

[64] D. E. Eastman, *Photoelectric work functions of transition, rare-earth, and noble metals*, Phys. Rev., 2 (1970) 1-2.

[65] N. Dasgupta, A. Dasgupta, *Semiconductor devices: modeling and technology*, Prentice-Hall, New Delhi, 2004, ch. 1.3.10., pp. 30.

[66] K. V. Rao and A. Smakula, *Dielectric Properties of cobalt oxide, nickel oxide, and their mixed crystals*, J. Appl. Phys., 36 (1965) 2031-2038.

[67] S. J. Musevi, A. Aslani, H. Motahari, H. Salimi, *Offer a novel method for size appraise of NiO nanoparticles by PL analysis: Synthesis by sonochemical method*, J. Saudi Chem. Soc., doi:10.1016/j.jscs.2012.06.009

[68] X. Chen, J. P. Cheng, Q. L. Shou, F. Liu, X. B. Zhang, *Effect of calcination temperature on the porous structure of cobalt oxide micro-flowers*, CrystEngComm, 14 (2012) 1271-1276.

[69] J. F. Marco, J. R. Gancedo, M. Gracia, J. L. Gautier, E. I. Ríos, H. M. Palmer, C. Greaves, F. J. Berry, *Cation distribution and magnetic structure of the ferrimagnetic spinel $NiCo_2O_4$*, J. Mater. Chem., 11 (2011) 3087-3093.

[70] C. Zhu, D. Wen, S. Leubner, M. Oschatz, W. Liu, M. Holzschuh, F. Simon, S. Kaskel, A. Eychmu, *Nickel cobalt oxide hollow nanosponges as advanced electrocatalysts for the oxygen evolution reaction*, Chem. Commun., 51 (2015) 7851-7854.

[71] H. B. Wu, H. Pang, X. W. Lou, *Facile synthesis of mesoporous $Ni_{0.3}Co_{2.7}O_4$ hierarchical structures for high-performance supercapacitors*, Energy Environ. Sci., 6 (2013) 3619-3626.

[72] G. Wu, N. Li, D.-R. Zhou, K. Mitsuo, B.-Q. Xu, *Anodically electrodeposited Co+Ni mixed oxide electrode: preparation and electrocatalytic activity for oxygen evolution in alkaline media*, J. Solid State Chem., 177 (2004) 3682-3692.

[73] P. Rasiyah, A. C. C. Tseung, *A mechanistic study of oxygen evolution on $NiCo_2O_4$*, J. Electrochem. Soc., 130 (1983) 2384-2386.

[74] D. Friebel, M. W. Louie, M. Bajdich, K. E. Sanwald, Y. Cai, A. M. Wise, M.-J. Cheng, D. Sokaras, T.-C. Weng, R. A. Mori, R. C. Davis, J. R. Bargar, J. K. Nørskov, A. Nilsson, A. T. Bell, *Identification of highly active Fe sites in (Ni,Fe)OOH for electrocatalytic water splitting*, J. Am. Chem. Soc., 137 (2015) 1305-1313.

[75] H. S. Jeon, J. H. Koh, S. J. Park, M. S. Jee, D.-H. Ko, Y. J. Hwang, B. K. Min, *A monolithic and standalone solar-fuel device having comparable efficiency to photosynthesis in nature*, J. Mater. Chem. A, 3 (2015) 5835-5842.

[76] M. S. Burke, M. G. Kast, L. Trotochaud, A. M. Smith, S. W. Boettcher, *Cobalt−iron (oxy)hydroxide oxygen evolution electrocatalysts: The role of structure and composition on activity, stability, and mechanism*, J. Am. Chem. Soc., 137 (2015) 3638-3648.

[77] F. A. Armstrong, *Dynamic electrochemistry of iron-sulfur proteins*, in: R. Cammack (Eds.), *Advances in inorganic chemistry*, Academic Press, London, 1992, p. 125.

[78] D. E. Pissinis, L. E. Sereno, J. M. Marioli, *Utilization of special potential scan programs for cyclic voltammetric development of different nickel oxide-hydroxide species on Ni based electrodes*, Open J. Phys. Chem., 2 (2012) 23-33.

[79] S. Kim, D. A. Tryk, M. R. Antonio, D. Scherson, *Applications of X-ray absorption fine structure to the in situ study of the effect of cobalt in nickel hydrous oxide electrodes for fuel cells and rechargeable batteries*, preprint of ACS symposium on recent advances in fuel cells, batteries, 1993 Fall (Chicago) 38 (4), 1457-1463.

[80] N. Wyrsch, S. Dunand, C. Ballif, *Bifacial a-Si:H solar cells: Origin of the asymmetry between front and back illumination*, Proceedings of NUMOS, 2007, 289-295.

[81] A. Kränzl, R. Kopecek, K. Peter, P. Fath, *Bifacial solar cells on multi-crystalline silicon with boron BSF and open rear contact*, Conference Record of the 2006 IEEE 4th World Conference on Photovoltaic Energy Conversion, 2006, 1, 968-971.

[82] D. L. Meier, H. P. Davis, R. A. Garcia, J. Salami, A. Rohatgi, A. Ebong, P. Doshi, *Aluminum alloy back p-n junction dendritic web silicon solar cell*, Sol. Energ. Mat. Sol. C., 65 (2001) 621-627.

[83] Panasonic headquarter news, http://panasonic.co.jp/corp/news/official.data/data.dir/2014/04/en140410-4/en140410-4.html, (accessed 10th September 2015).

[84] P. Bosshard, W. Hermann, E. Hung, R. Hunt, A. J. Simon, *An assessment of solar energy conversion technologies and research opportunities*, GCEP Energy Assessment Analysis, Stanford University, 2006.

[85] V. A Milichko, A. I. Nechaev, V. A. Valtsifer, V. N. Strelnikov, Y. N. Kulchin, V. P. Dzyuba, *Photo-induced electric polarizability of Fe_3O_4 nanoparticles in weak optical fields*, Nanoscale Res. Lett., 8 (2013) 317-323.

[86] F. Y. R. El Faituri, A. Y. Darkwi, *Computer simulation for current density in pn-Si solar cells*, Proceedings of the International Symposium on Solar Physics and Solar Eclipses, held at Waw an Namus, 2006.

[87] S.W. Boettcher, E. L. Warren, M. C. Putnam, E. A. Santori, D. Turner-Evans, M. D. Kelzenberg, M. G. Walter, J. R. McKone, B. S. Brunschwig, H. A. Atwater, N. S. Lewis, *Photoelectrochemical hydrogen evolution using Si microwire Arrays*, J. Am. Chem. Soc., 133 (2011) 1216-1219.

[88] W. R. Thurber, R. L. Mattis, Y. M. Liu, J. J. Filliben, *Resistivity-dopant density relationship for boron-doped silicon*, J. Electrochem. Soc., 127 (1980) 2291-2294.

[89] H. P. R. Frederikse, *CRC Handbook of Chemistry and physics*, ed. by D. R. Lide, 78th edition, 1997, pp 12.

[90] D. M. King, X. Du, A. S. Cavanagh, A. Weimer, *Confinement in amorphous TiO_2 films studied using atomic layer deposition*, Nanotechnology, 19 (2008) 445401-445406.

[91] J. Bisquert, A. Zaban, M. Greenshtein, I. Mora-Sero, *Determination of rate constants for charge transfer and the distribution of semiconductor and electrolyte electronic energy levels in dye-sensitized solar cells by open-circuit photovoltage decay method*, J. Am. Chem. Soc., 126 (2004) 13550-13559.

[92] T. W. Kim, K.-S. Choi, *Nanoporous $BiVO_4$ photoanodes with dual-layer oxygen evolutioncatalysts for solar water splitting*, Science, 343 (2014) 990-994.

[93] F. Feldmann, M. Simon, M. Bivour, C. Reichel, M. Hermle, and S. W. Glunz, *Carrier-selective contacts for Si solar cells*, Appl. Phys. Lett., 104 (2014) 181105.

[94] D. Garcia-Alonso, S. Smit, S. Bordihn, W. M. M Kessel, *Silicon passivation and tunneling contact formation by atomic layer deposited Al_2O_3/ZnO stacks*, Semicond. Sci. Tech., 28 (2013) 082002.

[95] A. Goodrich, P. Hacke, Q. Wang, B. Sopori, R. Margolis, T. L. James, M. Woodhouse, *A wafer-based monocrystalline silicon photovoltaics roadmap: Utilizing known technology improvement opportunities for further reductions in manufacturing costs*, Sol. Energ. Mat. Sol. C., 114 (2013) 110-135.

[96] J. Schmidt, M. Kerr, A. Cuevas, *Surface passivation of silicon solar cells using plasma-enhanced chemical-vapour-deposited SiN films and thin thermal SiO_2/plasma SiN stacks*, Semicond. Sci. Technol., 16 (2001) 164-170.

[97] Y. -S. Lin, S. –Y. Lien, C. –C. Wang, C. –H. Hsu, C. –H. Yang, A. Nautiyal, D. –S. Wuu, P. –C. Tsai, S. –J. Lee, *Optimization of recombination layer in the tunnel junction of amorphous silicon thin-film tandem solar cells*, Int. J. Photoenergy, 2011 (2011) 264709.

[98] W. Shockley, H. J. Queisser, *Detailed balance limit of efficiency of p-n junction solar cells*, *J. Appl. Phys.*, 32 (1961), 510-519.

[99] D. L. Young, W. Nemeth, S. Grover, A. Norman, B. G. Lee, P. Stradins, *Carrier-selective, passivated contacts for high efficiency silicon solar cells based on transparent conducting oxides*, Photovoltaic Specialist Conference (PVSC), 2014 IEEE 40th, 1-5.

[100] F. Feldmann, M. Simon, M. Bivour, C. Reichel, M. Hermle, S. W. Glunz, *Efficient carrier-selective p- and n-contacts for Si solar cells*, Sol. Energ. Mat. Sol. C., 131 (2014) 100-104.

[101] M. Taguchi, A. Yano, S. Tohoda, K. Matsuyama, Y. Nakamura, T. Nishiwaki, K. Fujita, E. Maruyama, *24.7% record efficiency HIT solar cell on thin silicon wafer*, IEEE J. of Photovoltaics, 4 (2014) 96-99.

[102] F. Einsele, P. J. Rostan, M. B. Schubert, U. Rau, *Recombination and resistive losses at ZnO/a-Si:H/c-Si interfaces in heterojunction back contacts for Si solar cells*, Appl. Phys. Lett., 102 (2007) 094507.

[103] D. V. Esposito, I. Levin, T. P. Moffat, A. A. Talin, *H_2 evolution at Si-based metal–insulator–semiconductor photoelectrodes enhanced by inversion channel charge collection and H spillover*, Nat. Mater., 12 (2103) 562-568.

[104] Y.-T. Cheng, J.-J. Ho, W. Lee, S.-Y. Tsai, L.-Y. Chen, J.-J. Liou, S.-H. Chang, H. Shen, K. L.Wang, *Efficiency improved by H_2 forming gas treatment for Si-based solar cell applications*, Int. J. Photoenergy, 2010 (2010) 634162.

[105] S. K. Dhunge, J. Yoo, K. Kim, B. Karunagaran, S. Hwang, D. Mangalaraj, J. Yi, *Effect of pressure on surface passivation of silicon solar cell by forming gas annealing*, Mater. Sci. Semicond. Process., 7 (2004) 427-431.

[106] H. C. Shiny, C. Hu, *Thin gate oxide damage due to plasma processing*, Semicond. Sci. Technol., 11 (1996) 463-473.

[107] J. G. Fossum, V. P. Trivedi, *Fundamentals of ultra-thin-body MOSFETs and FinFETS*, Cambridge University Press, 2013, United Kingdom.

[108] B. Van Zeghbroeck, *Principles of semiconductor devices*, web-book, University of Colorado at Boulder, 2011, http://ecee.colorado.edu/~bart/book/book/index.html (accessed Aug. 26, 2015)

[109] J. D. Benck, S. C. Lee, K. D. Fong, J. Kibsgaard, R. Sinclair, T. F. Jaramillo, *Designing active and stable silicon photocathodes for solar hydrogen production using molybdenum sulfide nanomaterials*, Adv. Energy Mater., 4 (2014) 1400739.

[110] M. J. Kenney, M. Gong, Y. Li, J. Z. Wu, J. Feng, M. Lanza, H. Dai, *High-performance silicon photoanodes passivated with ultrathin nickel films for water oxidation*, Science, 342 (2013) 836-840.

[111] K. Sarakinosa, J. Alami, S. Konstantinidis, *High power pulsed magnetron sputtering: A review on scientific and engineering state of the art*, Surf. Coat. Technol., 204 (2010) 1661–1684.

[112] J. T. Gudmundsson, N. Brenning, D. Lundin, U. Helmersson, *High power impulse magnetron sputtering discharge*, J. Vac. Sci. Technol. A, 30 (2012) 030801.

[113] A. P. Ehiasarian, R. New, W.-D. Münz, L. Hultman, U. Helmersson, V. Kouznetsov, *Influence of high power densities on the composition of pulsed magnetron plasmas*, Vacuum, 65 (2002) 147-154.

[114] A. P Ehiasarian, W.-D Münz, L Hultman, U. Helmersson, I. Petrov, *High power pulsed magnetron sputtered CrNx films*, Surf. Coat. Technol., 163-164 (2003) 267-272.

[115] A. E. Komlev, A. E. Lapshin, O. V. Magdysyuk, V. V. Plotnikov, V. I. Shapovalov, N. S. Shutova, *Effect of heat treatment on the structure of titanium dioxide films*, Tech. Phys. Lett., 36 (2010) 942-944.

[116] J. I. Langford, A. J. C. Wilson, *Scherrer after sixty years: A survey and some new results in the determination of crystallite size*, J. Appl. Cryst. 11 (1978) 102-113.

[117] Y. Han, H.-S. Kim, H. Kim, *Relationship between synthesis conditions and photocatalytic activity of nanocrystalline TiO_2*, J. Nanometer., 2012 (2012) 427453.

[118] Y.-F. Chena, C.-Y. Lee, M.-Y. Yeng, H.-T. Chiu, *The effect of calcination temperature on the crystallinity of TiO_2 nanopowders*, J. Cryst. Growth, 247 (2003) 363-370.

[119] H. Wadley, X. Zhou, and W. H. Butler, *Atomic assembly of magnetoresistive multilayers*, in: D. Depla, S. Mahieu (Eds.), *Reactive sputter deposition*, Springer, Heidelberg, 2008, pp. 498-599.

[120] D. Windover, E. Barnat, J. Y. Kim, M. Nielsen, T.-M. Lu, A. Kumar, H. Bakhru, C. Jin, S. L. Lee, *Thin film density determination by multiple radiation energy dispersive X-ray reflectivity*, JCPDS-International center of diffraction data 2000, Advances in X-ray analysis, Vol. 42.

[121] M. Alzamani, A. Shokuhfar, E. Eghdam, S. Mastali, *Influence of catalyst on structural and morphological properties of TiO_2 nanostructured films prepared by sol–gel on glass*, Prog. Nat. Sci., 23 (2013) 77-84.

[122] N. C. Lindquist, P. Nagpal, K. M. McPeak, D. J. Norris, S.-H. Oh, *Engineering metallic nanostructures for plasmonics and nanophotonics*, Rep. Prog. Phys. 75 (2012) 036501

[123] G. L. Hornyak, H. F. Tibbals, J. Dutta, J. J. Moore, *Introduction to nanoscience & nanotechnology*, CRC Press, Newark, 2008

[124] H.-C. Chen, K.-S. Lee, C.-C. Lee, *Annealing dependence of residual stress and optical properties of TiO_2 thin films deposited by different deposition methods*, Appl. Opt., 47 (2008) 284-287.

[125] Y. Chen, D. D. Dionysiou, *Effect of calcination temperature on the photocatalytic activity and adhesion of TiO_2 films prepared by the P-25 powder-modified sol-gel method*, J. Mol. Catal. A: Chem., 244 (2006) 73-82.

[126] Y. Hou, B. L. Abrams, P. C. K. Vesborg, M. E. Björketun, K. Herbst, L. Bech, A. M. Setti, C. D. Damsgaard, T. Pedersen, O. Hansen, J. Rossmeisl, S. Dahl, J. K. Nørskov, I. Chorkendorff, *Bio-inspired co-catalysts bonded to a Silicon photocathode for solar hydrogen evolution*, Nat. Mater., 10 (2011) 434-438.

[127] G. Coletti, P. C. P. Bronsveld, G. Hahn, W. Warta, D. Macdonald, B. Ceccaroli, K. Wambach, N. L. Quang, J. M. Fernandez, *Impact of metal contamination in silicon solar cells*, Adv. Funct. Mater., 21 (2011) 879–890.

[128] B. Sopori, *Impurities and defects in photovoltaic Si devices: A review*, NREL report, NREL/CP-520-27524, 1999.

Appendix A

Properties of semiconductors used for theoretical studies in this work

Parameter	Definition	Value
$N_{A,\ p\text{-}Si}$	Acceptor density of p-Si	$3 \cdot 10^{15}$ cm^{-3} [A]
$N_{C,\ Si}$	Density of states of Si in conduction band	$2.8 \cdot 10^{15}$ cm^{-3} [61]
$N_{V,\ Si}$	Density of states of Si in valence band	$1.8 \cdot 10^{19}$ cm^{-3} [61]
$N_{D,\ n\text{-}Si}$	Donor density of n^+-Si	$5 \cdot 10^{19}$ cm^{-3} [B]
$N_{A,\ p+\text{-}Si}$	Acceptor density of p^+-Si	$1 \cdot 10^{20}$ cm^{-3} [B]
$N_{C,TiO2}$	Density of states of TiO_2 in conduction band	$6.8 \cdot 10^{20}$ cm^{-3} [91]
$N_{D,TiO2}$	Donor density of TiO_2	$4.5 \cdot 10^{19}$ cm^{-3} [C]
$N_{A,NiCoOx}$	Acceptor density of $NiCoO_x$	$3.1 \cdot 10^{18}$ cm^{-3} [D]
χ_{Si}	Electron affinity of Si	4.15 V [62]
Φ_{Ti}	Work function of Ti	4.33 [89]
Φ_{Co}	Work function of Co	5.0 [64]
$\Phi_{m,n+Si}$	Work function of n^+-Si	4.15 V [108]
$\Phi_{m,p+Si}$	Work function of p^+-Si	5.27 V [108]
ε_o	Permittivity in vacuum	$8.85 \cdot 10^{-12}$ F m^{-1} [62]
ε_{si}	Relative permittivity of Si	11.7 [97]
ε_{TiO2}	Relative permittivity of TiO_2	75 [90]
ε_{NiCoOx}	Relative permittivity of $NiCoO_x$	12.3 [66]
ε_{SiO2}	Permittivity of SiO2	$3.45 \cdot 10^{-13}$ F m^{-1} [107]
m_h	Effective hole mass of NiO	0.75 [67]
n_i	Intrinsic carrier density of Si	$1.33 \cdot 10^{10}$ cm^{-3} [107]

[A] Provided by supplier (Topsil)
[B] Calculated using a process simulation program (Athena, SILVACO).
[C] Taken from the experimental Mott-Shottky analysis of TiO_2
[D] Taken from the experimental Mott-Shottky analysis of $NiCoO_x$

Appendix B

Acronyms

AM 1.5G	Air mass 1.5 global tilt
MTOE	Million tonnes of oil equivalent
R/P ratio	Reserves-to-production ratio
TW	Terawatt
TWh	Terawatt-hour
PV	Photovoltaic
PEC	Photoelectrochemical
STH%	Solar-to-hydrogen efficiency
RE	Reference electrode
CE	Counter electrode
WE	Working electrode
CV	Cyclic voltammetry
CA	Chronoamperometry
RHE	Reversible hydrogen electrode
IPCE	Incident photon to current efficiency
APCE	Absorbed photon to current efficiency
EC	Electrochemical
EQCM	Electrochemical quartz crystal microbalance
GC	Gas chromatography
XRD	X-ray diffraction
XPS	X-ray photoelectron spectroscopy
XRR	X-ray reflectometry
SEM	scanning electron microscope
EDS (or EDX)	Energy-dispersive X-ray spectroscopy
UV-Vis	Ultraviolet-visible spectroscopy
OER	Oxygen evolution reaction
HER	Hydrogen evolution reaction
MOS	Metal-Oxide-Semiconductor
DCMS	Direct current magnetron sputtering
HiPIMS	High power impulse magnetron sputtering
ALD	Atomic layer deposition

Appendix C

Appended publications

Energy & Environmental Science

PAPER

View Article Online
View Journal

Cite this: DOI: 10.1039/c4ee03723e

Back-illuminated Si photocathode: a combined experimental and theoretical study for photocatalytic hydrogen evolution†

Dowon Bae,[a] Thomas Pedersen,[b] Brian Seger,[a] Mauro Malizia,[a] Andrej Kuznetsov,[c] Ole Hansen,[b] Ib Chorkendorff[a] and Peter C. K. Vesborg*[a]

Received 26th November 2014
Accepted 11th December 2014

DOI: 10.1039/c4ee03723e

www.rsc.org/ees

Si is an excellent absorber material for use in 2-photon photoelectrochemical hydrogen production. So far nearly all studies of silicon photoelectrodes have employed frontal illumination despite the fact that in most water-splitting 2-photon device concepts the silicon is the "bottom" cell in the tandem stack and therefore illuminated from the back with respect to the electrolyte. In the present work, we investigate back-illuminated Si photoelectrodes experimentally, as well as by modelling, the dependence of induced photocurrent on various parameters, such as carrier diffusion length (L_e) and surface recombination velocity (v_s) to quantify their relative importance. A bifacial light absorbing structure (p^+pn^+ Si) is tested under back-illumination conditions which mimic the actual working environment in a tandem water splitting device. The thickness of the absorbing Si layer is varied from 30 to 350 μm to assess the impact of the diffusion length/thickness ratio (L_e/L) on photocatalytic performance. It is shown how the induced photocurrent (J_L) of a back-illuminated sample increases as wafer thickness decreases. Compared to the 350 μm thick sample, a thinned 50 μm thick sample shows a 2.7-fold increase in J_L, and consequently also a higher open circuit voltage. An analytical model is developed to quantify how the relative L_e/L-ratio affects the maximum J_L under back-illumination, and the result agrees well with experimental results. J_L increases with the L_e/L-ratio only up to a certain point, beyond which the surface recombination velocity becomes the dominant loss mechanism. This implies that further efforts should to be focused on reduction of surface recombination. The present study is the first experimental demonstration of a Si wafer based photocathode under back-illumination. Moreover, the comparative experimental and theoretical treatment also highlights which photoabsorber properties merit the most attention in the further development towards full tandem water splitting devices.

1. Introduction

The development of semiconductor photocatalytic water splitting devices has attracted recent interest[1–5] because the direct conversion of solar energy into hydrogen is an attractive route to produce a clean chemical fuel.[2,6,7]

In order to be competitive with fossil fuels, artificial photosynthesis must be efficient and cheap. The overall process consists of two parts: (i) light absorption resulting in charge carrier generation and (ii) the utilization of excited photo carriers to drive catalytic reactions at the surface. It is thus essential to harvest a large fraction of the solar spectrum while ensuring efficient charge separation. Dual-absorber systems (sometimes called Z-scheme[8]), represent an efficient way to achieve wide spectral coverage using two semiconductors of different band gaps (E_g) as shown in Fig. 1. Effectively, the dual-absorber system works by series-connecting the high bandgap- and low bandgap-cells enabling a higher total voltage at the expense of current density.

In the case where silicon is used as the low-gap absorber (and as a photocathode in a dual-absorber arrangement) the flat-band potential of p-type silicon places severe restrictions on the voltage in an aqueous electrolyte.[9] However, by replacing the semiconductor–liquid junction with a pn^+-junction at the surface the flat-band limitation is mitigated. Such pn^+-Si electrodes have shown efficient electron–hole pair separation and increased open circuit voltage along with a higher current density[3,4,10,11] compared to p-Si electrodes.[9,12] In our previous

[a]Center for Individual Nanoparticle Functionality, Department of Physics, Technical University of Denmark, 2800 Kgs. Lyngby, Denmark. E-mail: Peter.Vesborg@fysik.dtu.dk; Fax: +45 4593 2399; Tel: +45 4525 3276

[b]Department of Micro- and Nanotechnology, Technical University of Denmark, 2800 Kgs. Lyngby, Denmark

[c]Centre for Materials Science and Nanotechnology, Department of Physics, University of Oslo, 0316 Oslo, Norway

† Electronic supplementary information (ESI) available: Supplementary information accompanies this paper including supplementary Fig. S1–S8; mathematical derivation procedure for analytical modelling; detail sample fabrication and equipment information for the experiments. See DOI: 10.1039/c4ee03723e

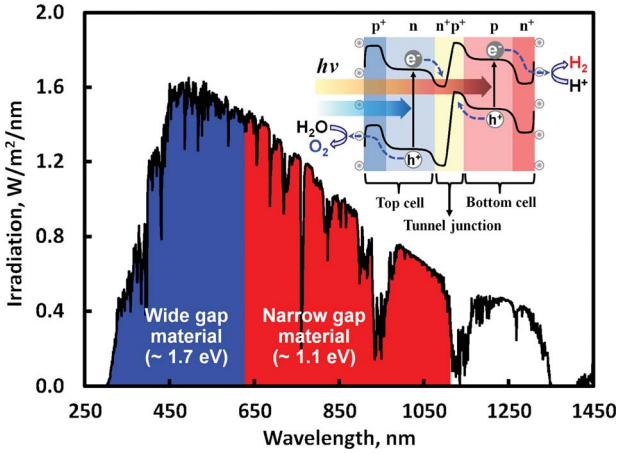

Fig. 1 Solar spectrum (AM 1.5G) coverage by dual absorbers based on a Z-scheme, and schematic of a device in a tandem design composed of dual pn-junctions, co-catalysts for oxygen and hydrogen evolution and recombination layer (tunnel junction) (inset). The top cell is formed in a wide band gap material and bottom cell in a narrow band gap material. The inset of this figure illustrates the carrier transfer along the band alignment under incident light. The short wavelength part of the light spectrum is absorbed by the top cell to oxidize water, while the longer wavelengths are absorbed by the bottom cell to produce H_2 gas.

work[10,11] it was found that pn^+-Si photocathodes with TiO_2 as a protection layer showed an open circuit voltage (V_{oc}) $\geq$ 0.5 V for the Hydrogen Evolution Reaction (HER). These electrodes also showed a maximum photocurrent (J_L) of 23 mA cm^{-2} under frontal illumination using the red spectrum shown in Fig. 1. This non-standard "red light only" illumination serves to simulate a real dual-absorber system where the blue light has been absorbed by the overlying (top) photoelectrode. In that case, 23 mA cm^{-2} corresponds to an Incident Photon to Current Efficiency (IPCE) of nearly 90%, while p-Si photocathodes (without the n^+ layer, but otherwise similar) showed V_{oc} of just 0.05 V with J_L of 17 mA cm^{-2} (IPCE of 61%).[9]

To date, various dual absorber water splitting devices have been demonstrated experimentally such as pn-$GaInP_2$/pn-GaAs,[13] pnp-$GaInP_2$/pn-GaAs.[14] These high-efficiency devices, however, are currently too expensive for large-scale applications. It seems that these materials also have severe scalability issues because Ga and In are elements which are by-products (of aluminum and zinc, respectively) and ultimately price-inelastic.[15] Various approaches have been demonstrated to substitute these high-cost materials with earth-abundant materials. A Si photocathode coupled to a metal oxide photoanode is one example.[16–18] However, the modest photocurrent density level of such structures ($J_{L,max} \approx$ 0.4 mA cm^{-2})[17] result in a low efficiency for water splitting. Nevertheless, progress is being made using oxides of lower band gap. A respectable state-of-the-art 3.6% solar-to-hydrogen (STH) efficiency tandem water splitting device based on a doped $BiVO_4$ photoanode in combination with single junction a-Si solar cell was recently demonstrated.[19] Despite recent progress,[3,20] developing a relatively simple dual absorber tandem structure is still an unsolved engineering challenge.

Using silicon as the bottom cell (*i.e.* under back-illumination – where light is incident from the "dry" side of the photoelectrode), a series of experiments showed that the photocurrent of a Si bottom cell was limited. The reason is that under back-illumination the electrode–electrolyte interface, which is the electron drain, is on the opposite side with respect to the incident light and since the wafer thickness is larger than the carrier diffusion length most electrons are lost to recombination near the back surface.[21,22] This problem of opposed light absorption and electrochemistry under back-illumination thus dictates a different approach to maximize the charge carrier utilization.

In this work we evaluate the experimental and theoretical maximum photocurrent ($J_{L,max}$) limit from the Si based photoelectrochemistry (PEC) system for hydrogen production under the back side illumination. The main focus is on maximum charge utilization of the Si photocathode under the assumption that it is used as a bottom cell in a tandem water splitting device. First we conducted experiments by using Czochralski (CZ) Si based cells with a pn-junction at the electrode/electrolyte interface side (type I configuration,[23] see Fig. S1a in ESI†), but varying the thickness to quantify the effect of the L_e/L-ratio on current–voltage (J–V) performance. We employed a light-permeable Al/p^+ charge collection backside layer, which allows illumination from the side opposing the solid/liquid interface while minimizing series resistance. A "buried junction" design (type II configuration,[23] see Fig. S1b in ESI†), whose pn^+-junction is on the illuminated side, can collect charge more efficiently. But the buried junction design requires a very highly doped layer (p^+) near the electrode–electrolyte interface to form an ultrathin space-charge region which allows electron tunnelling through the interface from the n-type bulk silicon to the electrocatalyst. Without such a layer the charge separation becomes very inefficient.[24] A key benefit of the type I structure is its ability to reduce the recombination loss of charge carriers by moving the pn-junction to opposite side with respect to the incident light since the presence of dopants increase local bulk recombination which can lead to reduced voltage loss.[25,26] Many state-of-art photovoltaic (PV) devices employ the same principle to enhance the blue-light response of the cells.[26,27] In addition, a shallow doped pn^+-junction formed at electrode–electrolyte interface provides band bending in the silicon independent of the electrolyte. On the other hand – moving the pn junction to the shadow-side of the device requires excellent surface passivation of the light incident side, as we shall see. Most devices in the literature are of a type I configuration, whereas a type II configuration has been demonstrated successfully by using multi-junction III–V [13-14] and by using a-Si PV devices.[19] In addition, we discuss a simplified model of the Si-based cell with the same cross-sectional structure as the aforementioned cell for the experiments to guide the choice of substrate properties: Surface recombination velocity (v_s), diffusion length (L_e) and thickness (L); for HER at maximum current density. The theoretical charge generation and collection models for the analytical calculation are discussed for this case, and finally, we compared the experimental results with the model-based calculation results verify the validity of the model.

2. Methods

2.1. Sample fabrication

CZ-Si based photocathodes of type I are fabricated with different wafer thickness in order to vary the L_e/L ratio (L = 30–350 μm) on otherwise similar electrodes. The thickness of the Si was varied by sample thinning (using photolithography and wet etching) of p-type Si substrates. Schematic drawings of samples used in this work are shown in Fig. 2 and S2a in ESI.† The shallow pn^+-junction was produced in p-type (100) Si wafers (Topsil, 1–20 ohm cm, boron-doped, acceptor density $N_A \approx 5 \times 10^{19}$ cm^{-3}) by thin n^+ doping using phosphorous ion implantation at 36 keV with a dose of 3×10^{15} cm^{-2} (donor density N_D of approximately 1×10^{20} cm^{-3}), which is expected to form a depletion width of 640 nm (described in detail in ESI†). As shown in our previous work,[10] this n^+ doping screens the band-bending in the silicon from the electrolyte, which allows for increased photovoltage.[3] As shown in Fig. 2c, the electron–hole pairs are separated by a built-in electric field which the pn^+ junction provides. The electrons are then transferred to the solid/liquid interface though the conduction band of TiO_2 using Mott-Schottky analysis (detail calculations are shown in ESI†). A mesa-isolated pn^+-Si structure with height of 3 μm is formed at the front side by photolithography and dry etching (Here, we used SF_6, O_2 and C_4F_8 gases in a Pegasus DRIE system from SPTS Technologies). The back side of the same samples were also doped with a thin p^+ doping using ion implantation of boron at 100 keV with a dose of 5×10^{16} cm^{-2} ($N_A \approx 1 \times 10^{20}$ cm^{-3}). A metallic charge collecting layer was deposited at room temperature by e-beam evaporation of Al. The Al layer was masked to create a circular hole over the active area in order to allow light transmission to the silicon. The resulting active area was precisely measured by image analysis using ImageJ 1.46r after the experiments. The p^+ doped layer in this device reduces overall series resistance by providing parallel path ways for holes to reach the Al charge collecting layer. Furthermore in actual tandem device operation condition it can also act as a part of the recombination layer (tunnel junction) for the injected holes from photocathode and the electrons from photoanode. Consequentially, the sample can be stated as a 'ready-made bottom cell' for tandem water splitting devices. Samples prepared without the p^+ doped layer are used to quantify the importance of the p^+ sheet-conducting layer (Fig. S5 in ESI†). In order to prevent the Si surface from photo-corrosion during the photo-electrochemical measurements, a Ti/TiO_2 (5/100 nm) protection layer was sputtered on the n^+ doped side (electrolyte side) of samples using previously published methods.[10,28] In case of TiO_2, Ti was reactively sputtered in an oxygen background. Prior to sputter deposition all wafers were dipped in buffered HF for 30 s, rinsed in Millipore water, dried and were then immediately placed in the sputter chamber to prevent the Si surface from deactivation by native oxide formation. All samples were cleaned with "piranha" solution (3 : 1 H_2SO_4 (96%) : H_2O_2 (30%)), washed with ultrapure water (18 MΩ cm) and dried before having 250 ng (Pt basis) of a dinitrosulphatoplatinate solution (Johnson Matthey) drop-cast on them. Pt was used as a co-catalyst in order to achieve high catalytic activity for HER. The thickness of the wafers was controlled using photolithographically thinned p-type Si substrates to keep the L_e value the same for all samples. Finally, they were coated with Teflon tape with a hole punched out yielding an active area of approximately 0.2 cm^2. This number was also precisely measured by optical image analysis after the experiments. In addition, the back side of the samples was covered with 50 μm thick quartz glass to protect back side from direct contact with the electrolyte. The quartz glass was mounted directly onto the Al layer using epoxy.

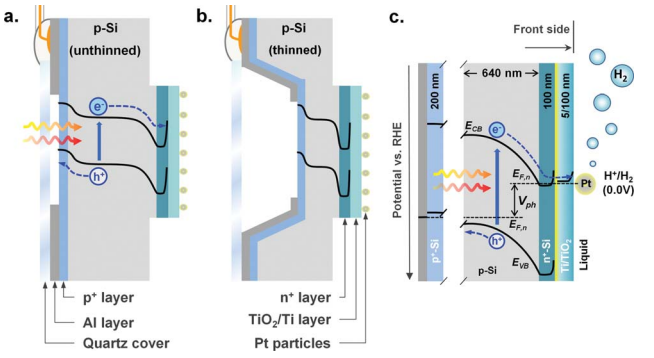

Fig. 2 Schematic cross section of the unthinned (a) and thinned device (b) used for photocatalytic activity (HER) experiments. The light is incident from the back side and HER occurs on the front side. In real device testing the back side of sample was protected by Quartz glass cover with epoxy to prevent corrosion in acidic electrolyte of the Cu-wire for electrical connection (covered with glue). Schematic energy diagram (c) of the illuminated sample in equilibrium with H^+/H_2 reaction is also shown. Detail calculation of energy diagram can be found in ESI (also in Fig. S3).†

2.2. Characterization

A 1000 W xenon lamp (Oriel) was used with a 635 nm cut-off filter and an AM 1.5 filter to simulate the red part of the solar spectrum. The light intensity reaching the sample was measured *via* a spectrophotometer (International Light Technologies Inc, RPS 900-R), and the light intensity was adjusted to match that of the total light intensity of red light in the AM 1.5G solar spectrum (λ > 635 nm, 41.8 mW cm^{-2}). For electrochemical measurements a Bio-Logic VSP potentiostat was used using EC Lab software. All cyclic voltammetry (CV) experiments were done in a 3 electrode H-cell design with an aqueous 1 M $HClO_4$ (Aldrich 99.99%) electrolyte. For all CV's the electrodes were scanned at a sweep rate of 10 mV s^{-1}. A Pt mesh was used as a counter electrode and the reference was a saturated $Hg/HgSO_4$ electrode (VWR International). The solution was purged with H_2 gas 30 minutes prior to any experiment and during the entire duration of the experiment. To determine efficiency as a function of wavelength, incident photon to current efficiency (IPCE) measurements were employed. An Oriel 74100 monochromator was combined with the Xenon lamp mentioned above to give monochromatic light. IPCE measurements were carried out from 500 to 900 nm for a thinned sample with a thickness of 50 μm under both front side and back side

illumination. Wavelengths below 500 nm are irrelevant in this (bottom cell) study and excluded using a filter. In order to determine the photocurrent, the electrodes were tested at 0.0 V *vs.* RHE using the same set-up and conditions as the CV measurements. The evolved H_2 was detected by gas chromatography (GC; Hewlett Packard 5890 Series II with a thermal conductivity detector, Ar carrier gas), and this is described in detail in ESI.†

2.3. Analytical model calculation

The generation rate is the number of electron–hole pairs generated at each point in the device due to the absorption of photons.[29,30] Neglecting reflection, the amount of incident light which is absorbed by a material depends on the absorption coefficient $\alpha = \alpha(\lambda)$ (unit cm^{-1}) and the thickness of the absorber. Assuming that the absorption of photons directly causes the generation of an electron–hole pair, the spectral generation rate, G, in a thin slice of absorber is determined by finding the change in light intensity across this thin slice, and consequently the electron–hole generation rate at any point in the device can be defined as follows:

$$G = \alpha H_0 e^{-\alpha z} \quad (1)$$

where H_0 is spectral photon flux density at the surface (photons per s per unit-area per wavelength increment), and z is distance into the absorber. The overall amount of generated charge at a certain depth is described in theoretical study section (Section 3.2). The spectral photon flux density H_0 can be calculated from measured irradiance $P(\lambda)$ of the solar simulator as the ratio of irradiance to photon energy using the equation shown below:

$$H_0 = \frac{\lambda P(\lambda)}{hc} \quad (2)$$

where λ is wavelength, c is the speed of light in vacuum, and h is Plank's constant. In the case where the surface is not perfectly non-reflecting, the irradiance is corrected by measured reflectivity at each wavelength (Fig. S8 in ESI†). The charge collection probability as a function of depth, $C_P(z)$, was calculated under the assumption that there is no excess electron density at the junction boundary (*i.e.* $n_e = 0$) while at $z = 0$ the surface recombination velocity requires $dn_e/dz = Sn_e$, where $S = v_s/D$ is the normalized surface recombination velocity, and v_s is the surface recombination velocity and D is diffusivity of Si. The excess electron density in steady state is governed by the steady state continuity equation:

$$\frac{d^2 n_e}{dz^2} = \frac{n_e}{{L_e}^2} \quad (3)$$

where $L_e = (D\tau_e)^{1/2}$ is the minority carrier diffusion length, and τ_e is carrier lifetime. The collection probability $C_P(z)$ is the probability that an electron–hole pair generated at a certain depth, z, will be collected (separated) by the pn-junction and consequently contribute to the photocurrent. The behavior of $C_P(z)$ and accompanying photo generated current densities J_L will be discussed later in theoretical study section, and details of the mathematical derivation can be found in the ESI.†

3. Results and discussion

3.1. Experimental study

Since we wish to illuminate from the back, a shallow boron doped p^+ layer, which is formed between the Al back current collector and the p-Si substrate, is used as a hole transport layer. The (control) sample without p^+ doped layer has a very low J_L at 0 V *vs.* RHE due to a high series resistance (Fig. S6 in ESI†). Furthermore, this p^+ doped layer works as a part of tunnel junction in practical tandem device. This structure makes the overall series resistance of the device comparable to a conventional Si device with direct back contact, and It was estimated that a doping concentration of 10^{20} cm^{-3} (5×10^{16} at per cm^2 implanted at 100 keV) of boron could provide a sufficiently low sheet resistance to the Si surface,[31] and consequently an efficient carrier transport pathway. Thus, a boron doped p^+ transport layer made by ion implantation method was used in the rest of samples in this study (device structure: p^+pn^+-Si). The photoelectrochemical properties of the p^+pn^+-Si photocathodes with different thicknesses (L = 350, 50 and 30 μm) were compared by measuring cyclic voltammetry. H_2 could be visually observed bubbling off from the semiconductor/liquid interface as the current increased, and it was confirmed by GC measurement that hydrogen is produced with high Faradaic efficiency (Fig. S9 in ESI†). As shown in Fig. 3 the fill-factor and photocurrent of 350 μm thick p^+pn^+-Si under front illumination (black dot) was considerably enhanced compared to that of the

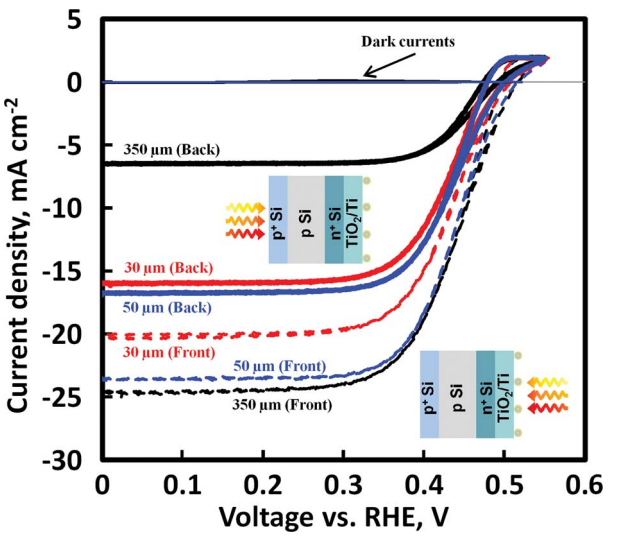

Fig. 3 CVs of Si photocathodes with unthinned design (black solid), *b* with 50 μm thick active area (blue solid) and 30 μm thick active area (red solid) under back-illumination, and under front-illumination (dotted lines). The total irradiance is 41.8 mW cm^{-2} (the light spectrum used in this figure can be found in Fig. 6). Assuming that L_e of all samples is same, this shows how L_e/L affects J_L of the device. The comparative study between back and front illumination indicates that the thinner the Si absorber is, the larger the ratio of J_L under back and front illumination is. However the $J_{L,max}$ of 30 μm thick sample with thinned design (red solid) is outperformed by the 50 μm thick sample indicating that absorption losses start to dominate the charge collection losses at around 50 μm thickness.

pn$^+$-Si in Fig. S6.† This demonstrates that adding the p$^+$ transport layer between the Al charge collector and p-Si significantly reduces the series resistance of the device. Under back-illumination the 350 μm thick p$^+$pn$^+$-Si sample showed a J_L of 6.2 mA cm^{-2}. This is significantly less current than the same sample generates under front-illumination. With the thinned design (Fig. 2b) a 50 μm Si slab increased the J_L to 17 mA cm^{-2} under back-illumination at the same light intensity. Since the only change between these samples is thickness, L, this can be considered a result of L_e/L ratio on overall charge to current conversion efficiency. As the *b* sample was thinned from its back side from 350 to 50 μm the L_e/L ratio should be seven fold larger. Since the diffusion length is the average distance that the excess carriers can cover before they recombine, increased L_e/L ratio should lead to improved J_L. Furthermore, V_{oc} of the thinned p$^+$pn$^+$-Si samples shifted slightly cathodic with increased J_L, and their slope improved under the back side illumination. This is likely due to the increased concentration of excited charge carriers. Indeed, the light induced open circuit voltage is given by the equation:

$$V_{oc} = \frac{nkT}{q}\ln\left(\frac{J_L}{J_0}+1\right) \quad (4)$$

where n is ideality factor of device, T is operating temperature, k is Boltzmann's constant, q is the electronic charge and J_0 is dark saturation current. Under the assumption that all samples have similar dark current and ideality factor, increased J_L leads to higher V_{oc}. In contrast, comparing unthinned sample with the thinned design (Fig. 2b) under front-illumination shows that thinning results in a lower J_L. The reason is that charge generation on average occurs closer to the pn-junction under front-illumination. As a result of the lower photocurrent density the V_{oc} is slightly lower under back-illumination than under front-illumination. This is probably due to a higher effective recombination velocity at the highly doped p$^+$ side than at the pn$^+$-side of the device.[32] Note also that the 30 μm thick Si sample with thinned design showed slightly lower current density (16.5 mA cm^{-2}) under back-illumination compared to the otherwise similar 50 μm thick sample even though it has a higher L_e/L ratio. This indicates a thickness of 30 μm is already below the critical thickness where the J_L starts to decrease (*i.e.* loss of photon absorption outweighs gain in $C_P(z)$).

Our spectrally resolved IPCE measurement results agree with this explanation. As shown in Fig. 4, the IPCE of a sample with thinned design increases gradually with wavelength under back-illumination, whereas it decreases gradually under the front-illumination. The absorption length δ_p is the distance into a material at which the light intensity drops by a factor of $1/e$ of its original intensity (*i.e.* the effective light penetration depth). Converting wavelength to δ_p in Si allows experimental estimation of $C_P(z)$ under the assumption of similar charge transfer and diffusion efficiency. As shown in the inset of Fig. 4, the IPCE was over 90% under front-illumination for photons, which are absorbed near the front side of the sample. Conversely, the same sample showed only approximately 50% IPCE under back-illumination. This shows that the pn$^+$-junction region separates charges better than the p$^+$p-region. The IPCE under back-illumination increases slowly from the short wavelength region and reaches a maximum at a wavelength near 900 nm. This behavior can be explained as follows: Photons with longer wavelengths penetrate deeper into the silicon. So under back-illumination electron–hole pairs generated from longer wavelength photons are therefore generated closer to the pn$^+$-junction boundary, whereas front illuminated case the photoabsorption depth as a function of wavelength is inverted, thus the IPCE shows the opposite behavior. This also can be supported by decrease of IPCE of thick samples under back illumination while IPCE under illumination from front side was almost invariable (Fig. S9 in ESI†).

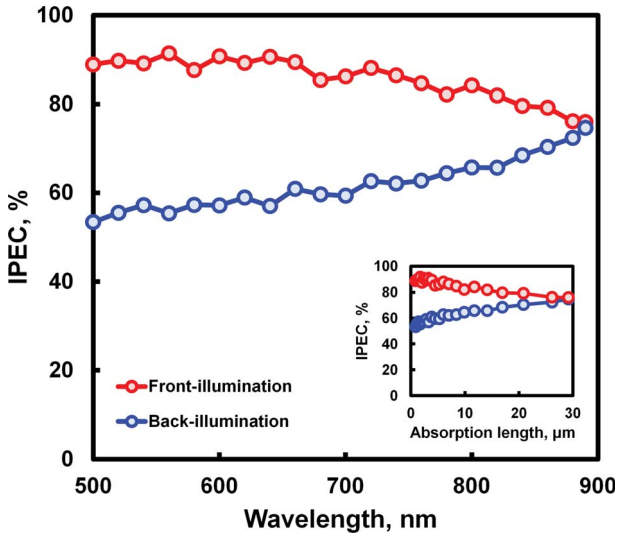

Fig. 4 IPCE measurement results under front and back-illumination using 50 μm thick thinned Si sample, and the inset is IPCE curve *versus* light absorption length (data is shown in Fig. S9 in ESI†) in Si.

Since the sample used for this IPCE measurement has a 50 μm thick Si slab, the IPCE response under both back and front illumination almost converge for wavelengths close to 900 nm.

3.2. Theoretical study

3.2.1. Ideal current density *vs.* effective thickness. Crystalline silicon has an indirect band gap (1.12 eV) and must therefore be thicker than most direct band gap light absorbers in order to have substantial optical absorption and electron–hole pair generation.[33] Fig. 5 shows, as an inset, the available photons *versus* wavelength in the reference solar spectrum (AM 1.5G).[34] The figure also shows the (red filtered) simulated solar spectrum used in this work where a Xe-lamp illumination is filtered using AM 1.5 and 635 nm-cut-off filters (*i.e.* $\lambda > 635$ nm to approximate the wavelengths and intensity would be received in a real tandem device).

The irradiance of solar light can be converted into a photogenerated electron–hole density (mA cm^{-2}) per unit wavelength for a Si-slab device of finite thickness. The resulting (integrated) current density is shown in Fig. 5 for both the AM 1.5G reference and for our simulated solar spectrum. If Si were to exhibit ideal

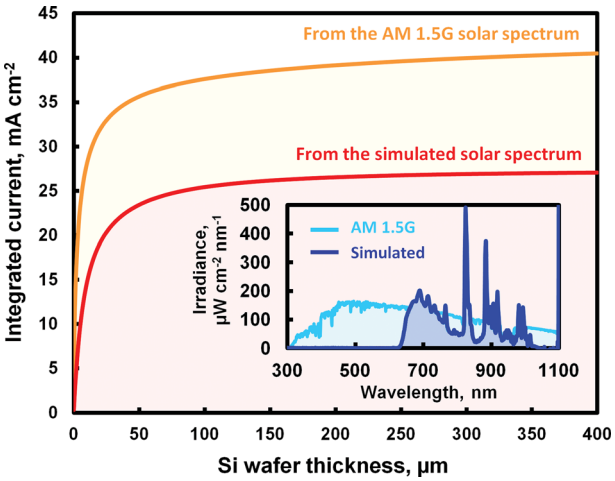

Fig. 5 Theoretical light-induced maximum current density in term of Si wafer thickness and the light spectrum of AM 1.5G and solar simulator with AM 1.5 and 635 nm-cut-off filters as an inset. The total irradiance of the simulated solar spectrum is 41.8 mW cm^{-2}, and for the standard AM 1.5G spectrum – 85.1 mW cm^{-2} with range from 250 to 1100 nm in wavelength.

behaviour of 100% internal quantum efficiency, *i.e.* zero recombination and infinite diffusion length, this electron–hole density ($J_{theo,max}$) would correspond to the measured photocurrent density. In the calculation of $J_{theo,max}$ the surface reflectance has been set to zero. The effect of surface reflectance will be addressed in detail later in this section. The current density due to photons which are absorbed during a single pass through the Si wafer with a certain thickness x can be theoretically calculated as follows:

$$J_{L,x} = \int_{\lambda_{min}}^{\lambda_g} q\frac{\lambda P(\lambda)}{hc}a(\lambda)\mathrm{d}\lambda \quad (5)$$

The integration limits are λ_g (the absorption edge of material), and λ_{min} (the shortest wavelength of the light) taken as 1100 nm and 250 nm in this work. The total irradiance of the (red filtered) simulated solar spectrum measured in this range was 41.8 mW cm^{-2}, which corresponds to the total light intensity of the standard AM 1.5G spectrum with range from 635 nm to 1100 nm. $a(\lambda)$ is the absorbance of the Si slab with a certain thickness, and can be approximated by Beer–Lambert law[35] (assuming that light only passes once through the cell and all light generated carriers are collected):

$$a(\lambda) = \frac{\alpha(\lambda)}{\ln 10}L \quad (6)$$

where L is Si thickness, and n is the index of refraction of the Si slab. The absorption coefficient $\alpha(\lambda)$ as a function of wavelength used in this work can be found in Fig. S7 in ESI.†

The absorbed light flux depends on the absorption length of the light in the silicon. As shown in Fig. 5, approximately 40 and 27 mA cm^{-2} of current density can be harvested in an ideal Si photoabsorber (if the Si is sufficiently thick), from AM 1.5G and (red filtered) simulated solar spectrum respectively. This figure also indicates that the integrated current density begins to saturate at thicknesses around 50 μm Si with a current density level of approximately 35.7 mA cm^{-2} and 23.5 mA cm^{-2}, under AM 1.5G and (red filtered) simulated solar spectrum respectively. This reveals that there is no need for using a thick wafer. In fact, a silicon back-electrode of just 15–25 μm thickness would be able to current match a 10 mA cm^{-2} – or even 15 mA cm^{-2} top electrode in a tandem device. However, as we shall see below, introduction of realistic losses recommends a somewhat thicker silicon absorber.

3.2.2. Charge collection model in a real Si device. In real Si devices finite charge recombination and charge diffusion lengths are major limiting factors reducing $J_{L,max}$. It is important to note that neither front nor back surface treatment for light trapping are used in experiments. Therefore we introduce the non-light trapping charge generation rate ($G(z)$), and the charge collection probability ($C_P(z)$) to quantify $J_{L,max}$ in real devices. We have introduced a simplified device model (Fig. 6) based on Si with a shallow pn^+-junction at the electrode–electrolyte interface. Schematic curves of $C_P(z)$ and $G(z)$ are shown in Fig. 7 to illustrate the principle. $C_P(z)$ depends on the distance that a light-generated carrier must travel compared to the diffusion length, L_e, and also on the surface properties of the device. If the carrier is generated further away from the junction than a diffusion length, ($z > L_e$), then the collection probability of this carrier is quite low. Similarly, if the carrier is generated closer to a region with high recombination (*e.g.* a non-passivated surface) than the junction, the carrier will recombine. Under, broad-band illumination most of the absorption (and electron–hole generation) takes place very close to the incident light surface (Fig. 6). Further absorption of low energy photons takes place throughout the bulk of the silicon, but the excitation density is small. However, the charge collection probability is highest near the pn^+-junction – *i.e.* the back side with respect to illumination. The dilemma is illustrated in Fig. 6.

The rate of light-generated carriers, G, as a function of depth z in Si can be theoretically calculated:

$$G(z) = \int_{\lambda_{min}}^{\lambda_g} \alpha(\lambda)H_0(\lambda)e^{(-\alpha(\lambda)z)}\mathrm{d}\lambda \quad (7)$$

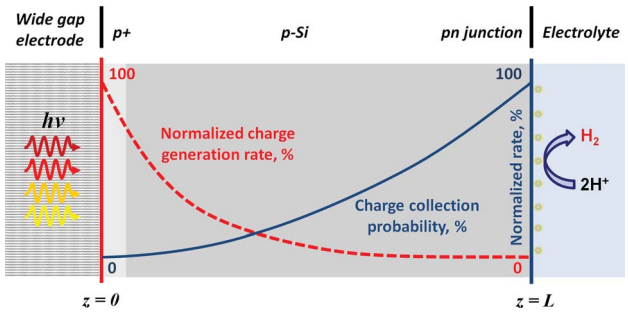

Fig. 6 Schematic of the simplified back-illuminated model device which is used in theoretical modelling. The normalized charge generation and charge collection probabilities in the device are also illustrated (not to scale) as a function of depth (z) inside the absorber with thickness L. It was assumed that optical properties of Si are homogeneous regardless of doping type.

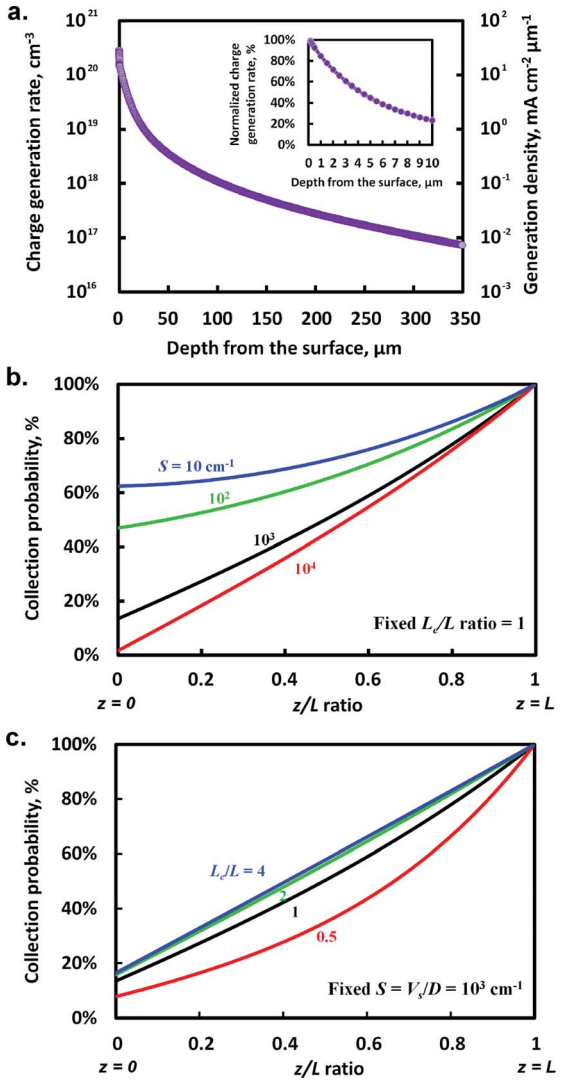

Fig. 7 Calculated charge generation induced by the light from the (red) simulated solar spectrum shown in Fig. 2a, calculated collection efficiency with various $S = V_s/D$ (b) and L_e/L (c) ratio. The normalized charge generation rate is ratio of charge generation rate to that at the surface ($z = 0$), where the value shows its maximum.

Fig. 8a shows behavior of $G(z)$ in terms of the depth from the light incident surface. An interesting point from Fig. 8a is that $G(z)$ drops below 50% of its initial value (*i.e.* at $z = 0$) just 5 μm from the surface. In fact, charge generation is almost zero at the junction boundary. This underscores the importance of charge collection probability ($C_P(z)$) since only collected charge become external photocurrent. The $C_P(z)$ as a function of depth, z, can be calculated from the equation shown below:

$$C_p(z) = \frac{1}{\cosh\frac{L-z}{L_e} + \sinh\frac{L-z}{L_e}\cdot\frac{\sinh\frac{z}{L_e} + SL_e\cosh\frac{z}{L_e}}{\cosh\frac{z}{L_e} + SL_e\sinh\frac{z}{L_e}}} \quad (8)$$

where S is the normalized surface recombination velocity (surface recombination velocity/diffusivity, $S = v_s/D$) and L, and L_e are the same as their previous definitions. eqn (8) was derived from the ratio of the charge flux at the pn-junction boundary to the sum of the fluxes generated in bulk as described in detail in ESI.† As shown in Fig. 7b and c, as one moves away from the junction at $z = L$, the collection probability drops. $C_P(z)$ becomes quite low at the surface (at $z = 0$) where electron–hole generation is fastest. The impact of surface recombination velocity and diffusion length on collection probability is also illustrated by varying S (and L_e/L) in eqn (8). As shown in Fig. 7b, $C_P(z)$ increases with the L_e/L ratio, and begins to saturate from an approximate ratio of $L_e/L = 2$ with $C_P(z)$ below 20% at the surface. Likewise, $C_P(z)$ increases with decreasing S, but unlike the L_e/L ratio, $C_P(z)$ at the surface ($z = 0$) increases significantly as S value decreases. This indicates that increasing the diffusion length (L_e) increases the charge collection efficiency ($C_P(z)$) only up to a certain point. Beyond this point further increase of diffusion length of the Si (*i.e.* the bulk quality of the Si) has little benefit for charge collection since in that limit the total recombination is dominated by surface recombination. This behavior of $C_P(z)$, and consequently $J_{L,max}$ for different thicknesses is shown as a function of S and L_e in Fig. 8. The $J_{L,max}$ can be calculated from the equation shown below by multiplying $G(z)$ and $C_P(z)$ of the carriers:

$$J_{L,max} = q\int_0^L G(z)C_p(z)dz \quad (9)$$

As shown in each plot of Fig. 8, once L_e reaches a certain value comparable to the absorber thickness, surface recombination (S) starts to become more significant. As shown in Fig. 8a ($L = 15$ μm), the slopes of contour lines are relatively moderate in the short diffusion length region and the gap between the lines have been broadened. This indicates J_L in a real device will be less sensitive to device parameters, but the maximum current for 15 μm thick Si is limited below 17 mA cm^{-2} while a 30 μm thick Si (Fig. 8b) can reach above 20 mA cm^{-2}. The thinnest samples are limited by photons with long wavelength passing through the Si with little absorption. On the other hand, a 350 μm thick device (Fig. 8f) shows a J_L limited at approximately 10 mA cm^{-2} and even this value requires good surface passivation and a very high L_e level which only can be achieved by using quality material such as float zone (FZ) Si.

The reason is that charge collection probability with identical S and L_e decreases with increased Si thickness due to the decreased L_e/L ratio and the impact of this ratio increases significantly as thickness of Si increases as already shown in Fig. 7c. Clearly, the choice of thickness is strongly dependent on L_e and S and must be optimized with respect to cost. Considering that conventional solar cell grade CZ Si wafer shows L_e of 100–300 μm,[35] using Si with thickness around 50 μm seems an appropriate compromise. As shown in Fig. 8c, 50 μm thick Si shows peak values up to 20.2 mA cm^{-2} under the $\lambda > 635$ nm simulated spectrum. This is a high J_L value compared to the other thicknesses with identical S and L_e.

However, in order to compare to experimental results it is necessary to include the surface reflectance from the light incident side. Considering measured reflectance from the back

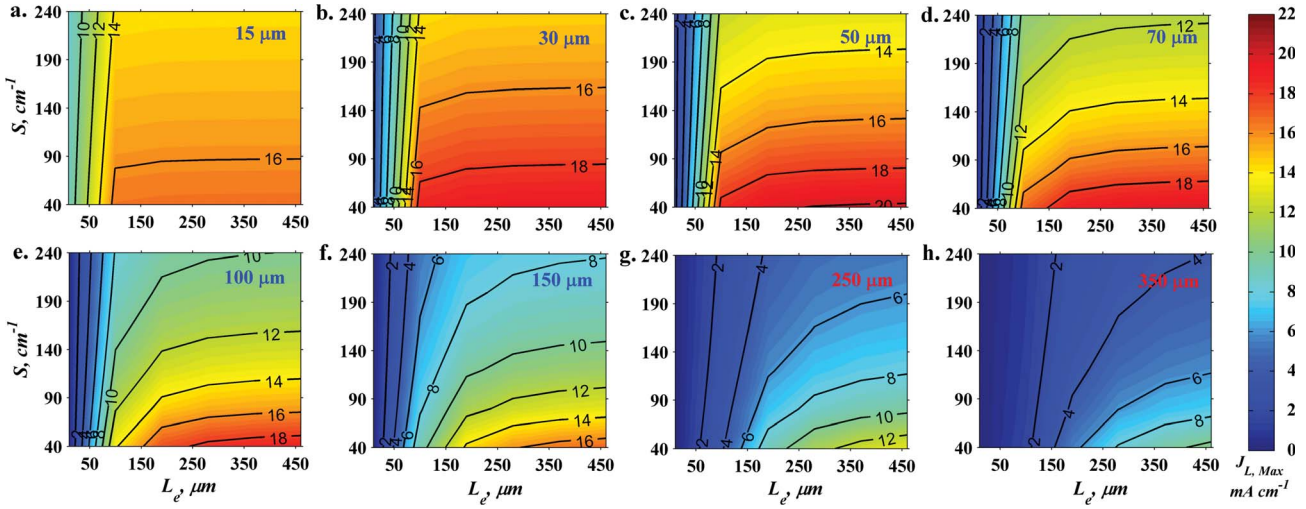

Fig. 8 Contour plots of theoretical maximum current density *versus* diffusion length and surface recombination rate for 15 μm thick (a), 30 μm thick (b), 50 μm thick (c), 70 μm thick (d), 100 μm thick (e), 150 μm thick (f), 250 μm thick (g), and 350 μm thick (h) bottom cell under the simulated bottom cell illumination (see Fig. 2). These plots illustrate impact of S and L_e on theoretical current density, and at the same time how these impacts change with Si thickness.

side of the device (solid blue curve in Fig. S11†), the theoretical maximum current with surface reflectance $J'_{L,\max}$ can be calculated. The result is reduced charge generation rate $G'(z)$ due to the surface reflectance. As shown in Fig. 10, it is observed that the overall current level is decreased by more than 15% for all three thicknesses due to the surface reflectance. Overlapping contour lines, which correspond to the experimental values with uncertainty, allows estimating approximate L_e and S values of the Si device used in this work (green colored area in Fig. 9d). It was found that a L_e of approximately 350 μm and S of 80 cm^{-1} best fit the experimental data. Assuming that Si has an electron diffusivity, $D \leq 36$ cm^2 s^{-1},[36] we estimate the surface recombination velocity, V_s, to be approximately 3×10^3 cm s^{-1} ($S = V_s/D$). This high value clearly indicates that there is room for improvement. Using these traced values one can determine the theoretical Absorbed Photon-to-Current Efficiency (APCE). For Pt, a material with fast HER kinetics, the yield of electron injection into the electrolyte is ~1, and therefore APCE can be obtained by dividing J_L by absorbed photon expressed as a current density (J_{abs}).[37] Details of the mathematical procedure can be found in the ESI.† It was determined that the APCE, which was calculated from the measured IPCE, was quite similar to $C_P(z)$ with L_e of 350 μm and S of 80 cm^{-1} (Fig. S12 in ESI†), indicating that the measured experimental behaviour agrees well with the model.

In Fig. 10, the calculated current density (using an empirical L_e and S extracted from Fig. 9) is shown as a function of thickness together with five experimentally measured values (Fig. S13 in ESI†). Calculated photocurrent density with enhanced L_e and S cases are also shown to point out how additional improvements can be made with further structural design modification. An important point is the impact of surface recombination velocity on $J'_{L,\max}$. According to the modeled data in Fig. 10, an improvement of S (dashed line) gives higher impact on $J_{L,\max}$ than an improvement in L_e. Case in point: $J_{L,\max}$ increased by 12% when S is reduced by 1/2, whereas a model of a device with 3× increased L_e (dot-dash line) shows only slight increase in current density with decreased thickness sensitivity. This analysis strongly suggests using (back) surface passivation – *e.g. via* application of a thermally grown SiO_2 layer[38] or an overlayer

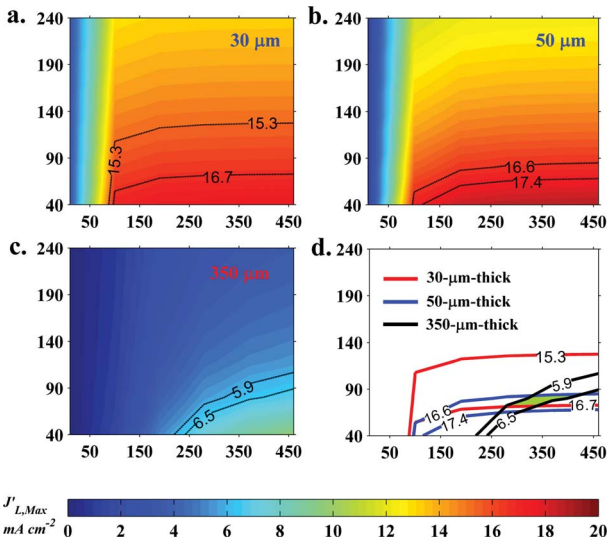

Fig. 9 Contour plot of theoretical maximum current density *versus* diffusion length and surface recombination rate under simulated illumination (Fig. 6) considering reflectance from the surface of the back side *versus* diffusion length and surface recombination rate for 30 μm thick (a), 50 μm thick (b), 350 μm thick (c). Overlapped contour lines (d) which correspond to the experimental uncertainty are also given to estimate diffusion length and surface recombination rate of the samples used for this work. Uncertainty ranges for each panel were derived from the uncertainty of the saturated current I_L and the active area measurement A, *i.e.* $I_L/A \pm (\Delta I_L + \Delta A)$.

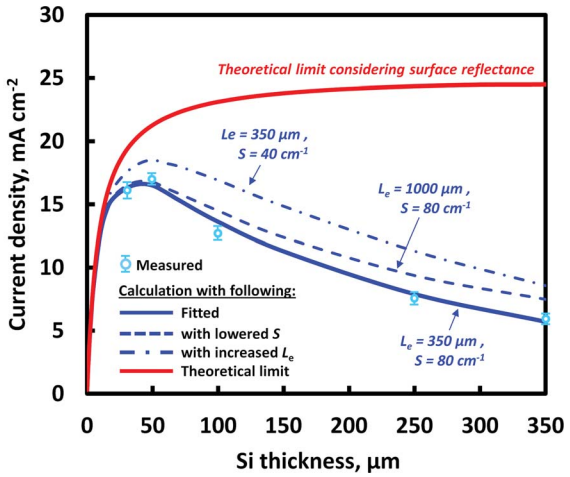

Fig. 10 Calculated theoretical limits of the current density: curve from the Si device with recombination rate and diffusion length value traced from the IPCE and modelling data ($L_e = 175$ μm; $S = 0.48$ cm^{-1}) (blue solid), and estimated behavior from the device with increased L_e and S (blue dots). Theoretical limit of an ideal Si device, *i.e.* $L_e = \infty$ and $S = 0$ (red curve) with surface reflectance is also given for comparison.

of ZnO or Al_2O_3 [39] – in order to reduce the surface recombination velocity. As described in Fig. S2,† the back side surface of the Si samples (the top surface in figure) is exposed to atmosphere, and thus one would expect there to be a native grown SiO_2 layer (~1 nm) of poor quality, which does not provide good surface passivation. Furthermore, since the back side of bottom cell must provide an Ohmic contact with the top cell in tandem designs the internal passivation layer should be conductive as well as transparent. This suggests that either a transparent conducting oxide (TCO) with locally opened-point contacts[40,41] or a design with a very thin dielectric passivation layer is attractive.[38,39] Amorphous Si (a-Si:H) with a TCO overlayer can be an excellent candidate as demonstrated by Panasonic HIT cell,[26] since a-Si:H has excellent passivation capability and enable good carrier transport. It should be noted that the conduction band position of the n-type TCO layer should be close to the valence band of p^+ Si surface,[42] since these layers should work as a tunnel junction in practical tandem device.

4. Conclusions

We have demonstrated, for the first time, a back-illuminated photocathode which is suited to work efficiently in a tandem PEC stack. Specifically we have shown that a photocathode with a p^+pn^+-Si – structure, whose pn-junction is formed at the solid/liquid side, can be used as a HER photoelectrode under back side (dry side) illumination which is similar to actual operational conditions in tandem water splitting devices. From an analytical calculation study, it was found that the balance between charge collection probability and light absorber thickness is an important design parameter to produce efficient back-illuminated devices. The photoelectrochemical investigation of p^+pn^+-Si with Si-thickness as parameter clearly demonstrates the impact of L_e/L ratio estimated from the above-mentioned theoretical results. A 50 μm thick thinned p^+pn^+-Si electrode showed a maximum J_L (17.0 mA cm^{-2}) under back-illumination, whereas a 350 μm thick sample, with a 7 times lower L_e/L ratio, showed only 6.1 mA cm^{-2}. In contrast, despite its enhanced L_e/L ratio, a 30 μm thick sample showed only slightly lower J_L due to its limited light absorption (loss of infrared photons). These results demonstrate how the charge collection limitation of a photocathode with its pn-junction at solid/liquid can be overcome. Importantly, the increased fill factor and increased V_{oc} of the thinned back-illuminated samples owe their success mostly to increased J_L, and such designs should lead to increased operational current density when coupled with a photoanode. Building on the experimental input, further modelling shows that surface recombination on the back side of the silicon is the dominant current loss mechanism. Therefore, the application of a conducting passivation layer, which allows transport of the carriers with minimum optical loss, seems one of the critical challenges to reduce the back side recombination rate and consequently enhance photocatalytic performance of practical Si-bottom cell.

Acknowledgements

This work was performed as a part of the Center for Individual Nanoparticle Functionality (CINF) which is funded by Danish National Research Foundation (DNRF54). Furthermore, most of sample fabrication work has been done using facilities in DTU Danchip.

Notes and references

1 N. S. Lewis and D. G. Nocera, Powering the planet: chemical challenges in solar energy utilization, *Proc. Natl. Acad. Sci. U. S. A.*, 2006, **103**, 15729–15735.
2 M. G. Walter, E. L. Warren, J. R. McKone, S. W. Boettcher, Q. Mi, E. A. Santori and N. S. Lewis, Solar water splitting cells, *Chem. Rev.*, 2010, **110**, 6446–6473.
3 S. W. Boettcher, E. L. Warren, M. C. Putnam, E. A. Santori, D. Turner-Evans, M. D. Kelzenberg, M. G. Walter, J. R. McKone, B. S. Brunschwig, H. A. Atwater and N. S. Lewis, Photoelectrochemical hydrogen evolution using Si microwire Arrays, *J. Am. Chem. Soc.*, 2011, **133**, 1216–1219.
4 M. Moriya, T. Minegishi, H. Kumagai, M. Katayama, J. Kubota and K. Domen, Stable hydrogen evolution from CdS-modified $CuGaSe_2$ photoelectrode under visible-light irradiation, *J. Am. Chem. Soc.*, 2013, **135**, 3733–3735.
5 C. G. Morales-Guio, S. D. Tilley, H. Vrubel, M. Grätzel and X. Hu, Hydrogen evolution from a copper(I) oxide photocathode coated with an amorphous molybdenum sulphide catalyst, *Nat. Commun.*, 2014, **5**, 3059.
6 S. Dahl and I. Chorkendorff, Solar-fuel generation: becoming practical?, *Nat. Mater.*, 2012, **11**, 100–101.
7 R. Schlögl, Chemistry's role in regenerative energy, *Angew. Chem., Int. Ed.*, 2011, **50**, 6424–6426.
8 A. J. Bard, Photoelectrochemistry and heterogeneous photocatalysis at semiconductors, *J. Photochem.*, 1979, **10**, 59–75.

9 Y. Hou, B. L. Abrams, P. C. K. Vesborg, M. E. Björketun, K. Herbst, L. Bech, A. M. Setti, C. D. Damsgaard, T. Pedersen, O. Hansen, J. Rossmeisl, S. Dahl, J. K. Nørskov and I. Chorkendorff, Bioinspiredco-catalysts bonded to a Silicon photocathode for solar Hydrogen evolution, *Nat. Mater.*, 2011, **10**, 434–438.

10 B. Seger, T. Pedersen, A. B. Laursen, P. C. K. Vesborg, O. Hansen and I. Chorkendorff, Using TiO_2 as a conductive protective layer for photocathodic H_2 evolution, *J. Am. Chem. Soc.*, 2013, **135**, 1057–1064.

11 B. Seger, A. B. Laursen, P. C. K. Vesborg, T. Pedersen, O. Hansen, S. Dahl and I. Chorkendorff, Hydrogen production using a molybdenum sulfide catalyst on a titanium-protected n+p-silicon photocathode, *Angew. Chem., Int. Ed.*, 2012, **51**, 9128–9131.

12 E. L. Warren, S. W. Boettcher, J. R. McKone and N. S. Lewis, Photoelectrochemical water splitting: silicon photocathodes for hydrogen evolution, *Proc. SPIE*, 2010, **7770**, 77701F.

13 B. O. Khaselev and J. A. Turner, A monolithic photovoltaic-photoelectrochemical device for hydrogen production *via* water splitting, *Science*, 1998, **280**, 425–427.

14 X. Gao, S. Kocha, A. J. Frank and J. A. Turner, Photoelectrochemical decomposition of water using modified monolithic tandem cells, *Int. J. Hydrogen Energy*, 1999, **24**, 319–325.

15 P. C. K. Vesborg and T. F. Jaramillo, Addressing the terawatt challenge: scalability in the supply of chemical elements for renewable energy, *RSC Adv.*, 2012, **2**, 7933–7947.

16 R. H. Coridan, M. Shaner, C. Wiggenhorn, B. S. Brunschwig and N. S. Lewis, Electrical and photoelectrochemical properties of WO_3/Si tandem photoelectrodes, *J. Phys. Chem. C*, 2013, **117**, 6949–6957.

17 M. R. Shaner, K. T. Fountaine, S. Ardo, R. H. Coridan, H. A. Atwater and N. S. Lewis, Photoelectrochemistryof core–shell tandem junction n-p^+-Si/WO_3 microwire array photoelectrodes, *Energy Environ. Sci.*, 2014, **7**, 779–790.

18 J. A. Turner, A nickel finish protects silicon photoanodes for water splitting, *Science*, 2013, **342**, 811–812.

19 F. F. Abdi, L. Han, A. H. M. Smets, M. Zeman, B. Dam and R. van de Krol, Efficient solar water splitting by enhanced charge separation in a bismuth vanadate-silicon tandem photoelectrode, *Nat. Commun.*, 2013, **4**, 2195.

20 J. Brillet, J.-H. Yum, M. Cornuz, T. Hisatomi, R. Solarska, J. Augustynski, M. Graetzel and K. Sivula, Highly efficient water splitting by a dual-absorber tandem cell, *Nat. Photonics*, 2012, **6**, 824–828.

21 N. Wyrsch, S. Dunand and C. Ballif, Bifacial a-Si:H solar cells: Origin of the asymmetry between front and back illumination, *Proceedings of NUMOS*, 2007, 289–295.

22 A. Kränzl, R. Kopecek, K. Peter and P. Fath, Bifacial solar cells on multi-crystalline silicon with boron BSF and open rear contact, *Conference Record of the 2006 IEEE 4th World Conference on Photovoltaic Energy Conversion*, 2006, vol. 1, pp. 968–971.

23 S. Hu, C. Xiang, S. Haussener, A. D. Berger and N. S. Lewis, An analysis of the optimal band gaps of light absorbers in integrated tandem photoelectrochemical water-splitting systems, *Energy Environ. Sci.*, 2013, **6**, 2984–2993.

24 J. J. H. Pijpers, M. T. Winkler, Y. Surendranath, T. Buonassisi and D. G. Nocera, Light-induced water oxidation at silicon electrodes functionalized with a cobalt oxygen-evolving catalyst, *Proc. Natl. Acad. Sci. U. S. A.*, 2011, **25**, 10056–10061.

25 D. L. Meier, H. P. Davis, R. A. Garcia, J. Salami, A. Rohatgi, A. Ebong and P. Doshi, Aluminum alloy back p–n junction dendritic web silicon solar cell, *Sol. Energy Mater. Sol. Cells*, 2001, **65**, 621–627.

26 Panasonic headquarter news,http://panasonic.co.jp/corp/news/official.data/data.dir/2014/04/en140410-4/en140410-4.html, accessed November 2014.

27 D. D. Smith, P. J. Cousins, A. Masad, A. Waldhauer, S. Westerberg, M. Defensor, R. Ilaw, T. Dennis, R. Daquin, N. Bergstrom, A. Leygo, Z. Xi, B. Meyers, B. Bourne, M. Shields and D. Rose, SunPower's Maxeon Gen III solar cell: High efficiency and energy yield, *Proc. 39th IEEE PVSC, IEEE*, New York, 2013, pp. 0908–0913.

28 Y. Lin, C. Battaglia, M. Boccard, M. Hettick, Z. Yu, C. Ballif, J. W. Ager and A. Javey, Amorphous Si thin film based photocathodes with high photovoltage for efficient hydrogen production, *Nano Lett.*, 2013, **13**, 5615–5618.

29 F. Y. R. El Faituri and A. Y. Darkwi, Computer simulation for current density in pn-Si solar cells, *Proceedings of the International Symposium on Solar Physics and Solar Eclipses*, Waw an Namus, 2006.

30 C. Hu and R. M. White, *Solar Cells: from basics to advanced systems*, ed. W. Stephen, McGraw-Hill college, New York, 1st edn, 1983, ch. 3.3, pp. 45–46.

31 W. R. Thurber, R. L. Mattis, Y. M. Liu and J. J. Filliben, Resistivity-dopant density relationship for boron-doped silicon, *J. Electrochem. Soc.*, 1980, **127**, 2291–2294.

32 A. F. Thomson and K. R. McIntosh, Light-enhanced surface passivation of TiO_2-coated silicon, *Prog. Photovoltaics*, 2012, **20**, 343–349.

33 P. Bosshard, W. Hermann, E. Hung, R. Hunt and A. J. Simon, An assessment of solar energy conversion technologies and research opportunities, *GCEP Energy Assessment Analysis*, Stanford University, 2006.

34 ASTM G173-03, Standard tables for reference solar spectral irradiances:direct normal and hemispherical on 37° tilted surface, 2012.

35 V. A. Milichko, A. I. Nechaev, V. A. Valtsifer, V. N. Strelnikov, Y. N. Kulchin and V. P. Dzyuba, Photo-induced electric polarizability of Fe_3O_4 nanoparticles in weak optical fields, *Nanoscale Res. Lett.*, 2013, **8**, 317–323.

36 D. L. Losee, Admittance spectroscopy of impurity levels in Schottky barriers, *J. Appl. Phys.*, 1975, **46**, 2204–2214.

37 T. W. Kim and K.-S. Choi, Nanoporous $BiVO_4$ photoanodes with dual-layer oxygen evolutioncatalysts for solar water splitting, *Science*, 2014, **343**, 990–994.

38 F. Feldmann, M. Simon, M. Bivour, C. Reichel, M. Hermle and S. W. Glunz, Carrier-selective contacts for Si solar cells, *Appl. Phys. Lett.*, 2014, **104**, 181105.

39 D. Garcia-Alonso, S. Smit, S. Bordihn and W. M. M. Kessel, Silicon passivation and tunneling contact formation by

atomic layer deposited Al_2O_3/ZnO stacks, *Semicond. Sci. Technol.*, 2013, **28**, 082002.

40 A. Goodrich, P. Hacke, Q. Wang, B. Sopori, R. Margolis, T. L. James and M. Woodhouse, A wafer-based monocrystalline silicon photovoltaics roadmap: Utilizing known technology improvement opportunities for further reductions in manufacturing costs, *Sol. Energy Mater. Sol. Cells*, 2013, **114**, 110–135.

41 J. Schmidt, M. Kerr and A. Cuevas, Surface passivation of silicon solar cells using plasma-enhanced chemical-vapour-deposited SiN films and thin thermal SiO_2/plasma SiN stacks, *Semicond. Sci. Technol.*, 2001, **16**, 164–170.

42 Y.-S. Lin, S.-Y. Lien, C.-C. Wang, C.-H. Hsu, C.-H. Yang, A. Nautiyal, D.-S. Wuu, P.-C. Tsai and S.-J. Lee, Optimization of recombination layer in the tunnel junction of amorphous silicon thin-film tandem solar cells, *Int. J. Photoenergy*, 2011, **2011**, 264709.

THE JOURNAL OF PHYSICAL CHEMISTRY Letters

ACS Editors' Choice

Letter

pubs.acs.org/JPCL

Terms of Use

Iron-Treated NiO as a Highly Transparent p-Type Protection Layer for Efficient Si-Based Photoanodes

Bastian Mei,[†,§] Anastasia A. Permyakova,[†,§] Rasmus Frydendal,[†,§] Dowon Bae,[†] Thomas Pedersen,[‡] Paolo Malacrida,[†] Ole Hansen,[‡] Ifan E. L. Stephens,[†] Peter C. K. Vesborg,[†] Brian Seger,[†] and Ib Chorkendorff*[,†]

[†]Department of Physics, Center for Individual Nanoparticle Functionality (CINF) and [‡]Department of Micro- and Nanotechnology, Technical University of Denmark, DK-2800 Kongens Lyngby, Denmark

Supporting Information

ABSTRACT: Sputter deposition of 50 nm thick NiO films on p^+−n-Si and subsequent treatment in an Fe-containing electrolyte yielded highly transparent photoanodes capable of water oxidation (OER) in alkaline media (1 M KOH) with high efficiency and stability. The Fe treatment of NiO thin films enabled Si-based photoanode assemblies to obtain a current density of 10 mA/cm^2 (requirement for >10% efficient devices) at 1.15 V versus RHE (reversible hydrogen electrode) under red-light (38.6 mW/cm^2) irradiation. Thus, the photoanodes were harvesting ∼80 mV of free energy (voltage), which places them among the best-performing Si-based photoanodes in alkaline media. The stability was proven by chronoamperometry at 1.3 V versus RHE for 300 h. Furthermore, measurements with electrochemical quartz crystal microbalances coupled with ICP-MS showed minor corrosion under dark operation. Extrapolation of the corrosion rate showed stability for more than 2000 days of continuous operation. Therefore, protection by Fe-treated NiO films is a promising strategy to achieve highly efficient and stable photoanodes.

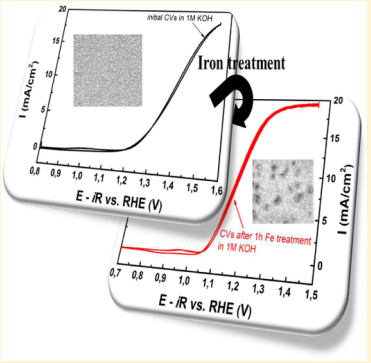

SECTION: Energy Conversion and Storage; Energy and Charge Transport

The sunlight-assisted electrolysis of water using a tandem device photoelectrochemical (PEC) cell theoretically has the potential to achieve an overall solar-to-hydrogen efficiency of about 29%.[1,2] Similar efficiencies can be obtained with a coupled photovoltaic−electrolyzer process, but the potential for low production costs of a tandem PEC cell renders it a favorable approach.[1,3] Nevertheless, there are still significant challenges in designing a highly efficient device.[2] The kinetically slow oxygen evolution reaction (OER) causes major efficiency losses, and the long-term stability of suitable semiconductors, like Si or GaAs, under highly oxidative conditions is poor. While rather complex structures can be used,[4,5] it was recently pointed out by Seger et al.[6] that anodic protection of unstable photoanodes might be possible by applying coatings of metals and their oxides. Here, the protection layer simultaneously acts as oxygen evolution catalysts. These films should be very thin due to their intrinsic high optical absorption properties. Consequently, some efforts have been made using thin films such as Ir/IrO_x[7] or MnO_x.[8] Semiconducting metal oxides constitute another class of suitable anode protection layer (APL). The requirements that the semiconductor should be p-type and that the valence band should be located cathodic of the oxygen evolution potential to allow for a hole accumulation layer limit the number of candidates.[6] Interestingly, Hu et al.[9] used a "leaky" amorphous TiO_2 film as an anodic protection layer. Although TiO_2 is well-known to be an n-type semiconductor, Hu et al. argued that they could introduce defects that permitted hole transfer. From the constraints described by Seger et al.,[6] NiO, a p-type semiconductor, appears to be an interesting candidate. It has a large band gap of 3.7 eV,[5,10−13] and the valence band is located at ∼1.0 V versus RHE.[10] In fact, Sun et al. used NiO or NiRuO on an n-Si photoanode and demonstrated the applicability of NiO as an APL; however, the photoanode assemblies suffered from a relatively poor performance.[5,11] While a severe degradation of the performance was reported with NiO over short time periods, the stability was improved by incorporation of Ru.[5,11] However, the Ru incorporation resulted in a reduced optical transmittance of the NiRuO film. Thus, the potential of highly transparent NiO thin films as an APL has not been successfully proven yet. Nevertheless, nickel oxides are widely used as OER catalysts.[9,14−17] Moreover, trace amounts of Fe incorporated into the NiO structure drastically improve the performance.[14−19] Therefore, NiO itself was concluded to be a mediocre OER catalyst, and instead, $Ni_{1-x}Fe_x$ oxyhydroxide electrocatalysts were reported to be the highly active species.[9] In alkaline electrolyte, these mixed metal OER catalysts exhibit almost an order of magnitude higher activities than noble metal electrocatalysts.[14,15]

Received: September 4, 2014
Accepted: September 24, 2014
Published: September 24, 2014

In this work, we report on the use of an inexpensive and highly transparent p-type NiO thin film as an APL for p^+−n-Si photoanodes for the PEC oxidation of water in strong alkaline conditions (pH 14). Furthermore, a NiO thin film prepared by sputter-deposition will be shown to serve as an active material for water oxidation itself. By employing a pretreatment in iron-containing KOH (10 mM Fe), the performance of the NiO-protected p^+−n-Si photoanode can be significantly improved without changing the "bulk" properties of the NiO anodic protection layer, that is, transparency and stability against corrosion. The iron-treated NiO thin film protection presented here can provide an attractive synthesis route with potentially low fabrication costs. Furthermore, the oxygen evolution performance in a highly alkaline solution achieved with these photoanode assemblies is among the best reported.

Photoanodes consisting of p^+−n-Si were prepared similar to n^+−p-Si in previous reports (for further information, see the Supporting Information (SI)).[7,20,21] Prior to the deposition of NiO films, the p^+−n-Si photoanode substrates were sputtered in Ar (20 mTorr, 50 sccm Ar, 35 W, for 2 min). Subsequently, a 5 nm Ni film was deposited in 3 mTorr of pure Ar at 140 W followed by the deposition of 50 nm of NiO in 3 mTorr at an Ar/O_2 ratio of 5:2 at 140 W. Electrochemical quartz crystal microbalance (EQCM) substrates or glass substrates were modified with NiO thin films using similar process conditions. All electrochemical measurements were performed in high-purity 1 M KOH (for further information, see the SI).

NiO thin films with a nominal thickness of 50 nm were prepared on glass substrates at different process conditions to optimize the transmittance of the obtained thin films. Independent of the process conditions used, the optical band gap of NiO was estimated to be 3.5−3.6 eV, which is in good agreement with that from previous studies on NiO thin films.[10−12,22] Due to their high crystallinity (Figure S1, SI) and good transmittance (Figure 1A), NiO thin films used for electrochemical testing were deposited by sputter-deposition at 573 K.

Scanning electron (SEM) and atomic force microscopy (AFM) showed that the morphology of a typical 50 nm NiO thin film sputtered on a Si substrate is rough (Figure S2, SI). The NiO film is typically grown with inclined orientation and a columnar grain structure with variations of up to 30 nm in height. SEM cross-sectional images coupled with energy dispersive spectroscopy (EDS) analysis (Figure S2, SI), however, indicated that the NiO film is continuous above the Si substrate, thus covering the surface completely.

NiO is well-known to be a hole-selective semiconductor.[10,22−24] To confirm the p-type semiconducting character of the sputter-deposited NiO thin film, dark electrochemical impedance measurements were performed. The resulting Mott−Schottky plot (Figure 1B) shows a negative slope, confirming the p-type behavior of the NiO films. The flat band potential (E_{FB}) and the acceptor density (N_A) were estimated to be E_{FB} = 0.99 V versus RHE and N_A = ~4.4 × 10^{19} cm^{-3}, respectively. These values are in good agreement with those from previous studies on NiO thin films.[24] Due to low current density through the film, the doping density may not be crucial for NiO films when used as protection layers and the catalytically active material on Si photoanodes. Nevertheless, this high dopant density should provide a sufficiently low series resistance.

The dark electrochemical properties of NiO thin films deposited on EQCMs were investigated by means of cyclic

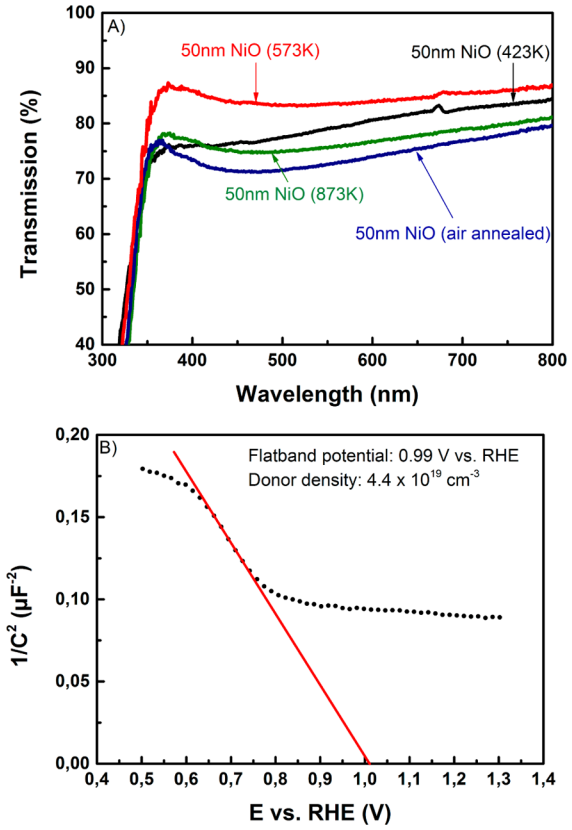

Figure 1. (A) UV−vis transmission spectra of differently prepared NiO thin films on glass substrates. (B) Mott−Schottky plot of a NiO thin film prepared at 573 K on Si substrate. The impedance measurement was performed in 1 M KOH.

voltammetry (CV), chronopotentiometry (CP), and chronoamperometry (CA) in 1 M KOH. The as-deposited NiO films show poor performance for the OER, and overpotentials of ~500 mV are required to achieve a current density of 10 mA/cm^2 (Figure 2A). However, subsequent cycling in the potential range from 0.7 to 1.7 V versus RHE revealed that the activity is increasing during cycling (Figure S3, SI). This behavior can be attributed to the incorporation of trace amounts of Fe and/or the transformation of NiO to NiOOH.[14,15] According to the Pourbaix diagram, the conversion of NiO to $Ni(OH)_2$ is possible during potential cycling in alkaline electrolyte to highly anodic potentials (>0.8 V versus SHE).[25] In order to improve the activity of NiO films further and overrule the influence of trace metal residues, Fe was intentionally added to the electrolyte. As expected,[14−16] the current increased significantly following this treatment (Figure 2A), which most likely can be attributed to a partial charge transfer from Ni to Fe.[15,26] Thus, Ni with higher oxidation power and lower overpotentials would be accessible for OER. Furthermore, an enhancement in conductivity might alter the OER performance.[15]

The EQCM results show a significant increase in mass during treatment of NiO in an Fe-containing solution (Figure 2B), which was found to level off after ~1 h of treatment. We attribute this increase in mass at least partially to Fe incorporation occurring in parallel to oxygen evolution (see the SI for further details). Furthermore, a significantly higher and relatively stable activity (current densities of 120 mA/cm^2) was achieved immediately after starting the treatment. In

dx.doi.org/10.1021/jz501872k | J. Phys. Chem. Lett. 2014, 5, 3456−3461

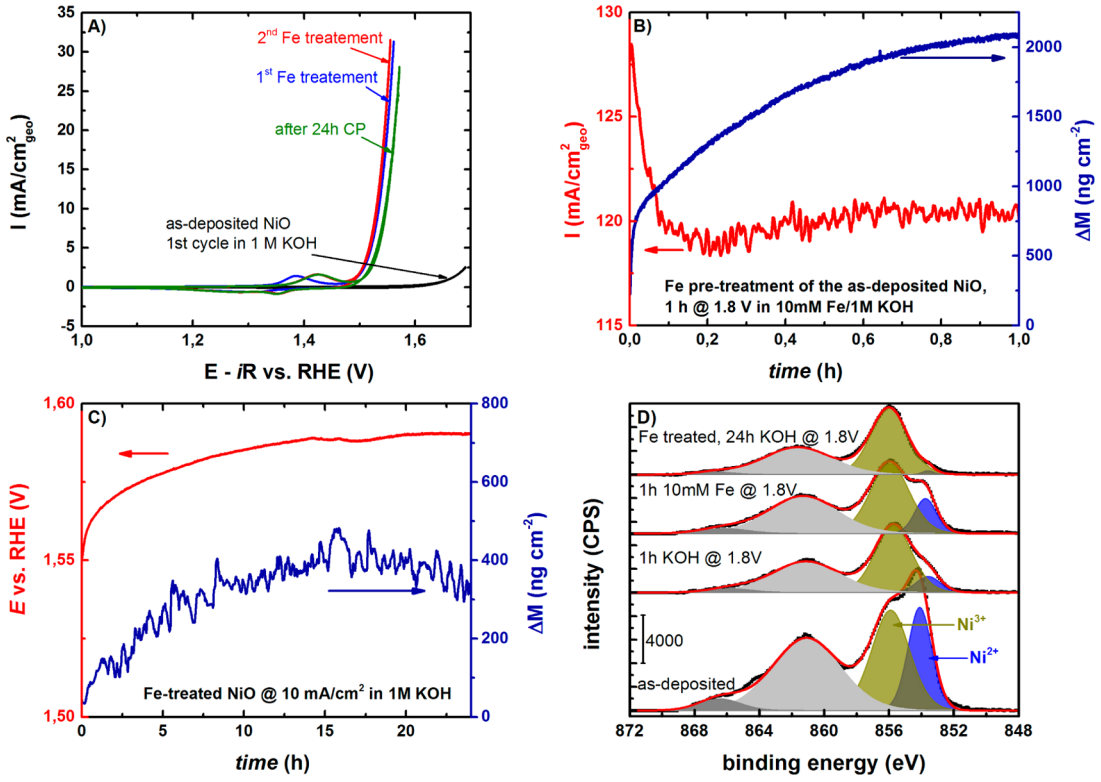

Figure 2. Dark eleochemical measurements. (A) CV curves of a NiO and Fe-treated NiO thin films on EQCM substrates. (B) CA performed with an as-deposited NiO thin film in a 10 mM Fe-containing 1 M KOH solution at 1.8 V versus RHE for 1 h. (C) CP measurement performed at a constant current density of 10 mA/cm^2 with Fe-treated NiO thin films on EQCM substrates in high-purity 1 M KOH for 24 h. (D) Ni 2p XPS spectra of NiO and Fe-treated NiO thin films after different electrochemical treatments.

contrast, only a slight increase in mass, presumably due to the conversion of NiO to NiOOH, and a decrease in current density (max. 20 mA/cm^2) with time was observed for the as-deposited NiO (Figure S4, SI). Hence, the Tafel slope (~24 mV/dec) and the OER overpotential (η = 300 mV) required to achieve meaningful current densities are significantly improved for the Fe-treated sample compared with the as-deposited NiO shown in Figure 2A. Due to the stable performance of the Fe-treated NiO thin film electrode and the rather slowly increasing mass of the film, it is reasonable to assume that the Fe incorporation into NiO is a fast process that might be limited to the first few nanometers of the NiO film. Therefore, a detailed mechanism of the iron incorporation into NiO thin films and the migration during electrochemical testing is currently under investigation. A first attempt to determine the Fe concentration by XPS failed due the unfavorable cross section of Fe and overlapping Ni Auger signals.

It was recently proposed by Frydendal et al.[27] that the most meaningful lifetime evaluation of thin films can be achieved by performing electrochemical long-term tests accompanied by inductively coupled plasma mass spectrometry (ICP-MS) to evaluate the metal content in the electrolyte due to corrosion. A long-term test was performed at a constant current density of 10 mA/cm^2 for 24 h in high-purity 1 M KOH with the Fe-pretreated NiO sample (Figure 2C), and the electrolyte was probed afterward to estimate the nickel content in solution. The chronopotentiometric measurement showed that the potential needed to maintain a stable current density of 10 mA/cm^2 was slightly increasing (25 mV) within the first 12 h of testing, whereafter the potential required to drive 10 mA/cm^2 stabilized. Accordingly, an anodic shift of the current−voltage curve was observed after the 24 h long-term test (Figure 2A). The anodic shift was found to be reversible after additional Fe-treatment (Figure 2A), suggesting Fe leaching out and equilibration with the electrolyte. This was confirmed by ICP-MS showing iron residues in the electrolyte. An additional gain of mass was observed for the Fe-treated NiO thin film during the CP measurement in high-purity 1 M KOH (no Fe) (Figure 2C). The mass increased by ~400 ng/cm^2 during the first 12 h of testing and stabilized afterward, thus following the same trend as the chronopotentiometric test (Figure 2C). Even though the mass increased, the ICP-MS results showed that ~16 ng of Ni dissolved away from the 1.37 cm^2 EQCM electrode. Because results indicate that Fe is lost due to solution equilibration and Ni is lost due to corrosion, we attribute the mass increase to a further oxidation of the NiO film. Indeed, characterization of the surfaces of different NiO samples by XPS showed that NiO is gradually oxidized during prolonged measurements (Figure 2D). With a mass loss of ~12 ng Ni/(cm^2 day), 0.06 monolayers (ML) of NiO would be lost every 24 h of continuous operation. In other words, the 50 nm NiO film would require ~2800 days or 7.6 years of continuous operation to fully corrode, based on extrapolation from the 24 h test. In a comparative CA measurement at 1.8 V versus RHE, a loss of 0.077 ML NiO/day was observed, giving an expected lifetime of ~2200 days for a 50 nm film. Thus, Fe-treated NiO appears to be highly stable. We note that a real water splitting device will only be evolving O_2 for a part of the day. Thus, the durability numbers that we present are conservative estimates of how long the NiO can function as a protection layer even though a certain thickness of NiO thin films is certainly

dx.doi.org/10.1021/jz501872k | J. Phys. Chem. Lett. 2014, 5, 3456−3461

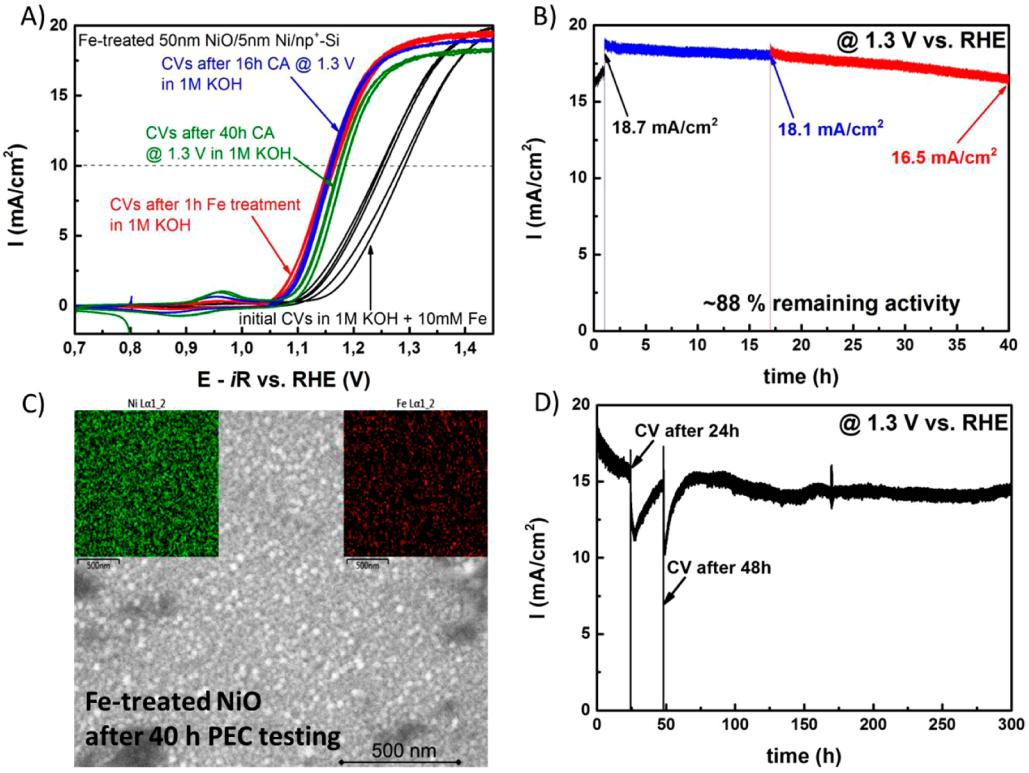

Figure 3. (A) CV curves of PEC measurements of Fe-treated NiO thin films on p^+−n-Si photoanodes after various treatments. (B) Corresponding CA measurement performed with an Fe-treated NiO thin film at 1.3 V versus RHE for 40 h. (C) SEM picture with the Ni and Fe distribution mapped by EDS of the Fe-treated NiO thin film after 40 h of chronoamperometric testing at 1.3 V versus RHE. (D) The 300 h long-term CA testing of an Fe-treated NiO-protected p^+−n-Si photoanode at 1.3 V versus RHE. All PEC measurements were performed in 1 M KOH under 38.6 mW/cm^2 of simulated sunlight (AM 1.5G, filtered $\lambda > 635$ nm).

required to chemically protect the underlying Si (for further information, see the SI).

Subsequently, PEC measurements were performed with NiO/p^+−n-Si and Fe-treated NiO/p^+−n-Si photoanodes to evaluate their applicability in a tandem device that consists of a large band gap photocathode and a small band gap photoanode. In this design, the photoanode could consist of Si, which has an almost optimal band gap (for the small band gap semiconductor) for highly efficient tandem device PEC cells.[28] As expected, the as-deposited pure NiO/p^+−n-Si photoanodes show poor performance for oxygen evolution. An applied potential of 1.4 V versus RHE is required to obtain a current density of 10 mA/cm^2 (Figure S5, SI), which is due to a poor Tafel slope (~170 mV/dec).

Accordingly, during CA measurements at 1.3 V versus RHE, a maximum current density of 3.5 mA/cm^2 was obtained (Figure S6, SI). The initial decay in the CA measurement could be attributed to the contamination of the electrode, presumably by potassium ions, whereas the slow increase with prolonged irradiation could be due to incorporation of small amounts of Fe present in the electrolyte. Indeed, the CV curve is slowly shifting cathodically, indicating the incorporation of Fe into the NiO film (Figure S5, SI).

The Fe pretreatment was subsequently performed by irradiating the as-deposited NiO/p^+−n-Si photoanodes at 1.3 V versus RHE with 38.6 mW/cm^2 of simulated sunlight ($\lambda >$ 635 nm, AM 1.5G) to match the conditions in a tandem device. The p^+−n-Si photoanodes are known to give a photovoltage of ~500 mV;[7] therefore, these conditions were chosen to obtain comparable treatments with the dark experiments (i.e., 1.3 V versus RHE + 500 mV = 1.8 V versus RHE). The CV (Figure 3A) curve obtained in the 10 mM Fe-containing 1 M KOH electrolyte before 1 h of treatment, as well as the CV curve immediately after Fe treatment in high-purity 1 M KOH, indicates that the photocurrent onset is already shifted cathodically by immersing the electrode in the Fe-containing electrolyte, but the main improvement takes place over 1 h of treatment. Furthermore, it should be noticed that saturation currents similar to the as-deposited NiO/p^+−n-Si photoanodes were obtained, indicating a high transparency of the films even after Fe treatment. Thus, after 1 h of treatment, 10 mA/cm^2 was achieved at an applied potential of 1.15 V versus RHE, making it an almost perfect match for a well-protected PbI_2-based perovskite photocathode. This is a significantly improved result for the NiO-catalyzed OER over those reported by Hu et al.[9] and Kenney et al.[17] as an applied potential of 1.23 V versus RHE was usually required to obtain current densities of 10 mA/cm^2 with their photoanodes. It is important to point out that in our experiment, only the red part of the solar spectrum (38.6 mW/cm^2 of simulated sunlight $\lambda >$ 635 nm, AM 1.5G) was used, whereas using the full spectrum (and even higher light intensities) as done by Hu et al.[9] and Kenney et al.[17] would have further improved the performance because increased light intensity increases the photovoltage. Even Ir-catalyzed Si-based photoanodes showed worse performance.[29] Thus, to the best of our knowledge, this functionalization results in the highest photoelectrocatalytic OER performance for a Si-based photoanode in alkaline electrolyte yet.

During 40 h of CA testing at 1.3 V versus RHE, the electrode was relatively stable, and a decrease of only 12% over the

dx.doi.org/10.1021/jz501872k | J. Phys. Chem. Lett. 2014, 5, 3456−3461

extended time period was observed (Figure 3B). The decrease was due to a lower saturation current, most likely caused by adventitious contamination, which was also observed for the as-deposited NiO/p^+−n-Si photoanode (Figure S5, SI). Simply rinsing the electrode surface with distilled water recovered the initial saturation current. Additionally, after 40 h, the photocurrent onset was anodically shifted by 20 mV. This shift is in good agreement with the observed shift in dark electrochemical measurements, and therefore, most likely, the initial activity can be recovered by additional Fe treatment. Comparing the SEM images of the as-deposited NiO (Figure S2, SI) with the Fe-treated NiO (Figure S7, SI) reveals that the surface of the latter is less rough. However, there are no obvious changes in the film morphology of the 40 h tested Fe-treated NiO compared to the 1 h tested Fe-treated NiO material.

Finally, a Fe-treated NiO/p^+−n-Si was subjected to a 300 h stability test at 1.3 V versus RHE (Figure 3D). In-between CVs were taken after 24 and 48 h of operation. While there are no differences in the iron pretreatment for the photoanodes subjected to the 40 h (Figure 3B) and the 300 h (Figure 3D) CA long-term tests, some variations in the performance were observed. Generally, the behavior of the 300 h tested Fe-treated NiO/p^+−n-Si was similar to that of the 40 h test, but a sharp decay and a slow recovery of the performance was observed for the 300 h tested sample after taking a CV (Figure 3D). However, a stable photocurrent of 14.5 mA/cm^2 was observed when the sample was continuously operated at 1.3 V versus RHE for 5 additional days. The decrease in current was most likely due to contamination. Furthermore, the current−voltage curves indicate that a larger fraction of Ni atoms participate in the $Ni^{2+/3+}$ redox wave (Figure S8, SI) at peak potentials at 0.98 and 0.92 V versus RHE in the anodic and cathodic sweeps, respectively. Thus, aging of the films appears to occur over a relatively long time scale, and the implications for stability should be further explored.

In conclusion, we have demonstrated that Fe-treated NiO thin films are suitable, highly transparent protection layers for p^+−n-Si photoanodes enabling OER at low overpotentials. This was shown by a combination of electrochemical measurements and various characterization techniques. According to Ni dissolution rates measured for dark electrochemical oxygen evolution, an expected lifetime of more than 2000 days can, in principle, be achieved with a 50 nm thick Fe-treated NiO film. Utilizing these Fe-treated NiO films to protect p^+−n-Si photoanodes, current densities of 10 mA/cm^2, which is the requirement for a >10% efficient tandem device, could be achieved at an applied potential of 1.15 V versus RHE. A stable performance for at least 300 h was obtained with these devices. Furthermore, the Fe-treated NiO/p^+−n-Si assembly reported herein is among the best-performing Si-based photoanodes in the literature. The presented Fe-treated NiO thin films might additionally be a suitable protective layer for large band gap photoanodes. Future studies will aim to understand the photoanode assembly in greater detail, particularly the Fe incorporation into the NiO structure and its influence on the long-term stability.

■ ASSOCIATED CONTENT

Supporting Information

Experimental details, further electrochemical characterization, and further characterization by XRD, SEM, and AFM measurements. This material is available free of charge via the Internet at http://pubs.acs.org.

■ AUTHOR INFORMATION

Corresponding Author

*E-mail: ibchork@fysik.dtu.dk.

Author Contributions

§B.M., A.A.P., and R.F. contributed equally to the manuscript.

Notes

The authors declare no competing financial interest.

■ ACKNOWLEDGMENTS

B.M. acknowledges funding from the Ruhr-University Research School Plus throughout the Gateway Fellowship Initiative. For further funding, we gratefully acknowledge the Danish Ministry of Science's UNIK initiative Catalysis for Sustainable Energy (CASE), the Danish National Research Foundation's Center for Individual Nanoparticle Functionality (DNRF54), and the Danish Council for Strategic Research's project MEDLYS (10-093906). We thank K. Nielsen for support with XPS measurements.

■ REFERENCES

(1) McKone, J. R.; Lewis, N. S.; Gray, H. B. Will Solar-Driven Water-Splitting Devices See the Light of Day? *Chem. Mater.* **2014**, *26*, 407−414.

(2) Walter, M. G.; Warren, E. L.; McKone, J. R.; Boettcher, S. W.; Mi, Q.; Santori, E. A.; Lewis, N. S. Solar Water Splitting Cells. *Chem. Rev.* **2010**, *110*, 6446−6473.

(3) Pinaud, B. A.; Benck, J. D.; Seitz, L. C.; Forman, A. J.; Chen, Z.; Deutsch, T. G.; James, B. D.; Baum, K. N.; Baum, G. N.; Ardo, S.; et al. Technical and Economic Feasibility of Centralized Facilities for Solar Hydrogen Production via Photocatalysis and Photoelectrochemistry. *Energy Environ. Sci.* **2013**, *6*, 1983.

(4) Cox, C. R.; Winkler, M. T.; Pijpers, J. J. H.; Buonassisi, T.; Nocera, D. G. Interfaces between Water Splitting Catalysts and Buried Silicon Junctions. *Energy Environ. Sci.* **2013**, *6*, 532.

(5) Sun, K.; Park, N.; Sun, Z.; Zhou, J.; Wang, J.; Pang, X.; Shen, S.; Noh, S. Y.; Jing, Y.; Jin, S.; et al. Nickel Oxide Functionalized Silicon for Efficient Photo-Oxidation of Water. *Energy Environ. Sci.* **2012**, *5*, 7872.

(6) Seger, B.; Castelli, I. E.; Vesborg, P. C. K.; Jacobsen, K. W.; Hansen, O.; Chorkendorff, I. 2-Photon Tandem Device for Water Splitting: Comparing Photocathode First versus Photoanode First Designs. *Energy Environ. Sci.* **2014**, *7*, 2397.

(7) Mei, B.; Seger, B.; Pedersen, T.; Malizia, M.; Hansen, O.; Chorkendorff, I.; Vesborg, P. C. K. Protection of p^+-n-Si Photoanodes by Sputter-Deposited Ir/IrO_x Thin Films. *J. Phys. Chem. Lett.* **2014**, *5*, 1948−1952.

(8) Strandwitz, N. C.; Comstock, D. J.; Grimm, R. L.; Nichols-Nielander, A. C.; Elam, J.; Lewis, N. S. Photoelectrochemical Behavior of n-Type Si(100) Electrodes Coated with Thin Films of Manganese Oxide Grown by Atomic Layer Deposition. *J. Phys. Chem. C* **2013**, *117*, 4931−4936.

(9) Hu, S.; Shaner, M. R.; Beardslee, J. A.; Lichterman, M.; Brunschwig, B. S.; Lewis, N. S. Amorphous TiO_2 Coatings Stabilize Si, GaAs, and GaP Photoanodes for Efficient Water Oxidation. *Science* **2014**, *344*, 1005−1009.

(10) Bai, S.; Cao, M.; Jin, Y.; Dai, X.; Liang, X.; Ye, Z.; Li, M.; Cheng, J.; Xiao, X.; Wu, Z.; et al. Low-Temperature Combustion-Synthesized Nickel Oxide Thin Films as Hole-Transport Interlayers for Solution-Processed Optoelectronic Devices. *Adv. Energy Mater.* **2014**, *4*, 1301460.

(11) Sun, K.; Pang, X.; Shen, S.; Qian, X.; Cheung, J. S.; Wang, D. Metal Oxide Composite Enabled Nanotextured Si Photoanode for

Efficient Solar Driven Water Oxidation. *Nano Lett.* **2013**, *13*, 2064−2072.
(12) Trotochaud, L.; Mills, T. J.; Boettcher, S. W. An Optocatalytic Model for Semiconductor−Catalyst Water-Splitting Photoelectrodes Based on In Situ Optical Measurements on Operational Catalysts. *J. Phys. Chem. Lett.* **2013**, *4*, 931−935.
(13) Miller, E. L. Electrochemical and Electrochromic Behavior of Reactively Sputtered Nickel Oxide. *J. Electrochem. Soc.* **1997**, *144*, 1995.
(14) Trotochaud, L.; Ranney, J. K.; Williams, K. N.; Boettcher, S. W. Solution-Cast Metal Oxide Thin Film Electrocatalysts for Oxygen Evolution. *J. Am. Chem. Soc.* **2012**, *134*, 17253−17261.
(15) Trotochaud, L.; Young, S. L.; Ranney, J. K.; Boettcher, S. W. Nickel−Iron Oxyhydroxide Oxygen-Evolution Electrocatalysts: The Role of Intentional and Incidental Iron Incorporation. *J. Am. Chem. Soc.* **2014**, *136*, 6744−6753.
(16) McCrory, C. C. L.; Jung, S.; Peters, J. C.; Jaramillo, T. F. Benchmarking Heterogeneous Electrocatalysts for the Oxygen Evolution Reaction. *J. Am. Chem. Soc.* **2013**, *135*, 16977−16987.
(17) Kenney, M. J.; Gong, M.; Li, Y.; Wu, J. Z.; Feng, J.; Lanza, M.; Dai, H. High-Performance Silicon Photoanodes Passivated with Ultrathin Nickel Films for Water Oxidation. *Science* **2013**, *342*, 836−840.
(18) Louie, M. W.; Bell, A. T. An Investigation of Thin-Film Ni−Fe Oxide Catalysts for the Electrochemical Evolution of Oxygen. *J. Am. Chem. Soc.* **2013**, *135*, 12329−12337.
(19) Song, F.; Hu, X. Exfoliation of Layered Double Hydroxides for Enhanced Oxygen Evolution Catalysis. *Nat. Commun.* **2014**, *5*, 1−9.
(20) Seger, B.; Pedersen, T.; Laursen, A. B.; Vesborg, P. C. K.; Hansen, O.; Chorkendorff, I. Using TiO_2 as a Conductive Protective Layer for Photocathodic H_2 Evolution. *J. Am. Chem. Soc.* **2013**, *135*, 1057−1064.
(21) Seger, B.; Laursen, A. B.; Vesborg, P. C. K.; Pedersen, T.; Hansen, O.; Dahl, S.; Chorkendorff, I. Hydrogen Production Using a Molybdenum Sulfide Catalyst on a Titanium-Protected n^+p-Silicon Photocathode. *Angew. Chem., Int. Ed.* **2012**, *51*, 9128−9131.
(22) Irwin, M. D.; Buchholz, D. B.; Hains, A. W.; Chang, R. P. H.; Marks, T. J. p-Type Semiconducting Nickel Oxide as an Efficiency-Enhancing Anode Interfacial Layer in Polymer Bulk-Heterojunction Solar Cells. *Proc. Natl. Acad. Sci. U.S.A.* **2008**, *105*, 2783−2787.
(23) Xiong, D.; Xu, Z.; Zeng, X.; Zhang, W.; Chen, W.; Xu, X.; Wang, M.; Cheng, Y.-B. Hydrothermal Synthesis of Ultrasmall $CuCrO_2$ Nanocrystal Alternatives to NiO Nanoparticles in Efficient p-Type Dye-Sensitized Solar Cells. *J. Mater. Chem.* **2012**, *22*, 24760.
(24) Chan, X.-H.; Robert Jennings, J.; Anower Hossain, M.; Koh Zhen, Yu. K.; Wang, Q. Characteristics of p-NiO Thin Films Prepared by Spray Pyrolysis and Their Application in CdS-Sensitized Photocathodes. *J. Electrochem. Soc.* **2011**, *158*, H733.
(25) Beverskog, B.; Puigdomenech, I. Revised Pourbaix Diagrams for Nickel at 25−300 °C. *Corros. Sci.* **1997**, *39*, 969−980.
(26) Yeo, B. S.; Bell, A. T. In Situ Raman Study of Nickel Oxide and Gold-Supported Nickel Oxide Catalysts for the Electrochemical Evolution of Oxygen. *J. Phys. Chem. C* **2012**, *116*, 8394−8400.
(27) Frydendal, R.; Paoli, E. A.; Knudsen, B. P.; Wickman, B.; Malacrida, P.; Stephens, I. E.L.; Chorkendorff, I. Benchmarking the Stability of Oxygen Evolution Reaction Catalysts: The Importance of Monitoring Mass Losses. *ChemElectroChem* **2014**, DOI: 10.1002/celc.201402262.
(28) Laursen, A. B.; Kegnæs, S.; Dahl, S.; Chorkendorff, I. Molybdenum Sulfides—Efficient and Viable Materials for Electro- and Photoelectrocatalytic Hydrogen Evolution. *Energy Environ. Sci.* **2012**, *5*, 5577.
(29) Chen, Y. W.; Prange, J. D.; Dühnen, S.; Park, Y.; Gunji, M.; Chidsey, C. E. D.; McIntyre, P. C. Atomic Layer-Deposited Tunnel Oxide Stabilizes Silicon Photoanodes for Water Oxidation. *Nat. Mater.* **2011**, *10*, 539−544.

Journal of Material Chemistry A

ARTICLE

Back-illuminated Si based photoanode with nickel cobalt oxide catalytic protection layer

Received 00th January 20xx,
Accepted 00th January 20xx

DOI: 10.1039/x0xx00000x

www.rsc.org/

Dowon Bae[a], Bastian Timo Mei[a], Rasmus Frydendal[a], Thomas Pedersen[b], Brian Seger[a], Ole Hansen[b], Peter C. K. Vesborg[a], Ib Chorkendorff[a*]

Si is an excellent photoabsorber for use in dual band gap photoelectrochemical water splitting. So far most of studies on Si photoelectrodes have employed illumination from the front side despite the fact that the silicon is the "bottom" cell in the tandem water splitting device concept. In the present work, we investigate back-illuminated photoanodes with n^+pp^+-Si configuration which has the pn-junction at the side opposing the solid/liquid interface. A 50-nm-thick co-sputtered $NiCoO_x$ film was coupled to this Si photoanode to be used as a protective catalyst for the water oxidation reaction in alkaline media (1M KOH). The sample showed quite high photocurrent of 21 mA cm^{-2} under the red-light illumination (38.6 mW cm^{-2}) from the back side. Long-term chronoamperometry test showed gradual decrease of activity in the beginning, and then the activity was increased, yielding a cathodic shift of the onset voltage by around 50 mV (at 10 mA cm^{-2}) likely due to divergent response of Ni and Co components to incorporation of trace amounts of Fe present in KOH. Once the activity of the sample is stabilized, no further changes or degradation were observed for the following 6 days, indicating that the demonstrated back illuminated photoanode configuration can be considered as a promising strategy to be applied as a bottom cell in a practical tandem water splitting device under alkaline conditions.

Introduction

For efficient hydrogen (H_2) production via water splitting reaction, both hydrogen evolution reaction (HER) and oxygen evolution reaction (OER) need to proceed with a high-rate[1,2]. However, the kinetically slow OER process has been a major bottleneck[3], since it comprises several intermediate steps with high activation energy barriers and thus requires a high overpotential (η) to transfer the 4 electrons: $2H_2O \rightarrow 4H^+ + O_2 + 4e^-$ (in acid) or $4OH^- \rightarrow 2H_2O + O_2 + 4e^-$ (in alkaline). To overcome this problem, efficient OER catalysts are required, but the state of the art electrocatalysts for OER, such as IrO_2 and RuO_2[4-6], are precious metal oxides and too expensive to scale-up, despite of their excellent OER activity in acidic media. In this context, earth-abundant transition metal oxides have been intensively investigated to develop cost-effective alternative OER materials with high activity[7,8]. As one of the non-noble catalyst for OER, nickel cobalt oxide (hereinafter $NiCoO_x$) has recently attracted considerable attention, despite it is stable only in alkaline media, mainly because of its excellent electrical conductivity and rich redox kinetics due to the large number of active sites[9]. Compared to elemental oxides, such as NiO and Co_3O_4, $NiCoO_x$ is, therefore, ideal as candidate for applications, such as electrocatalytic anodic oxygen evolution, supercapacitors, sensors, or optical limiters and switches[9-12]. Similarly in recent studies[13,14] Fe modified NiO compounds have been demonstrated to be efficient OER catalysts. The Boettcher's group[14] found that Fe enhances the film conductivity of nickel-based oxide, and claimed that incorporated Fe enhances the OER activity through a Ni-Fe partial charge transfer activation process, as has been proposed by Corrigan et al.[15]. Furthermore, this study also reported that the overpotential of $Ni(OH)_2$ film for OER can be reduced during cyclic voltammetry (CV) process in 1M KOH due to incorporation of trace amounts of Fe present in KOH[13]. Thus, unintentional, but beneficial Fe alloying or doping occurs. So far, a number of approaches to obtain functional Ni-Fe-O compounds have been reported[13-16]. Large-scale combinational screening studies[17,18] have shown that not only Ni with Fe, but also other metallic elements (e.g., Co, Al, Ce) do appear to enhance OER activity of Ni based oxides. These recent studies indicate that various combinations of cations provide the possibility to change the electrochemical properties. At the same time, it also implies that the OER activity of $NiCoO_x$ would be also enhanced simply by aging in the electrolyte without any intentional doping procedure.

[a] *Center for Individual Nanoparticle Functionality, Department of Physics, Technical University of Denmark, Building 311, Fysikvej, DK-2800 Kgs, Lyngby, Denmark.*
[b] *2Department of Micro- and Nanotechnology, Technical University of Denmark, DK-2800 Kgs. Lyngby, Denmark.*
*Corresponding author E-mail: ibchork@fysik.dtu.dk; Tel: +45) 45 25 31 70; Fax: +45) 45 93 23 99

†Electronic Supplementary Information (ESI) available: Electronic Supplementary Information (ESI) available: Supplementary information accompanies this paper including supplementary Figures S1-6; Cross-sectional SEM image with EDX result, Mott-Schottky plot, J-E characteristics under dark and light condition, cyclic voltammetry characteristics for n^+pp^+-Si/Co/CoO_x in 1M KOH, 6-days long-term chronoamperometry measurement for n^+pp^+-Si/Co/$NiCoO_x$, Repeated 3-days long-term CA measurement for n^+pp^+-Si/Co/$NiCoO_x$. See DOI: 10.1039/x0xx00000x

To date, many research groups have demonstrated catalytic behaviour of element nickel or cobalt oxides[16,19-23] while a relatively small number of studies report the electrocatalytic activity of the binary nickel-cobalt oxides[9-11]. In the present work we demonstrate the time-dependant behaviour of the OER kinetics of $NiCoO_x$ thin films in 1M KOH (pH = 14) electrolyte. The $NiCoO_x$ with Co interlayer is deposited by DC-sputtering on p^+pn^+ Si photoelectrodes, and we evaluate the OER kinetic variation of the sample according to the operating time under back side illumination. According to the Pourbaix diagram, both nickel and cobalt oxide can be converted to hydroxides during potential cycling in alkaline electrolyte[24,25], and thus these binary oxide have been used as a protection layer of Si photoabsorbers with frontal illumination[16,19,22,23]. However, in actual tandem device operation conditions a low band gap absorber, such as Si, should be used as bottom cell of the tandem water splitting device, where the light is incident from the "dry" side of the photoanode. We have demonstrated successful hydrogen production using a light-permeable ring-shaped Al back contact under back-illumination condition[26], and this approach is also employed in this study to allow illumination from the side opposing the solid/liquid interface (i.e. $NiCoO_x$ side). Since the photons are irradiated from the back contact side, transparency of the protection layer is not a required property anymore, indicating that thick non-transparent protection layers can be employed.

Experimental

Sample fabrication

The shallow n^+p-junction was produced in p-type (100) czochralski (CZ) Si wafers (Topsil, 1-20 ohm-cm, boron-doped) by a shallow phosphorous ion implantation at 36 keV with a dose of 3×10^{15} cm^{-2}. After annealing a mesa-isolated n^+p-Si structure with height of 3 µm is formed at the back side (light illumination side) by photolithography and dry etching (Here, we used Ar, O_2 and CHF_3 gases in an Oxford Instruments RIE80). The front side of the same samples was also doped with boron doping using ion implantation at 100 keV with a dose of 5×10^{16} cm^{-2} to form a thin p^+ layer. An Al charge collecting layer with a circular hole for light irradiation was deposited by e-beam evaporation with a metallic shadow mask to make circular rings for light irradiation. More fabrication details also can be found in our previous work[26] and ESI†.

Prior to the deposition of the $NiCoO_x$ protective OER catalyst, the Si was sputtered in Ar to clean the surface and remove the native oxide. Subsequently, a 10 nm Co metallic film was reactively sputtered in 3 mTorr of pure Ar followed by the deposition of 50 nm of $NiCoO_x$ in 3 mTorr at an O_2/Ar ratio of 40% by co-sputtering of Ni and Co targets with same deposition rate (i.e. Ni:Co ≈ 1:1). In case of electrochemical quartz crystal microbalance (EQCM) and glass substrates, $Co/NiCoO_x$ thin films were deposited using the same process conditions as mentioned above. Samples prepared only with cobalt oxide (Co/CoO_x) are used to verify qualitatively the role of the Ni component in the binary oxide layer during the reaction. The Co interlayer was introduced to prevent oxidation of the Si surface during the metal oxide deposition at high temperature, and to provide an efficient pathway for the carrier injection by forming an Ohmic contact.

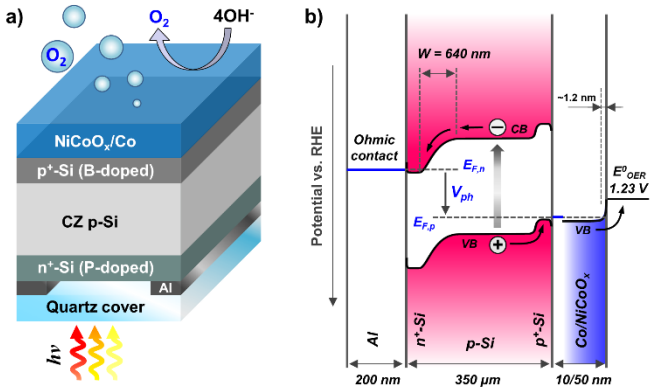

Figure 1 (a) Schematic drawing of the back illuminated photoanode with Al/n^+pp^+-$Si/Co/NiCoO_x$ ($NiCoO_x$ on top) and (b) band alignment under illumination. Detail energy diagram calculation process can be found in ESI†

The back side of the samples was covered with a 300 µm thick quartz glass to protect back side from direct contact with the electrolyte. The quartz cover glass was mounted directly onto the Al layer, and finally the sample was covered with epoxy. The resulting active area was measured by image analysis using ImageJ 1.46r after the experiments. Schematic cross-sectional configuration and its energy band diagram are shown in Figure 1, and a more detailed description of the related calculation procedure also can be found in ESI†.

Characterization

Photoanodes consisting of $n^+pp^+Si/Co/NiCoO_x$ were evaluated under back-side illumination using a 1000 W Xenon lamp (Oriel) with AM 1.5g and 635 nm cut-off filters to appropriately approximate the wavelengths and intensity that this electrode would receive in a practical tandem water splitting device. All cyclic voltammetry and chronoamperometry experiments were done in a 3 electrode quartz cell, since intensive corrosion of conventional pyrex can poison or cover the active surface with glass corrosion products[27], and consequently hinder the light absorption. All (photo) electrochemical measurements were performed in high-purity aqueous 1 M KOH (Aldrich, TraceSELECT®, ≥ 99.995%) using a Bio-Logic VSP potentiostat with EC Lab software. A Pt mesh was used as a counter electrode and the reference was a saturated Hg/HgO electrode (Koslow Scientific Company). The detailed experimental setup and procedure are provided in the ESI†. The solution was purged with Ar gas 30 minutes prior to any experiment. To determine efficiency as a function of wavelength, incident photon to current efficiency (IPCE) measurements were employed. An Oriel 74100 monochromator was combined with the Xenon lamp mentioned above to give monochromatic light. IPCE measurements were carried out from 400 to 800 nm under both front side and back side illumination. To confirm the conductivity type of the present $NiCoO_x$ thin film, electrochemical impedance measurements were performed (Mott-Schottky plot analysis) under the dark condition. Both IPCE and Mott-Schottky analyses were carried out using same equipment and setup as that used for cyclic voltammetry measurements.

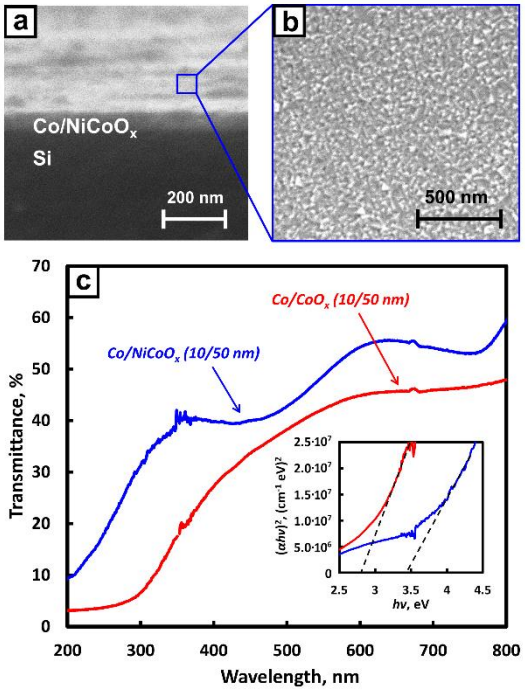

Figure 2 (a) Cross-sectional SEM image of $n^+pp^+Si/Co/NiCoO_x$ and (b) top-view SEM. The $NiCoO_x$ film was deposited at 300°C. These SEM images well demonstrate excellent surface coverage without any obvious crack or pinholes. Band gap of $NiCoO_x$ and CoO_x deposited on quartz substrate with 10 nm thick Co interlayer were determined from the Tauc plot obtained from the (c) UV-Vis transmittance spectra. The signal from the quartz substrate was substracted as a background spectrum.

The results in the present work also cover the electrochemical stability of the $NiCoO_x$ film, and therefore, emphasis also has been put on electrochemical measurements using EQCM samples under the dark conditions to monitor the mass change that occurs during the electrochemical reaction. For this purpose, a three electrode setup similar to that of photocatalytic cyclic voltammetry and chronoampherommetry measurements was used. The EQCM measurements were performed with a 5 MHz QCM200 supplied by Stanford Research Systems.

In order to determine the structural properties, X-ray photoelectron spectroscopy (XPS) analysis was carried out in an UHV (ultra-high vacuum) system provided by Thermo Scientific. In this work, an Al Kα X-ray source emitting photons with energy 1486.7 eV has been used.

Scanning electron microscopy (SEM) with energy dispersive X-ray spectroscopy (EDX) was also carried out for the surface morphology and cross-sectional investigations using Quanta FEG SEM. The provided electron beam energy was 5 to 20 kV with a working distance of around 10 cm. The transmittance spectra were recorded using a Varian Cary 1E UV-Vis Spectrophotometer to estimate band-gap and optical absorption of the deposited $Co/NiCoO_x$ ($NiCoO_x$ on top) and Co/CoO_x layers on quartz substrate. To avoid the effect of background signal, including the absorption by the substrate and/or light scattering particulates in the instrument, a baseline correction using a bare quartz substrate has been carried out prior to the measurements for the $NiCoO_x$ and CoO_x deposited samples.

Results and discussion

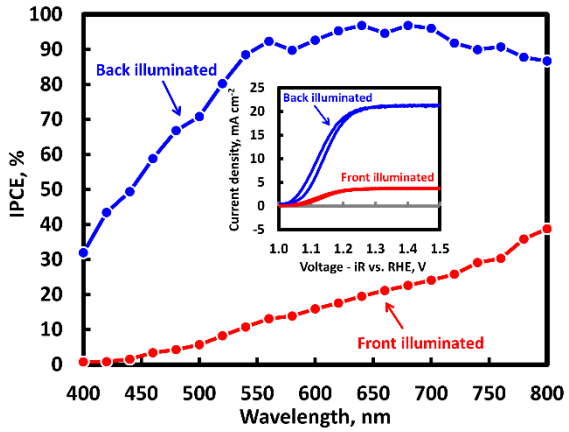

Figure 3 IPCE measurement results under front and back-illumination using $n^+pp^+Si/Co/NiCoO_x$ photoanode sample, and the inset is cyclic voltammetry scans under front and back side illumination (AM 1.5G and 635 nm cut-off filters were used in the cyclic voltammetry scans).

SEM images of the $NiCoO_x$ with Co interlayer deposited on a Si substrate are shown in Figure 2. Figure 2a and b correspond to cross-sectional and top-view image of the film, respectively. The cross-sectional SEM image indicates that the $NiCoO_x$ film is continuous above the Si substrate and has a thickness of about 50 nm, and thus the surface is covered completely. This also can be found from the top-view SEM image (Figure 2b) exposing a dense $NiCoO_x$ surface without any obvious cracks or pin-holes. Note that the investigated films were deposited on the Si photoelectrodes using the same conditions as those used for the PEC samples, and the presence of nickel and cobalt in the binary oxide layer was confirmed by EDX analysis (Figure S1). The optical behaviour of the deposited films was investigated by UV-Vis transmittance spectroscopy as shown in Figure 3. Transmittance of deposited $NiCoO_x$ was approximately 53% at 600 nm in wavelength in spite of its wide band-gap of 3.4eV extracted from the Tauc plot (inset). As shown in our recent work[15] NiO thin film with 50 nm thickness shows over 80% transmittance at 600 nm wavelength due to its high band gap (3.5 ~ 3.6 eV), and thus the optical loss of $Co/NiCoO_x$ would partially due to the Co interlayer. However, a Co/CoO_x layer with same thickness shows transmittance of 43% at the same wavelength having a band-gap of around 2.8 eV, and it is suggested that the optical loss and decreased band gap of $NiCoO_x$ can be mainly attributed to the mixed cobalt oxide phase which shows a drastic increase of absorption coefficient with increased growth temperature[28]. This illustrates how back illumination is beneficial for photoanodes based on such overlayers.

$NiCoO_x$ is a well-known p-type, mixed-valence oxide with Ni occupying octahedral sites and Co distributed over both octahedral and tetrahedral sites[29]. To confirm the conductivity type of the present $NiCoO_x$ thin film, electrochemical impedance measurements were performed (i.e. Mott-Schottky analysis). The resulting Mott−Schottky plot (Figure S2) shows a negative slope, confirming the p-type behaviour of the deposited $NiCoO_x$ films. The flat band potential (E_{FB}) and the acceptor density (N_A) were estimated to be $E_{FB} \approx 0.85$ V versus RHE and $N_A \approx 3.1 \cdot 10^{18}$ cm^{-3}, respectively, and this high dopant density should provide sufficient conductivity to transport holes through the valence band.

To verify the photoelectrochemical properties of $NiCoO_x$, this film was coupled with the n^+pp^+-Si photoanode with a Co interlayer between the p^+-Si and $NiCoO_x$ regions, and the sample was examined by cyclic voltammetry and IPCE measurements. The difference between the overpotentials η required to obtain a 10 mA cm^{-2} with the p^+-Si/Co/$NiCoO_x$ (under dark) and n^+pp^+-Si/Co/$NiCoO_x$ (38.6 mW cm^{-2} under the back illumination) reveals a photovoltage (V_{ph}) of ~ 510 mV (Figure S3), which is in good agreement with the V_{ph} determined for our previous p^+pn^+ Si photocathode with Pt catalyst under same light spectrum condition[26]. Figure 3 shows spectrally resolved IPCE measurement results of the n^+pp^+-Si/Co/$NiCoO_x$ photoanode under back side and front side illumination. Each data point was measured at an applied bias of 1.4 V vs. RHE, at which the sample shows a saturated photocurrent for both front and back side illumination. As shown in Figure 3, the IPCE under the back side illumination increases gradually and shows over 90% IPCE at 550 nm for photons, which are absorbed near the back side of the sample. Considering the light absorption depth of Si as a function of the wavelength[26], this high IPCE response is natural since the charge collecting pn-junction is placed at the back side of the sample, and this shows that this n^+pp^+-Si/Co/$NiCoO_x$ structure is an efficient configuration to be used as a bottom cell of the tandem device. The low IPCE response in the short wavelength range (~ 500 nm) is mainly attributed to the high recombination rate at the n^+-Si surface. Note that we did not apply any surface passivation treatment, and there is no significant optical loss due to the quartz cover glass in this wavelength range[26]. Conversely, the IPCE of the same sample under front side illumination increases slowly from the short wavelength region and reaches merely 35% at a wavelength of 800 nm because most of the electron-hole pairs are generated far from the pn-junction under the front illumination. This difference in IPCE behaviour between the front and back side illumination is reflected in the cyclic voltammetry measurement results (inset in Figure 3). The saturated photocurrent of the n^+pp^+-Si/Co/$NiCoO_x$ photoanode sample is around 21 mA cm^{-2} under the back side illumination with approximate AM 1.5G + 635 nm long pass filters, whereas significantly lower photocurrent, less than 5 mA cm^{-2} was measured under front illumination.

In order to investigate time-dependant behaviour of the sample, repeated cyclic voltammetry measurements with long-term chronoamperometry measurements were carried out. As shown in Figure 4a, the potential required to achieve a photocurrent density (J_{ph}) of 10 mA cm^{-2} was found to depend on the operating time. An applied potential of 1.13 V was required for the initial cyclic voltammetry curve. This performance compares well our previously study with an as-deposited NiO, which showed relatively gradual slope, having onset potentials of ~ 1.24 V (at 10 mA cm^{-2})[16]. This enhanced performance of $NiCoO_x$ is in good agreement with that from the previous electrochemical study on as-deposited Ni-Co-O OER catalyst[10], and this can be attributed to the favourable electric properties towards the OER. Addition of Co, which abounds in the spinel structure of nickel oxide, is known to provide more active sites, and reduce intrinsic electrical resistivity[9,30]. Tseung and Jasem[31] suggested that the mixed valences of the nickel and cobalt cations are helpful in the reversible adsorption of oxygen by providing donor-acceptor sites for chemiabsorption, thus lowering

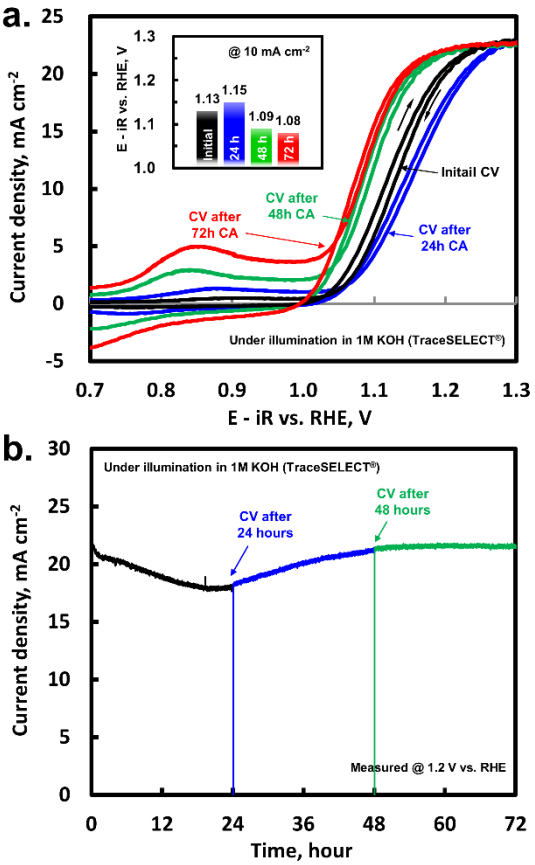

Figure 4 (a) Cyclic voltammetry graphs of n^+pp^+Si/Co/$NiCoO_x$ photoanode measured before chronoamperometry measurement (black), after the 24 hours long chronoamperometry (blue), after the 48 hours (green), and after the 72 hours long chronoamperometry (red). (b) CA measurements carried out at 1.2 V vs. RHE. The potentials required to achieve a photocurrent density of 10 mA cm^{-2} measured every 24 hours can be found in inset of 4a.

the overpotential. Such synergetic effects are not limited to Ni-Co oxides, for instance recent studies on Ni-Fe-O oxides[13,14] can be understood in the same context. Nevertheless, 1.18 V (at 10 mA cm^{-2}) was required for the cyclic voltammetry measured after 24 hours chronoamperometry test at 1.2 V, reflecting the changes in OER kinetics. These cyclic voltammetry curves (initial and 24h after) showed somewhat similar saturation current J_{ph} (~ 22 mA cm^{-2}), but behaved differently. Compared with the initial cyclic voltammetry curve, the curve taken after 24 hours had an anodic shift of 20 mV at 10 mA cm^{-2} and decreased slope resulting a significant loss at the maximum power point (i.e. lower fill factor), which can result in significant loss of operating current density in tandem devices[32] and can be attributed to the $NiCoO_x$ catalyst layer. The anodic shift accompanying with the decreased slop might be explained by the reaction of Co-O compounds with the alkaline electrolyte. Boettcher's group reported in their recent work that iron impurities in KOH electrolyte substitute for Co^{3+} under the applied potential, and this substitution incorporation decreases the electrical conductivity of the CoOOH phase[33]. In this report, the reduced conductivity appears as a lowered the fill factor (i.e. decreased slope). Since our photoanode sample with sputtered CoO_x showed a continuous anodic shift of onset potential with decreased fill factor, this resulted in a decrease in overpotential of approximately 40 mV after 3 days operation (Figure S4). This is in agreement with the recent report by the Lewis' group that the CoO_x coupled with a Si

photoanode shows a gradual loss in catalytic activity associated with the conversion of CoO_x to $Co(OH)_2$ and then to ion-permeable cobalt oxyhydroxide (CoOOH)[22].

Interestingly, the required bias potential to reach 10 mA cm^{-2} rebounded in the cathodic direction after the first 24 hours and reached 1.07 V vs. RHE after the 3 days of chronoamperometry measurement. Furthermore, the slope of cyclic voltammetry curves increased sharply compared to that of the cyclic voltammetry curve taken right after the first 24 hours. Since the photoanode with Co/CoO_x showed a continuous anodic shift of onset voltage as well as degradation in photocurrent, it appears reasonable to assume that the increased activity is mainly attributed to the incorporation of Fe^{3+} with Ni^{2+}. A number of recent studies[13,14,16] have revealed that the apparent OER activity of NiO is dramatically affected by small amounts of Fe impurities in alkaline electrolyte, causing a cathodic shift in the OER onset potential. The increased redox peak in Figure 4a also implies a strong interaction of Fe with metal sites, such as Co and/or Ni. The integrated area under the redox feature yields the total charge exchanged between the incorporated ions and the active sites of the electrode[34], and thus the increased redox features shown in Figure 4a may indicate that a significant number of metallic sites have become electrochemically accessible. The redox wave peak of the oxidative current slightly shifted cathodically for the cyclic voltammetry curves taken after 24h and 48h relative to that of the initial cyclic voltammetry curve, then anodically shifted toward the OER current peak. The later anodic shift of the redox wave is well known for the binary metal oxides, i.e. CoO_x and NiO. This anodic redox wave shift observed in Figure 4a is consistent with the previous reports[13,33], where the redox wave for $Co^{2+/3+}$ and $Ni^{2+/3+}$ shifts anodically as the Fe content in the oxide films increases.

However, only few studies reported the presence of the negative shift of redox peak. J. M. Marioli et al.[35] observed that this negative shift takes place for the Ni-Cr binary oxide films, whereas single component nickel oxide showed only anodic redox peak shift. S. Kim et al. also reported[36] that the shifts in the $Ni^{2+/3+}$ redox features in the negative direction (ca. 50 mV) is induced by the presence of Co in the Ni hydrous oxide lattice. In agreement with the previous observations by other groups[10,35,36], no discernible voltammetry features associated with the $Co^{2+/3+}$ redox couple can be identified for the composite Ni-Co oxide film. Despite of a harmony with previous observations, the precise effect on the catalysis mechanism remains unknown.

The chronoamperometry study performed at 1.2 V versus RHE for 3 days (Figure 4b) reflects the above mentioned behaviour of cyclic voltammetry curves. At a fixed potential of 1.2 V vs. RHE, the J_{ph} of the n^+pp^+-Si/Co/$NiCoO_x$ dropped quite quickly from around 22 to 20.5 mA cm^{-2} over about half an hour, after which photocurrent output appears to degrade slowly with constant rate. This degradation continued during the first 20 hours of CA measurement, followed by a slow increase in J_{ph} after ~ 22 hours followed by a stabilized J_{ph} from the 3rd day of the CA experiment. Once the J_{ph} saturated, the sample showed stable J_{ph} output until 144th hours (6 days) without any further changes or degradation (Figure S5). Assuming that incorporation rate or diffusion rate of Fe thought the ion-permeable oxyhydroxide structures is independent of time, these cyclic voltammetry and chronoampherommetry behaviours are

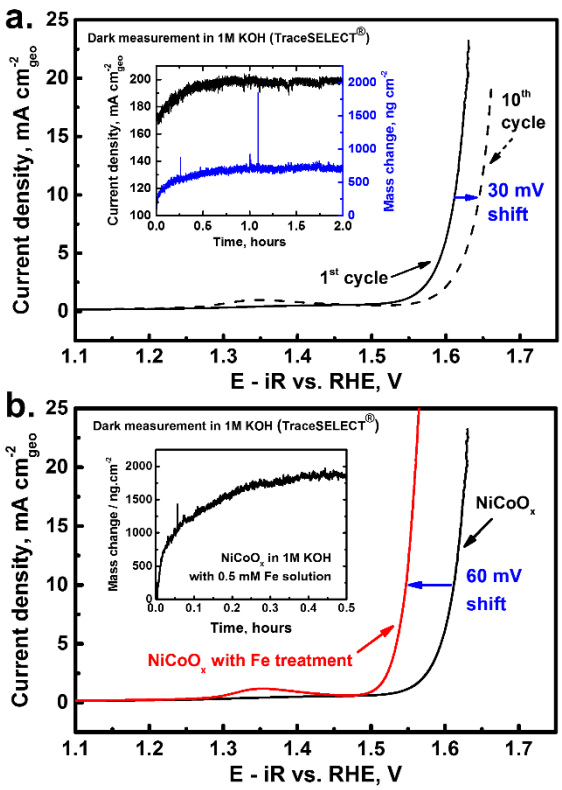

Figure 5 (a) Electrochemical cyclic voltammetry measurement result for the $NiCoO_x$ deposited on EQCM sample with Co interlayer with subsequent 2 hours long chronoamperometry and mass change measurement data (inset), and (b) electrochemical current-potential of $NiCoO_x$ before (black) and after Fe-treatment (red). Both chronoamperometry and mass change measurements were carried out with fixed applied potential of 1.8 V vs. RHE using EQCM's.

interesting. They suggest that Fe incorporation in the beginning is insufficient to lead to increased activity, but sufficient to lead to decreased activity due to the iron incorporated cobalt oxyhydroxide components. Subsequently the Fe incorporation becomes sufficient to cause an improved OER activity after a certain point. It was found that this V-shape behaviour of the Si photoanode with $Co/NiCoO_x$ is not a coincidence, but reproducible, as an additional CA experiment using a new, but similar, sample showed the same time-dependent behaviour (see Figure S6).

The electrochemical properties of $NiCoO_x$ thin film deposited on EQCM sample were investigated by means of cyclic voltammetry and chronoampherommetry in 1 M KOH (TraceSelect) under dark condition (Figure 5). The as-deposited $NiCoO_x$ films (Figure 5, black trace) show quite good performance for the OER. An overpotential of ~ 380 mV is required to achieve a current density of 10 mA cm^{-2} which is in good agreement with the overpotentials obtained in the photoelectrochemical tests (Figure 4a). Nevertheless, after 10 cycles the potential at 10 mA cm^{-2} is shifted anodically by 30 mV. The anodic shift closely resembles the drop in current density in the long-term stability PEC tests and the corresponding anodic shift of the cyclic voltammetry curves (Figure 4a). Subsequent 2 hours long chronoampherommetry measurement (Figure 5a inset) showed increase in current density along with mass change during the first 0.5 hours. Afterwards, the $NiCoO_x$ thin film deposited on EQCM were intentional doped with Fe (Figure 5b, $NiCoO_x$ in KOH with 0.5 mM Fe) according to a procedure previously used for NiO thin films[16]. The EQCM result (Figure 5b

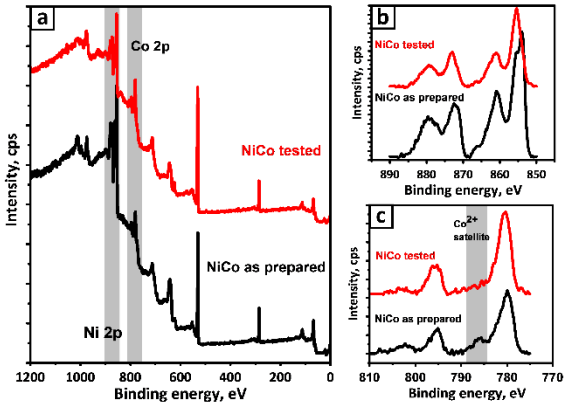

Figure 6 (a) XPS survey spectra of the $NiCoO_x$ thin film deposited on EQCM substrate with Co interlayer, and zoomed in (b) Ni 2p XPS spectra, (c) Co 2p region. Black and red color correspond to the curve for the as prepared and after the electrochemical test, respectively.

inset) shows a significant increase in mass during treatment of NiO in a Fe-containing solution, which was found to be saturated after ~ 0.5 h of treatment. Irrespective of obtained mass amount, this behaviour is similar to the behaviour of mass change for as-deposited $NiCoO_x$ in Figure 5a. We attribute this increase in mass at least partially to Fe incorporation occurring in parallel to oxygen evolution. Interestingly, in the subsequently performed cyclic voltammetry measurement (Figure 5b) a cathodic shift of 60 mV compared to the as-prepared $NiCoO_x$ thin film was observed. Thus, an overpotential of ~ 320 mV was required to obtain a current density of 10 mA cm^{-2}. This enhanced performance of the Fe-doped $NiCoO_x$ thin film is in good agreement with the enhancement during prolonged chronoampherommetry of the $NiCoO_x$ thin film used for the back-illuminated PEC studies and can therefore be attributed to a self-driven enhancement of nickel cobalt oxide by metallic Fe-contamination during photoelectrochemical oxygen evolution reaction. To further elaborate on this X-ray photoelectron spectroscopy was performed. XPS measurements were performed on as-prepared $NiCoO_x$ thin films (prepared on EQCM substrates) and on $NiCoO_x$ thin films after 24h of continuous operation at a potential of 1.8 V vs. RHE. Detailed scans of the Ni 2p and Co 2p regions derived from the survey spectra in Figure 6a are included in Figure 6b and 6c. The as prepared $NiCoO_x$ thin film consists of a mixture of Ni^{2+}/Ni^{3+} (at binding energies of 854/856 eV) and Co^{2+}/Co^{3+} (suggested by the satellite feature at 785 eV). After continuous testing for 24 h XPS measurements reveal that Ni and Co are mainly present in their 3+ oxidation state (binding energy of 856 eV for Ni^{3+} shown in Figure 6b. For Co^{3+} a characteristic binding energy of 780.5 eV was measured. Furthermore, the characteristic Co^{2+} satellite signal at 785 eV was significantly reduced as shown in Figure 6c). The presence of different oxidation states in the as-prepared $NiCoO_x$ thin film as well as its further oxidation during prolonged testing is in good agreement with previously reported NiO thin films prepared and tested under similar conditions[16] and can be ascribed to the transformation into its more porous NiOOH and CoOOH oxidation states which act as host for Fe-impurities[19,33]. The direct detection of Fe by means of XPS is not possible in this case due to the Al source's strong overlap with Ni LMM Auger signal and the unfavorable Fe cross section. However, the transformations into more open NiOOH and CoOOH in the $NiCoO_x$ thin film accompanied with the presented data of $NiCoO_x$ studied on EQCM substrate strongly suggest the self-driven enhancement of nickel cobalt oxide by metallic Fe-contamination during prolonged photoelectrochemical oxygen evolution reaction. In addition, Ni and Fe distribution mapped by EDX (Figure S7) of the porous $NiCoO_x$ deposited on the Si photoanode after 6 days of CA testing at 1.2 V versus RHE also supports the presence of Fe, along with above mentioned EQCM results.

Conclusions

A back-illuminated n^+pp^+-Si has been coupled to earth-abundant Ni-Co based catalysts and investigated as photoanode for the oxygen evolution reaction. Specifically we have demonstrated the performance of a n^+pp^+-Si/Co/$NiCoO_x$ structure, whose pn-junction is formed at the side opposing the solid/liquid interface, may efficiently drive the OER under back side (dry side) illumination which will be the actual operational condition in a tandem water splitting device. Importantly, taking advantage of the synergetic effects between nickel and cobalt, the $NiCoO_x$ OER catalyst coating exhibit excellent catalytic activity as well as long-term stability in highly concentrated alkaline media, which makes it a prospective candidate for the practical OER catalysts. Interestingly, the photoanode samples coupled to $NiCoO_x$ showed a non-trivial time-dependent current-voltage behaviour in OER activity. The sample studied exhibits an anodic shift of onset potential, then rebounded cathodically 1M KOH – likely due to Fe incorporation with NiOOH and CoOOH which act as a host for Fe incorporation. This work highlights an approach to using a low band gap photoanode in actual tandem device operation condition, and enhancing its photocatalytic activity simply by an aging process.

Acknowledgements

This work was performed as a part of the Center for Individual Nanoparticle Functionality (CINF) which is funded by Danish National Research Foundation (DNRF54).

References

1. N. S. Lewis and D. G. Nocera, Powering the planet: chemical challenges in solar energy utilization, *Proc. Natl. Acad. Sci. U. S. A.*, 2006, **103**, 15729–15735.
2. A. B. Laursen, S. Kegnæs, S. Dahl, I. Chorkendorff, Molybdenum sulfides—efficient and viable materials for electro - and photoelectrocatalytic hydrogen evolution, *Energy Environ. Sci.*, 2012, **5**, 5577-5591.
3. S. Dah, I. Chorkendorff, Solar-fuel generation: Towards practical implementation, *Nat. Mater.*, 2012, **11**, 100–101.
4. Y. Lee, J. Suntivich, K. J. May, E. E. Perry, Y. Shao-Horn, Synthesis and activities of rutile IrO_2 and RuO_2 nanoparticles for oxygen evolution in acid and alkaline solutions, *J. Phys. Chem. Lett.*, 2012, **3**, 399–404.
5. E. A. Paoli, F. Masini, R. Frydendal, D. Deiana, C. Schlaup, M. Malizia, T. W. Hansen, S. Horch, I. E. L. Stephens, I. Chorkendorff, Oxygen evolution on well-characterized massselected Ru and RuO_2 nanoparticles, *Chem. Sci.*, 2015, **6**, 190-196.
6. B. Mei, B. Seger, T. Pedersen, M. Malizia, O. Hansen, I. Chorkendorff, Protection of p^+-n-Si photoanodes by sputter-deposited Ir/IrO_x thin films, *J. Phys. Chem. Lett.*, 2014, **5**, 1948-1952.
7. W. Chen, H. Wang, Y. Li, Y. Liu, J. Sun, S. Lee, J.-S. Lee, Y. Cui, In situ

electrochemical oxidation tuning of transition metal disulfides to oxides for enhanced water oxidation, *ACS Cent. Sci.*, 2015, **1**, 244-251.

8. W. T. Hong, M. Risch, K. A. Stoerzinger, A. Grimaud, J. Suntivich, Y. Shao-Horn, Toward the rational design of non-precious transition metal oxides for oxygen electrocatalysis, *Energy Environ. Sci.*, 2015, **8**, 1404-1427.
9. H. B. Wu, H. Pang, X. W. Lou, Facile synthesis of mesoporous $Ni_{0.3}Co_{2.7}O_4$ hierarchical structures for high-performance supercapacitors, *Energy Environ. Sci.*, 2013, **6**, 3619-3626.
10. C. Zhu, D. Wen, S. Leubner, M. Oschatz, W. Liu, M. Holzschuh, F. Simon, S. Kaskel, A. Eychmu, Nickel cobalt oxide hollow nanosponges as advanced electrocatalysts for the oxygen evolution reaction, *Chem. Commun.*, 2015, **51**, 7851-7854.
11. M. Hussain, Z. H. Ibupoto, M. A. Abbasi, X. Liu, O. Nur, M. Willander, Synthesis of three dimensional nickel cobalt oxide nanoneedles on nickel foam, their characterization and glucose sensing application, *Sensors*, 2014, **14**, 5415-5425.
12. S. Goodwin-Johansson, P. H. Holloway, G. McGuire, L. Buckley, R. Cozzens, R. Schwarz, G. Exarhos, Artificial eyelid for protection of optical sensors, in Smart Structures and Materials 2000: Electroactive polymer actuators and devices, *Proc. of SPIE*, 2000, **3987**, 225-231.
13. L. Trotochaud, S. L. Young, J. K. Ranney, S. W. Boettcher, Nickel−iron oxyhydroxide oxygen-evolution electrocatalysts: The role of intentional and incidental iron incorporation, *J. Am. Chem. Soc.*, 2014, **136**, 6744-6753.
14. D. Friebel, M. W. Louie, M. Bajdich, K. E. Sanwald, Y. Cai, A. M. Wise, M.-J. Cheng, D. Sokaras, T.-C. Weng, R. A. Mori, R. C. Davis, J. R. Bargar, J. K. Nørskov, A. Nilsson, A. T. Bell, Identification of highly active Fe sites in (Ni,Fe)OOH for electrocatalytic water splitting, *J. Am. Chem. Soc.*, 2015, **137**, 1305-1313.
15. D. A. Corrigan, R. S. Conell, C. A. Fierro, D. A. Scherson, In-situ Moessbauer study of redox processes in a composite hydroxide of iron and nickel, *J. Phys. Chem.*, 1987, **91**, 5009-5011.
16. B. Mei, A. A. Permyakova, R. Frydendal, D. Bae, T. Pedersen, P. Malacrida, O. Hansen, I. E. L. Stephens, P. C. K. Vesborg, B. Seger, I. Chorkendorff, Iron-Treated NiO as a highly transparent p-type protection layer for efficient Si-based photoanodes, *J. Phys. Chem. Lett.*, 2014, **5**, 3456-3461.
17. J. A. Haber, Y. Cai, S. Jung, C. Xiang, S. Mitrovic, J. Jin, A. T. Bell, J. M. Gregoire, Discovering Ce-rich oxygen evolution catalysts, from high throughput screening to water electrolysis, *Energy Environ. Sci.*, 2014, **7**, 682-688.
18. J. B. Gerken, S. E. Shaner, R. C. Massé, N. J. Porubsky, S. S. Stahl, A survey of diverse earth abundant oxygen evolution electrocatalysts showing enhanced activity from Ni–Fe oxides containing a third metal, *Energy Environ. Sci.*, 2014, **7**, 2376-2382.
19. J. Yang, K. Walczak, E. Anzenberg, F. M. Toma, G. Yuan, J. Beeman, A. Schwartzberg, Y. Lin, M. Hettick, A. Javey, J. W. Ager, J. Yano, H. Frei, I. D. Sharp, Efficient and sustained photoelectrochemical water oxidation by cobalt Oxide/Silicon photoanodes with nanotextured interfaces, *J. Am. Chem. Soc.*, 2014, **136**, 6191-6194.
20. I. M. Sadiek, A. M. Mohammad, M. E. El-Shakre, M. I. Awad, M. S. El-Deab, B. E. El-Anadouli, Electrocatalytic evolution of oxygen gas at cobalt oxide nanoparticles modified electrodes, *Int. J. Electrochem. Sci.*, 2012, **7**, 3350-3361.
21. Y. Zhao, S. Chen, B. Sun, D. Su, X. Huang, H. Liu, Y. Yan, K. Sun, G. Wang, Graphene-Co_3O_4 nanocomposite as electrocatalyst with high performance for oxygen evolution reaction, *Sci. Rep.*, 2015, **5**, 7629.
22. X. Zhou, R. Liu, K. Sun, D. Friedrich, M. T. McDowell, F. Yang, S. T. Omelchenko, F. H. Saadi, A. C. Nielander, S. Yalamanchili, K. M. Papadantonakis, B. S. Brunschwig and N. S. Lewis, Interface engineering of the photoelectrochemical performance of Ni-oxide-coated n-Si photoanodes by atomic-layer deposition of ultrathin films of cobalt oxide, *Energy Environ. Sci.*, 2015, just accepted, DOI: 10.1039/C5EE01687H.
23. K.Sun, F. H. Saadi, M. F. Lichterman, W. G. Hale, H.-P. Wang, X. Zhou, N. T. Plymale, S. T. Omelchenko, J.-H. Hee, K. M. Papadantonakis, B. S. Brunschwig, N. S. Lewis, Stable solar-driven oxidation of water by semiconducting photoanodes protected by transparent catalytic nickel oxide films, *Proc. Natl. Acad. Sci. U. S. A.*, 2015, **12**, 3612-3617.
24. B. Beverskog, I. Puigdomenech, Revised Pourbaix Diagrams for Nickel at 25−300 °C, *Corros. Sci.*, 1997, **39**, 969−980.
25. E. M. Garcia, J. S. Santos, E. C. Pereira, M. B. J. G. Freitas, Electrodeposition of cobalt from spent Li-ion battery cathodes by the electrochemistry quartz crystal microbalance technique, *J. Power Sources*, 2008, **185**, 549-553.
26. D. Bae, T. Pedersen, B. Seger, M. Malizia, A. Kuznetsov, O. Hansen, I. Chorkendorff, P. C. K. Vesborg, Back-illuminated Si photocathode: a combined experimental and theoretical study for photocatalytic hydrogen evolution, *Energy Environ. Sci.*, 2015, **8**, 650-660.
27. K. J. J. Mayrhofer, G. K. H. Wiberg, M. Arenz, Impact of glass corrosion on the electrocatalysis on Pt electrodes in alkaline electrolyte, *J. Electrochem. Soc.*, 2008, **155**, 1-5.
28. X. Chen, J. P. Cheng, Q. L. Shou, F. Liu, X. B. Zhang, Effect of calcination temperature on the porous structure of cobalt oxide micro-flowers, *CrystEngComm*, 2012, **14**, 1271-1276.
29. J. F. Marco, J. R. Gancedo, M. Gracia, J. L. Gautier, E. I. Ríos, H. M. Palmer, C. Greaves, F. J. Berry, Cation distribution and magnetic structure of the ferrimagnetic spinel $NiCo_2O_4$, *J. Mater. Chem.*, 2001, **11**, 3087-3093.
30. G. Wu, N. Li, D.-R. Zhou, K. Mitsuo, B.-Q. Xu, Anodically electrodeposited Co+Ni mixed oxide electrode: preparation and electrocatalytic activity for oxygen evolution in alkaline media, *J. Solid State Chem.*, 2004, **177**, 3682-3692.
31. P. Rasiyah, A. C. C. Tseung, A mechanistic study of oxygen evolution on $NiCo_2O_4$, *J. Electrochem. Soc.*, 1983, **130**, 2384-2386.
32. H. S. Jeon, J. H. Koh, S. J. Park, M. S. Jee, D.-H. Ko, Y. J. Hwang, B. K. Min, A monolithic and standalone solar-fuel device having comparable efficiency to photosynthesis in nature, *J. Mater. Chem. A*, 2015, **3**, 5835-5842.
33. M. S. Burke, M. G. Kast, L. Trotochaud, A. M. Smith, S. W. Boettcher, Cobalt−iron (oxy)hydroxide oxygen evolution electrocatalysts: The role of structure and composition on activity, stability, and mechanism, *J. Am. Chem. Soc.*, 2015, **137**, 3638−3648.
34. F. A. Armstrong, Dynamic electrochemistry of iron-sulfur proteins, in: Advances in inorganic chemistry vol. 38: Iron-sulfur proteins, ed. R. Cammack, Academic Press, London, 1992, p. 125.
35. D. E. Pissinis, L. E. Sereno, J. M. Marioli, Utilization of special potential scan programs for cyclic voltammetric development of different nickel oxide-hydroxide species on Ni based electrodes, *Open J. Phys. Chem.*, 2012, **2**, 23-33.
36. S. Kim, D. A. Tryk, M. R. Antonio, D. Scherson, Applications of X-ray absorption fine structure to the in situ study of the effect of cobalt in nickel hydrous oxide electrodes for fuel cells and rechargeable batteries, *preprint of ACS symposium on recent advances in fuel cells*, batteries, 1993 Fall (Chicago) **38** (4), 1457-1463.
37. D. A. Corrigan, R. M. Bendert, Effect of coprecipitated metal ions on the electrochemistry of nickel hydroxide thin films: Cyclic voltammetry in 1M KOH, *J. Electrochem. Soc.*, 1989, **136**, 723-728.

Protection of Si photocathode using TiO_2 deposited by high power impulse magnetron sputtering for H_2 evolution in alkaline media

Dowon Bae[1], Seyedmohammad Shayestehaminzadeh[2], Einar B. Thorsteinsson[2], Thomas Pedersen[3] Ole Hansen[1,3], Brian Seger[1], Peter C.K. Vesborg[1], Sveinn Olafsson[2], Ib Chorkendorff[1†]*

[1]Center for Individual Nanoparticle Functionality, Department of Physics, Technical University of Denmark, Building 311, Fysikvej, DK-2800 Kgs, Lyngby, Denmark

[2]Science Institute, University of Iceland, Dunhaga 3, 107 Reykjavik, Iceland

[3]Department of Micro- and Nanotechnology, Technical University of Denmark, DK-2800 Kgs. Lyngby, Denmark.

**Current address: Institute of Materials Chemistry, RWTH Aachen University, Kopernikusstr. 10, DE-52074 Aachen, Germany*

[†]Corresponding author E-mail: ibchork@fysik.dtu.dk; Tel: +45) 45 25 31 70; Fax: +45) 45 93 23 99

Keywords: photocatalysis, titanium dioxide, high power impulse magnetron sputtering, hydrogen evolution

Abstract

Si is an excellent absorber material to be used in photoelectrochemical (PEC) hydrogen production. Only a few studies have been done using Si in alkaline electrolyte for hydrogen evolution due to its poor chemical stability in high pH electrolyte, indicating that a chemically stable protection layer is essential. Here we investigate thin TiO_2 films deposited by high power impulse magnetron sputtering (HiPIMS) as protection layer for a p-type silicon photocathode for photoelectrochemical H_2 evolution in high pH electrolyte. The X-ray reflectometry analysis reveals that the HiPIMS process provides improved film density for TiO_2 films (4.15 g/cm^3), and consequently a significantly less corroded Si surface is obtained. The Si photocathode protected by the HiPIMS grown TiO_2 film along with Pt as co-catalyst afforded a photocurrent onset potential of ~ 0.5 V vs. RHE in 1 M KOH, showing 4% decay over 24 h in KOH, whereas the sample with the TiO_2 deposited using conventional DC sputtering technique of similar thickness shows 20% loss in photocurrent for the same time interval. Considering the experiments were carried out not in the cleanroom, much less corrosion loss can be obtained if done in dust-free condition. Hence, it suggests the HiPIMS technique as an improved approach for the protection of photoelectrodes, which are unstable in alkaline solution.

1. Introduction

Photoelectrochemical (PEC) solar fuel conversion is a promising approach to solar fuel generation because of the direct conversion of solar energy into hydrogen. To date, considerable effort has been invested to identify durable photoactive semiconductor materials [1-6]. Si is one of the most studied

materials, which is potentially able to perform effective photocatalytic hydrogen evolution in an acidic electrolyte [2,3,7,8]. While Si easily passivates to SiO_2 in an acidic environment (which covers the surface and hinders current flow), previous research [3,8,9], has shown that TiO_2 can be used as an intermediate layer between the photoabsorber and the catalyst with good chemical stability under the hydrogen evolution reaction (HER) at pH 0. This approach prevents Si from passivating, thus allowing efficient PEC activity. Even if there are pinholes, which allow the electrolyte to contact the Si, the Si will only be locally passivated (the passivation is self-limiting in acid). Thus there will be no noticeable effect on overall performance.

Since the eventual role of Si in this work is for use as a photocathode in a 2-photon overall water splitting system [8,9], Si will need to perform in the same electrolyte as the photoanode side. Also there are no good oxygen evolution reaction (OER) - catalysts without noble metals, which are stable in acid electrolyte, alkaline electrolytes have a key advantage because non-noble OER catalysts with reasonable activity exist which may allow substantial cost savings and better scalability [10,11, 12]. Beyond the stability of the catalyst there is also the issue of stability of the light absorber. For instance, most potential absorber materials quite easily dissolve or photocorrode in acidic solution while many show stable photocatalytic performance in neutral and alkaline electrolytes [10-15]. For Si, however, it is the other way around. When Si interacts with alkaline solution it corrodes via dissolution since SiO_2 is not stable under alkaline conditions and therefore the self-limiting passivation mechanism does not work at high pH media. The lack of a self-limiting passivation entails that the underlying Si under any pinholes in a protection layer will corrode continuously. Thus, preventing pinholes in protection layers is mandatory in alkaline environments.

Fortunately TiO_2 has a wide stability window and even at pH > 15 implying that Si protected by a dense layer of TiO_2 can also be employed in alkaline electrolyte as demonstrated in recent research which used Si protected by atomic layer deposited (ALD) TiO_2 for the oxygen evolution reaction (OER) [16]. However, to the best of our knowledge, only a few stability studies under HER condition have been carried out using the Si-based electrode in high pH alkaline electrolyte. Kast et al. [17] demonstrated a ~ 24 h stable HER photocurrent using Si protected by solution processed TiO_2/F:SnO_2/Ti multilayer. Meanwhile, Feng et al. [18] demonstrated the Si photocathode protected by Ni/Ti metallic bilayer showing slow degradation after the 12h of HER due to the gradual loss of Ni in KOH. A protective oxide layer deposited by atomic layer deposition [19-21] can provide precisely controlled surface coverage, but it may be not very practical for high throughput production [22]. This study aims to evaluate the advantage of high power impulse magnetron sputtering (HiPIMS) grown TiO_2 as a conducting protective material for HER in a high pH alkaline solution.

We evaluate the chemical stability and photo-electrochemical stability of TiO_2 deposited on pn^+-Si photocathodes using HiPIMS and conventional DC magnetron sputtering (DCMS) for the reference sample.

HiPIMS is a novel ionized physical vapor deposition technique in which its major advantages include a denser coating and smoother surface morphology [23,24] due to a high degree of ionization of plasma (up to10^{13} ions cm^{-3} [25]) containing high fractions of target metal and reactive gas ions. Consequently, the grown film has an enhanced corrosion resistance without large-scale defects [26]. The main focus is on investigating the effect of TiO_2 packing density and tighter grain boundaries on its protection performance in 1M KOH electrolyte. Here, we compare the TiO_2 films grown by mentioned deposition methods (DCMS and HiPIMS) at various growth temperatures. Hence, the effect of the improved film density on the stability and durability of the films is investigated in high pH electrolyte (1M KOH) under dark conditions. Furthermore, we evaluate the long-term photocatalytic H_2 production performance using TiO_2/Ti/pn^+-Si electrodes under illumination in the same electrolyte condition as mentioned above. Finally, we examine the correlation of the stability of TiO_2-protected electrodes with the TiO_2 packing density measured by means of X-ray reflectometry.

2. Experimental details

2.1. Si-based photocathode fabrication process

Czochralski crystalline silicon (CZ c-Si) based photocathodes were fabricated as previously described [8,9]. The shallow pn^+-junction was formed on p-type (100) Si wafers (Topsil, 1-20 ohm-cm, boron-doped) with $POCl_3$ as the phosphorus dopant source for n^+ doping using a vapor phase surface doping process in an atmospheric pressure tube furnace. The doping process was carried out at 900℃ for 10 min. Subsequently a shallow pn^+-junction was formed on the surface of the p-type wafer, which was expected to form a depletion width of approximately 500 nm [8]. As previously shown [8,9], the pn-junction screens the band-bending in Si from the electrolyte (buried junction), which allows for increased photovoltage. A 3 μm deep part of the pn^+-Si was patterned by photolithography technique and etched away by reactive ion etching (SF_6, O_2 and C_4F_8 gases were used in a Pegasus DRIE system from SPTS Technologies) to fabricate a 10 mm diameter isolated circular pn^+-junction area (mesa structure).

Ti and TiO_2 protecting layers were grown by the DCMS and HiPIMS processes. In case of DCMS process, the Si samples were sputter-cleaned by Ar to remove any adventitious carbon-based contaminations and oxide layers at 35 W for 120 s. Then, approximately 8 nm of Ti was deposited followed by 100 nm of TiO_2 under oxygen and argon gas flow using conventional DC power mode. The base pressure of the vacuum chamber (AJA inc.) was below $8x10^{-8}$ mbar. The detailed procedure can be found elsewhere [8,9].

For the case of HiPIMS process, the samples were cleaned ultrasonically using isopropanol, acetone, and methanol each for 5 min. In order to remove the native oxide, the samples were dipped in HF acid (4%) for 5 min then taken out of HF and put into DI water and carried over to the chamber to be loaded. Before

loading, the samples were taken out of the DI water and dried by blowing N_2 on them. A custom-built sputtering chamber was employed to perform the following depositions. The base pressure of the chamber was below $5x10^{-9}$ mbar. A 3 inch (75 mm) Ti target with the purity of 99.995% was used in a planar magnetron system for growth of both Ti and TiO_2 layers. The sputtering gas was Ar (99.999%) for the case of Ti growth and Ar mixed with O_2 (99.999%) in the case of TiO_2 growth. Total growth pressures of $4x10^{-3}$ mbar for the growth of Ti and $7x10^{-3}$ mbar for the growth of TiO_2 were achieved using an adjustable throttle valve. To prevent any deposition gradient due to the chamber geometry, the samples were rotated during growth.

In the case of the HiPIMS grown Ti interlayers, the power was supplied by a SPIK1000A pulse unit (Melec GmbH) operating in the unipolar negative mode at constant voltage, which in turn was charged by a dc power supply (ADL GS30). The discharge current and voltage were monitored using a combined current transformer and voltage divider unit (Melec GmbH). LabVIEW software acquired the data and calculated the average power using the measured discharge current and voltage for each applied pulse and then set pulse repetition frequency. The pulse repetition frequency was 50 Hz. The pulse length was 110 μs and the cathode voltage was set to 485 V. The resulting average power was then 120 – 125 W and the achieved target peak power density was ~ 850 – 900 W cm^{-2}. The Ti interlayer growth temperature was room temperature (hereafter RT). Using such parameters resulted in 5 Å/min of growth rate and approximately 10 nm Ti with native oxide.

The TiO_2 films were grown using the same setup for HiPIMS grown Ti layers. The pulse voltage was 423 V with 200 μs long duration at frequency of 270 Hz. The average power and peak power density during growth were 340 W and 240 W cm^{-2}, respectively. The TiO_2 layers were grown at various growth temperatures of RT, 300, 400, and 500˚C. The mentioned growth parameters resulted in growth rate of 5 nm/min and the growth time of 20 min produced 100 nm TiO_2 layers. The growth temperature was kept steady during the deposition.

Ohmic contacts were made using an eutectic gallium-indium alloy and Cu-wire on the backside of the Si substrates as described elsewhere [8,9]. The inactive parts of the electrodes were covered with epoxy, and the Pt was deposited as a co-catalyst by having 500 ng (Pt basis) of a dinitrosulfatoplatinate solution drop-cast on the TiO_2 surface as described previously [8,9,19]. Since the Pt exists in form of well distributed nanoparticles its effect on the protective property of TiO_2 is negligible. Schematic drawings of samples used in this work are shown in Figure1.

2.2. Characterization

In order to determine the structural properties and stoichiometry of TiO_2 films X-ray reflectometry (XRR) and grazing incidence diffractometry (GIXRD) measurements were performed using a

PANalytical's X'pert diffractometer (Cu K_α, wavelength 0.1541 nm) mounted with a hybrid monochromator/mirror on the incident side and a 0.27˚ collimator on the diffracted side. A line focus was used with a beam width of approximately 1 mm. Using low–angle XRR measurements, the film thickness, film density and surface roughness can be obtained with an angular resolution of 0.001˚. The Parratt formalism [27] for reflectivity was used to fit the XRR data and gave an accuracy of 0.1 nm for thickness analysis The growth rates were calculated based on the fitting results of thickness analysis. The GIXRD scans were carried out with the incident beam at $\theta = 1^\circ$ to investigate the crystalline structure of the films.

The corrosion test under the dark condition was carried out in a Teflon beaker with 1M KOH (Sigma-Aldrich 99.995%) for 3 days. As-prepared electrodes with TiO_2 protection layers were dipped into the KOH solution and attached on the cell wall vertically. Number and size of cavities were quantified using the image analysis program ImageJ (1.46r) after the experiments.

A 1000 W Xenon lamp (Oriel) was used with a 635 nm cut-off filter and an AM1.5 filter to simulate the red part of the solar spectrum. The light intensity reaching the sample was measured with a spectrophotometer (Ocean Optics Inc, USB4000-UV-Vis), and the light intensity was adjusted to match that of the total light intensity of red part of the AM 1.5G solar spectrum ($635 \leq \lambda \leq 1020$ nm, 38.6 mW cm^{-2}). For electrochemical measurements a Bio-Logic VSP potentiostat was used using EC Lab software. All cyclic voltammograms (CV) and chronoamperometry (CA) experiments were done in a quartz cell with a 1M KOH electrolyte. For all CVs the electrodes were scanned at a sweep rate of 10 mV s^{-1}. A Pt mesh was used as a counter electrode and the reference was a Teflon incased Hg/HgO electrode (Koslow Scientific Company). Glass corrodes in an alkaline solution and the arising contaminants and/or poisoning of the Pt catalyst (mainly due to lead and silica) [28,29] can significantly influence the HOR/HER activity of Pt electrodes, and therefore the samples were rinsed with deionized water and piranha solution every 8 hours for removing any organic impurities that may have accumulated, and then re-platinized using same method abovementioned to evaluate the protection property of TiO_2 layer (and not the contamination of the Pt catalyst).

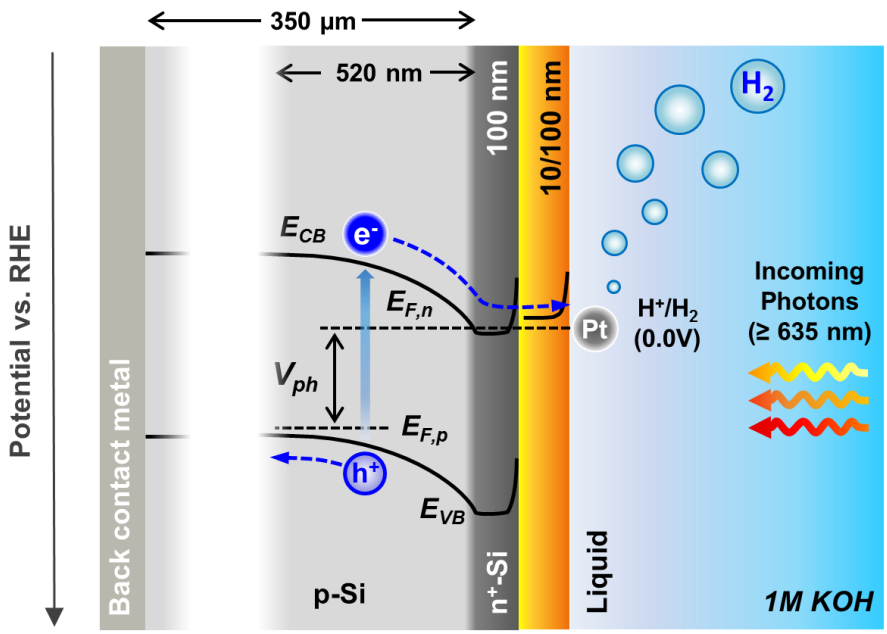

Figure 1. Schematic cross section of the sample used for photocatalytic activity (HER) experiments. The light is illuminated at the TiO_2 side. Schematic energy diagram of the illuminated sample in equilibrium with H^+/H_2 reaction is also shown. The detailed procedure for depletion width calculation can be found in the previous studies [8,9].

3. Results and discussion

3.1. Characterization of TiO_2 layers

Physical properties of TiO_2 layers were investigated by GIXRD, XRR, and cross sectional SEM measurements. In general, the rutile phase is the most stable structure of TiO_2, while the anatase phase can transform to rutile phase at high temperatures (500 ~ 700˚C [30,31]). In the present work, as expected, TiO_2 shows a strong phase dependency on the substrate growth temperature. The peaks corresponding to the anatase and rutile phases of TiO_2 are marked with *A* and *R* in GIXRD patterns (Figure 2a,b), respectively. The patterns reveal that the crystalline structure of anatase is well preserved even at high temperature with trace of rutile phase, indicating that both DCMS and HiPIMS grown TiO_2 films have a mixture of anatase and rutile phases. However it has to be pointed out that the HiPIMS grown films are mostly in rutile phase for higher growth temperatures. A transition from anatase to rutile is also obvious as the growth temperature is increased and it is more pronounced for the films deposited at 500˚C. The crystallinity of both anatase and rutile phases obviously increases with increased growth temperature, as shown by the reduced full width at half maximum (FWHM) of the peaks. Based on the relationship between the broadening of XRD peaks and crystallite size by the Scherrer method [32], it was found that the crystallite size of TiO_2 increased with growth temperature. Generally, increasing of the TiO_2 crystallite size is accompanied by a distinct decrease in its surface area [33,34], and consequently the TiO_2 deposited at high temperature should have

relatively less pinholes which can be formed at the grain boundaries. Interestingly, the reference sample protected by the DCMS grown TiO_2 shows peaks from TiO_2 anatase (mainly) and rutile mixed phases in its GIXRD pattern, and this may be due to the relatively low energy distribution of the sputtered ions at DCMS discharge condition which reduce the diffusivity of the incoming species on the substrate surface, and thus forms relatively lower density phase (anantase), restricting densification of the grown film [35,36].

The XRR measurements were conducted to quantify the film density of the TiO_2 layers deposited on the Si substrate. The density of the films (shown in Figure 3) was extracted from the numerical calculation as a result of fitting the XRR patterns (Figure S1 in SI‡) using Parratt formalism [27,37]. As expected from the GIXRD measurements, the values plotted in Figure 2b demonstrate the film density increases with increasing growth temperature for both DCMS and HiPIMS grown films. In addition, the HiPIMS grown TiO_2 shows a higher film density than the TiO_2 deposited by DCMS. The HiPIMS grown TiO_2 film shows its maximum film density of 4.15 g/cm^3 at 400˚C (see Figure 2c), which is enhanced by around 20.6 % and 15.0 % compared to that of the sample deposited at room temperature (RT) and the reference sample deposited by DCMS at the same growth temperature, respectively. Another interesting aspect is the decreased film density of TiO_2 grown at 500˚C. On one hand, Alzamani *et al.* reported [38] that a too high growth temperature might lead to non-uniformity and crack formation of TiO_2 films, and increased porosity consequently. However, any obvious microscopic scale crack formation on TiO_2 layer has not been found under SEM investigation (will be discussed later). On the other hand, elevating the growth temperature up to 500˚C can also cause the diffusion of pre-deposited Ti into the Si and formation of an intermixed interface [39]. Cross-sectional SEM investigation (Figure 4) well demonstrates the irregular boundary between the Si and TiO_2 layer due to the intermixing of Ti and Si at 500˚C (Figure 4b) whereas clear and planar boundary between Si and TiO_2 is observed at 400˚C (Figure 4a) indicating that decrease of film density at 500˚C can be ascribed to the thermal diffusion of Ti at too high temperature (EDX profile can be found in Figure S2 in SI‡).

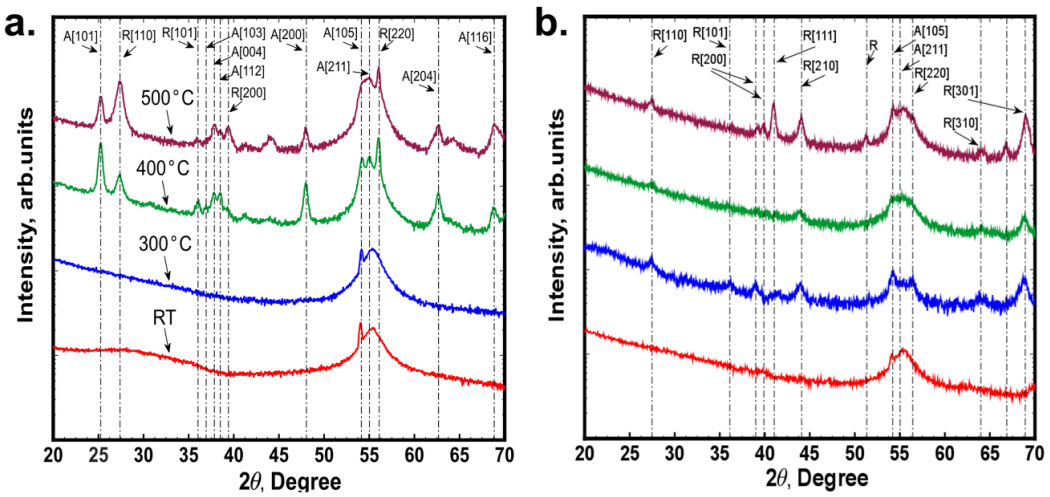

Figure 2. GIXRD patterns of DCMS grown (a) and HiPIMS grown (b) TiO_2 deposited on Si substrate at various temperatures (RT, 300˚C, 400˚C and 500˚C). The anatase and rutile phases of TiO_2 are marked with *A* and *R*, respectively.

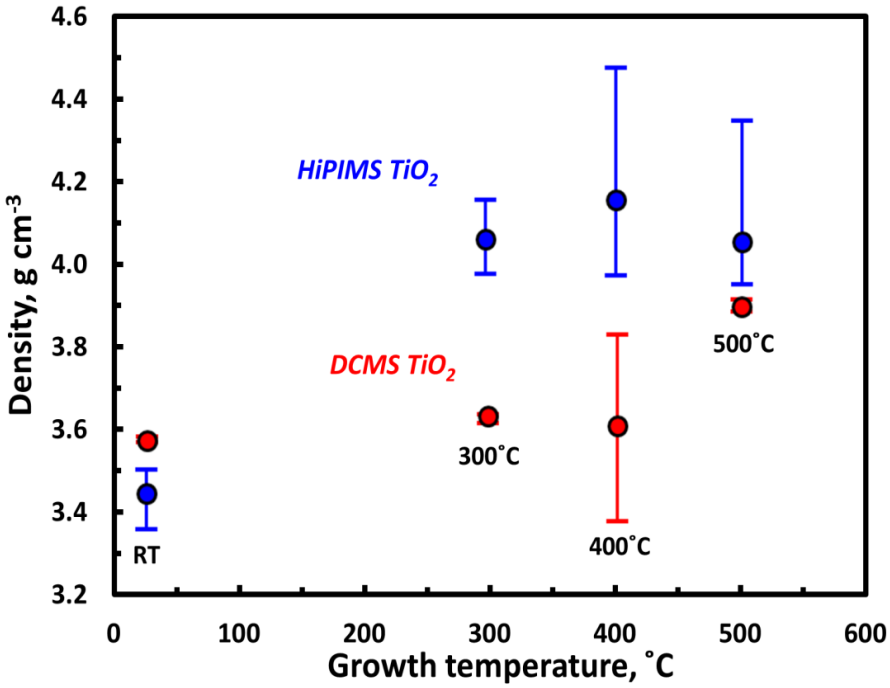

Figure 3. The film density of the DCMS grown (red) and HiPIMS grown (blue) TiO_2 deposited on Si substrates at various temperatures (RT, 300˚C, 400˚C and 500˚C) derived from the XRR pattern (Figure S1 in SI‡) fitting.

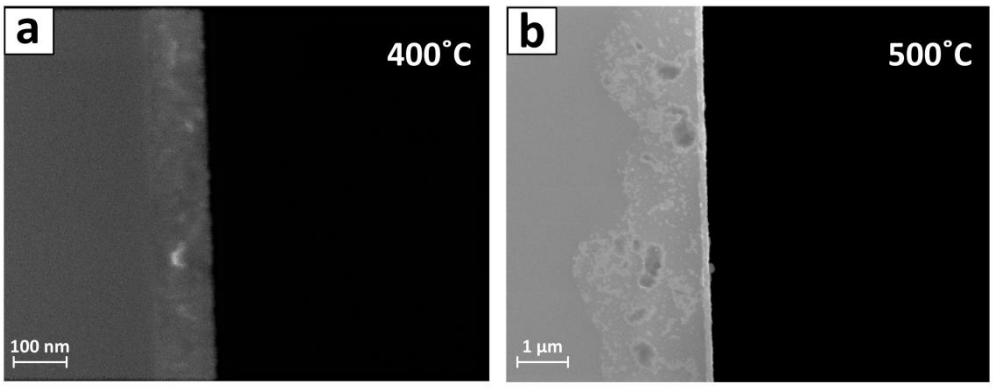

Figure 4. Cross-sectional SEM images of TiO_2 deposited on Si substrate at 400˚C (a) and 500˚C (b). A clear planar interface between the Si and the TiO_2 deposited at 400˚C can be found whereas an irregular interface, which is due to the intermixing/interdiffusion of Ti with/into Si (confirmed by EDX), is observed from the TiO_2 sample deposited at 500˚C.

3.2. Chemical stability test results

The Si photocathode samples were immersed in 1M KOH, which was the same electrolyte used for photoelectrochemical testing. As shown in Figure 5a, severe surface damage was observed after a 3 days immersion test from the unprotected Si surface, whereas the Si surface protected by the DCMS grown TiO_2 layer at 400˚C showed a flat surface with distributed typical pyramid-like pits in the Si due to due to the anisotropic corrosion rate between the <100> and <111> planes of Si [40]. The formation of a large number of (inverse) pyramids on TiO_2 protected side is clear evidence that the current sputtered TiO_2 layer cannot properly prevent the corrosion of Si in KOH. The high magnification plane-view SEM micrographs (see insets of Figure 5a) further show that the damage (i.e. etching process) begins on the Si underneath the TiO_2 protection layer. The Si etching can be explained by the presence of pin-holes within the TiO_2 layer, through which highly concentrated KOH permeates, and results in the corrosion of the underlying Si as illustrated in Figure 5b. As the etching process progresses, the width of pyramid increases, which leaves the top TiO_2 protection layer without a substrate to support it. Thus underetching of TiO_2 eventually occurs and causes delamination of the film. Logically, the higher film density results in minimizing the number of pinholes, and thus enhances the protection of the underlying Si.

While the vast majority of the pinholes led to square-like etch pits, there were a few large cracks in the film that were irregularly shaped. Upon careful examination it was realized that this is most likely due to dust particles that had settled on the Si before Ti or TiO_2 deposition. Dust particles can easily be larger than the TiO_2 thickness. These large dust particles could potentially form cracks in the TiO_2 film and subsequently increased corrosion. In this case the shape of the Si corrosion pit should be as irregular as the dust particle which causes it. Neither the DCMS nor the HiPIMS sputter chamber were located in a clean room, so dust deposition was an issue we could minimize, but not eliminate. Nevertheless, the degradation effect caused

by pinholes was more pronounced than that of caused by dust (as seen by the SEM images in Figure 6 for both DCMS and HiPIMS). Therefore the dust issue has no bearing on the comparison between the two methods.

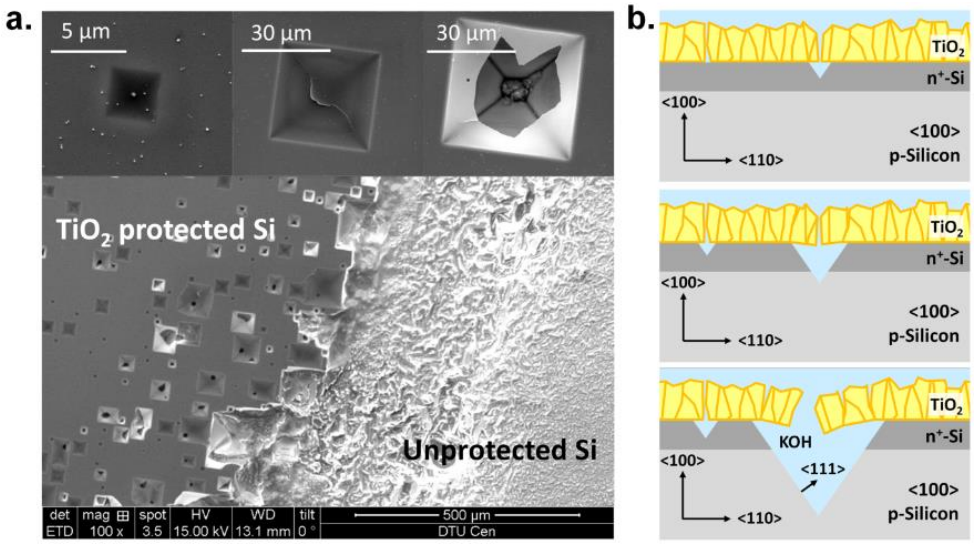

Figure 5. SEM images of a <100> oriented Si substrate with and without DCMS deposited TiO_2 at 400˚C after immersion in an 1M KOH electrolyte for 3 days (a), and shape illustrations of the etch profiles of a <100> oriented silicon with TiO_2 protection layer during etching process in KOH solution.

Both the DCMS and HiPIMS grown TiO_2 layers at various growth temperatures have been evaluated in 1M KOH for 3 days under dark condition. As shown in Figure 6 (a ~ h), the Si electrodes with the HiPIMS grown TiO_2 protection layer shows superior stability to those with the DCMS grown TiO_2 layer for all growth temperatures. The number of pyramid etch pits and their average size have been used as indicators to quantify the protection efficiency of the TiO_2 films. Figure 7 shows that the advantage of using HiPIMS for the growth of TiO_2 as a protection layer is a significantly reduced average etch pit size. The HiPIMS deposited TiO_2 samples showed 5 ~ 20 times smaller size compared to the DCMS deposited TiO_2 samples for the entire growth temperature range. It is worth noticing that the number of holes per specific area (inset of Figure 7) is almost unchanged regardless of deposition type but varies with the growth temperature. This result agrees well with previous reports that the elevated growth temperature enhances the packing density of TiO_2 film [41] due to the improved mobility of adatoms on the film surface [41,42], and consequently, this implies that sufficient thermal energy should be provided to secure good surface coverage as well as high density of sputtered ions as mentioned earlier. Also note that both DCMS and HiPIMS deposited TiO_2 samples at 500˚C show slightly increased hole density compared to those that deposited at 400˚C. Naturally, this can be attributed to the decreased film density owing to the Ti and Si intermixing as shown in Figure 4b.

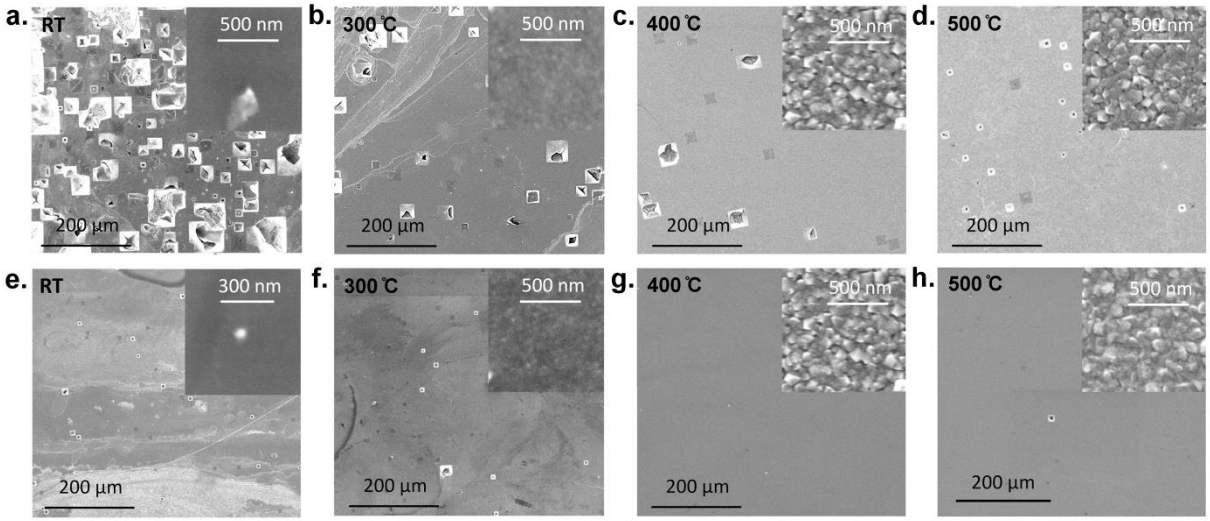

Figure 6. Surface SEM images of Si photoelectrodes with TiO_2 film deposited by DCMS (a ~ d) and HiPIMS (e ~ h) at different growth temperatures (a, e – room temperature; b, f - 300˚C; c, g - 400˚C and d, h - 500˚C).

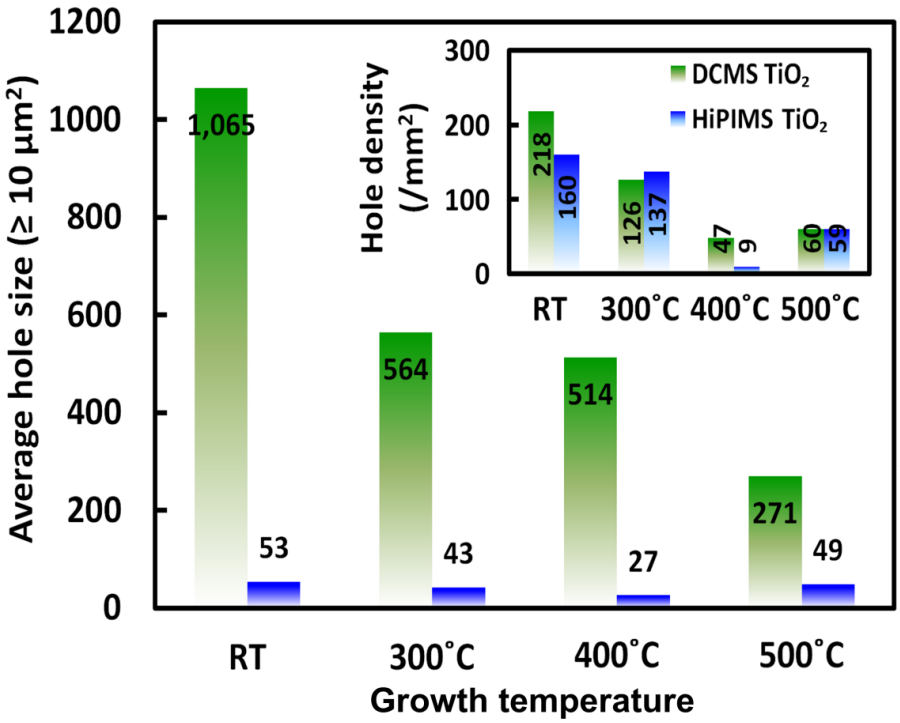

Figure 7. Average hole size and the hole density as an inset (counted larger than 10 μm^2 only) measured from the samples in Figure 6 after the 3 days dipping test in 1M KOH under the dark.

3.3. Photoelectrochemical test results

The primary purpose of this work is to protect Si photoelectrode during its photocatalytic HER in 1M KOH electrolyte. We have already observed that the HiPIMS grown TiO_2 layer has significantly enhanced protection properties compared to that deposited by DCMS, but it does not directly show that it can be applied to a photoelectrode as a protection layer. The photoelectrode must remain conductive during

photoelectrochemical testing, in order that the injection of photo-generated carriers toward the electrolyte through the Pt catalysts is not limited as shown in schematic drawing of Figure 1.

To examine the effectiveness of the HiPIMS grown TiO_2 film as a protection layer, CAs with periodical CVs were conducted in 1M KOH electrolyte for 24 hours under the red-part of AM 1.5g illumination (635 nm cut-off filter and AM 1.5g filters have been used for experiments). The samples were re-platinized every 8 hours since the corroded Si and other trace metals may lead contamination of Pt, and consequently lower the current density [28,29]. The CV characteristics in Figure 8 reflect both the protection property of the HiPIMS grown TiO_2 film and charge transfer occurring across the solid/liquid interface. Throughout all growth temperatures, the initial CVs of samples with the HiPIMS grown TiO_2 films illustrate that the charge transfer through the HiPIMS grown TiO_2 film has good conductivity and the TiO_2/Pt interface seems to have a good ohmic contact since they showed similar onset voltage (~ 0.5 V vs. RHE) and slopes to that of the reference sample with the DCMS grown TiO_2 protection layer. In addition, the sample with the HiPIMS grown TiO_2 film at 400˚C showed considerably enhanced stability compared to the sample grown by DCMS with TiO_2 protection layer at the same growth temperature. As shown in Figure 8d, photocurrent saturation of the sample with the HiPIMS grown TiO_2 protection layer at 400˚C decreased by approximately 4% from its initial photocurrent, whereas the reference sample with the DCMS grown TiO_2 protection layer showed almost 20% decreased photocurrent after 24 hours. On the other hand, it was found that the photocurrent degradation rate of the samples with the HiPIMS deposited TiO_2 at room temperature (Figure 8b) and 300˚C (Figure 8c) show approximately 30 % and 10 % degradation in photocurrent after 24 hours long-term test. Therefore it indicates that the protection property of TiO_2 increases with the growth temperature up to 400˚C. Interestingly, the stability of the HiPIMS grown TiO_2 sample at RT is less than the reference DCMS grown TiO_2 sample even though it showed smaller etch pit size in Figure 6e. It seems that this may be attributed to the TiO_2 layer peeling off from the surface during the hydrogen gas bubbling process due to the residual stress of TiO_2 which could not be relaxed by annealing [42], and consequently lowered the adhesion property of TiO_2 [43].

One other remarkable aspect is that the onset voltage is anodically shifted with time concurrent with the decrease of photocurrent. On the assumption that the deposited Pt catalyst reaches the same activity after every re-platinization process, an obvious decrease of onset voltage from Figure 8a, b, c is mainly attributed to the damaged pn-junction by KOH. As shown in our previous study, the flat-band potential (V_{fb}) of the p-type Si-water junction places severe restrictions on the voltage in an aqueous electrolyte (≈ 0.2 V vs. RHE), and thus charge separation will only happen at low potential below its V_{fb} [44]. Since the highly doped n^+ region is around 100 nm deep from the liquid/solid interface, long KOH exposure times can significantly etch away this n^+ layer as shown in Figure 4b, and thus deteriorate the photovoltage produced by the Si. In the case of the HiPIMS grown TiO_2 at 500˚C, the sample showed a slight increase

in photocurrent degradation (≈ 5%) in comparison to that of the sample grown at 400˚C by HiPIMS. This result agrees with the film density measurement results using XRR and hole density measurement as shown in Figure 7. However the onset voltage of the HiPIMS grown TiO_2 at 500˚C decreased by approximately 25 mV compared to initial CVs of other samples. As shown in Figure 4b, Ti intermixing with Si has been found at 500˚C. The transition metals, such as Ti, Fe, and Cr are well-known metallic defects, which reduce the minority carrier diffusion length of Si significantly [45], and a previous study [46] has demonstrated that Si solar cell defected by metallic impurities have major reductions in their open circuit voltage (V_{oc}) as well as saturation photocurrent (J_{sc}), and this is in good agreement with the present results.

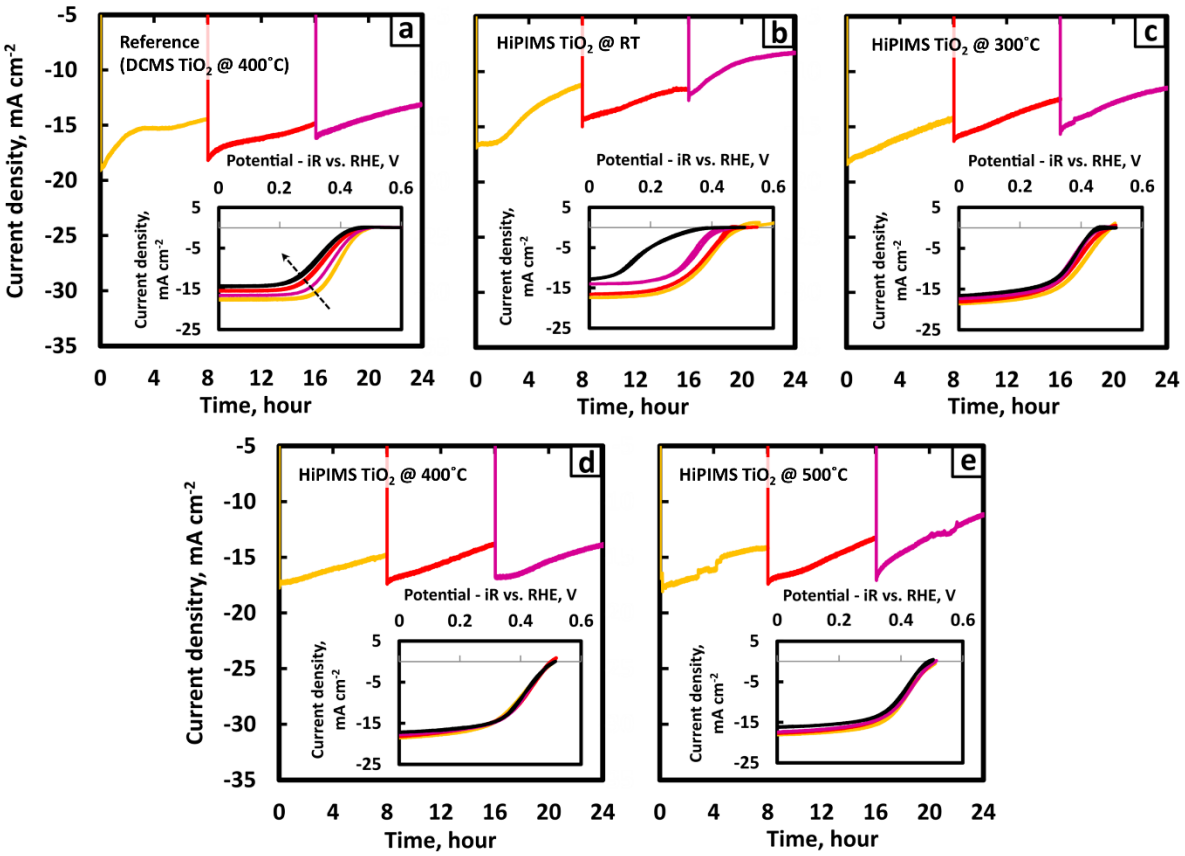

Figure 8. CAs of Si photocathodes with the reference DCMS grown TiO_2 (a), HiPIMS deposited TiO_2 at various growth temperatures (b ~ e). CVs (inset) were taken prior to the initial CA measurements (yellow), after 8 hours (red), after 16 hours (purple), and after 24 hours (black). The samples were re-platinized every 8 hours prior to the CV measurements. All measurements were done in 1M KOH electrolyte under illumination (the total irradiance is 38.6 mW/cm^2).

4. Conclusion

In summary, we demonstrated a Si based photocathode protected by the HiPIMS grown TiO_2 layer with good stability as well as high activity in 1M KOH (pH 14) under HER conditions. Deposition of TiO_2 using HiPIMS technique provides enhanced film density which surpassed that of the TiO_2 protection layer deposited by conventional DC sputtering technique. This approach resulted in an apparent enhanced stability owing to the higher degree of ionization for the HiPIMS plasma during sputtering process, and

consequently to the minimization of unprotected Si surface. The sample with the HiPIMS grown TiO_2 protection layer at 400˚C shows the minimum degradation rate (4%) in photocurrent after 24 hours long-term stability test, whereas the DCMS deposited TiO_2 at the same temperature shows significantly higher degradation rate (20%) with anodically shifted onset voltage due to the loss of the pn-junction area of Si. Increased growth temperature improves the stability of the photoelectrodes due to the increased film density of TiO_2 as well as improved adhesion between the TiO_2 and the substrate, but too high growth temperature (500˚C) causes intermixing of protection layer with substrate due to the thermal interdiffusion resulting in lowered photovoltage and photocurrent. Considering these experiments were not carried out in clean-room condition, much less corrosion loss can be obtained by minimizing dust build-up on the surface that potentially can form pin-holes. Furthermore, since the use of HiPIMS technique enables the fabrication of dense protection layers with high purity unlike those obtained from other technique such as sol-gel process, the HiPIMS approach involving TiO_2 or other metal oxides can be considered promising for photoelectrodes, which are unstable in alkaline solution.

Acknowledgements

This work was performed as a part of the Center for Individual Nanoparticle Functionality (CINF) which is funded by Danish National Research Foundation (DNRF54) and also it was partially funded by University of Iceland Research Fund.

‡Electronic Supplementary Information (SI) available: Supplementary information accompanies this paper including supplementary figures S1 and S2; Cross-sectional EDX profile for the HiPIMS grown TiO_2 deposited at 500˚C on Si; Experimental and fitted XRR data for the DCMS and HiPIMS grown TiO_2 layers.

1. X. Gao, S. Kocha, A.J. Frank, J. A. Turner, Photoelectrochemical decomposition of water using modified monolithic tandem cells, Int. J. Hydrogen Energ., 24 (1999) 319-325.
2. L. Ji, M. D. McDaniel, S. Wang, G. B. Posadas, X. Li, H. Huang, J. C. Lee, A. A. Demkov, A. J. Bard, J. G. Ekerdt, E. T. Yu, *A silicon-based photocathode for water reduction with an epitaxial $SrTiO_3$ protection layer and a nanostructured catalyst*, Nature Nanotech. 10 (2015) 84–90.
3. S. W. Boettcher, E. L. Warren, M. C. Putnam, E. A. Santori, D. Turner-Evans, M. D. Kelzenberg, M. G. Walter, J. R. McKone, B. S. Brunschwig, H. A. Atwater, N. S. Lewis, Photoelectrochemical hydrogen evolution using Si microwire Arrays, J. Am. Chem. Soc., 133 (2011) 1216-1219.
4. C. G. Morales-Guio, S. D. Tilley, H. Vrubel, M. Grätzel, X. Hu, Hydrogen evolution from a copper(I) oxide photocathode coated with an amorphous molybdenum sulphide catalyst, Nat. Commun., 5 (2014) 3059.
5. C.-W. Huang, C.-H. Liao, C.-H. Wu, J. C. S. Wu, *Photocatalytic water splitting to produce hydrogen using multi-junction solar cell with different deposited thin films*, Sol. Energ. Mat. Sol. C., 107 (2012) 322–328.

6. T. J. Jacobsson, V. Fjällström, M. Edoff, T. Edvinsson, *CIGS based devices for solar hydrogen production spanning from PEC-cells to PV-electrolyzers: A comparison of efficiency, stability and device topology*, Sol. Energ. Mat. Sol. C., 134 (2015) 185–193

7. J. D. Benck, S. C. Lee, K. D. Fong, J. Kibsgaard, R. Sinclair, T. F. Jaramillo, *Designing active and stable silicon photocathodes for solar hydrogen production using molybdenum sulfide nanomaterials*, Adv. Energy Mater., 4 (2014) 1400739.

8. B. Seger, T. Pedersen, A. B. Laursen, P. C. K. Vesborg, O. Hansen, I. Chorkendorff, *Using TiO_2 as a conductive protective layer for photocathodic H_2 evolution*, J. Am. Chem. Soc., 135 (2013) 1057−1064.

9. D. Bae, T. Pedersen, B. Seger, M. Malizia, A. Kuznetsov, O. Hansen, I. Chorkendorff, P. C. K. Vesborg, *Back-illuminated Si photocathode: a combined experimental and theoretical study for photocatalytic hydrogen evolution*, Energy Environ. Sci., 8 (2015) 650-660.

10. B. Mei, A. A. Permyakova, R. Frydendal, D. Bae, T. Pedersen, P. Malacrida, O. Hansen, I. E. L. Stephens, P. C. K. Vesborg, B. Seger, I. Chorkendorff, *Iron-Treated NiO as a highly transparent p-type protection layer for efficient Si-based photoanodes*, J. Phys. Chem. Lett., 5 (2014) 3456-3461.

11. M. J. Kenney, M. Gong, Y. Li, J. Z. Wu, J. Feng, M. Lanza, H. Dai, *High-performance silicon photoanodes passivated with ultrathin nickel films for water oxidation*, Science, 342 (2013) 836-840.

12. P. C. K. Vesborg, T. F. Jaramillo, *Addressing the terawatt challenge: scalability in the supply of chemical elements for renewable energy*, RSC Adv., 2 (2012) 7933-7947.

13. F. F. Abdi, L. Han, A. H. M. Smets, M. Zeman, B. Dam, R. van de Krol, Efficient solar water splitting by enhanced charge separation in a bismuth vanadate-silicon tandem photoelectrode, Nat. Commun., 4 (2013) 2195.

14. K. Sun, M. T. McDowell, A. C. Nielander, S. Hu, M. R. Shaner, F. Yang, B. S. Brunschwig, N. S. Lewis, Stable solar-driven water oxidation to O2(g) by Ni-oxide-coated silicon photoanodes, J. Phys. Chem. Lett., 6 (201) 592−598.

15. J. Yang, K. Walczak, E. Anzenberg, F. M. Toma, G. Yuan, J. Beeman, A. Schwartzberg, Y. Lin, M. Hettick, A. Javey, J. W. Ager, J. Yano, H. Frei, I. D. Sharp, Efficient and sustained photoelectrochemical water oxidation by cobalt oxide/silicon photoanodes with nanotextured interfaces, J. Am. Chem. Soc., 136 (2014) 6191−6194.

16. S. Hu, M. R. Shaner, J. A. Beardslee, M. Lichterman, B. S. Brunschwig, N. S. Lewis, *Amorphous TiO_2 coatings stabilize Si, GaAs, and GaP photoanodes for efficient water oxidation*, Science, 344 (2014) 1005-1009.

17. M. G. Kast, L. J. Enman, N. J. Gurnon, A. Nadarajah, S. W. Boettcher, *Solution-deposited $F:SnO_2/TiO_2$ as a base-stable protective layer and antireflective coating for microtextured buried-junction H_2-evolving Si photocathodes*, Appl. Mater. Interfaces, 6 (2014) 22830−22837.

18. J. Feng, M. Gong, M. J. Kenney, J. Z. Wu, B. Zhang, Y. Li, H. Dai, *Nickel coated silicon photocathode for water splitting in alkaline electrolytes*, Nano Res., DOI: 10.1007/s12274-014-0643-4.

19. B. Seger, D. S. Tilley, T. Pedersen, P. C. K. Vesborg, O. Hansen, M. Grätzel, I. Chorkendorff, *Silicon protected with atomic layer deposited TiO_2: durability studies of photocathodic H_2 evolution*, RSC Adv., 3 (2013) 25902.

20. Y. W. Chen, J. D. Prange, S. Dühnen, Y. Park, M. Gunji, C. E. D. Chidsey, P. C. McIntyre, *Atomic layer-deposited tunnel oxide stabilizes silicon photoanodes for water oxidation*, Nat. Mater., 10 (2011) 539–544.

21. N. C. Strandwitz, D. J. Comstock, R. L. Grimm, A. C. Nichols-Nielander, J. Elam, N. S. Lewis, *Photoelectrochemical behavior of n-Type Si(100) electrodes coated with thin films of manganese oxide grown by atomic layer deposition*, J. Phys. Chem. C, 117 (2013) 4931–4936.

22. M. Leskel, M. Ritala, *Atomic layer deposition chemistry: Recent developments and future challenges,* Angew. Chem. Int. Ed., 42 (2003) 5548 –5554.

23. K. Sarakinosa, J. Alami, S. Konstantinidis, *High power pulsed magnetron sputtering: A review on scientific and engineering state of the art*, Surf. Coat. Technol., 204 (2010) 1661–1684.

24. J. T. Gudmundsson, N. Brenning, D. Lundin, U. Helmersson, High power impulse magnetron sputtering discharge, J. Vac. Sci. Technol. A, 30 (2012) 030801.

25. A. P. Ehiasarian, R. New, W.-D. Münz, L. Hultman, U. Helmersson, V. Kouznetsov, *Influence of high power densities on the composition of pulsed magnetron plasmas*, Vacuum, 65 (2002) 147-154.

26. A. P Ehiasarian, W.-D Münz, L Hultman, U. Helmersson, I. Petrov, *High power pulsed magnetron sputtered CrN_x films*, Surf. Coat. Technol., 163-164 (2003) 267-272.

27. L. G. Parratt, *Surface studies of solids by total reflection of x-rays*, Phys. Rev., 95 (1954) 359-369.

28. K. J. J. Mayrhofer, A. S. Crampton, G. K. H. Wiberg, M. Arenz, *Analysis of the impact of individual glass constituents on electrocatalysis on Pt electrodes in alkaline solution*, J. Electrochem. Soc., 155 (2008) 78-81.

29. K. J. J. Mayrhofer, G. K. H. Wiberg, M. Arenz, *Impact of glass corrosion on the electrocatalysis on Pt electrodes in alkaline electrolyte*, J. Electrochem. Soc., 155 (2008) 1-5.

30. N. Wetchakun, B. Incessungvorn, K. Wetchakun, S. Phanichphant, *Influence of calcination temperature on anatase to rutile phase transformation in TiO_2 nanoparticles synthesized by the modified sol–gel method*, Mater. Lett., 82 (2012) 195-198.

31. A. E. Komlev, A. E. Lapshin, O. V. Magdysyuk, V. V. Plotnikov, V. I. Shapovalov, N. S. Shutova, *Effect of heat treatment on the structure of titanium dioxide f*ilms, Tech. Phys. Lett., 36 (2010) 942-944.

32. J. I. Langford, A. J. C. Wilson, *Scherrer after sixty years: A survey and some new results in the determination of crystallite size*, J. Appl. Cryst. 11 (1978) 102-113.

33. Y. Han, H.-S. Kim, H. Kim, *Relationship between synthesis conditions and photocatalytic activity of nanocrystalline TiO_2*, J. Nanometer., 2012 (2012) 427453.

34. Y.-F. Chena, C.-Y. Lee, M.-Y. Yeng, H.-T. Chiu, *The effect of calcination temperature on the crystallinity of TiO_2 nanopowders*, J. Cryst. Growth, 247 (2003) 363-370.

35. A. P. Ehiasarian, Y. A. Gonzalvo, T. D. Whitmore, *Time-resolved ionisation studies of the high power impulse magnetron discharge in mixed argon and nitrogen Aatmosphere*, Plasma Process. Polym., 4 (2007) S309-S313.

36. H. Wadley, X. Zhou, and W. H. Butler, *Atomic assembly of magnetoresistive multilayers*, in: D. Depla, S. Mahieu (Eds.), *Reactive sputter deposition,* Springer, Heidelberg, 2008, pp. 498-599.

37. D. Windover, E. Barnat, J. Y. Kim, M. Nielsen, T.-M. Lu, A. Kumar, H. Bakhru, C. Jin, S. L. Lee, *Thin film density determination by multiple radiation energy dispersive X-ray reflectivity*, JCPDS-International center of diffraction data 2000, Advances in X-ray analysis, Vol. 42.

38. M. Alzamani, A. Shokuhfar, E. Eghdam, S. Mastali, *Influence of catalyst on structural and morphological properties of TiO_2 nanostructured films prepared by sol–gel on glass*, Prog. Nat. Sci., 23 (2013) 77-84.

39. L. Borucki, R. Mann, G. Miles, J. Slinkman, T. Sullivan, *A model for titanium silicide film growth*, Int. Electron Devices Meeting Technol. Dig., (1988) 348-351.

40. N. C. Lindquist, P. Nagpal, K. M. McPeak, D. J. Norris, S.-H. Oh, *Engineering metallic nanostructures for plasmonics and nanophotonics*, Rep. Prog. Phys. 75 (2012) 036501.

41. G. L. Hornyak, H. F. Tibbals, J. Dutta, J. J. Moore, *Introduction to nanoscience & nanotechnology*, CRC Press, Newark, 2008.

42. H.-C. Chen, K.-S. Lee, C.-C. Lee, *Annealing dependence of residual stress and optical properties of TiO_2 thin films deposited by different deposition methods*, Appl. Opt., 47 (2008) 284-287.

43. Y. Chen, D. D. Dionysiou, *Effect of calcination temperature on the photocatalytic activity and adhesion of TiO_2 films prepared by the P-25 powder-modified sol-gel method*, J. Mol. Catal. A: Chem., 244 (2006) 73-82.

44. Y. Hou, B. L. Abrams, P. C. K. Vesborg, M. E. Björketun, K. Herbst, L. Bech, A. M. Setti, C. D. Damsgaard, T. Pedersen, O. Hansen, J. Rossmeisl, S. Dahl, J. K. Nørskov, I. Chorkendorff, *Bio-inspired co-catalysts bonded to a Silicon photocathode for solar hydrogen evolution*, Nat. Mater., 10 (2011) 434-438.

45. G. Coletti, P. C. P. Bronsveld, G. Hahn, W. Warta, D. Macdonald, B. Ceccaroli, K. Wambach, N. L. Quang, J. M. Fernandez, *Impact of metal contamination in silicon solar cells*, Adv. Funct. Mater., 21 (2011) 879–890.

46. B. Sopori, *Impurities and defects in photovoltaic Si devices: A review*, NREL report, NREL/CP-520-27524, 1999.